

Cross verified independent measurements of  
correlated bubble property distributions as part of the  
scale-up of a catalytic bubbling fluidized bed reactor

Présentée le 15 décembre 2022

Faculté des sciences de base  
Groupe Kröcher  
Programme doctoral en chimie et génie chimique

pour l'obtention du grade de Docteur ès Sciences

par

**Philipp Fedor RIECHMANN**

Acceptée sur proposition du jury

Prof. C. Bostedt, président du jury  
Prof. O. Kröcher, Dr T. J. Schildhauer, directeurs de thèse  
Prof. C. Boyce, rapporteur  
Prof. M. Lehner, rapporteur  
Dr M. Rüdisüli, rapporteur



In infinite time, in infinite matter, in infinite space, is formed a bubble organism,  
and that bubble lasts a while and bursts,  
and that bubble is Me.  
— Leo Tolstoy

Für meine Mutter...





# Acknowledgements

Throughout my research, I felt blessed to have been supported by my family, numerous friends, mentors and colleagues, who have all contributed in many different ways to the success of this work. I am very grateful for the support I received during the last couple of years, which I would like to acknowledge in the following.

I want to thank Prof. Oliver Kröcher for giving me the opportunity to write my doctoral thesis under his supervision, for his scientific guidance and for all his trust and support I received throughout my doctorate. I would also like to thank Prof. Markus Lehner, Prof. Chris Boyce and Dr. Martin Rüdisüli for their contribution as co-referees of this thesis and their valuable feedback and Prof. Christoph Bostedt for being the jury president. To my direct supervisor Dr. Tilman Schildhauer I want to express my gratitude for the many engaging and fruitful discussions we had. Our conversations were always driven by an inquisitive scientific approach, which often led to new creative ideas, theories and solutions. Above all, I truly appreciated his understanding and sincere encouragement during the more challenging phases of my work. I would also like to thank Dr. Serge Biollaz for giving me the opportunity to be part of his group and for all of the support for my projects.

I also want to express my appreciation for my colleagues Dr. Andreas Gantenbein, Dr. Frank Schillinger, Dr. Julia Witte and Dr. Emanuele Moioli, who I shared my office with over the last four years. The atmosphere was always great and I truly enjoyed the unique sense of humor that we developed together. I also want to thank Frank for providing an excellent starting point for my thesis and for the continued feedback throughout the years, even after he left PSI. A special thank you to Andreas, who was a great companion through the ups and downs of this PhD journey that we started and completed together.

I want to thank Hansjörg Wagenbach, Marcel Hottiger, Peter Hottinger and Daniel Willemin for their assistance with the construction and successful operation of several precisely designed experimental setups. Thank you to Daniel Meyer for his dedication to implement the control systems of several of these setups and for all of his technical aid, which made a smooth execution of the measurements possible. Sergio Rodríguez Durán, I thank you for teaching

---

me the operation of the GanyMeth pilot plant and various analytical devices. I also thank Martin Künstle for the many suggestions he gave me that often led to great improvements of the applied methods and especially for the cooperation during the measurement campaigns at the GanyMeth pilot plant. I am very thankful to the entire team I became a part of for all the support I received during the preparation and execution of the experiments as well as for the scientific interpretation of the results and above all for making my years at PSI an enjoyable experience filled with good memories. I thank you Julian Indlekofer, Tanja Wieseler, Dr. Hossein Madi, Dr. Adelaide Calbry-Muzyka, Jörg Schneebeil and Robert Janz for all the good talks and the many laughs we shared.

I would also like to acknowledge several people outside of PSI for their contributions to this work. I want to thank Roham Seif, who did his master thesis as well as an internship in our group. I especially appreciated his hard work during the preparation of the experiments in Delft, which greatly helped to enable a successful series of experiments. I thank our colleagues from TU Delft, Prof. Ruud van Ommen and Evert Wagner, for giving me the opportunity to conduct experiments at their excellent facilities, which provided experimental data that proved to be crucial for this thesis. I also want to thank them for all the great discussions and exchange of know-how and particularly Evert for his dedicated effort to ensure the experiments would be successful.

I want to give a special thank you to Aleksandra Treichel and Dr. Sebastian Hellmann, who I met on my very first day at PSI and who became dear friends since then. Thank you Aleks, for having my back especially during the final phase of my doctorate. You were there for me during the most stressful days and I am very grateful for that. Sebastian, I thank you for proofreading my thesis and providing very meticulous feedback and for all of your technical advice. I also want to thank my close friend Lukas Schnürpel for his sincere support throughout my PhD studies. I thank all three of you for being friends I know I can count on.

Jürgen Reimann and Volker Schmidt I want to thank you for giving me guidance and always having an open ear. No matter the situation of life I would be dealing with, you would always be able to recommend the perfect book on the subject. Thank you both.

Finally, I want to thank my mother for providing me with so many opportunities in life. Thank you so much for being there for me, for your love and patience over all these years. I would not have been able to achieve this without you. Thank you.

*Wettingen, 7<sup>th</sup> September 2022*

Philipp Fedor Riechmann

# Abstract

Methanation can be applied as part of a Power-to-Gas (PtG) concept to store renewable electricity. Using a catalytic bubbling fluidized bed (BFB) methanation reactor allows a flexible and economic operation. Properties of bubbles rising through the fluidized bed significantly influence the performance of such reactors. In this work, the hydrodynamics in a BFB reactor with vertical heat exchanger tubes are investigated. The aim is to develop and verify the experimental methods and to establish a hydrodynamic data base for the development of a reactor model, which shall facilitate the scale-up of the process towards an industrial scale. Independent experimental methods, namely X-ray tomography, X-ray radiography and optical probe measurements, have been applied to measure bubble property distributions and their correlations, and to cross verify the results. The X-ray measurements were conducted in a cold-flow model with and without vertical internals that represent the heat exchanger tubes. The cold-flow model matches the geometry of a pilot plant, referred to as GanyMeth, in which the optical probe measurements were carried out, to ensure the comparability of the results.

X-ray tomography was used to reconstruct individual bubbles in a BFB. It could be shown that the sizes, rise velocities and shapes of the bubbles are broadly distributed and correlated. When vertical internals are present, the mean sizes and rise velocities of the bubbles decrease, their shapes elongate on average and the mean cross-sectional bubble hold-up is reduced. Systematic tomography simulations were performed for the case without internals, to verify the applicability and to determine the limitations of the method. Accordingly, the results of all measurements conducted between the heights of 16 and 56 cm for fluidization numbers in the range of 1.5 – 6 are credible.

Radiographic X-ray imaging was used to independently verify the bubble size distributions in BFBs that were measured by means of X-ray tomography for a chosen measurement height and two superficial gas velocities without vertical internals. Through the measurement of injected single bubbles, the correlations between the size, rise velocity and shape of bubbles were also confirmed, again only for the case without internals. The evaluation of measurements with internals proved to be challenging: While a reduction of the bubble sizes and rise velocities could be confirmed, the shape of injected bubbles were observed to be flattened

---

rather than elongated as expected from the X-ray tomography results. X-ray radiography was also used to verify the optical probe methodology through simultaneous measurements of injected bubbles, and to assess the dynamic evolution of bubbles in BFBs qualitatively.

Comprehensive hydrodynamic experiments were conducted in the GanyMeth pilot plant. Chord lengths and rise velocities of bubbles were measured for two types of bed material, at seven pressures between 1 and 11 bar, at six fluidization numbers between 2 to 10, at six heights of up to 137 cm and six evenly spaced radial positions. With increasing pressures, the chord lengths shortened, the bubble hold-up increased and an earlier onset of slugging fluidization appeared to occur. The results at ambient pressure matched those obtained via X-ray tomography at comparable settings. The feasibility to retrieve the volume equivalent bubble diameters from the measured chord lengths and rise velocities could be demonstrated.

## **Keywords**

Power-to-gas, methanation, bubbling fluidized bed, hydrodynamic investigations, bubble property distributions, X-ray tomography, X-ray radiography, optical probe measurements

# Zusammenfassung

Methanisierung kann als Teil eines Power-to-Gas-Konzepts eingesetzt werden, um erneuerbaren Strom zu speichern. Der Einsatz eines katalytischen blasenbildenden Wirbelschichtreaktors (BBW) zur Methanisierung ermöglicht einen flexiblen und wirtschaftlichen Betrieb. Die Eigenschaften der in der Wirbelschicht aufsteigenden Blasen beeinflussen die Leistung solcher Reaktoren erheblich.

In dieser Arbeit wird die Hydrodynamik in einem BBW-Reaktor mit vertikalen Wärmeübertragerrohren untersucht. Ziel ist es, die notwendigen experimentellen Methoden zu entwickeln und zu verifizieren, um eine hydrodynamische Datenbasis für die Entwicklung eines Reaktormodells zu schaffen, welches die Risiken des Scale-up des Prozesses in den industriellen Maßstab verringern soll. Unabhängige experimentelle Methoden, nämlich Röntgentomographie, Röntgenradiographie und Messungen mit optischen Sonden, wurden angewandt, um die Verteilungen der Blaseneigenschaften und deren Korrelationen zu bestimmen und die Ergebnisse untereinander zu verifizieren. Die Röntgenmessungen wurden in einem Kaltströmungsmodell mit und ohne vertikale Einbauten, welche die Wärmeübertragerrohren repräsentieren, durchgeführt. Das Kaltströmungsmodell entspricht geometrisch der Pilotanlage GanyMeth, in welcher die Messungen mit den optischen Sonden durchgeführt wurden, um die Vergleichbarkeit der Ergebnisse zu gewährleisten.

Mit Hilfe der Röntgentomographie wurden einzelne Blasen in einer BBW rekonstruiert. Es konnte gezeigt werden, dass die Größen, Aufstiegsgeschwindigkeiten und Formen der Blasen breit verteilt und untereinander korreliert sind. Wenn vertikale Einbauten vorhanden sind, nehmen die mittleren Größen und Aufstiegsgeschwindigkeiten der Blasen ab, ihre Formen werden im Durchschnitt länglicher und die gemittelte Blasenfraktion ist geringer. Für den Fall ohne Einbauten wurden systematische Tomographiesimulationen durchgeführt, um die Anwendbarkeit zu überprüfen und die Grenzen der Methode zu ermitteln. Demnach sind die Ergebnisse aller Messungen, die im gegebenen Versuchsaufbau zwischen 16 und 56 cm Höhe für Fluidisierungszahlen im Bereich von 1,5 - 6 durchgeführt wurden, plausibel. Mit Hilfe der Röntgenradiographie wurden die mittels Röntgentomographie gemessenen Blasengrößenverteilungen in BBWen für eine ausgewählte Messhöhe und zwei Leerrohrgeschwindigkeiten

---

ohne vertikale Einbauten unabhängig verifiziert. Durch die Messung von injizierten Einzelblasen wurden die Korrelationen zwischen Größe, Aufstiegsgeschwindigkeit und Form der Blasen ebenfalls bestätigt, wiederum nur für den Fall ohne Einbauten. Die Interpretation der Messungen mit Einbauten erwiesen sich als schwierig: Während eine Verringerung der Blasengröße und der Aufstiegsgeschwindigkeit bestätigt werden konnte, wurde beobachtet, dass die Form der injizierten Blasen eher abgeflacht war. Dies steht im Gegensatz zu den Ergebnissen der Röntgentomographie, welche eine langgestreckte Blasenform erwarten ließen. Die Röntgentomographie wurde auch eingesetzt, um die Methodik der optischen Sonde durch gleichzeitige Messungen der injizierten Blasen zu verifizieren und die dynamische Entwicklung der Blasen in BBWen qualitativ zu bewerten.

In der GanyMeth-Pilotanlage wurden umfassende hydrodynamische Experimente durchgeführt. Die Sehnenlängen und Aufstiegsgeschwindigkeiten der Blasen wurden für zwei Arten von Bettmaterial, bei sieben Drücken zwischen 1 und 11 bar, bei sechs Fluidisierungszahlen zwischen 2 und 10, bei sechs Höhen von bis zu 137 cm und sechs gleichmäßig verteilten radialen Positionen gemessen. Mit zunehmendem Druck verkürzten sich die Sehnenlängen, die mittlere Blasenfraktion nahm zu und das so genannte „Slugging“ setzte scheinbar früher ein. Die Ergebnisse bei Umgebungsdruck stimmten mit denen überein, die mittels Röntgentomographie bei vergleichbaren Einstellungen erzielt wurden. Es konnte zudem gezeigt werden, dass die volumenäquivalenten Blasendurchmesser aus den gemessenen Sehnenlängen und Aufstiegsgeschwindigkeiten abgeleitet werden können.

## **Schlagwörter**

Power-to-Gas, Methanisierung, blasenbildende Wirbelschicht, hydrodynamische Untersuchungen, Blaseigenschaftenverteilungen, Röntgentomographie, Röntgenradiographie, optische Sondenmessungen

# Contents

<b>Acknowledgements</b>	<b>i</b>
<b>Abstract (English/Deutsch)</b>	<b>iii</b>
<b>List of Acronyms</b>	<b>xi</b>
<b>List of Symbols</b>	<b>xiii</b>
<b>1 Introduction</b>	<b>1</b>
1.1 Motivation . . . . .	1
1.2 Methanation processes . . . . .	4
1.2.1 Catalytic methanation . . . . .	5
1.3 Methanation research at PSI . . . . .	8
1.3.1 Process development and techno-economic analysis . . . . .	8
1.3.2 Catalyst lifetime investigations . . . . .	9
1.3.3 Hydrodynamic investigations . . . . .	10
1.4 Open research questions . . . . .	12
<b>2 Theory on fluidized bed technology</b>	<b>15</b>
2.1 Fluidization: Definition, history and applications . . . . .	15
2.2 Fundamental theory on fluidized beds . . . . .	17
2.2.1 Characterization of particles and fluids . . . . .	17
2.2.2 Minimum fluidization velocity . . . . .	22
2.2.3 Fluidization regimes . . . . .	24
2.3 Bubbling fluidized beds . . . . .	26
2.3.1 Two phase model . . . . .	27
2.3.2 Hydrodynamics in bubbling fluidized beds . . . . .	29
2.3.3 Bubble properties . . . . .	34
2.4 Scale-up of bubbling fluidized bed reactors . . . . .	38
2.4.1 General scale-up approach . . . . .	39
2.4.2 Hydrodynamic scale-up bubbling fluidized bed reactors . . . . .	40
2.4.3 Scale-up of reactive bubbling fluidized bed reactors . . . . .	41
	vii

2.4.4	Sectoral scale-up of bubbling fluidized bed reactors with internals . . . .	42
<b>3</b>	<b>Experimental setups</b>	<b>45</b>
3.1	Pilot-scale plant GanyMeth . . . . .	45
3.1.1	Functional description of the pilot plant GanyMeth . . . . .	46
3.2	Horizontal optical probes . . . . .	48
3.3	Cold-flow model . . . . .	51
3.3.1	X-ray measurement setups . . . . .	52
3.3.2	Single bubble injection setup . . . . .	55
3.3.3	Heat flux measurements . . . . .	57
3.4	Bed material . . . . .	58
<b>4</b>	<b>X-ray measurements</b>	<b>61</b>
4.1	X-ray attenuation measurements of bubbling fluidized beds . . . . .	62
4.2	X-ray tomography . . . . .	63
4.2.1	Tomographic reconstruction of the cross-sectional bubble hold-up . . .	64
4.2.2	Experimental methods . . . . .	67
4.2.3	Pseudo three-dimensional image reconstruction . . . . .	67
4.3	Results of X-ray tomography measurements without vertical internals . . . . .	72
4.3.1	Cross-sectional bubble hold-up . . . . .	73
4.3.2	Pseudo three-dimensional visualizations . . . . .	74
4.3.3	Statistical evaluation of the measured bubble properties . . . . .	78
4.3.4	Bubble property distributions and their correlations . . . . .	84
4.3.5	Fitted correlated bubble property distributions . . . . .	92
4.4	Verification of the applied X-ray tomography methods . . . . .	94
4.4.1	Tomography simulations . . . . .	94
4.4.2	Two-dimensional tomography simulations . . . . .	95
4.4.3	Dynamic bubble events . . . . .	98
4.4.4	Pseudo three-dimensional tomography simulation . . . . .	100
4.4.5	Post processing of the X-ray tomography measurements . . . . .	104
4.5	Results of X-ray tomography measurements with vertical internals . . . . .	106
4.5.1	Cross-sectional bubble hold-up . . . . .	109
4.5.2	Pseudo three-dimensional visualizations . . . . .	110
4.5.3	Statistical evaluation of the measured bubble properties . . . . .	114
4.5.4	Bubble property distributions and their correlations . . . . .	118
4.6	X-ray radiography measurements . . . . .	123
4.6.1	X-ray radiography calibration and evaluation . . . . .	124
4.6.2	X-ray radiography measurements of bubbling fluidized beds . . . . .	127
4.6.3	X-ray radiography measurements of injected bubbles . . . . .	132



4.6.4	Results of the X-ray radiography measurements of single injected bubbles	137
4.6.5	X-ray radiography measurements of controlled bubble interactions . . .	153
<b>5</b>	<b>Hydrodynamic measurements at the GanyMeth pilot plant</b>	<b>157</b>
5.1	Review on the influence of the pressure on the hydrodynamics in fluidized beds	159
5.2	Preparation of the measurements . . . . .	160
5.2.1	Overhaul of the electronic components of the optical sensor system . . .	160
5.2.2	Revision of the evaluation algorithm . . . . .	162
5.2.3	Limitations of the optical probe sensor system . . . . .	166
5.2.4	Estimation of geometric bubble property distributions from optical measurements . . . . .	170
5.2.5	Design of experiments . . . . .	175
5.3	Results of the measurements in the pilot plant GanyMeth . . . . .	180
5.3.1	Cross verification between the X-ray and optical probe measurements .	180
5.3.2	Measured cross-sectional bubble hold-up . . . . .	184
5.3.3	Measured mean bubble properties . . . . .	187
<b>6</b>	<b>Discussion, conclusions and outlook</b>	<b>193</b>
6.1	Achieved results . . . . .	194
6.1.1	X-Ray tomographic measurements . . . . .	194
6.1.2	X-Ray radiographic measurements . . . . .	195
6.1.3	Optical probe measurements . . . . .	196
6.2	Conclusions . . . . .	198
6.3	Recommendations for further research . . . . .	200
<b>A</b>	<b>Fitted distributions for the X-Ray tomography data</b>	<b>205</b>
	<b>Bibliography</b>	<b>213</b>
	<b>Curriculum Vitae</b>	<b>233</b>



# Acronyms

<b>AGA</b>	Adaptive Genetic Algorithm
<b>BET</b>	Brunauer-Emmett-Teller
<b>BFB</b>	bubbling fluidized bed
<b>CCUS</b>	carbon dioxide capture and use/storage
<b>CFB</b>	circulating fluidized bed
<b>CFD</b>	computational fluid dynamics
<b>DAC</b>	direct air capture
<b>ESI</b>	Energy System Integration
<b>FCC</b>	fluidized catalytic cracking
<b>FICFB</b>	fast internally circulating fluidized bed
<b>GEV</b>	generalized extreme value
<b>MFC</b>	mass flow controller
<b>MLR</b>	multiple linear regression
<b>MRI</b>	magnetic resonance imaging
<b>n.a.</b>	not available
<b>OSL</b>	one-step-late
<b>PDF</b>	probability density function
<b>PSD</b>	particle size distribution
<b>PSI</b>	Paul Scherrer Institute
<b>PtG</b>	Power-to-Gas
<b>RSD</b>	relative standard deviation
<b>RSE</b>	relative standard error
<b>SART</b>	Simultaneous Algebraic Reconstruction Technique

## Acronyms

---

<b>SEM</b>	scanning electron microscopy
<b>SNG</b>	synthetic natural gas
<b>TCP</b>	Thermochemical Processes
<b>TEA</b>	techno-economic analysis
<b>TFM</b>	two flow model
<b>XR-AD</b>	X-ray tomography area detector
<b>XR-LD</b>	X-ray tomography line detector

# Symbols and terms

$A$	surface area	[cm <sup>2</sup> ]
$A_R$	reactor cross section	[m <sup>2</sup> ]
$a_b$	specific surface area of bubble	[m <sup>2</sup> g <sup>-1</sup> ]
$a_e$	specific surface area of fitted ellipsoid	[m <sup>2</sup> g <sup>-1</sup> ]
$B$	bed depth	[cm]
$d$	distance	[cm]
$D$	reactor diameter, bed diameter	[cm]
$d_b$	bubble diameter	[cm]
$d_{b,eq}$	sphere volume equivalent bubble diameter	[cm]
$d_{b,horiz}$	horizontal bubble diameter	[cm]
$d_{b,hyd}$	hydraulic bubble diameter	[cm]
$d_{b,vert}$	vertical bubble diameter	[cm]
$d_p$	Sauter particle diameter	[cm]
$D$	reactor diameter, bed diameter	[cm]
$f$	measurement frequency	[Hz]
$H$	bed height	[cm]
$I$	radiation intensity	[W sr <sup>-1</sup> ]
$l_{chord}$	chord length	[cm]
$l : w$	aspect ratio: length to width	[-]
$p$	pressure	[bar]
$P$	probability	[%]
$r$	radial position	[mm]
$R$	reactor radius, bed radius	[cm]
$T$	temperature	[°C]

## Acronyms

---

$t$	time	[s]
$u$	superficial velocity	[m s <sup>-1</sup> ]
$u_{mf}$	minimum fluidization velocity	[m s <sup>-1</sup> ]
$u_{mb}$	minimum bubbling velocity	[m s <sup>-1</sup> ]
$u_b$	bubble phase velocity	[m s <sup>-1</sup> ]
$u_d$	dense phase velocity	[m s <sup>-1</sup> ]
$u_{br}$	single bubble rise velocity	[m s <sup>-1</sup> ]
$V$	volume	[cm <sup>3</sup> ]
$V_p$	total pore volume	[cm <sup>3</sup> g <sup>-1</sup> ]
$W$	weighting factor	[-]
$X_{cor}$	sample cross correlation function	[%]
$\epsilon$	bed voidage	[-]
$\epsilon_b$	bubble hold-up	[-]
$\eta$	dynamic viscosity	[Pa s]
$\nu$	kinematic viscosity	[m <sup>2</sup> s <sup>-1</sup> ]
$\mu$	attenuation coefficient	[m <sup>-1</sup> ]
$\rho$	density	[kg m <sup>-3</sup> ]
$\rho$	shape factor	[-]
$\tau$	signal length ratio	[-]
$\Theta$	wake angle	[°]

# 1 Introduction

## 1.1 Motivation

One of the biggest current challenges of humanity is the anthropogenic climate change, which will have drastic effects on the living conditions in a global scale, if we cannot reduce global warming significantly [1]–[3].

The implementation of renewable energies with the aim to reduce the emission of the greenhouse gas carbon dioxide ( $\text{CO}_2$ ) is one of the technical strategies to slow down and possibly stop the rise of the average global temperature.

Switzerland is committed to the Paris agreement on climate change from 2015 [4], which states that the greenhouse gas emissions will be halved by 2030 in comparison to what they were in 1990. It was also decided that no new nuclear power plants will be built, and that the existing ones may continue to operate as long as their safety can be ensured. Further, the Swiss federal council resolved to reach net zero greenhouse gas emissions also by 2050. The Energy Strategy 2050 [5] describes the framework for the energy policies of Switzerland to restructure the energy supply to reach these goals. Additionally, the share of renewable gases for domestic heating purposes in Switzerland will be increased to 30% by 2030 according to a declaration of the Swiss gas providers [6]. In the European Union, the share of renewable energies in the gross final consumption of energy has risen from 8.5% in 2004 to 17.5% in 2017 [7] and in Switzerland it was at 23.3% in 2018 [8]. The share of renewable energy sources for the consumed electricity was 31% for the European Union in 2017 and 55.7% for Switzerland in 2018, with a share of 15% for the EU and 3.25% for Switzerland generated from solar and wind [8], [9].

The transition to an increased use of solar and wind energy for the production of electricity is a technical challenge, due to the volatile nature of these energy sources. In order to guarantee

a stable supply of electricity, it is necessary to find technical solutions to adjust the production to the demand in long-, mid- and short-term time scales. New methods to store electricity in times of overproduction become therefore necessary. Fluctuations of the energy production on the minutely, hourly, daily and eventually weekly time scale can be managed reasonably by the utilization of technologies such as batteries [10], smart grid technologies [11], pumped hydro storage [12], compressed air energy storage [13] or industrial processes with flexible operation modes [14]. However, the seasonal imbalance of supply and demand of electricity that accompanies the increased use of renewable energies remains a challenge. While the demand for electricity peaks during winter, the availability of solar energy peaks during summer as shown in Figure 1.1 for Europe.

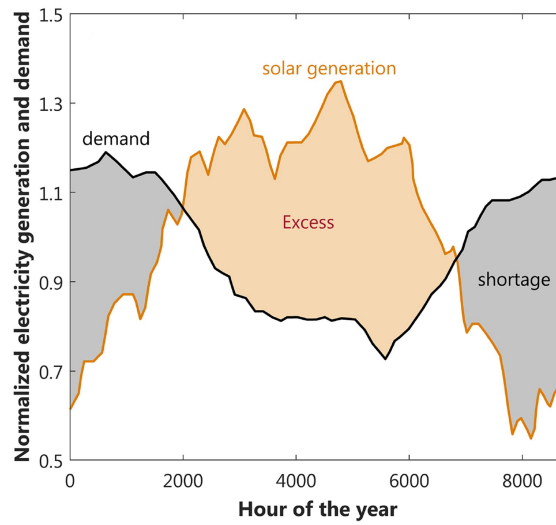
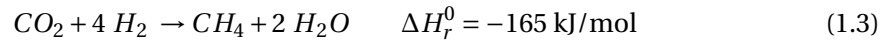
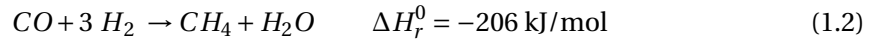
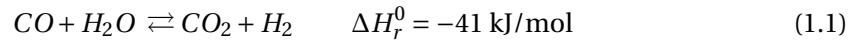


Figure 1.1: Comparison of the normalized annual electricity demand (black line) and solar generation (orange line) for Europe. Figure adapted from Gabrielle *et al.* [15].

Excess electricity can also be stored chemically through the electrolysis process, which uses electricity to produce hydrogen from water. The hydrogen can then be used to generate electric energy in a fuel cell at times of demand. However, large hydrogen storage capacities would be necessary for seasonal storage of energy in this way. Due to the volatility of hydrogen this is technically challenging and would require major capital investments[15], [16].

A possible solution to this issue could be the methanation process, in which the hydrogen is converted to methane ( $\text{CH}_4$ ) together with carbon dioxide ( $\text{CO}_2$ ) via the water-gas shift reaction, described by Equation 1.1 and the corresponding methanation Equations 1.2 and 1.3.





The advantage of the methanation of hydrogen is that methane can be stored and transported in the existing natural gas grid and consequentially there would not be a need to invest in additional storage infrastructure. The concept of storing electricity chemically in form of hydrogen or further as methane is generally referred to with the term Power-to-Gas (PtG).

At the Paul Scherrer Institute (PSI), the entire process chain of a PtG concept is being investigated. This includes research on electrolysis, fuel cells, biomass gasification, gas cleaning and upgrading, methanation as well as the techno-economic analysis of the process chain. Figure 1.2 shows the Energy System Integration (ESI) platform, which is a demonstration facility of the entire PtG process chain that is being developed at PSI.

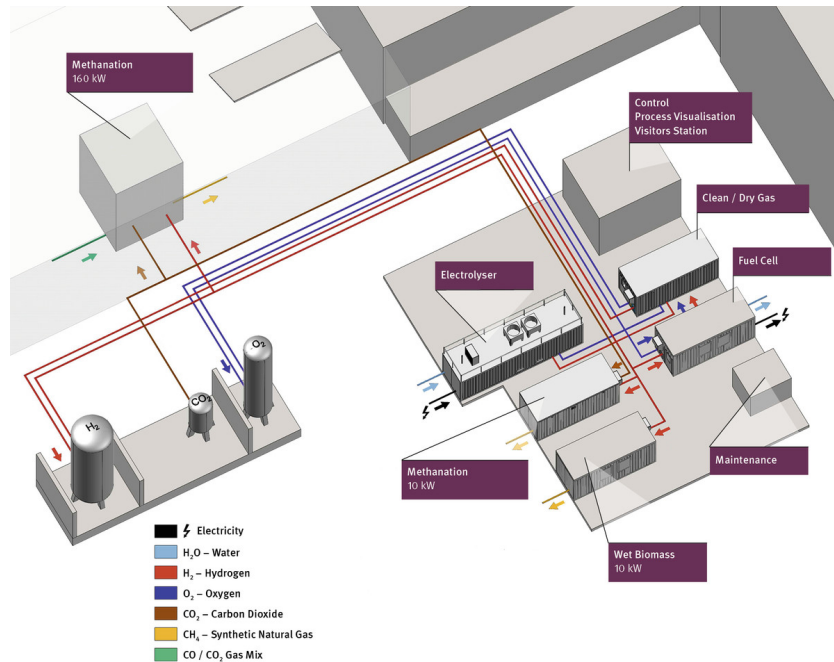


Figure 1.2: Energy System Integration (ESI) platform at the Paul Scherrer Institute (PSI).

### 1.2 Methanation processes

Sabatier and Senderens were the first to describe the methanation reaction in 1902 [17]. The first large scale industrial application of methanation was the removal of carbon monoxide from synthesis gases, in the Haber-Bosch and Fischer-Tropsch processes. Later, in the 1970s during the oil crisis, methanation was developed and later used for the production of synthetic natural gas (SNG) from coal. Recently, as part of the global initiative to reduce the emission of greenhouse gases, the methanation process has become popular for PtG applications and the upgrading of gas produced through biomass gasification, which still contains significant amounts of carbon dioxide [18], with added hydrogen from electrolysis. A comprehensive overview on methanation can be found in the review by Rönsch *et al.* [19], which covers the fundamentals, historical developments as shown in Figure 1.3, as well as recent trends. Kopyscinski *et al.* [20] provides an overview of the historical development of the production of SNG through the methanation process, which is closely related to the background of the research that led to this thesis.

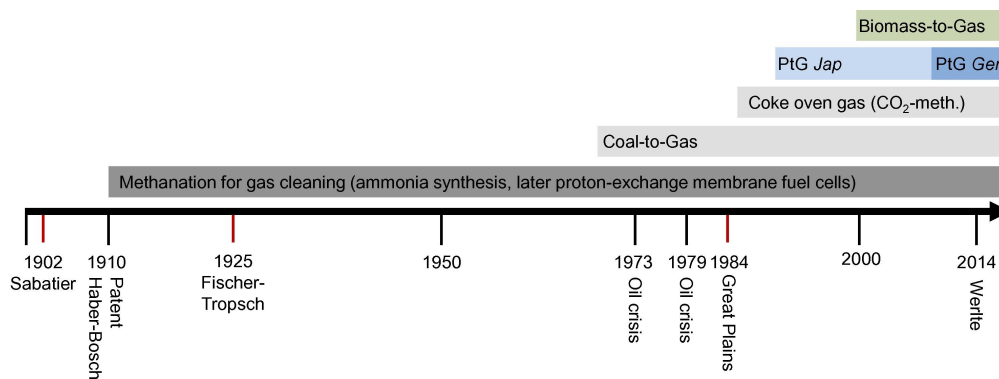


Figure 1.3: Historical development of methanation technology, adapted from Rönsch *et al.* [19].

There is a variety of potential CO<sub>2</sub> sources for the methanation process. One option is the application of methanation to upgrade gas obtained through the anaerobic digestion of biomass, which is often referred to simply as biogas. Due to the high concentrations of 30-50%v CO<sub>2</sub> in biogas, it is attractive for the methanation as part of a PtG concept [18]. However, biogas also contains various trace components in the ppb<sub>v</sub> – ppm<sub>v</sub> range of sulfur compounds, such as hydrogen sulfide (H<sub>2</sub>S), mercaptans/thiols, and others [18], [21] with significant variations in their concentrations, depending on changes in the feedstocks of the anaerobic digester [22]. Costly and technically challenging gas cleaning would therefore be necessary for the catalytic methanation to avoid the deactivation of the catalyst [21], [23]. Currently the investments in biogas plants remain low in Switzerland, with 1406 TJ produced from biomass and a combined 2497 TJ from waste and waste water treatment facilities in 2020 [24]. However, there is a large potential for available wet bioenergy resources suitable for

anaerobic digestion in Switzerland, which is estimated to reach 44.3 PJ in 2035 and 45.4 PJ in 2050 [25]. Other potential CO<sub>2</sub> sources could be direct carbon capture technologies, which can be divided into two categories: Direct air capture (DAC) technologies, which extract CO<sub>2</sub> directly from the air, and carbon dioxide capture and use/storage (CCUS) technologies that separate CO<sub>2</sub> from industrial flue gases [26]–[29]. Further viable options are capturing CO<sub>2</sub> as a byproduct of the lime, clinker, steel, ammonia, ethylene and methanol production [29], [30].

For the application in PtG process chains, two general methanation concepts can be applied: biological methanation and catalytic methanation. In biological methanation processes, methanogenic microorganisms are used to produce methane. It is operated at low temperatures below 65 °C and pressures below 15 bar, which are the necessary conditions to allow the growth of living microorganisms. Advantages of the biological methanation are the robustness to impurities in the reactant gas supply and the possibility for a wide range part load operation without the necessity of complex process control systems. However, due to the low mass transfer rates of hydrogen to the liquid phase, especially at these low pressures, biological methanation reactors suffer from lower space-time yields and therefore significantly larger reactors are necessary [23], [31], [32]. The research described in the present thesis is based on a catalytic methanation process, which will be discussed in greater detail in the following. Further information on biological methanation technology can be found in a review by Lecker *et al.* [33].

### 1.2.1 Catalytic methanation

The methanation reaction is highly exothermic and controlled by the chemical equilibrium. It is generally favored by lower temperatures of about 100 °C, where the conversion rate is close to 100% [34]. However, due to the low activity of the typically used catalysts at temperatures below 200 - 300 °C, catalytic methanation reactors are usually operated above this temperature level, at temperatures between 200 °C and 500 °C [32], [35]. The typical pressure range is between 1 and 100 bar with higher pressures leading to increased methane yields [32]. Figure 1.4 shows CO<sub>2</sub> conversion rates as well as the H<sub>2</sub> and CH<sub>4</sub> contents at different thermodynamic equilibriums for the methanation reaction.

In the order of their activity from most to least active according to Mills and Steffgen [36], the most important catalysts for the methanation reaction are ruthenium, iron, nickel, molybdenum and cobalt. While ruthenium is the most active catalyst, it is rarely used due to its high cost. Nickel is highly active and the most selective out of the named materials while also being relatively cheap. It is therefore the preeminent catalyst material for catalytic methanation processes. The main disadvantage of nickel is that it is cancerogenic and oxidizes in oxidizing atmospheres [36], [37].

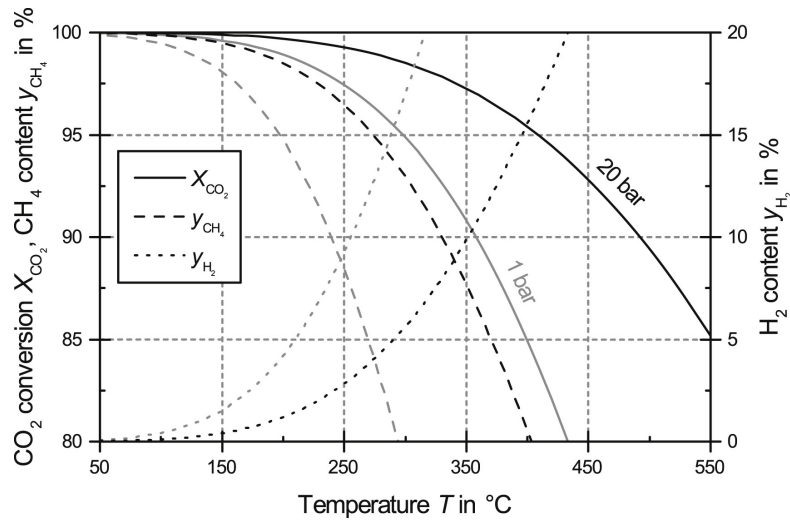


Figure 1.4: Conversion rates as well as H<sub>2</sub> and CH<sub>4</sub> contents for CO<sub>2</sub> methanation at different thermodynamical equilibria, adapted from Götz *et al.* [32].

Commonly used reactor types for the catalytic methanation process are series of adiabatic fixed-bed reactors, cooled fixed-bed reactors, fluidized-bed reactors, three-phase reactors and metal or ceramic monolith reactors [19], [38], [39]. The requirements for the reactor primarily depend on the composition and flow rates of the gas sources, as they determine the requirements for the removal of the reaction heat and the prevention of catalyst deactivation [20], [38], [40].

Fixed bed methanation reactors are an established method for the gas cleaning in the ammonia synthesis process chain. In this application, relatively small concentrations of carbon oxides have to be eliminated from the hydrogen rich feed streams. No additional cooling is required in this case due to the large ratio between the inert gas and reactant gas volumes and the resulting large heat capacity of the gas stream, relative to the generated heat. For the production of SNG however, concentrations of inert gases are relatively low and cooling becomes necessary. This can be achieved through intermittent cooling of the gas stream in between multiple fixed bed reactor stages. Additionally, gas can be recirculated for the cooling. Adiabatic reactors require robust catalyst materials that can withstand a broad temperature range without sintering or cracking [41]. For the production of SNG from coal gasification gas, this reactor type is well established and plants in the GW-scale have been realized [40]. It is also possible to directly cool a multi-tubular fixed bed reactor with an appropriate cooling medium.

Metal monolith reactors are designed to overcome some of the drawbacks of fixed bed reactors. They are characterized by their high specific surface area, which allows compact reactor designs. Their metal framework, usually based on aluminum or copper, increases the radial heat transfer, while the pressure drop is reduced significantly in comparison to fixed bed

reactors [40], [42]. In this way, heat transfer coefficients of more than  $1000 \text{ W m}^{-2} \text{ K}^{-1}$  can be reached [40], [43]. However, the deposition of the catalyst material on the structured framework is technically complex, especially when the catalyst is deactivated and the reactor has to be re-coated with catalyst. In contrast, the application of ceramic monolith reactors, which have similar benefits and drawbacks, is characterized by comparatively low thermal conduction. This can be advantageous for dynamic PtG-concepts, as the heat storage within the reactor supports a flexible process operation [44].

In three-phase reactors, also referred to as slurry bubble column reactors, the catalyst is suspended in an inert liquid by the reactant gas flow. On one hand, the liquid phase is beneficial as it facilitates the heat removal significantly, leading to almost isothermal conditions within the reactor and allowing a dynamic plant operation where the reactor temperature can be maintained stable due to the thermal inertia of the liquid phase. On the other hand, the liquid phase induces an additional mass transfer resistance and needs to fulfill several specifications such as high thermal stability, chemical inertness, low evaporation rates, low viscosity and surface tension [40], [45].

Gas-solid fluidized bed reactors are characterized by nearly isothermal conditions resulting from an intensive particle circulation, which facilitates the removal of the reaction heat. This is considered to be the main advantage of this technology. Additionally, an internal regeneration of the catalyst material was demonstrated for the methanation in a fluidized bed reactor [46]. A commonly stated disadvantage of fluidized bed reactors is the attrition of the catalyst material resulting from the comparatively high mechanical stress exerted on the particles through elastic collisions with other particles or the reactor walls. Such attrition can lead to the deactivation and elutriation of the catalyst particles, which therefore would have to be replaced periodically. Additionally, the formation of bubbles, which are beneficial as they are the main cause for the intensive particle circulation, may lead to a bypass of reactants through the reactor within the bubbles and thus to an incomplete conversion of the  $\text{CO}_2$  in the feed stream. Other frequently named disadvantages are the possible erosion of internals, such as heat exchanger tubes, varying solids residence time distributions and the frequently complex hydrodynamics, which make scaling-up difficult [32], [47]–[49]. Choice of suited bed materials and detailed knowledge on the fluid dynamics of BFBs allows to overcome these challenges during scale-up.

The present thesis investigates the hydrodynamics within a BFB reactor. Consequently, the theoretical fundamentals of this technology and their consequences for the reactor design will be discussed in greater detail in Section 2.2.

The PtG process chain poses additional challenges for the methanation process. Ensuing its main purpose of managing the fluctuating availability of electricity it is by definition a dynamic

process. Large  $H_2$  storage facilities would be required to enable steady state methanation at full capacity, which would vastly reduce the overall economic efficiency of the process chain [39], [50]. Here, switching between full and part load can be a solution for optimized operation [51]. Another possible issue is the purity of the  $CO_2$  feed stream in the biogas upgrading application as described above.

### 1.3 Methanation research at PSI

Initially, beginning in the year 2000, the research of the Thermochemical Processes (TCP) group at PSI focused on the gasification of dry biomass. First studies led to the conclusion that the fast internally circulating fluidized bed (FICFB) gasification process, which was developed in the group of Prof. Hofbauer at TU Vienna, was the best suited for the project [52]. Crucial process steps, such as the gas cleaning, which is necessary to remove organic sulfur species from the feed gas to increase the lifetime of the catalyst, were identified and developed. This led to the construction of a  $1\text{ MW}_{SNG}$  demonstration scale plant in Güssing, Austria, which included the entire process chain from wood to SNG. Further details on the early stages of the fluidized bed methanation process development at PSI are provided by Schildhauer *et al.* [53].

Eventually, PSI aimed to broaden the range of applications for the fluidized bed methanation technology. This included the investigation of alternative gas sources, mainly biogas for biogas upgrading, as well as the integration in PtG process chains. The main research objectives are therefore to investigate the feasibility of the technology for these scenarios, to optimize the process design accordingly and to reduce the risks that typically accompany the upscaling of thermochemical processes. Ultimately, the goal of the ongoing research is the commercialization of the process. The research and development at PSI can be divided into five categories: Process modelling, process optimization, techno-economic analysis, catalyst lifetime investigations and scale-up investigations. A brief summary of the stated research tasks and some of the main findings are shown in the following.

#### 1.3.1 Process development and techno-economic analysis

Kopyscinski *et al.* [54] modeled the process as a pseudo-homogeneous two-phase system. Several correlations obtained from literature were implemented to describe the hydrodynamics within the catalytic BFB reactor. For the determination of the bubble properties, a correlation by Werther *et al.* [55] was applied for the determination of the bubble diameter  $d_b$ , which is given by Equation 2.20. The bubble rise velocities were calculated with a correlation that was proposed by Hillgardt & Werther [56], which is given by Equation 2.28. Further details on the referenced correlations can be found in this work in Section 2.3.3. The reaction kinetics were obtained through concentration and temperature measurements in a catalytic plate reactor

[57] and were implemented in the reactor model in form of Langmuir-Hinshelwood type rate equations.

The model was further modified and used for comprehensive techno-economic analysis (TEA) by Witte *et al.* [58]–[60]. It could be demonstrated that the model predictions were in accordance with experimental results from 1100 h of regular operation [60]. For the TEA, the catalytic fixed bed methanation was compared with the catalytic BFB methanation. For each technology, three process designs were analyzed and it was concluded that the BFB methanation with a subsequent membrane upgrading unit can produce biomethane in a cost-efficient way.

The work of Gantenbein *et al.* focused on increasing the operational flexibility of the a catalytic BFB biogas upgrading process [23], [51], [61]. A process concept was developed that allows to switch between a conventional membrane-based separation of CO<sub>2</sub> from the biogas and direct methanation of biogas and subsequent H<sub>2</sub> recycling. By means of TEA, it could be shown that the proposed concept reduces the sensitivity on electricity cost and that the catalytic BFB methanation is about 17-19% more cost efficient than biological methanation. Additionally, a symmetric part load operation concept was developed. The feasibility of the concept was confirmed through simulations and in a experimental field campaign.

#### 1.3.2 Catalyst lifetime investigations

Seeman *et al.* [62] showed that an internal regeneration of catalysts with carbon depositions takes place in BFB methanation reactors operated with producer gas from wood gasification. Accordingly, the fluidized bed reactor can be divided into three different zones. At the inlet zone the deposition of carbon takes place due to high concentrations of CO and unsaturated hydrocarbons (ethene, benzene). In the zone above, steam gasification and hydrogenation of the carbon deposits or their precursors are predominant. Ultimately, an equilibrium between carbon deposition and the regeneration of the catalyst can be reached in this way.

For the upgrading of biogas, the gas cleaning process step was identified to be of crucial importance for the extension of the catalyst lifetime. Several studies with different feed gas sources were conducted to investigate the deactivation of the catalysts resulting from deposition of sulfur and trace organic compounds. Suitable absorbent materials were tested and evaluated in preliminary studies, which were carried out in laboratory conditions with precisely defined gas compositions provided by gas manufacturers. Subsequently, an extensive long-term field study (1030 h) was conducted, which showed that the concentrations of H<sub>2</sub>S and siloxane could be kept below required concentration limits throughout the entire campaign, while some non-H<sub>2</sub>S sulfur compounds required specific solutions and would eventually break through. This and another field study highlighted the problem that biogas

may contain various contaminants of various concentrations that depend on the specific conditions of the digester and the used biomass, which again may vary seasonally. Because standardized solutions do not yet exist, specialized solutions have to be engineered for each case [22], [63].

As part of a long-term field test of over 1100 h regular operation, the particle elutriation rate of catalyst material was measured for a reactor with a diameter 5.2 cm and an original catalyst mass of 800 g. Throughout the campaign only 70 g of the catalyst were elutriated from the reactor. The measured elutriation rate spiked when fresh catalyst material was inserted, because fine particles are elutriated at much higher rates. It was therefore concluded that attrition rates are low and the catalyst material has to be replaced only once per year [60]. These findings were later confirmed for a pilot-scale reactor with a diameter of 22.4 cm, which is referred to as GanyMeth and described in Section 3.1, in currently unpublished measurements.

### 1.3.3 Hydrodynamic investigations

Understanding the hydrodynamics of BFB reactors is of great importance for the design, scale-up and optimization of the reactor, especially in the case of the highly exothermic methanation process, where efficient heat removal is essential. Rising bubbles and correlated hydrodynamic phenomena strongly influence key properties of catalytic BFB reactors such as the heat transfer between the bed and heat exchanger surfaces, gas-solid contacting, mass transfer between bubbles and the bed, as well as within the bed, residence time distributions, bed expansion, solids segregation and mixing as well as catalyst lifetime, specifically the attrition and elutriation of catalysts particles [53], [64]–[67]. The most relevant bubble properties are the diameter  $d_b$ , the rise velocity of the bubble  $u_{br}$ , the bubble hold-up  $\varepsilon_b$  and eventually the shape of the bubble, which allow an estimation of the above-mentioned phenomena. Extensive experimental studies have been conducted over several decades that led to numerous correlations that predict the bubble properties in dependence of the reactor geometry, properties of gas and solids, gas velocities as well as axial and radial position. However, the majority of the correlations to predict bubble properties are empirical or semi-empirical and often are only valid for a specific range of conditions [68]. Additionally, the increase of available computational power in recent years led to significant advancement in the field of computational fluid dynamics (CFD), which allow the investigation of fluidized bed hydrodynamics through numerical simulations. While certain properties such as the bubble hold-up  $\varepsilon_b$ , the average bed expansion or the minimum fluidization velocity  $u_{mf}$  can be predicted accurately through CFD simulations, it usually requires empirically determined tuning parameters to reach an agreement between simulated and experimentally measured bubble properties.



Considering the reactor design that PSI is researching, which involves vertically inserted heat exchanger tube bundles that significantly influence the hydrodynamics, the corresponding research is still sparse. PSI has therefore carried out profound investigations on the hydrodynamics in BFB reactors with vertical internals that led to three dissertations in the years 2012 to 2018 [69]–[71].

The work of Rüdisüli [69] primarily focused on experimental measurements with optical and piezo-electric probe in a lab-scale reactor model. The measurements were conducted with various arrangements of vertical internals of different diameters. Statistical analysis and a Monte Carlo study led Rüdisüli to the conclusion that the mean chord length measured with optical probes is a good approximation for the mean bubble diameter. For the measurements of the pressure fluctuations with piezo-electric probes, spectral decomposition was applied to retrieve the average bubble size. The results of these measurements were compared with the optical probe measurements as well as with correlations from literature, and were found to be in good agreement for given particle properties and sufficiently high gas velocities. Rüdisüli also presented a modified approach for the up-scaling of fluidized bed reactors with vertical internals, which considers defined sectors of internals as autonomous regions. With this approach the up-scaling depends on the hydraulic diameter of the autonomous sectors alone and is independent of the reactor diameter.

Building upon the findings of Rüdisüli, Maurer [70] continued the optical probe measurements in reactor models with an expanded range of investigated diameters between 5 and 22.4 cm. He verified Rüdisüli's sectoral scale-up approach and defined the limits for its applicability. In cooperation with the Delft University of Technology, X-ray tomography measurements were conducted in reactor models of two diameters with and without bundles of vertical internals of different arrangements. Distributions of bubble properties were measured this way and a correlation to predict such distributions in dependence of the height in the reactor, the diameter and the superficial gas velocity was proposed. Maurer came to the conclusion that there were no correlations between the measured bubble properties. The abrasion of catalyst support materials was also investigated in a single 500 h experiment, which led to the development of a simple correlation to describe the particle attrition as a function of the gas velocity, time and particle type. Furthermore, Maurer developed and tested an optical probe sensor, which is able to measure under reactive conditions with pressures of up to 25 bar and temperatures of up to 400 °C, for measurements in the pilot plant GanyMeth, which was being constructed at the time.

The dissertation of Schillinger [71] continued the evaluation of the X-ray measurements provided by Maurer with a focus on the influence of the arrangement of the vertical internals. It could be shown that the way the internals are arranged had no influence on the bubble properties and that the diameter of the reactor model did not influence the observed bubble

sizes when internals were present. This finding further supports the sectoral scale-up approach described above, as in reference experiments without internals, the bubble properties clearly depend on the reactor diameter. An algorithm for the evaluation of the new optical probe sensor was developed, and first cold flow measurements in the pilot plant GanyMeth with pressurized air and alumina particles at pressures of up to 5 bar were conducted. Additionally, the X-ray tomography reconstructions were used to simulate the measurements of an ideal virtual optical probe. The resulting chord lengths and rise velocities were then compared to the bubble properties derived from the X-ray tomography reconstructions. Statistical effects resulting from the assumed shape of the bubbles, such as chord length distributions and the reduced probability of the optical probe to pierce elongated bubbles in comparison to oblate bubbles, were identified and correction factors were proposed correspondingly.

### 1.4 Open research questions

While many of the original research questions could be answered in previous studies, some remained unanswered and many new ones arose. One question that was identified to be of critical importance for further hydrodynamic investigations in the pilot plant GanyMeth originated in the scope of the work of Schillinger *et al.* [72]. The author describes a discrepancy between optical measurements in the pilot plant GanyMeth and results from X-ray tomography reconstructions for the same column geometry, same particle system, the same fluidization number and a similar measurements height, as it is shown in Figure 1.5. While the evaluation of the X-ray data showed large bubbles with slow rise velocities, as indicated by the yellow area in the figure, and small bubbles with fast rise velocities, marked in green in the figure, no such bubbles were measured with the optical probes.

As a possible explanation the author suggests that deviations of the bubble aspect ratio from the value, which was assumed for the evaluation of the optical probe data might be responsible for the observed inconsistency. In that case, the volume equivalent diameter of bubbles that were comparatively elongated would be overestimated while it would be underestimated for bubbles that were more oblate in comparison. Additionally, there would be a bias towards oblate bubbles, because they would statistically be more likely to be pierced by the optical probe and would therefore be over represented. The first open research objective addressed within this thesis is therefore the investigation of this assessment and in case it is confirmed, the derivation of the according statistical correlations, which can be applied to the optical probe measurements to account for the phenomena. Ultimately, the optical probe measurements need to be verified with appropriate and robust methods to reduce the risk of false assumptions that could potentially lead to an erroneous reactor model and with that to false implications for the up-scaling of the reactor.

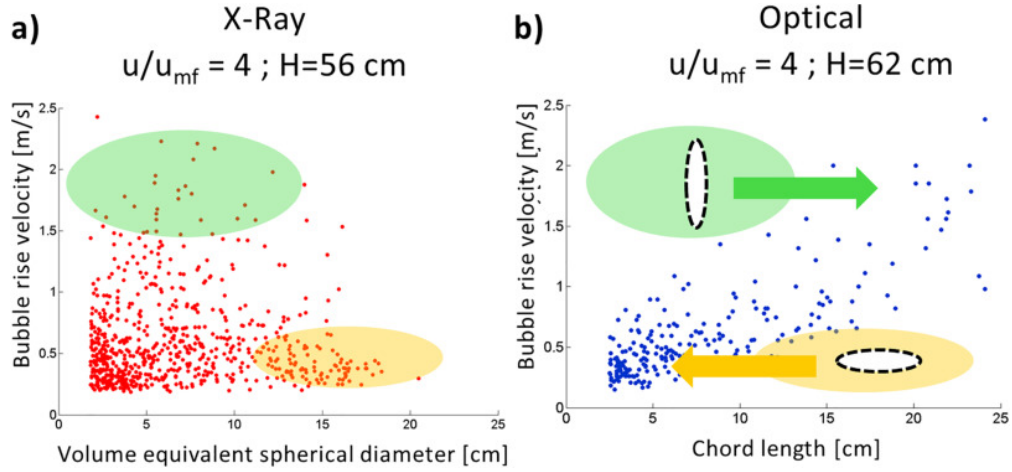


Figure 1.5: Comparison of distributions of bubble properties (bubble rise velocity and volume equivalent diameters) obtained via X-ray tomography reconstructions in a model reactor (a) and with optical probe measurements in a pilot plant of the same geometric dimensions (b) at similar experimental settings (fluidization number  $u/u_{mf} = 4$  and measurements heights of 56 cm for the X-ray measurements and 62 cm for the optical measurements). Illustration adapted from Schillinger *et al.* [72].

Additional open research are:

1. How does the pressure influence the development of selected bubble properties, such as the rise velocity  $u_{br}$ , the volume equivalent diameter  $d_{b,eq}$  and the bubble hold-up  $\epsilon_b$  for the investigated reactor geometry of the pilot plant GanyMeth?
2. Is the measurement of individual bubble properties by means of X-ray tomography or optical probes feasible?

Furthermore, the evaluation of the X-ray tomography measurements was revised, which led to a detailed analysis of the distribution of bubble properties and their correlations. It could be shown that the bubble shape is correlated to the bubble rise velocity  $u_{br}$ . This brought up the question of how these findings could be applied for the statistical evaluation of chord length distributions measured by means of optical probes.

Beyond the scope of this work, the general goal of the hydrodynamic investigations in the pilot plant GanyMeth at PSI is the implementation of the findings into the reactor model. In the future, experiments under reactive conditions will be conducted in GanyMeth plant, to validate previous findings and to expand the model to enable predictions of the reactor performance, including concentration and temperature profiles as well as the heat exchange rates, for the scale-up of the reactor to the industrial scale.



## 2 Theory on fluidized bed technology

### 2.1 Fluidization: Definition, history and applications

Fluidization occurs, when a stream of gas or liquid flows upwards through a bed of particles after it reaches a certain superficial gas velocity, which is referred to as the minimum fluidization velocity  $u_{mf}$ . When  $u_{mf}$  is reached, the drag force that the gas flow exerts on the particles is equal to the gravitational force pulling the particles downwards. Consequently, the particles are held in suspension, which causes the particles to behave similar to a liquid: They can be stirred and poured; objects with a higher density than the particles will sink to the ground of the bed, while objects with a smaller density will float on the surface. In liquid-solid systems, increasing the flow rate above minimum fluidization usually leads to a smooth and progressive expansion of the bed, where no heterogeneous separation of the two phases is observed and flow instabilities are damped and thus insignificant. This can be referred to as a homogeneously fluidized bed [73]. For gas-solid fluidized beds, a heterogeneous behavior is characteristic. Here, an increase of the flow rate usually leads to large instabilities causing the two phases to partially separate, resulting in the formation of mostly particle free voids, generally referred to as bubbles. This type of the fluidized bed is usually called a heterogeneous fluidized bed or a bubbling fluidized bed (BFB). There are rare cases, where liquid-solid beds fluidize heterogeneously. This may happen when very dense particles are fluidized by low-density liquids. Similarly, gas-solid systems can fluidize homogeneously, when fine low-density particles are fluidized with dense gas at high pressures. In gas-liquid-solid systems, particles are fluidized by an up-flowing liquid as a continuous phase, while a co-current gas flow is introduced to the system, forming a discontinuous, bubbling phase. Most of the important industrial fluidization plants, as well as the reactor discussed in this thesis, are gas-solid systems. Therefore, this type of fluidized bed is described in more detail in the following.

## Chapter 2. Theory on fluidized bed technology

---

The first industrial application of fluidization was the gasification of fine-grained coal in a process developed by Winkler in 1922 [74]. In 1926 a first reactor, which was 13 m high and had a cross section of 12 m<sup>2</sup>, went into operation to supply the chemical industry with synthesis gas consisting of CO and H<sub>2</sub>.

Until the 1940s, fluidization remained a niche technology. In the anticipation of war in Europe in the years before 1939, the United States needed to find new ways to produce large amounts of high-octane aviation gasoline. Since 1937, the Houdry process had been successfully applied for the catalytic cracking of mineral oil fractions. However, since fixed bed reactors with alumina catalysts were applied, complex intermittent operation was required for the regeneration of the catalyst material and the temperature control. The process was therefore not suited for the rapid up-scaling of production that was needed. With the goal to enable the large-scale production of the required aviation fuels independently of Houdry's patents, the company Standard Oil of New Jersey, today known as ExxonMobil, started the development of a catalytic cracking process in 1938, in a joint project with several other companies.

In the timespan of less than four years, the process was developed from the initial concept to the successful commissioning of full-scale catalytic cracking plants in 1942 [75]. With around 1,000 workers involved, the project is considered by some as one of the greatest scientific efforts directed at a single project [76], which made a significant impact on the war efforts of the United States [77]. The developed process is referred to as fluidized catalytic cracking (FCC). More than 30 FCC units had been built by the end of World War II. It was the first major application of fluidization technology, which was subsequently used in virtually every major oil refinery in the world [78].

By the mid 1940s there were attempts to use fluidization for the production of gasoline from synthesis gas produced via the Fischer-Tropsch process, which led to the development of a process called Hydrocol. After the successful operation at the pilot scale in a reactor with a diameter of 20 cm, an industrial scale reactor with a diameter of 5 m was constructed in Brownsville, Texas, USA. It was commissioned in 1951 but failed to reach the design capacities by a significant margin, which among other reasons ultimately led to the suspension of the plant after only six years of operation and failed attempts to optimize the plant operation [79]. This case demonstrated in a spectacular fashion the necessity of hydrodynamic investigations in fluidized beds for the development of scale-up procedures for fluidized bed applications.

Since then, fluidized bed technology has been applied in a variety of important industrial processes. There are purely physical applications, such as heat exchange, drying, adsorption and desorption, granulation and coating, which benefit from the intensive gas-solid contacting in fluidized beds. The technology has also become widely applied for catalytic reactions, especially highly exothermic or endothermic and temperature-sensitive reactions, due to

the exceptional temperature uniformity within fluidized beds. Additionally, fluidization is extensively used for many non-catalytic reactions, such as combustion for energy generation, metallurgical operations and calcination. For these applications circulating fluidized bed (CFB) reactors have become popular since the 1980s, where no upper surface of the fluidized bed exists and gas-solid separators are used to allow the continuous recirculation of the particles within the reactor [66], [80].

Realizing fluidized bed reactors in the industrial scale requires a good understanding of the hydrodynamics of a fluidized bed in relation to the reactor dimensions and the range of operation conditions. Especially for BFB reactors, the scale-up is considered to be highly complex, demanding and risky [81], [82]. Decades of comprehensive investigations have made it possible that today fluidized bed reactors are among the largest commercially available chemical reactor types. A recent impressive example is a 660 MW<sub>el</sub> supercritical CFB boiler that has been commissioned in China in 2020 [83].

## 2.2 Fundamental theory on fluidized beds

In this section, the theoretical foundation of fluidized beds, with an additional focus on catalytic BFB reactors is presented.

### 2.2.1 Characterization of particles and fluids

The quality of the fluidization strongly depends on the properties of the particles and fluids. In this context, the size, shape and density of the particles as well as the viscosity and the density of the fluid are the most relevant characteristics.

#### Particle properties

The size of the particle is usually expressed as a diameter, which can be determined through sieving of the material or through specific analytical devices such as a laser diffraction particle size analyzer, which was used in this work. To account for irregular particles shapes and the consequently unclear definition of the diameter, the Sauter diameter is usually applied, which is defined by Equation 2.1, where  $V_p$  is the volume of the particle and  $A_p$  is the exterior surface area.

$$d_p = 6 \frac{V_p}{A_p} \quad (2.1)$$

## Chapter 2. Theory on fluidized bed technology

---

In practice, the particle size distribution (PSD) is not monodisperse and consists of particles of various size fractions. Therefore, the mean Sauter diameter is usually determined by its weighted mean as shown in Equation 2.2, where  $w_i$  is the weight fraction of particles with a Sauter diameter  $d_{p,i}$ .

$$\bar{d}_p = \frac{\sum w_i d_{p,i}^3}{\sum w_i d_{p,i}^2} = \frac{1}{\sum \frac{w_i}{d_{p,i}}} \quad (2.2)$$

Additionally, it is important to measure the amount of fine particles with diameters in the range of 50  $\mu\text{m}$  and less, as even small weight fractions of fine particles may significantly impact the behavior of the fluidized bed [84], [85].

The particle shape can be described with the sphericity  $\phi$ , which is the ratio between the surface area of a sphere with the same volume as the particle and the exterior surface area of the particle, as it is defined by Equation 2.3.

$$\phi = \frac{A_{p,eq}}{A_p} \quad (2.3)$$

It is difficult to determine the sphericity of particles. Often, the measurement of two-dimensional projections through a microscope is used under the assumption that the particles are symmetric in all three spatial dimensions. In that case, the sphericity is approximated as the ratio between the perimeter of a circle with the same area as that of the particle projection and its actual perimeter. In general, the sphericity is only a simplified description of the particle shape as one value of the sphericity can describe particles with completely different complex shapes.

Catalyst particles are usually porous to increase the active surface area. The density  $\rho_p$  of particles depends on the particle porosity  $\epsilon_p$  and the density  $\rho_s$  of the particle material itself as shown in Equation 2.4.

$$\rho_p = \rho_s (1 - \epsilon_p) \quad (2.4)$$

The particle porosity  $\epsilon_p$  can be measured directly e.g. via nitrogen physisorption as it was done in this work. When the particle density is known, the bulk voidage can be calculated according to Equation 2.5, where  $\rho_{bulk}$  is the density of a bulk of particles which can be determined easily through weighing a defined volume of loosely packed particles.



$$\epsilon_{bulk} = 1 - \frac{\rho_{bulk}}{\rho_p} \quad (2.5)$$

The distinction between loosely and tightly packed material and an appropriate preparation of the samples for the determination of its characteristics is important as the corresponding bulk densities may differ significantly. A very commonly used characterization of particles in the context of fluidization was proposed by Geldart [86], who classified the solids into four groups (A-D) according to their fluidization behavior:

**Group C:** Powders of this group are very fine grained with diameters smaller than 30  $\mu\text{m}$ , where interparticle cohesive forces dominate over the drag force exerted by the fluid stream. Accordingly, such particles tend to agglomerate, which makes fluidization difficult. Without the application of fluidization aids, such as agitators [87], vibrators [88], flow pulsators [89], [90] or flowability additives [91], the gas usually flows through fissures or channels that form in the particle bed when a gas flow is initiated. Typical examples for group C powders are flour or starch.

**Group A:** Interparticle forces are relevant but they do not dominate the fluidization behavior of this particle class. Group A particles have diameters in the range of 30 - 150  $\mu\text{m}$  and particle densities below 1500  $\text{kgm}^{-3}$ . They are characterized by an easy fluidization, which initially is smooth and homogenous with a uniform bed expansion, even when the superficial gas velocity  $u$  is increased beyond the minimum fluidization velocity  $u_{mf}$ . With further increase of  $u$ , the fluidized bed eventually destabilizes and bubbles start to form once the minimum bubbling velocity  $u_{mb}$  is reached. The minimum bubbling velocity is dependent on the density and viscosity of the gas as well as on the content of fine material in the bed [92]. The bubbles rise at velocities significantly above that of the gas flow in the dense phase and coalesce as they rise, which leads to larger bubbles. A dynamic equilibrium between coalescence and breakage of bubbles is eventually reached resulting in an upper limit for the bubble sizes, which is usually less than 10 cm [73]. Even when only few bubbles are present, a gross particle circulation is reached [73]. It has been reported that internals do not improve the fluidization of group A particles considerably [73]. Catalysts for FCC applications are typical examples for group A materials.

**Group B:** For group B material the interparticle forces are neglectable in comparison to the drag forces. Particles of this group have moderate particle sizes in the range of 40 - 500  $\mu\text{m}$  and moderate densities in the range of 1500 - 4000  $\text{kgm}^{-3}$ . They fluidize well and bubbles start to form immediately when the bed reaches the fluidized state ( $u_{mb} \approx u_{mf}$ ). This immediate

onset of bubbling after fluidization begins is the criterion defined by Geldart to distinguish between the groups A and B [86]. As with group A particles, the bubbles rise at velocities much above the dense phase gas velocity. They coalesce as they rise upwards but unlike the bubbling fluidization of group A powders there is no upper limit for the growth of the bubbles and highly dynamic bubbling action occurs resulting in a substantial circulation of particles. Eventually the bubble diameters approach the diameter of the fluidization vessel and bubbles rise in form of what is referred to as slugs. The bed expansion in fluidized beds of group B material almost entirely results from the formation of bubbles, while the void fraction of the dense phase stays nearly constant [93]. Most gas-solid reactions are operated with group B material, as it simply represents the most commonly available PSD of feed particles [73]. A typical example for this particle class is sand.

**Group D:** Particles of this group are coarse and comparatively large with diameters in the range above 0.5 mm. The fluidization of these particles is difficult, especially for deep beds. Similar to group B particles, bubbles start to form immediately once the bed is fluidized. However, the quality of the bubbles differs significantly. They coalesce rapidly, growing to large sizes and tend to rise with slower velocities than the interstitial velocity of the gas stream. Gas from the dense phase flows through the bubbles, which is the phenomenon that defines the boundary between group B and D powders according to Geldart [86]. The bubbles often behave inconsistently; spouting, severe channeling, slugging and large bubble eruptions are common occurrences [73]. A stable bubbling operation can be achieved with shallow beds and superficial gas velocities only slightly above  $u_{mf}$ . Additional measures, such as vibration, can facilitate the fluidization further [94]. A typical application for group D particle fluidization is the drying of agricultural products, such as peas or corn.

A graphical implementation of the particle classification as it was proposed by Geldart is shown in Figure 2.1, which shows the boundaries between the particle groups in dependence of the average particle diameter and the density difference between gas and particle. The exact definition of the shown boundaries has been debated [66], [91], [95]. Especially the boundaries between the groups C and A as well as A and B are not clearly defined, as they depend on particle properties that influence the interparticle forces, such as the compressibility and roughness, dielectric properties and Hamaker's constant [66]. Furthermore, the original classification was obtained through analysis of data that was measured at ambient pressures and temperatures with only air used as the fluidization medium. However, it has been reported that the particle group boundaries may shift at elevated pressures and temperatures or for other gases than air. For instance, some particles that behave like group B powders at ambient pressures, can behave like group A powders at elevated pressures [95]. Consequently, various modifications for Geldart's particle classification have been suggested.

Valverde Millán [91] proposed to apply the equilibrium between interparticle forces and the particle weight, as shown in Equation 2.6, for the definition of the AB boundary.

$$\text{Granular bond number} = \frac{\text{Sum of interparticle attractive forces}}{\text{Particle weight}} = 1 \quad (2.6)$$

An empirical dimensional correlation of the AB boundary was suggested by Grace [95], based on a various experimental datasets that were measured at a broad range of pressures and temperatures and with a variety of gases. This is shown in Equation 2.7.

$$d_{p,AB} = \frac{101 \mu^{\frac{2}{3}} \rho_g^{0.092}}{g^{\frac{1}{3}} (\rho_p - \rho_g)^{0.759}} \quad (2.7)$$

For the definition of the BD boundary, Grace [95] suggests a correlation, which is based on the conditions where the inertia term of the pressure gradient of the dense phase starts to dominate the viscous term, for which Grace proposed the boundary at a constant Archimedes number of  $Ar = 145,000$ . The proposed modifications from above are also shown in Figure 2.1.

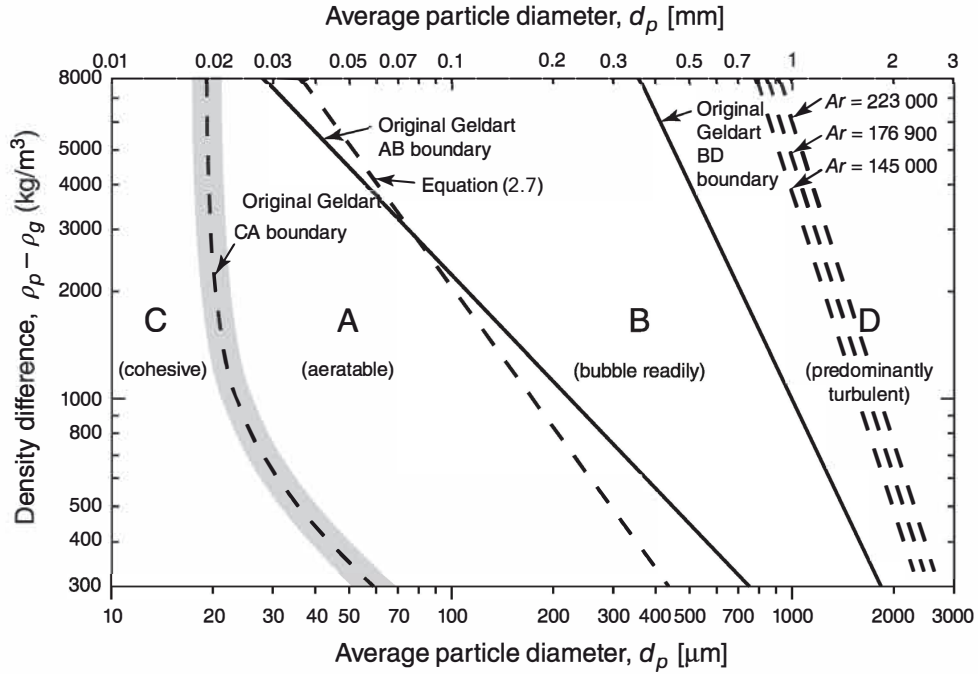


Figure 2.1: Powder classification group boundaries according to Geldart including proposed modifications for the fluidization with air at ambient conditions. Adapted from Grace *et al.* [66].

Yang [96] also investigated the consequences for fluidization behavior at elevated pressures and temperatures and proposed a reinterpretation of Geldart's classification. He suggested plotting a dimensionless density,  $(\rho_p - \rho_g)\rho_g$ , against the Archimedes number for Geldart's classification group boundaries. In this way, particles that behaved like group B powders at low pressures and like group A powders at elevated pressures were classified correctly.

Additional important particle properties and their influence on the fluidization are briefly summarized in the following:

- The surface roughness affects the frictional resistance between particles, the drag force from the fluid flow, the heat transfer from particle to particle and particle to wall and the interparticle van der Waals and electrostatic forces [66].
- The coefficients of restitution (particle to particle and particle to wall) describe the elasticity of particle collisions with other particles or the wall, which influence the motion of gas and particles within the fluidized bed according to the preservation of kinetic energy after collisions [97], [98].
- The terminal settling velocity  $u_t$  determines the onset of particle entrainment in a fluidized bed.

### Gas properties

The density of gases increases with pressure and decreases with temperature. With higher gas densities, the drag on the particles is enhanced which leads to an earlier onset and an increased intensity of fluidization. The viscosity of the gas is only relevant for small particles, which experience increased drag forces with increased viscosity. An increase of the pressure does not affect the viscosity of the gas, whereas the viscosity increases with temperature. Additionally the humidity as well as the possible adsorption of the gas on the surfaces of the particles can affect the fluidization behavior [66].

#### 2.2.2 Minimum fluidization velocity

A fixed bed becomes fluidized once the superficial gas velocity reaches the minimum fluidization velocity. Then, the flow pressure drop  $\Delta p_{bed}$  through the fixed bed, which can be described with the Ergun [99] equation (Eq. 2.8), is equal to the buoyancy-reduced gravitational force applied to the cross-section of the vessel  $A_R$  (Eq. 2.9).

$$\frac{\Delta p_{bed}}{\Delta h} = 150 \frac{(1 - \epsilon_{bed})}{\epsilon_{bed}^3} \frac{\eta_g u}{(\phi d_p^2)} + 1.75 \frac{(1 - \epsilon_{bed})}{\epsilon_{bed}^3} \frac{\rho_g u^2}{\phi d_p} \quad (2.8)$$

$$\frac{\Delta p_{bed}}{\Delta h} = \frac{F_G - F_A}{A_R \Delta h} = (\rho_p - \rho_g) g (1 - \epsilon_{bed}) \quad (2.9)$$

Equating the two expressions allows the calculation of  $u_{mf}$ . Wen and Yu [100] provided a simplified equation, which is shown in Equation 2.10. It can be used in case the sphericity  $\phi$  and the bed voidage  $\epsilon_{bed}$  at minimum fluidization is unknown.

$$u_{mf} = \frac{\eta_f}{\rho_f d_p} \left( \sqrt{33.7^2 + 0.0408 Ar} - 33.7 \right) \quad (2.10)$$

Here,  $Ar$  is the Archimedes number, which describes the ratio of the gravitational to the viscous forces as defined in Equation 2.11.

$$Ar = \frac{\rho_f g (\rho_s - \rho_f) d_p^3}{\eta_f^2} \quad (2.11)$$

The minimum fluidization velocity  $u_{mf}$  is one of the most important characteristics of fluidized beds. Many of the hydrodynamic properties of fluidized beds, such as the local bubble hold-up or their sizes and rise velocities, depend on the ratio between the superficial gas velocity and the minimum fluidization velocity. This ratio  $u/u_{mf}$  is also referred to as the fluidization number. Anantharaman *et al.* [101] provide a comprehensive summary of more than 100 correlations for the minimum fluidization velocity in gas-solid fluidization. Their key conclusion was that the considered correlations are highly empirical and system-specific. Accordingly,  $u_{mf}$  is usually determined experimentally by measuring pressure drop  $\Delta p_{bed}$  over the bed in dependence of the superficial gas velocity  $u$ . While the particles are in a fixed bed stage, the pressure drop is proportional to the superficial gas velocity until fluidization is reached. Increasing the superficial gas velocity further eventually leads to the entrainment of particles which causes the pressure drop to decrease. In practice, it is very likely that the pressure drop first peaks at a value above that of the fully fluidized bed when the bed is first fluidized. This is explained by the interlocking of the particles in the fixed bed, which requires additional drag force to overcome. Such a hysteresis may disappear, when a certain amount of fine particles is present in the bed [84]. When the bed is fluidized and the superficial gas velocity is decreased, then the transition back to the fixed bed state happens without the pressure drop increasing first. The transition may occur abruptly, which is the case for monodisperse particle systems, or smoothly when the PSD is wide and partial fluidization may occur for

smaller particles within the gaps between larger particles. Usually, the minimum fluidization velocity is determined as the intersection of the linear extension of the fixed bed pressure drop and the linear extension of the static pressure drop of the fluidized bed. This is indicated in Figure 2.2, which shows the pressure drop over the superficial velocity for the transition between fixed bed and fluidized bed as it was described above.

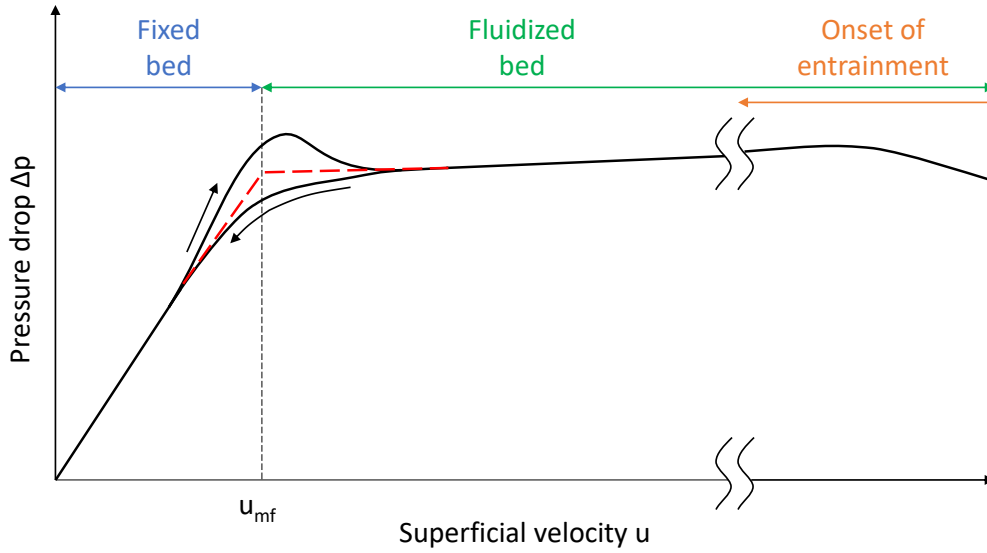


Figure 2.2: Illustration of the determination of the minimum fluidization velocity  $u_{mf}$ .

### 2.2.3 Fluidization regimes

Fluidized beds can be operated in different flow regimes depending on the superficial gas velocity and the characteristics of the gas and particles as they were described in Section 2.2.1. The fluidization regimes influence various characteristics of the fluidized bed such as the heat and mass transfer, mixing and overall reactor performance, which can be beneficial or detrimental depending on the application. As described in Section 2.1, the bed first fluidizes when the superficial gas velocity reaches the minimum fluidization velocity  $u_{mf}$  and particles behave similar to a liquid as they are held in suspension by the fluid flow. Depending on the combined characteristics of the bed material and the fluid, bubbling may occur immediately after fluidization has been reached ( $u_{mf} \approx u_{mb}$ ), as it is the case for Geldart groups B and D powders. For Geldart group A material, a further increase of the superficial gas velocity is required to reach the minimum bubbling velocity  $u_{mb}$ . In that case, a bubble-free fluidization regime exists, which is characterized by a smooth uniform expansion of the bed and only locally limited particle motion. A correlation by Abarahamsen and Geldart [92], which is shown in Equation 2.12, can be used to predict  $u_{mb}$ . Here,  $F_{45}$  is the fraction of particles smaller than  $45\text{ }\mu\text{m}$ .

$$\frac{u_{mb}}{u_{mf}} = \frac{2300\rho_g^{0.126}\eta_g^{0.523}\exp(0.716F_{45})}{d_p^{0.8}g^{0.923}(\rho_p - \rho_g)^{0.934}} \quad (2.12)$$

Accordingly, the onset of bubbling may be delayed with increasing temperatures and pressures, which is confirmed by the observation, that Geldart B group material can behave like Geldart A group material at elevated pressures and or temperatures as discussed in Section 5.1. Once the minimum bubbling velocity is reached, bubbles start to form near the gas distributor. The bubbles coalesce as they rise towards the surface, which leads to increasing bubble diameters and reduced numbers of bubbles at higher positions in the fluidized bed. The surface of the fluidized bed is well defined and periodic bubble eruptions can be observed, which are accompanied by the ejection of particles into the zone above the fluidized bed. Depending on the size and the rise velocity of the erupting bubble, particles can experience a significant vertical acceleration as they are being ejected, which may cause entrainment and elutriation of particles in the freeboard region of the reactor [102]–[104]. With increasing superficial gas velocities, the bubble sizes increase. Once the bubble volume-equivalent diameter reaches about 10% of the column diameter, wall effects begin to significantly impact bubble properties such as its shape and rise velocity [105]. A further growth of the bubbles to volume-equivalent diameters  $d_{b,eq}$  that are similar to the column diameter  $D$ , e.g.  $d_{b,eq} > 0.6D$  [105] or  $d_{b,eq} > 0.5D$  [73], defines the onset of the slugging fluidization regime, where the bubbles are significantly influenced by wall effects. Such bubbles are referred to as slugs.

In general, one can distinguish between two types of slugging regimes: Slugging with axisymmetric round-nosed slugs, or so-called wall slugs, which appear like half round-nose slugs that rise against the wall, is typically observed for Geldart group A material, while square-nosed flat slugs are typical for Geldart group B and D powders [48], [106]. Slugging significantly affects a variety of characteristics of the fluidized beds. Bubbling fluidized beds (BFB) are characterized by specific bubbling patterns that lead to an intensive particle circulation and with that to radial and axial transport of both gas and solids. The bubbles themselves are responsible for a significant axial solid mixing as they transport particles in their wake. In the slugging regime however, the hydrodynamics differ substantially from that of BFBs. Slugs continue to coalesce until the distance between the individual bubbles equals twice the column diameter or more. From then on, the flow pattern stabilizes and a distinctive periodic behavior can be observed. The bed expansion increases smoothly until a slug reaches the surface, which then collapses and starts to expand again through the formation and rise of the new slugs. For round-nosed slugs, the particles are pushed upwards by the slug and flow downwards in the narrow space between the slug and the wall, whereas for square-nosed slugs the particles “rain” through the slug. Due to a decreased transport of particles in the wakes of slugs, in comparison to that of bubbles in BFBs, and the locally restricted paths for drifts at the walls of the column,

the vertical particle transport is slower than that in BFBs [107]. No particle drift flows occur for square-nosed slugs, which are also significantly slower than bubbles in BFBs which leads to a further decrease of gas and solids mixing. Therefore, slugging is undesired for catalytic fluidized bed reactors and it is important for the reactor design to determine the conditions for the onset of slugging.

With a further increase of the superficial gas velocity to values slightly below the terminal free-fall velocity  $u_t$  of the particles, the fluidized bed eventually reaches the fluidization regime referred to as turbulent fluidization. This regime is characterized by a highly dynamic and irregular turbulent flow pattern. There is no clear distinction between bubble and dense phase but rather a gradually transformation into a continuous phase [108]. Finally, when the superficial gas velocity  $u$  exceeds the terminal free-fall velocity  $u_t$  of the particles, entrainment of particles takes place resulting in the pneumatic transport of the particles with the gas flow. Both turbulent fluidization and the pneumatic transport are well outside the operation range of the BFB reactor investigated in this thesis and are therefore only briefly mentioned. Further information on gas-solid turbulent fluidization can be found in the comprehensive state-of-the-art review provided by Bi *et al.* [109], whereas the work by Molerus [110] provides a good overview on the pneumatic transport of solids. An illustrated overview of the fluidization regimes described above is shown in Figure 2.3.

### 2.3 Bubbling fluidized beds

This work focuses on the investigation of the hydrodynamics within a catalytic BFB reactor, more specifically on the determination of the bubble properties in dependence of the bed material, the superficial gas velocity  $u$ , the position within the reactor and the pressure. Bubbles play a crucial role in catalytic BFB reactors as they significantly influence key properties of the fluidized bed, such as the heat and mass transfer, the mixing of gas and solids as well as elutriation of bed material. Rising bubbles transport particles in their wake, which causes an intensive particle motion resulting in a uniform temperature profile of the fluidized bed and an intensive heat transfer between the bed and cooling or heating surfaces. However, the intensive particle circulation also has drawbacks as they may cause an increased attrition of the bed material as well as an erosion of the surfaces within the reactor. In the case of heterogenous catalytic reactions, such as the one investigated in this thesis, bubbles pose the risk of bypassing reactant gas through the reactor inside the bubble phase and thus reducing the overall conversion rate of the reactor. A profound understanding of the BFBs is therefore necessary to optimize the reactor design. There have been extensive experimental and theoretical studies in the field of BFBs. A selection of some of the most important findings in respect to the topic of this thesis are presented in the following.



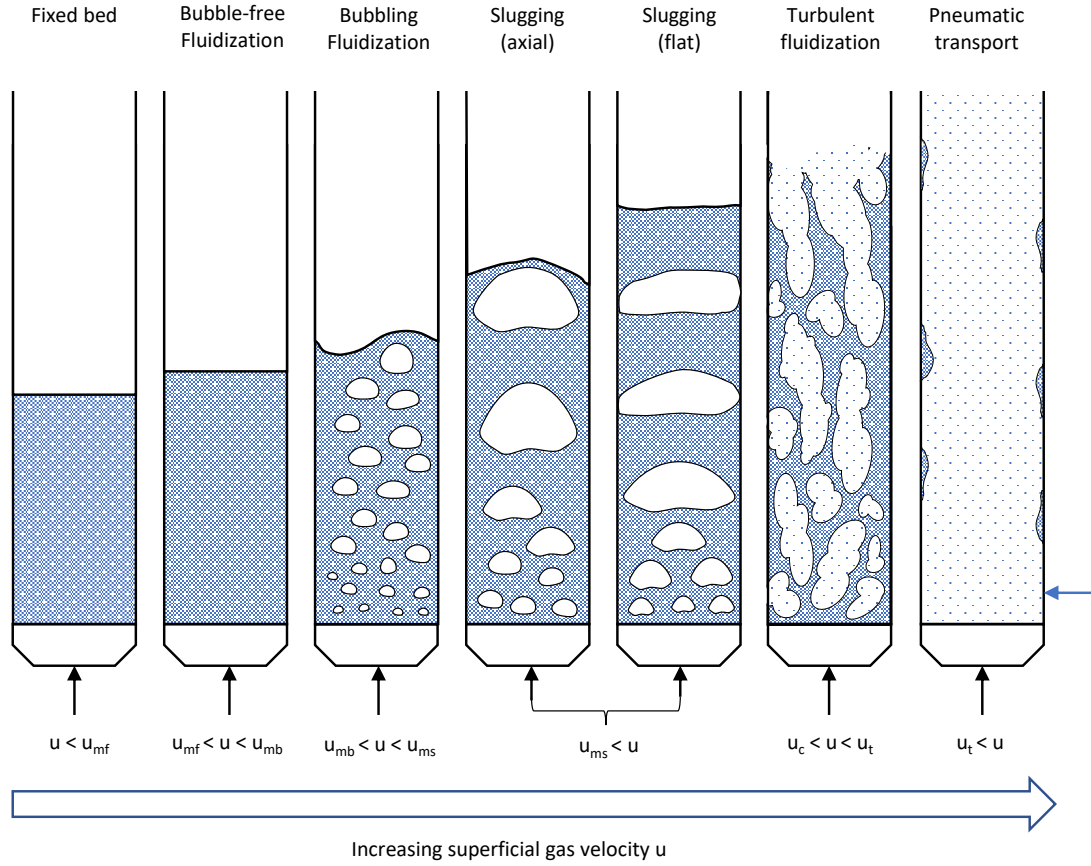


Figure 2.3: Illustration of fluidization regimes in dependence of the superficial gas velocity  $u$ .

### 2.3.1 Two phase model

BFB reactors are usually modelled as a two-phase system, based on the work of Toomey and Johnstone [111]. In the two flow model (TFM), the bed volume is divided into two separate phases: the bubble phase, which is considered to be mostly particle free, and the dense phase, which represents the homogenous gas-solid emulsion. The total gas flow  $\dot{V}_{total}$  entering the system is described by Equation 2.13, where  $A_{cs}$  is the horizontal cross section of the bed and  $u$  is the superficial gas velocity.

$$\dot{V}_{total} = A_{cs}u \quad (2.13)$$

In the classic TFM, it is assumed that once the bed is fluidized at the minimum fluidization velocity  $u_{mf}$ , any additional gas flow resulting from a further increase of the gas velocity enters the bubble phase, as described by Equation 2.14, where  $A_{cs,b}$  is the horizontal cross section, that is occupied by the bubble phase.

$$\dot{V}_b = A_{cs,b} u_b = A_{cs} \varepsilon_b (u - u_{mf}) \quad (2.14)$$

Whereas the gas flow through the dense phase is described by Equation 2.15.

$$\dot{V}_d = A_{cs,d} u_d = A_{cs} (1 - \varepsilon_b) u_{mf} \quad (2.15)$$

The mass transfer between the two phases can be described by two mechanisms: Diffusion and convection. Diffusion describes the mass transfer resulting from concentration gradients at the interface between a bubble and the dense phase. The diffusive mass transfer rate between the two phases is therefore strongly dependent on the specific surface area of the bubbles and with that on their sizes and shapes. Convective mass transfer results from the throughflow of gas from the dense phase into the bubble phase and vice versa. This transport mechanism is especially relevant for volume contracting reactions, such as methanation, where the reduction of the gas volume in the dense phase leads to an increased convective mass transfer from the bubbles into the dense phase. Additional assumptions of the classic TFM are that the voidage of the dense phase stays constant after fluidization is reached, even with a further increase of  $u$  and that the bubble phase is homogeneous for a given height within the bed. However, since the TFM was first proposed, several adjustments of these assumptions have been made and a various new correlations for the description of the two phases have been proposed in the literature, some of which are shown in Section 2.3.3. An illustration of the TFM is shown in Figure 2.4.

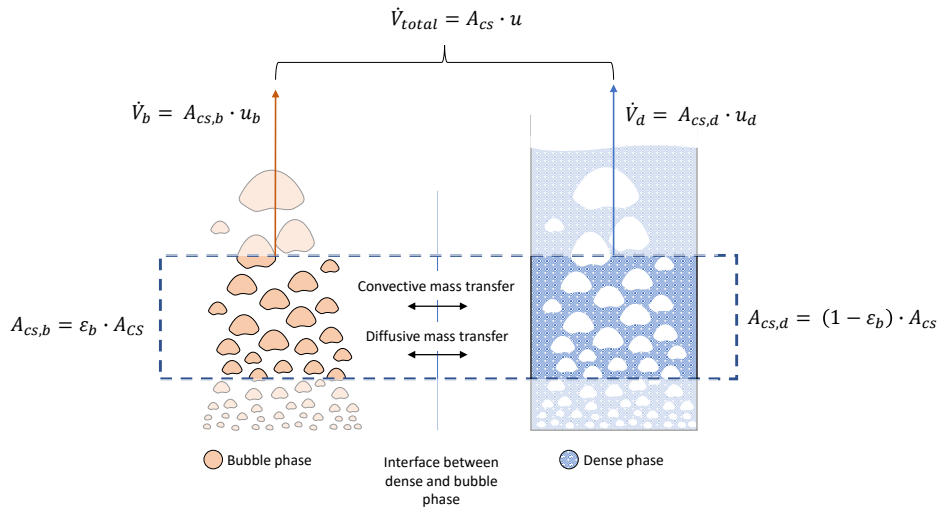


Figure 2.4: Illustration of the two-phase model of a BFB according to Toomey and Johnstone [111].

### 2.3.2 Hydrodynamics in bubbling fluidized beds

Similar to the development of turbulences in single-phase flow, the formation of bubbling is explained as the consequence of growing flow instabilities [112]–[114], which, depending on the properties of the gas and solids, can occur immediately after the bed has been fluidized or with a further increase of the superficial gas velocity. Davidson *et al.* [115] described the remarkable similarity between bubble properties in liquids and in fluidized beds. In both cases the bubble shapes can be described as spherical-cap shaped as can be seen in Figure 2.5. Their time averaged rising velocities can be described with Equation 2.16, where  $a_b$  is the radius of the curvature of the bubble top.

$$u_{br} = 0.67\sqrt{ga_b} \quad (2.16)$$

Additionally, the motion of the dense phase around the bubbles as they rise, the coalescence and bubble breakup mechanisms as well as the wake structure are very similar for bubbles in liquids and in fluidized beds [115].

#### Bubble wakes and particle transport

One of the most important aspects of bubbles in fluidized bed is the vertical transport of particles in the wake of the bubble, which is the main reason for the pronounced particle circulation in BFBs [73], [116], [117]. For small bubbles, the wake can be approximated by the volume that would be necessary to complete the sphere of the spherical-cap shaped bubble and is often described by the wake angle  $\Theta$  as shown in Figure 2.5. Rowe and Partridge [118] measured the wake angles for a variety of bed materials and bubble sizes by means of X-ray projections and observed that the volume of the wake is 25% of the bubble volume on average with a tendency to increase with decreasing particle sizes and more spherical particle shapes. Grace [119] used the measured wake angles to estimate the apparent dense phase viscosity, following the above-described similarity between bubbles in liquids and fluidized beds. Particles are continuously fed into the wake as the bubbles rise and shed periodically from the wake into the dense phase for which bubble coalescences seems to be mainly responsible [116], [117]. Besides the vertical transport of particles inside the bubble wake, they also are displaced by the drift of the bubble, which is qualitatively similar to the drift of a sphere moving through an inviscid fluid and the resulting return flow [116], [120], [121].

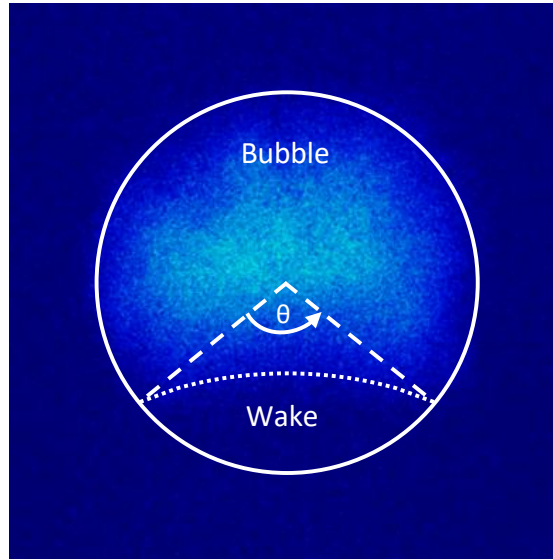


Figure 2.5: X-ray image of a bubble in a fluidized bed including illustrations of the spherical-cap shape, the wake and the wake angle.

### Davidson model of bubble flow

The Davidson model [122] describes the characteristic flow pattern of bubbles as they rise upwards in the fluidized bed. Accordingly, the flow patterns depend on the rise velocity of the bubble in relation to the gas velocity within the dense phase. This ratio can be expressed by a parameter  $\alpha$  as shown in Equation 2.17.

$$\alpha = \frac{u_{br}}{u_{mf}\epsilon_{mf}} = \frac{u_{br}}{u_d} \quad (2.17)$$

Depending on the value of  $\alpha$  the flow patterns of rising bubbles can be vastly different. This has significant implications for the gas-solid contacting in BFBs. Generally, a distinction can be made between slow rising bubbles, with  $\alpha < 1$  and fast rising bubbles, with  $\alpha > 1$ . For the case  $\alpha < 1$ , a significant throughflow of gas occurs that enters the bubble from the bottom and exits it again at the top, while only part of the gas recirculates within the bubble. The other case, where  $\alpha > 1$ , is characterized by the formation of a thin layer of suspension, often referred to as “cloud”, that surrounds the bubble. In this layer the gas of the bubble recirculates while comparatively little throughflow takes place. The thickness of the cloud and the corresponding ratio between throughflow and recirculating flow depends on  $\alpha$ . Figure 2.6 shows the resulting bubble flow patterns for various values of  $\alpha$  as presented by Kunii and Levenspiel [73]. Accordingly, bubbles in fluidized bed materials of Geldart group D typically show significant throughflow, whereas most gas recirculates within the bubble for Geldart group A and B material.

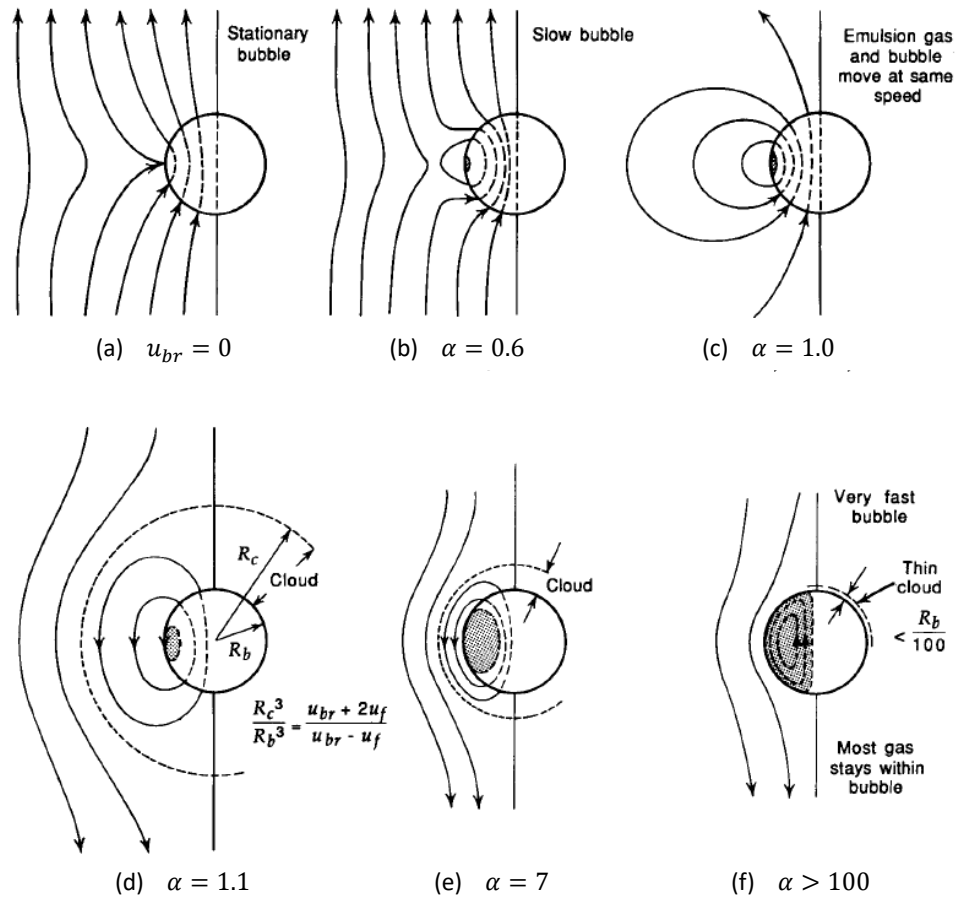


Figure 2.6: Typical flow patterns of bubbles rising at different velocities in relation to the velocity of the gas in the dense phase. Illustration adapted from Kunii and Levenspiel [73].

The gas flows through and around bubbles according to the pressure gradients that are shown in Figure 2.7, where the pressure within the bubble equals the static pressure of the bed at the height of the center of weight of the bubble [123].

### Bubble interactions, coalescence and breakup

The bubbles in BFBs dynamically interact with each other as they experience the drift flow of other bubbles causing them to follow the direction of the drift and accelerate towards the leading bubbles, which usually results in the coalescence of the bubbles. Such coalescence events are highly dynamic: the upper bubble typically experiences a moderate widening, whereas the lower bubble substantially accelerates, distorts and elongates throughout its approach towards the leading bubble [124], [125]. During the early stages of coalescence, a thin layer of particles separates the bubbles. This layer eventually collapses when the lower

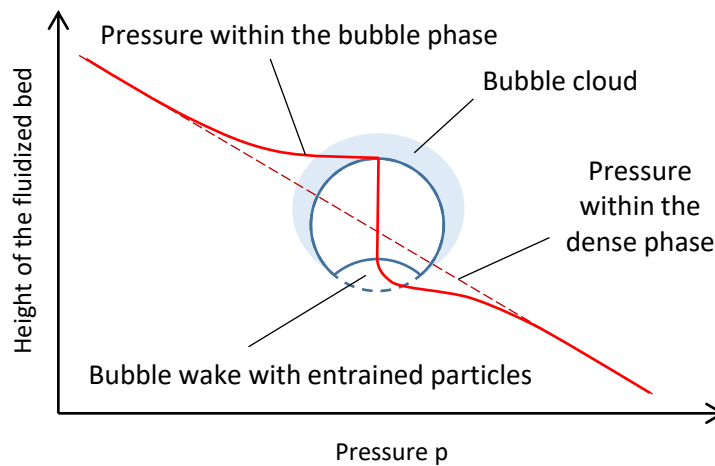


Figure 2.7: Pressure profile of a single rising bubble in a fluidized bed. Illustration adapted from Kraume [123].

bubble finally merges rapidly into the upper bubble [124]. Dynamic bubble interactions and coalescences in particular cause an increased interphase mass transfer between the bubble phase and the dense phase, which is especially pronounced immediately prior to the coalescence of the bubbles [126]. The dynamics in BFBs also enhance the interphase mass transfer through an increased throughflow in comparison to that of isolated bubbles [126], [127]. Due to the porosity of the bed, gas can also flow from one bubble to another without coalescence happening [128]. Further, coalescences near the bed surface can cause the ejection of particles into the freeboard at significantly increased velocities, which may lead to particle entrainment [103]. By means of bubble coalescence, the mean bubble diameter increases with increasing height in the bed. However, the net growth of the mean bubble size also depends on the rate of bubble break-up. For the explanation of bubble break-up, the so-called wake collapse theory and roof collapse theory are often discussed. The wake collapse theory was first proposed by Davidson and Harrison [129]. It states that particles are lifted upwards from the wake into the bubble once the toroidal gas circulation, which occurs within rising bubbles due to the relative downward motion of the particles surrounding the bubble, reaches the terminal velocity  $u_t$  of the particles. Clift and Grace [130] proposed the roof collapse theory, according to which bubbles also break through what they referred to as a knife or curtain of particles descending through the bubble roof into the bubbles, which eventually splits the bubble. This is explained by the Taylor instability [131], which states that irregularities occur at horizontal interfaces between phases if the upper phase has a higher density than the lower phase. Taylor instabilities typically lead to the formation of bubbles or drops and are also said to be the principle behind the formation of bubbles in fluidized beds [130]. Figure 2.8 shows a sequence of dynamic bubble interactions, in which a first bubble splits into two separate bubbles followed by a rapid coalescence with a trailing bubble.

The X-ray images show a controlled sequence of two bubble injections that were captured at a framerate of 22 Hz in column with a diameter of 22.4 cm filled with Geldart group B bed material as described in Sections 3.3, 3.3.1 and 3.3.3. A detailed description of X-ray imaging of controlled bubble injection experiments is presented in Section Section 4.6.5.

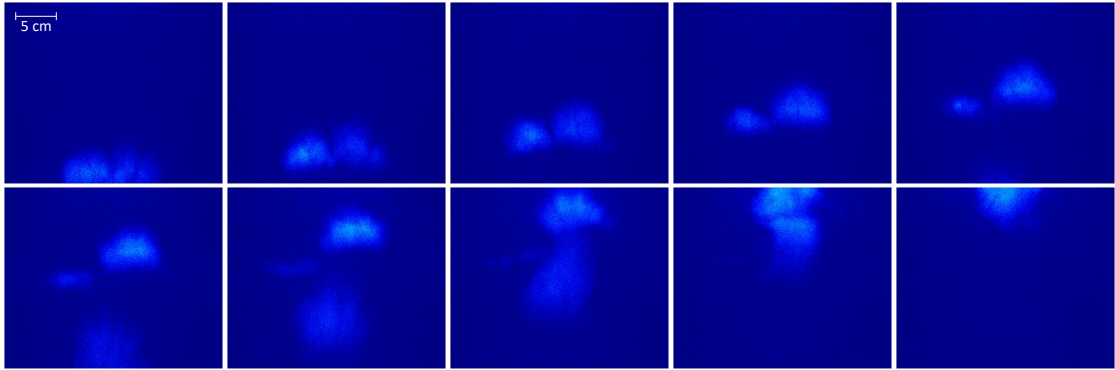


Figure 2.8: Sequence of X-ray images captured at a framerate of 22 Hz that show the breakup of a bubble followed by the coalescence with a trailing bubble.

### Bubble and particle flow patterns

Even when bubbles are distributed evenly at the bottom of the fluidized bed, their radial distribution shifts towards the middle through a series of coalescences, as bubbles at the wall can only coalesce vertically or away from the wall. A non-uniform distribution of bubbles with an increased bubble frequency close to the wall has often been reported for the zone right above the gas distributor [132], [133]. As a result of the non-uniform spatial distribution of the bubbles and the above described motion of the dense phase induced by the rising bubbles, specific particle circulation patterns develop. These flow patterns also depend on the aspect ratio of the bed, the bed material and the gas distribution and reported experimental results were not all consistent [73]. Therefore, a generalized pattern for relatively deep beds and Geldart B material, as it is described by Kunii and Levenspiel [73] and illustrated in Figure 2.9, is presented in the following.

There are two regions in which particles circulate. In the region immediately above the gas distributor, a relatively weak circulation occurs, in which the particles are transported upwards close to the walls and downwards at the center of the bed. Due to the shift of the bubble locations towards the center at higher heights, a second zone of particle develops as a direct result of the vertical particle transport in the wakes of bubbles as well as in their drifts. In this zone, the particles move downwards near the walls and upwards in the central region of the bed. The particle flow is directed upwards in the region where bubbles rise predominantly, while only few bubbles, if any at all, are found in regions where the particle flow is downwards. Understanding the flow patterns within a fluidized bed is important for the description of the

mixing of gas and solids, whereas axial and radial dispersion mixing models tend to perform poorly [128].

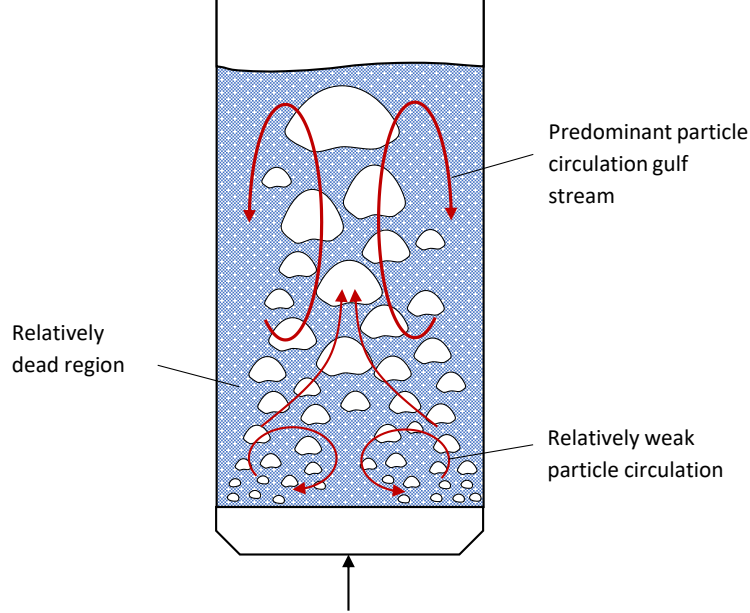


Figure 2.9: Schematic of a typical non uniform spatial distribution of rising bubbles in bubbling fluidized bed and the resulting particle circulation patterns. Adapted by Grace [128] and customized according to additional reports [73], [132], [133] and results of the present work.

### 2.3.3 Bubble properties

Bubbles are the dominant feature of BFB reactors and the precise description of their properties is necessary for the development of accurate models to describe their impact on the reactor performance.

#### Bubble size

The diameter of a bubble can be defined in various ways. Often the diameter that is equivalent to that of a sphere with the same volume as the bubble is used, which in this work is referred to as the volume-equivalent diameter  $d_{b,eq}$ , as shown in Equation 2.18.

$$d_{b,eq} = \sqrt[3]{\frac{6V_b}{\pi}} \quad (2.18)$$

The hydraulic diameter  $d_{b,hyd}$  is also often used. It is defined by Equation 2.19, where  $S_b$  is the horizontal cross-section and  $P_b$  the horizontal perimeter at the center of weight of the bubble.



$$d_{b,hydr} = \frac{4S_b}{P_b} \quad (2.19)$$

Other times, only specific characteristic sizes such as the mean chord length or width of the bubble are stated. This is usually the case, when the method used to measure the bubble sizes is restricted, for example when optical probes are used that can only measure the vertical chord length of a bubble.

There are many correlations available in the literature for the determination of the bubble diameter. Here, some popular choices are presented which according to a comprehensive review by Karimipour *et al.* [68] performed well on average. Correlations by Werther [55], Mori & Wen [134] and Darton *et al.* [135] were chosen.

Werther [55]:

$$d_{b,eq} = d_0 [1 + 0.272(u - u_{mf})]^{1/3} (1 + 0.0684h)^{1.21} \quad (2.20)$$

$$d_0 = \begin{cases} 0.610 & \text{for Geldart group A material} \\ 0.853 & \text{for Geldart group B material} \\ 1.230 & \text{for Geldart group D material} \end{cases}$$

Mori & Wen [134]:

$$\frac{d_{bm} - d_v}{d_{bm} - d_{b0}} = \exp\left(-\frac{0.3h}{D}\right) \quad (2.21)$$

$$d_{b0} = 0.00376(u - u_{mf})^2$$

$$d_{bm} = 0.652[A_R(u - u_{mf})]^{2/5}$$

Darton *et al.* [135]:

$$d_v = 0.54g^{-0.2}(u - u_{mf})^{0.4}(h + 4A_0^{0.5})^{0.8} \quad (2.22)$$

### Bubble shape

It is important to correctly describe the shape of the bubbles, especially for the calculation of the mass transfer between the bubble phase and the dense phase, which requires the knowledge of the specific surface area of the bubble  $a_b$  that is the ratio between the surface area and the volume of the bubble. Knowing the bubble shape is also important for the evaluation of locally constricted methods for the measurements of bubble properties, such as optical probes or capacitive probes. A transformation of a measured chord length distribution to the bubble size distribution by means of statistical methods is only possible if the bubble shape is known [136]. Often, a spherical cap shape is assumed, as it is shown in Figure 2.5, with wake angles in the range of  $120^\circ$  -  $135^\circ$  [118], [137]. Hemispherical, ellipsoidal and truncated ellipsoidal shapes are also common assumptions [118], [138]–[140]. Werther [141] proposed a correlation for a shape factor  $\alpha$ , as shown in Equations 2.23 and 2.24, which describes the ratio of the vertical to the horizontal diameter. By definition, the shape factor  $\alpha$  is always less or equal to one and experiments showed values for the form factor between 0.8 and 0.9 [142].

$$\alpha = (1 - 0.3 \exp[-8(u - u_{mf})]) e^{-\varphi h} \quad (2.23)$$

$$\varphi = 7.2(u - u_{mf}) \exp[-4.1(u - u_{mf})] \quad (2.24)$$

### Bubble rise velocity

Another important property of bubbles in a BFB is their rise velocity as it determines the residence time of the bubble and with that the contact time between the dense phase and the bubble phase and the corresponding mass transfer. The bubble rise velocity also influences the intensity of the particle circulation and thus the mixing of the solids and the heat transfer between the fluidized bed and the surfaces of the walls or internal heat exchanger surfaces. Davidson and Harrison [143] proposed a correlation, which is shown in Equation 2.25 and is often used to calculate the rise velocity of single bubbles.

$$u_{br} = 0.711 \sqrt{g d_b} \quad (2.25)$$

Rowe and Partridge [118] adapted the correlation and distinguished between particles of Geldart group A and B:

$$u_{br} = k \sqrt{g d_{b,eq}} \quad (2.26)$$

$$k = \begin{cases} 0.926 & \text{for Geldart group A material} \\ 1.020 & \text{for Geldart group B material} \end{cases}$$

For the determination of the rise velocity of bubbles in freely bubbling beds, the correlations have been expanded by an additional term  $(u - u_{mf})$ , which can be regarded as a correction term which accounts for dynamic bubble interactions when the bubbles rises as part of a swarm of bubbles [144]. Equation 2.27 shows the adaptation.

$$u_b = u_{br} + (u - u_{mf}) \quad (2.27)$$

Hillgardt and Werther [56] expanded the correlation to account for different heights, reactor geometries and bed materials:

$$u_b = \psi (u - u_{mf}) + \vartheta u_{br} \quad (2.28)$$

For Geldart group A particles:

$$\psi = 0.8 \quad (2.29)$$

$$\vartheta = 0.7 D^{\frac{1}{3}} \quad (2.30)$$

For Geldart group B particles:

$$\Psi = \begin{cases} 0.67 & h/D < 1.7 \\ 0.51 \sqrt{h/D} & \text{for: } 1.7 < h/D < 4 \\ 1 & h/D > 4 \end{cases} \quad (2.31)$$

$$\vartheta = 0.2 D^{0.5} \quad (2.32)$$

For the calculation of the bubble size as well the rise velocity of bubbles, there are many more correlations available in the literature. Karimipour *et al.* [68] provide a detailed review of 25

bubble size correlations and 16 bubble rise velocity correlations from literature, including a ranking of their performance in comparison to experimental data available in the literature.

### Bubble hold-up

One of the most fundamental ways to characterize the bubble phase in a fluidized bed is the bubble hold-up  $\epsilon_b$ , which describes the ratio of the volume of the bubble phase to that of the entire bed, as defined in Equation 2.33.

$$\epsilon_b = \frac{V_{b,total}}{V_{bed}} \quad (2.33)$$

The bubble hold-up can be defined for the entire bed or for a defined volume, area or location within the bed. The cross-sectional bubble hold-up describes the spatial distribution of the bubble phase at a horizontal cross-section of the bed for a specified height, whereas the local hold-up describes the bubble-hold up at a specific point in the fluidized bed. Usually, the time averaged value of the bubble hold-up is used.

## 2.4 Scale-up of bubbling fluidized bed reactors

One of the biggest challenges of any chemical reactor development are the various non-linear dependencies between reactor characteristics and the reactor scale. The limiting step and therefore the performance of the reactor may vary with the scale. A simple example for this is the ratio between the surface area and the volume of a reactor. While the surface area increases with the reactor diameter  $D_R$  squared, the reactor volume increases cubic with  $D_R$ . This can have significant consequences, *e.g.* for exothermic reactions, where heat can be removed sufficiently via cooling through the reactor wall for reactors with large specific surface areas. This may not be the case for an increased reactor diameter and the resulting reduced specific surface area.

Determining the scale dependencies experimentally, is considered particularly difficult for fluidized bed reactors, due to the manifold scale dependent design parameters, such as the bubble growth, mass and heat transfer, particle properties, and flow patterns [145], [146]. Fluidized bed reactors also often show scale dependent wall effects (*e.g.* slugging) which can significantly impact the reactor performance and may occur at small reactor scales and disappear for larger reactor diameters. A detailed scale-up procedure is especially important for catalytic fluidized bed reactors, where the economic risks are very high [147].

### 2.4.1 General scale-up approach

The scale-up of processes typically involves several development stages at plants of increasing complexity. According to the recommendations by Kelkar and Ng [148], Chen *et al.* [149], Ellis and Botero [147], Knowlton *et al.* [81] and Rüdüsüli [146], a general approach for catalytic fluidized bed reactors typically involves the following steps:

#### Screening

In the screening phase, the general suitability of fluidization regimes and reactor designs are investigated. It involves generic reactor models and requires basic knowledge on the reaction kinetics and physicochemical properties of the process. The reaction kinetics can typically be determined in a micro-scale fixed bed reactor.

#### Lab-scale investigations

Initial hydrodynamic investigations are carried out in lab-scale units to determine basic characteristics of the fluidized bed, such as its ability to fluidize, the minimum fluidization velocity, particle attrition and elutriation, or bed expansion. Such investigations are often carried out in non-reactive systems that are referred to as cold-flow models. Cold-flow systems are usually operated with air as the fluid and a substitute material for the catalyst, typically the catalyst carrier. The kinetics of possible side-reactions and catalyst deactivation are usually also determined in a lab-scale reactor. Usually, the diameter of lab-scale reactors is in the range of 1 - 5 cm for fixed bed investigations and 5 – 20 cm for fluidized bed investigations.

#### Scale-up

Pilot-scale units with diameters in the range of 20 – 60 cm are typically used for scale-up investigations [147]. The required diameter depends on the type of used bed material. For Geldart group A material, diameters in the range of 15 - 30 cm are usually sufficient, whereas larger diameters in the range of 60 - 100 cm are recommended for Geldart group B material [81]. Certain aspects of the hydrodynamics, such as the bubble growth, flow patterns, effects of internals, effect of the feed compositions, influence of elevated pressures and temperatures, pressure, temperature and concentration profiles, and the distributor design can only be investigated adequately in the pilot-scale. Another purpose of pilot-scale investigations is to confirm the reliability of the reactor design, which usually requires long term continuous operation in the range of 1,000 or more hours at reactive conditions.

Typical concerns in this context are: the attrition and elutriation of bed material, the attrition of reactor surfaces, the deactivation of catalyst, and the reliability of equipment and process control. Knowlton *et al.* [81] suggests developing a larger cold-flow model to demonstrate the hydrodynamic similarity, which is given when two reactors of different scales are designed and operated with identical non-dimensional parameters and their dependent variables are identical throughout the entire bed [148].

### Demonstration plant

A demonstration plant with a diameter that usually is in the range of 80 – 150 cm and a similar height to that of the designated commercial plant size may be built to further confirm the long-term operational stability. Demonstration plants are typically designed to verify the cost-effectiveness of the plant and are therefore usually optimized for economic viability, whereas pilot plants are normally designed in a more robust way, considering the level of uncertainties encountered at that stage of the process development. There are two common approaches for the scale-up of equipment. One is the application of the Buckingham Pi-Theorem [150], which states that if  $n$  independent parameters *e.g.* density, viscosity, etc. can be identified to completely describe a physical process, then a relationship of  $(n - p)$  dimensionless parameters, where  $p$  is the number of fundamental dimensions, such as time, length or mass, is sufficient to fully describe the process. The other approach is inspectional analysis, which is a method to transform the governing equations and boundary conditions of a physical process in a non-dimensional form. Ultimately, they both yield the same results if applied correctly [151]. However, applying the Buckingham Pi-Theorem can be problematic if not all relevant parameters can be identified. It is also considered to be not well suited for open systems, which are common in chemical engineering [146].

#### 2.4.2 Hydrodynamic scale-up bubbling fluidized bed reactors

Glicksman [67] identified the full set of relevant dimensionless numbers, through transformation of the equations that describe the motion and conservation of mass of both gas and solids in fluidized beds to their non-dimensional form. Accordingly, the following dimensionless groups have to be matched to obtain similar hydrodynamic conditions for different reactor scales:

$$\frac{u\rho_g d_p}{\eta}, \frac{u^2}{gD}, \frac{\rho_g}{\rho_p}, \frac{D}{H}, \frac{d_p}{D}, \phi, \text{ dimensionless } PSD \quad (2.34)$$

Here, the first term represents the Reynolds number and the second term represents the Froude number. One issue with this full set of parameters is its constrictiveness, which can

lead to scenarios where the hydrodynamics within large hot reactors cannot be investigated in a lab-scale cold-flow reactor of reasonable dimensions and a similarly scaled cold-flow model to fulfill the dimensionless group criteria [146].

To overcome these constraints, Glicksman [152] proposed a reduced set of scaling laws by adapting the Ergun equation. Accordingly, the scaling laws can be reduced by removing parameters containing the fluid density for  $Re_p < 4$  for air at ambient conditions, where viscous forces are dominant, whereas the parameters containing the fluid viscosity can be removed for  $Re_p > 1,000$ , where inertial forces are dominant. Additionally, the ratio between the particle and the reactor diameter were replaced by the fluidization number  $u/u_{mf}$ .

Rüdisüli *et al.* provide a comprehensive review on the scale-up of bubbling fluidized beds, which includes a detailed list of scale-up validation studies. The author notes that many of the early studies showed successful applications of the scaling laws, in contrast to more recent studies, which were more critical and find the applicability of the proposed scaling laws to be limited. Sanderson *et al.* [153] reports that Glickman's scaling laws are only accurate for smaller scales. A computational investigation by means of CFD, where two fluidized beds with diameters of 15 and 30 cm were simulated, was conducted by van Ommen *et al.* [154], which showed that neither the complete nor the simplified scaling laws lead to complete similarity. Surprisingly, the simplified set outperformed the full set of scaling laws in that study. Leckner *et al.* [155] applied the scaling laws for the hydrodynamic scaling between a small-scale solids test rig and a large boiler relatively successful. The authors emphasized that a general scaling approach is not practical and differentiated between fluid-dynamic, combustion and boiler scaling.

Commonly stated critique of Glicksman's scaling rules are the lack of a particle pressure term, which is necessary for the description of homogeneous fluidization [156], the omission of interparticle forces, which may be critical for Geldart group C and sometimes group A powder [147], and particle collisions, which have been proven to significantly influence the hydrodynamics of fluidized beds by means of CFD simulations [157]–[159]. Another commonly cited scale-up approach, which also applies dimensional similitude, was proposed by Horio *et al.* [160]. The method requires two conditions to be fulfilled: similarity in bubble coalescence and similarity in bubble splitting and interstitial flow patterns.

### 2.4.3 Scale-up of reactive bubbling fluidized bed reactors

The scaling rules by Glicksman were derived for non-reactive systems. Therefore, they do not include the equations related to the reaction and heat transfer. While the hydrodynamics can be maintained for a change in scale if the dimensionless parameters maintain unchanged, this may not apply for the heat and mass transfer. This is especially relevant, when the reaction

kinetics is limited by diffusive or intraparticle mass transfer, in which case changing the particle diameter could significantly influence the reactor performance. Consequently, it is necessary to determine which mass transfer mechanism, convection or diffusion, is rate-determining. Davidson and Harrison [129] proposed a correlation for the mass transfer coefficient  $k_{be}$ , shown in Equation 2.35, where  $D^*$  is the molecular diffusivity. Horio *et al.* [160] derived a factor  $\beta$  from  $k_{be}$ , as shown in Equation 2.36 to determine whether convection or diffusion is dominant. For the case  $\beta < 0.1$  the mass transfer is dominated by diffusion, whereas  $\beta > 10$  indicates that convection is rate-determining. The reactor diameter significantly influences the value of  $\beta$ , which scales proportional to  $D^{-0.75}$  [148].

$$k_{be} = 4.5 \frac{u_{mf}}{d_b} + 5.85 \frac{\sqrt{D^*} g^{0.25}}{d_b^{1.25}} \quad (2.35)$$

$$\beta = \frac{\sqrt{D^*} g^{0.25}}{u_{mf} d_b^{0.25}} \quad (2.36)$$

#### 2.4.4 Sectoral scale-up of bubbling fluidized bed reactors with internals

Rüdisüli *et al.* [161] developed a sectoral scale-up method that can significantly simplify the scale-up procedure, if vertical internals are present. In this approach, the hydraulic diameter  $d_{hyd}$  of a unit cell of vertical tubes is used as the characteristic length scale for the complete set of scaling laws by Glicksman [67], rather than the reactor diameter. Therefore, the scaling is independent of the absolute scale of the reactor and of particle sizes. This is one of the great benefits of the approach, as it removes challenging constrictions from Glicksman's full set of scaling laws and allows to directly transfer the particle mass transfer mechanisms derived at the lab-scale to larger scales. The sectoral approach can be applied, given that the hydrodynamics in a defined sector are autonomous. Here, the hydraulic diameter is defined by the free cross-sectional area between internals and their wetted perimeters as described by Equation 2.37 and shown in Figure 2.10.

$$d_{hyd} = \frac{4S}{P_{wet,int}} = \frac{4 \left( L^2 - \pi \frac{d_{int}^2}{4} \right)}{\pi d_{int}} \quad (2.37)$$

Maurer *et al.* [162] expanded the sectoral approach and determined the representative size of a sector by means of optical probe measurements. Accordingly, a pattern of 4 x 4 internals is necessary for further up-scaling as illustrated in Figure 2.11.



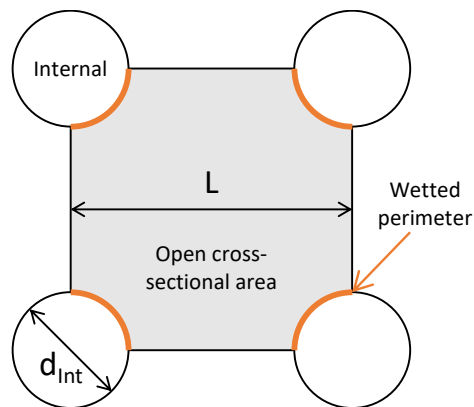


Figure 2.10: Illustration of a unit cell of vertical tubes including labeled parameters used for the definition of the hydraulic diameter.

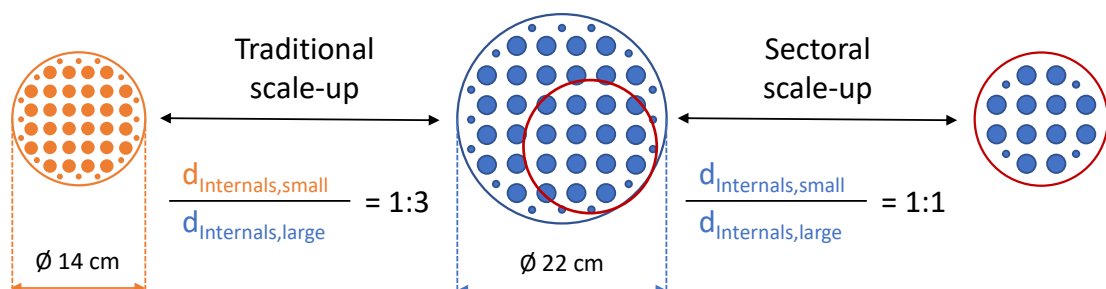


Figure 2.11: Illustration of the sectoral scale-up in comparison to the traditional scale-up.



## 3 Experimental setups

In this chapter, the experimental setups that were used to obtain the results presented in Chapters 4 and 5 are described. All experiments were carried out at ambient temperatures, using pressurized air for the fluidization. A BFB reactor in the pilot scale, referred to as GanyMeth or GAM, is equipped with a variety of sensors. Those that are not relevant for the present work are mentioned briefly in the following. Additionally, a detailed description is provided for the optical measurement lances that were used in the scope of this work for the measurement of rising bubbles at elevated pressures. Due to the unique reactor design with a inserted vertical heat exchanger tube bundle, significant wall effects have to be considered and comprehensive efforts were made to account for them in the experiments. A Perspex<sup>®</sup> column, referred to as cold-flow model, was used for several experimental campaigns. The cross-sectional geometry of cold-flow model equals that of the GanyMeth plant. It was used to elucidate the uncertainties of the measurements in the GanyMeth and to expand the general understanding of the respective hydrodynamic phenomena by utilizing additional experimental methods. This included the application of a variety of auxiliary equipment, such as optical probes, vertical internals representing heat exchanger tubes, a heated vertical internal equipped with heat flux sensors, a single bubble injection mechanism and two independent X-ray tomography setups.

### 3.1 Pilot-scale plant GanyMeth

In the following, the general concept of the reactor design and auxiliary equipment with an additional focus on the measurement technology required for the experiments described in Chapter 5 is explained. The pilot-scale fluidized bed methanation reactor GanyMeth is designed to produce a nominal output of 180 kW of SNG at temperatures of up to 400 °C and pressures of up to 12 bar. It is 250 cm high, has an inner diameter of 22.4 cm and includes a system of vertical internals, which are connected to the cooling circuit. The main objective of

the plant is the measurement of the hydrodynamics of the fluidized bed at reactive conditions at a representative scale. Ultimately, the GanyMeth plant will be used to verify the reactor model that is currently being developed at PSI.

### 3.1.1 Functional description of the pilot plant GanyMeth

A gas panel provides defined mixtures of the gas components  $H_2$ ,  $CO_2$ ,  $CO$ ,  $CH_4$ ,  $C_2H_4$ ,  $He$ ,  $N_2$  and air. The preheating of these gases is possible via two electrical heater rod bundles with a heating power of up to 15 kW each. There are two operation modes available for the gas flow; one is designed for the accurate control of the mass flow of mixtures of inert and burnable gases in the range up to  $200 \text{ kg h}^{-1}$  while the second enables large airflow rates of up to  $350 \text{ kg h}^{-1}$ . The flow rates were measured with Coriolis flow meters by Endress & Hauser and the mass flow was controlled with Metso Neles rotary globe control valves. A perforated gas distributor plate, manufactured by Tridelta Siper GmbH, made from sintered steel with a mean pore size of  $6 \mu\text{m}$  and a porosity of 33-38 % was used to ensure an even gas distribution.

The reactor has 22 flanges for the insertion of analytical and measurement devices, shown in a technical drawing in Figure 3.1. A measurement lance is inserted vertically into the reactor at a central location (Flange N9). The measurement of the vertical temperature profile is possible, whereas the measurement of the vertical concentration profile of the gas phase through gas probing and subsequent online analysis via gas chromatography is not yet available. The sampling of catalysts at reactive condition will also be possible by means of a sampling device, which will be inserted vertically (Flange N10). There are two pressure sensors; one is installed upstream of the gas inlet (Flange N1), while the other one is placed downstream of the outlet of the reactor (Flange N2). The temperature of the reactor is measured at the gas inlet below the gas distributor plate (Flange N3), in the lower zone of the bed (Flange N11) and in the freeboard of the reactor (Flange N14). For the hydrodynamic investigations, two measurement principles can be applied for the GanyMeth plant: pressure fluctuation and optical probe measurements. While the origin of pressure fluctuations that accompany rising bubbles in fluidized bed is still debated [163], it has been demonstrated that they can be used to determine characteristic lengths that are proportional to the bubble size [82]. However, it is not possible to distinguish between several individual bubbles passing the sensor at the same time and to identify their individual properties when applying this method. In addition, no information on the radial position of the bubbles can be determined by such measurement. Optical probes allow the measurement of the pierced chord length  $d_{b, \text{chord}}$  and the rise velocity  $u_{br}$  of individual bubbles as well as the bubble frequency and bubble hold-up  $\varepsilon_b$  at the position the sensor is placed. While the measurement of pressure fluctuations is non-intrusive and therefore does not influence the hydrodynamics of the fluidized bed, optical probes are inserted which may have an impact on the measured bubble properties.

### 3.1 Pilot-scale plant GanyMeth

There are eight flanges (N24-N31) at which pressure fluctuation sensors (Kistler® Type 7261) can be installed and eight flanges (N15-N22) at which optical probe sensors can be installed. In total, there are six pressure fluctuation sensors and six optical probe sensors available. In the present work, the optical probes were applied for extensive experimental investigation, while no pressure fluctuations measurements were conducted. The design and functionality of the optical probes are therefore discussed in detail in the next section.

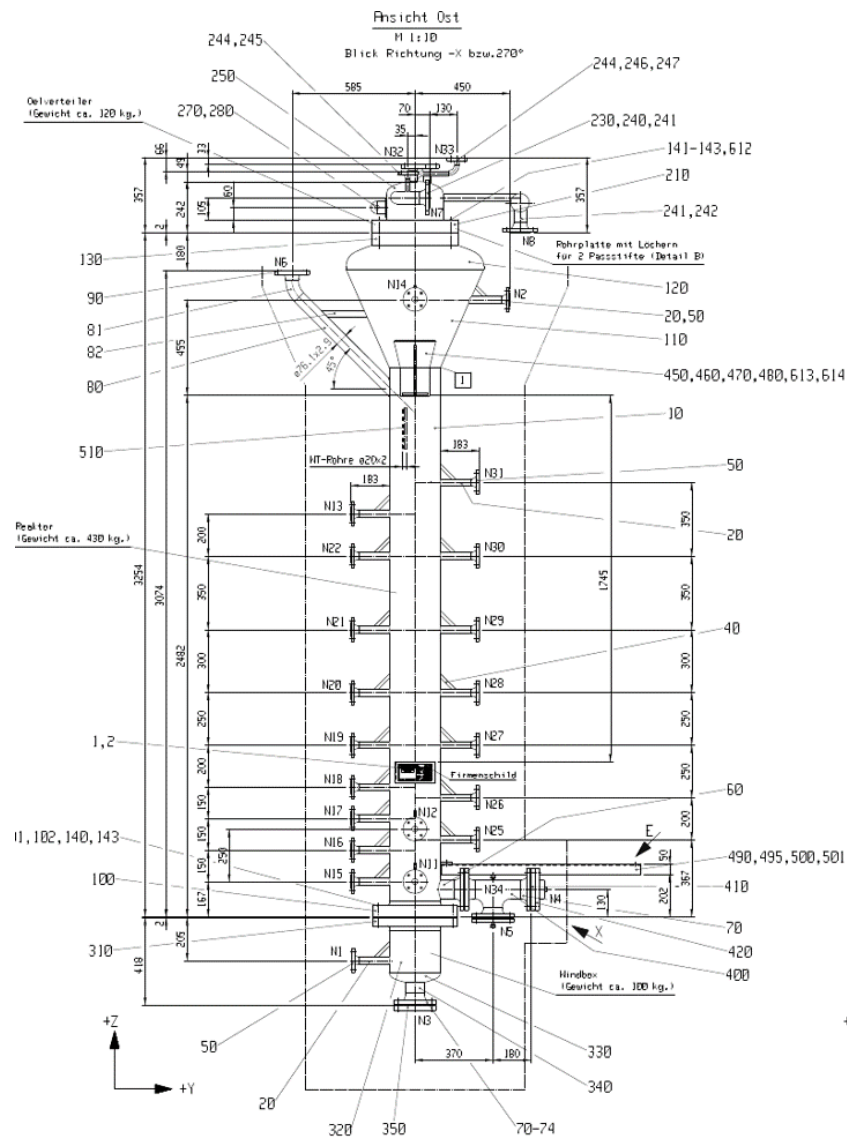


Figure 3.1: Technical drawing of the pilot-scale reactor GanyMeth with dedicated measurement locations.



transistor. If there is a bubble present, little or no light will reflect back. Thus, a virtually binary signal for the presence of bubbles is measured.

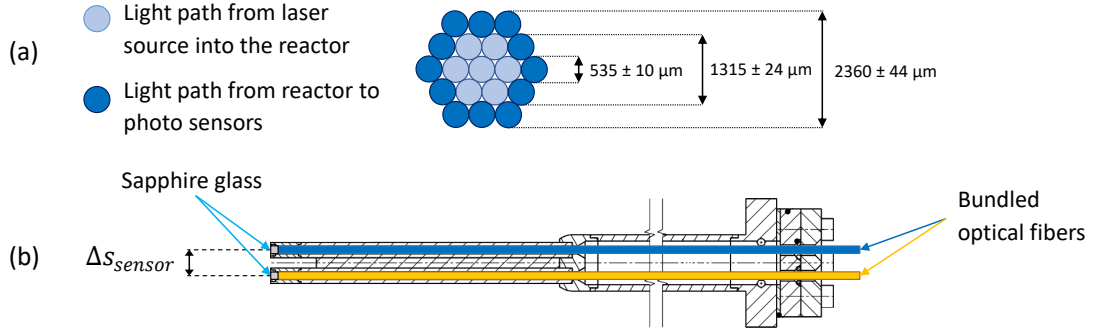


Figure 3.3: Schematic illustration of optical probe details:

a) Arrangement of glass fibers inside the optical probe.

b) Vertically coupled optical probe.

Since the distance between the coupled sensors is known, the bubble rise velocity  $u_{br}$  can be determined via the time difference between the corresponding signals of each sensor. Once  $u_{br}$  is known, it can be multiplied with the time duration of the signal and thus, the pierced chord length of the bubble can be determined. This is shown in equations 3.1 & 3.2 and illustrated in Figure 3.4.

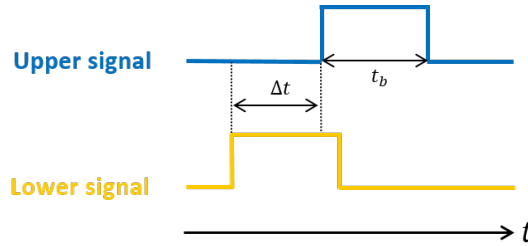


Figure 3.4: Schematic example of vertically coupled optical probe signal.

$$u_{br} = \frac{\Delta s_{sensor}}{\Delta t} \quad (3.1)$$

$$d_{b, chord} = u_{br} t_b \quad (3.2)$$

The optical probes were developed and built by PSI as described in the dissertation of Maurer [70]. They are designed to withstand temperatures of up to 400 °C and pressures of up to 25 bar. In addition, they are technically tight, which is necessary to ensure the safe operation under reactive conditions where toxic and explosive gases as well as carcinogenic catalyst particles

are present in the reactor. One problem for the measurements at reactive conditions is that the nickel catalyst is black and therefore absorbs most of the light. To account for this, the optical probes were originally designed to enable the attachment of a small mirror in front of the sensor tip while leaving a gap through which the fluidized particles can flow. An illustration of this is shown in Figure 3.5.

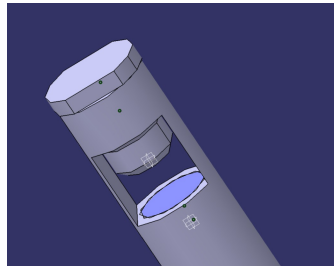


Figure 3.5: Sensor tip of the optical probe with attached reflector screw. Illustration adapted from Maurer [70].

However, in the course of comprehensive preliminary measurements, which are presented in Section 5.2.5, it could be shown that the reflector attachments significantly influenced the measurements. Therefore, they were removed from five of the available sensors prior to the experimental campaigns, leaving only one sensor with a reflector attachment for possible future measurements under reactive conditions. A test bench was developed to carry out evaluations of the sensor system under laboratory conditions, which led to an overhaul of the electronic hardware of the sensor system. A detailed description of these preliminary investigations can also be found in Section 5.2.5.

Ultimately, the electronic components described in the following have been used for the hydrodynamic experiments presented in this work. Laser diodes of the type L785P25 that are manufactured by Thorlabs GmbH, were used as light sources. They generate laser light with a typical wavelength of 785 nm at a typical output power of 25 mW. Potentiometers were installed to adjust the diode forward voltage and with that, the optical power of the laser. This made it possible to calibrate each individual sensor system, so that the signal to noise ratio of the photodiode voltage output is maximized and consistent for all used sensors. Photo transistors of the type BPY 62-4 that are manufactured by Osram Licht AG, were selected for the light detection, as they are highly sensitive to light emitted from the chosen laser. The photo transistors transform the light intensity into a voltage signal which is read with a framerate of 5 kHz. A description of the evaluation of the voltage data is provided in Section 5.2.2.



### 3.3 Cold-flow model

Several Perspex<sup>®</sup> columns with diameters in the range of 5-22.4 cm were used for fluidization experiments. A variety of vertical Perspex<sup>®</sup> tube bundles are available to represent the heat exchanger tubes of the reactor. Since the influence of the diameter and the different arrangements of the vertical internals have already been investigated thoroughly in previous studies [133], [161], [164], [166], [167], only the column with an inner diameter of 22.4 cm, which from here on will be referred to as cold-flow model, and a circularly arranged tube bundle, which both match the design of the GanyMeth plant, are used for the experimental studies in this work.

The cold-flow model was originally designed for a first series of X-ray tomography measurements at TU Delft in the scope of the dissertation of Maurer [70] in 2014, with the goal to obtain further knowledge on the hydrodynamics of the GanyMeth plant that could not be achieved with optical probes or pressure fluctuation measurements. For the experiments conducted in this work, the column has been slightly modified. The following description of the cold-flow model refers to its current stage.

This thesis also includes the evaluation of X-ray tomography experiments that were obtained prior to these adaptations in the work of Maurer. The modifications that may influence the measurements are specified accordingly. The column is 80.8 cm tall, has an inner diameter of 22.4 cm and a wall thickness of 10 mm. Slotted holes, which allow the insertion of the optical probes used in the GanyMeth plant, are placed vertically aligned with a spacing of 10 cm between their centers starting at a height of 10 cm above the gas distributor plate. Two additional holes, one of which is placed 5.5 cm below the lowest slotted hole while the other is placed horizontally aligned at the other side of the column, allow the insertion of bubble injection nozzles. The internals have a diameter of 2 cm and are connected by so-called U-connectors at a distance of 3 cm above the distributor plate. There are three tube spacers, which are used to keep the internals in their designated positions along their entire length. Similar tube spacers are installed in the GanyMeth plant. Figure 3.6 shows a comparison between the heat exchanger tube bundle, including the tube spacers, which is installed in the pilot plant and the internals and tube spacers which are used in the cold-flow model.

For the X-ray tomography experiments, it is important to ensure that the internals do not change their position during the measurements. Even a slight rotation may impact the measurements because the evaluations are based on calibrations with the intensity profiles from the original orientation of the internals. Therefore, the top tube spacer was designed with a raised height of 2 cm to increase the stiffness and an additional outer ring that is fixed between two flanges at the top of the column. The gas distributor plate is identical to the one that is installed in GanyMeth plant. An additional Perspex<sup>®</sup> cylinder, which is often referred

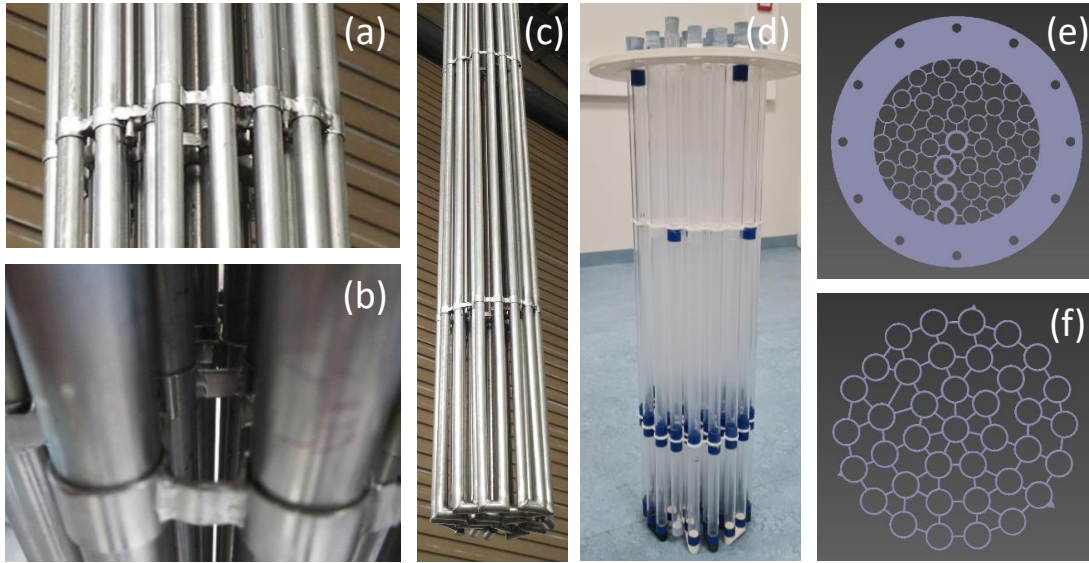


Figure 3.6: Series of images showing various perspectives of the vertical heat exchanger tube bundle including the tube spacer, as they are installed in the GanyMeth plant (images (a),(b),(c)), the vertical tube bundle, as it can be inserted in the cold-flow model (image (d)) as well as the respective tube spacers. Image (e) shows the top tube spacer and image (f) shows one of the lower tube spacers.

to as plenum chamber or windbox, is installed below the gas distributor plate. The gas feed is directed centrally downwards through a pipe into packing material inside of the windbox. This is done to assure a uniform distribution of the air flow through the distributor plate. However, preliminary measurements have shown a significant maldistribution of the gas flow. For this reason, the filling material, the gaskets between the perforated plate and the flanges as well as the perforated plate itself have been replaced for the measurements conducted in the scope of this thesis. As a result, no further maldistribution was observed. It is unclear if the observed maldistribution was already present during the measurements as part of the work of Maurer *et al.* and Schillinger *et al.* [133], [164], [167]–[169] which are also evaluated in this work. However, the measured cross sectional bubble hold-up  $\varepsilon_b$  at lower heights, which are shown in Sections 4.3.2 and 4.5.2, indicate that this is likely the case.

In this work, the cold-flow model has been used in combination with a variety of experimental setups that are described in the following.

#### 3.3.1 X-ray measurement setups

In this work, experimental results from two independent X-ray tomography setups are presented. To distinguish between the two, the setup described in the following section will henceforth be referred to as X-ray tomography line detector (XR-LD) setup, while the setup described

further below, will be designated as X-ray tomography area detector (XR-AD). A detailed descriptions of the fundamental principles of X-ray measurements is provided in Section 4.1.

### X-ray line detector tomography setup (XR-LD)

Throughout the research on the hydrodynamics of BFB reactors, a close collaboration between PSI and the Delft University of Technology (TU Delft) developed. In 2014, the first joint X-ray tomography experiments were conducted, where a fast double X-ray tomography scanner was applied to measure the cross-sectional solid distribution in two parallel measurement planes [133]. Figure 3.7 shows the setup, which consists of three X-ray sources positioned at angles of  $120^\circ$  around a fluidized bed and two sets of three horizontal detector arrays, which were installed opposite of the sources at two heights separated by 40 mm. In this way, two measurement planes were formed with vertical distances between 15.5 mm and 21 mm resulting in an average vertical distance of 18.2 mm.

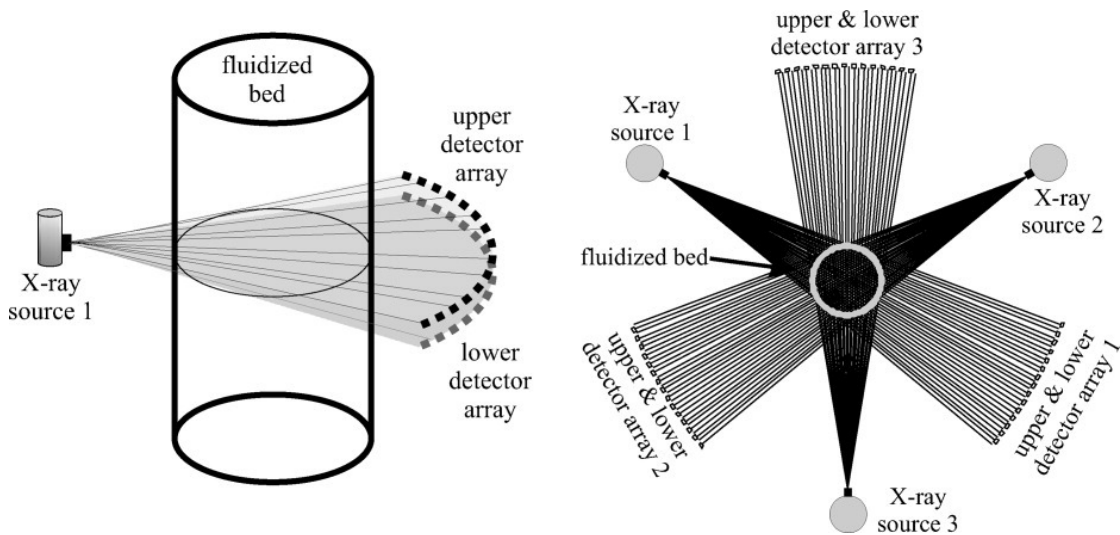


Figure 3.7: Schematic illustration of the X-ray tomography setup. Left: Reduced representation of the setup showing the fluidized bed with only one of the X-ray sources and its corresponding detector arrays. Right: Top view of the complete setup. Adapted from Mudde [170].

The X-ray sources were manufactured by Yxlon International GmbH and provide a maximum X-ray energy of 150 keV. For the experiments evaluated in this work, the sources were usually operated at currents of less than 1 mA [133]. Each of the horizontal X-ray detector arrays contains 32 individual detectors, which consist of  $\text{CdWO}_4$  scintillation crystals that are optically coupled to a PIN photodiode. The detectors have a crystal size of 10 x 10 x 10 mm and were manufactured by Hamamatsu (type: S 1337 – 1010BR). They are arranged with a curvature so that the distance between the individual detectors and the focal point of the X-ray source is consistent. Only 30 detectors of each array are used for the tomography measurements,

while the other two are used for the alignment of the fluidized bed column and to monitor the proper functioning of the setup by measuring the unattenuated X-ray intensities. The transmitted X-ray intensity is measured at a frame rate of 2.5 kHz. A detailed descriptions of the tomographic reconstruction procedure is provided in Sections 4.2.1 and 4.2.3.

#### **X-ray area detector tomography setup (XR-AD)**

In this work, a second experimental X-ray campaign was carried out using a new X-ray tomography setup at TU Delft. While the X-ray sources remained the same as the ones used in the XR-LD setup described above, new high-resolution X-ray flat panel area detectors were placed opposed to the X-ray sources. The detectors were manufactured by Teledyne DALSA (type Xineos-3131) and consist of monolithic crystalline silicon. The panels apply the complementary metal-oxide-semiconductor (CMOS) active pixel technology and produce images with a resolution of 1,548 x 1,524 pixels for an active area of 307 mm x 302 mm. Their framerate is 22 Hz for measuring images at full resolution. The resolution can be reduced in one dimension of the detector panel to increase the framerate. A maximum framerate of 220 Hz can be achieved when the resolution is reduced to 100 x 1,524 pixels, which essentially turns the detector into a high-resolution line detector that can be applied in the same way as the XR-LD setup described above.

In comparison to measurements with the XR-LD setup, the application of high-resolution X-ray flat panel area detectors allows the observation of entire bubbles, rather than pseudo three-dimensional representations that are based on the frame-by-frame stacking of the reconstructed bubble cross sections and are dependent on the assumed bubble rise velocity  $u_{br}$ . In this way the dynamic evolution of the bubble as it rises in the fluidized bed can be observed. The shape and rise velocity of individual bubbles fluctuate significantly in a bubbling fluidized bed as they experience the draft of other bubbles, the draft of the circulating particles, the shedding of particles carried in their wake and pressure fluctuations. Additionally, this method allows the observation of highly dynamic bubble coalescence and breakage events. In a partnership with the Dutch national research institute Centrum Wiskunde Informatica (CWI), TU Delft is currently working on an algorithm that will allow the three-dimensional reconstruction of bubbles from single frames. While first results are promising, the high computational demand for the reconstructions makes it unfeasible for the evaluation of the experiments conducted for the present work.

For this thesis, the XR-AD setup was used to measure shape, size and rise velocities of individually injected bubbles, to verify results obtained with the XR-LD setup and to support various assumptions made throughout the thesis to explain experimental results.

#### 3.3.2 Single bubble injection setup

The injection of single bubbles with specified volumes in a fluidized bed that is not yet bubbling allows the investigation of single bubble properties in a controlled environment. When two injection nozzles are installed, it is possible to inject two bubbles with defined spatial and temporal distances to observe the evolution of dynamic bubble interactions. By injecting single bubbles it is possible to measure bubble properties with the XR-AD setup without requiring complex tomographic reconstructions but through the comparatively simple evaluation of the bubble projection images. Assuming symmetry and by imaging the bubbles from multiple angles allows the determination of the dynamic evolution of the shape, volume and rise velocity of the measured bubble.

For the present work a setup has been developed with the purpose to verify the applied measurement techniques that were used in the experimental studies and to further investigate the results from XR-LD measurements. A framework was constructed, which enables the installation of the horizontal optical probes that were used in the measurements at the pilot plant GanyMeth, described in Section 3.2. In this way, the optical probe measurements and the corresponding evaluation methods can be verified through the simultaneous measurement of the bubble properties with the XR-AD setup.

Figure 3.8 shows an illustration of the framework, which enables the insertion of three optical probes with distances of 20 cm between each of them. The column is placed on a lifting platform to position it at the chosen height for the measurement and is fixed to the frame with ratchet straps.

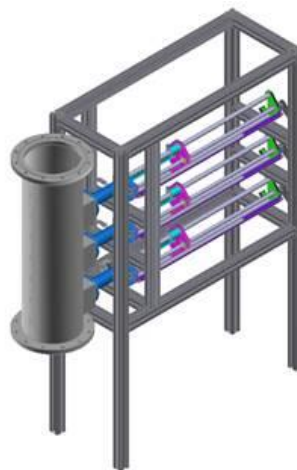


Figure 3.8: Framework that enables the insertion of the horizontal optical probes into the cold-flow model.

### Chapter 3. Experimental setups

The single bubble injection mechanism is illustrated in Figure 3.9. It includes a pressure vessel with a volume of 2.5 L which is connected to an air supply at a pressure of 2-3 bar and served as a pressurized air reservoir to ensure consistent injection volumes. A mass flow controller (MFC) of type EL-FLOW Select F-201CV manufactured by Bronkhorst is installed upstream of the pressure tank. In this setup, the MFC is not used to control the flow rate, it is simply set to “always open”. However, the MFC allows the measurement of the flow rate of pressurized air into the pressure vessel. This is possible when bubbles are injected with a frequency that causes a semi steady air flow due to the inertia of the flow system. In this way, the volume of each specific injection can be calculated.

Downstream of the pressure vessel the air stream is split into two pathways leading to high-speed solenoid valves of the type 166B-871JM manufactured by Mac Valves Europe Inc. The solenoid valves are able to open with a time delay of 2 ms and close with a time delay of 7 ms. A LabVIEW® program controls the valve opening times according to provided experimental settings. The settings include the injection times for each nozzle, the time gap between each injection of each individual nozzle, the time gap between the injection of one nozzle in relation to the injection of the other nozzle as well as the total amount of injections. Pneumatic silencers of various sizes that are made from sintered metal are used as nozzles to reduce the formation of air jets during the injections and to stabilize the generated bubbles thereby. In the experimental series described in Section 4.6.3, it is shown that injection times as low as 20 ms were possible, which allowed the consistent generation of bubbles with a volume equivalent diameter  $d_{b,eq}$  of about 2 cm. The upper limit of  $d_{b,eq}$  for stable and reproducible bubbles is 10 cm.

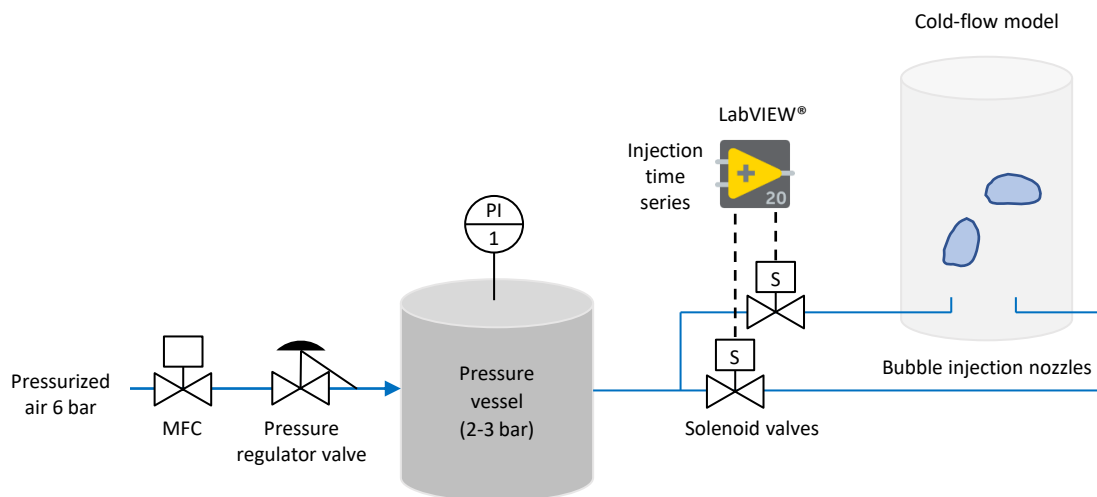


Figure 3.9: Simplified and stylized P&ID flowsheet of the bubble injection setup.

### 3.3.3 Heat flux measurements

A new setup that has been developed for this work allows the measurement of the local heat flux within a fluidized bed. For this, a jacketed pipe has been constructed from stainless steel where the inner pipe has an outer diameter of 1 cm and a length of 11 cm and the outer pipe has an outer diameter of 2 cm and a length of 12 cm. The wall thickness of both pipes is 1 mm. The jacketed pipe is connected to a circulation thermostat manufactured by Julabo GmbH (type 12 MC) which is operated with water. It is able to control the temperature with a precision of  $\pm 0.01$  °C and can be operated with circulation flowrates of 11-16 Lmin<sup>-1</sup>. This results in a change rate of the water volume within the pipe of 0.14 - 0.2 s<sup>-1</sup>. The temperature of the water within the pipe can therefore be assumed as constant. The local heat flux is measured by thermoelectric sensors, which consist of thermocouples that are connected in series referred to as differential-temperature thermopiles. By integrating the thermopiles within a filling material, a thermal resistance layer is created through which heat is conducted when the opposing sides of the layer have different temperatures. This is described by Fourier's law shown in Equation 3.3, where  $\dot{q}$  is the specific heat flux,  $\lambda$  is the thermal conductivity of the sensor material,  $\Delta T$  is the temperature difference at both sides of the sensor and  $\delta$  is the thickness of the thermal resistance layer.

$$\dot{q} = -\lambda \frac{\Delta T}{\delta} \quad (3.3)$$

The thermopiles are arranged in a way so that they form thermocouple junctions at either side of the sensor layer. This is depicted in Figure 3.10. As a consequence of the Seebeck effect [171], a voltage is generated for each of these junctions which is directly proportional to the applied temperature difference. By connecting multiple thermocouples in series, the voltage is amplified which increases the overall signal to noise ratio of the sensor. The response time of such sensors depends on the thermal inertia of the sensor layer and thus on its thickness and conductivity.

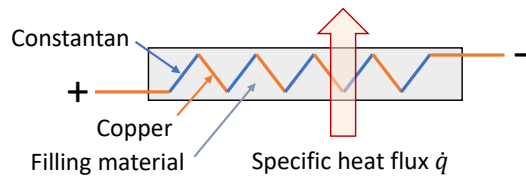


Figure 3.10: Illustration of the heat flux sensor showing the arrangement of the thermopiles.

For the experiments presented in this thesis, heat flux sensors of the type Micro-foil 27036-1 that were manufactured by RdF Corporation were chosen. They are suited to measure the influence of single bubbles on the local heat flux between the fluidized bed and the heated jacketed pipe due to their small size of 6.5 x 18 mm and their fast response time of 50 ms as

a consequence of their thickness of only 0.07 mm. The sensors also measure the outer wall temperature of the heated pipe. Additionally, thermocouples of the type PT-100 are used to measure the bed temperature. Therefore, the bed temperature, the wall temperature of the heated pipe as well as the specific heat flow can be measured within the fluidized bed at a specific position which allows the calculation of the local heat transfer coefficient  $\alpha$  according to Equation 3.4, which is derived from Fourier's law.

$$\dot{q} = \alpha \Delta T \quad (3.4)$$

By measuring simultaneously with the optical probes described in Section 3.2, it is possible to correlate the time resolved heat transfer coefficient with the measured bubble properties respectively. In addition to that, a correlation between the time averaged heat transfer coefficient and the experimental settings, namely the measurement height, the radial position, the fluidization number  $u/u_{mf}$  and the local bubble hold-up  $\varepsilon_b$ , can be derived. The jacketed pipe can be installed in the vertical tube bundle described in Section 3.3 by removing one of the Perspex<sup>®</sup> internals at the desired measurement position and replacing it with the heated pipe. Three heat flux sensors are available, which are positioned vertically aligned on the heated pipe in distances of 20 cm to allow the simultaneous measurement with three optical probes. The 3D-printed tube holder includes four designated radial positions, as shown in Figure 3.6 (e), where the heated pipe can be placed and fixed. By attaching a Perspex<sup>®</sup> pipe, the jacketed pipe can be extended by 10 cm, which allows the measurements at a total of six different height positions ranging from 10 - 60 cm in increments of 10 cm.

## 3.4 Bed material

For all experiments, porous  $\gamma$ -alumina ( $\gamma$ -Al<sub>2</sub>O<sub>3</sub>) particles, which were manufactured by Sasol Germany GmbH, were used as bed material. Two types of particles are available, that can be classified as Geldart A and an intermediate between Geldart B and A, according to their particle densities and sizes according to the respective categorization by Geldart [86], which was described in Section 2.2.1. The properties of the chosen bed materials are shown in Table 3.1. Following the labels provided by the manufacturer, the Geldart A material will from now on be referred to as SCCa and the Geldart B material as NWa. The table includes values that were provided by the manufacturer and values that were measured at PSI, marked in blue. The pore volumes of the material was measured via nitrogen physisorption on an Autosorb-1 analyzer manufactured by Quantochrome Instruments in liquid N<sub>2</sub> at a temperature of 77 K. The samples were outgassed over a period of at least 3 h in dynamic vacuum. By applying the Brunauer-Emmett-Teller (BET) model [172] the specific surface area could be determined and the total pore volume was determined at a relative pressure  $pp_0^{-1} \geq 0.99$ . The bulk density



was determined by filling a 10 mL flask with the material while applying vibration and then weighing it. Once the pore volumes and the bulk densities of the materials as well as the density of Alumina are known, their voidage can be calculated. The particle density can then be calculated by dividing the bulk density with the respective solid fraction. The minimum fluidization velocity  $u_{mf}$  was determined with the method described in Section 2.2.2 at a pressure of 1.14 bar in the GanyMeth plant. Some particle properties have been reported in a previous publication by Rüdüsili *et al.* [173]. The particle sphericity was determined via scanning electron microscopy (SEM) imaging and the internal angle of friction was calculated with what is referred to as bin flow method [174].

Type	Puralox® NWA-155	Puralox® SCCa-150/200
Manufacturer	Sasol Germany GmbH	Sasol Germany GmbH
Material	$\gamma$ -Al <sub>2</sub> O <sub>3</sub>	$\gamma$ -Al <sub>2</sub> O <sub>3</sub>
Mean Sauter diameter $\bar{d}_p$ [μm]	289	60-150
Particle density $\rho_p$ [kg/m <sup>3</sup> ]	1350/1390	1340
Bulk density $\rho_{bulk}$ [kg/m <sup>3</sup> ]	800/800	700-1150/850
Loose bulk density $\rho_{bulk,loose}$ [kg/m <sup>3</sup> ]	760	600-850
Pore volume $V_{pore}$ [cm <sup>3</sup> /g]	0.467	0.35-0.5/0.5413
Bulk voidage $\epsilon_{max}$ [-]	0.424	0.325
Loose bulk voidage $\epsilon$ [-]	0.453	not available (n.a.)
Voidage at fluidization $\epsilon_{mf}$ [-]	~0.5 [173]	n.a.
Geldart classification [-]	A/B	A
Minimum fluidization velocity [m/s]	0.03	0.01
Sphericity [-]	0.59 [173]	n.a.
Internal angle of friction [°]	33 [173]	n.a.

Table 3.1: Properties of the particles used in this work. Values that are marked blue were measured as part of this work or previous works, others were provided by the manufacturer.

For the NWA material additional efforts were made to specify its properties and elutriation rates. A laser diffraction particle sizer of the type LA-950 manufactured by Horiba was used to determine the particle size distribution of the bed material as it was delivered as well as after specified durations of fluidization. Figures 3.11 and 3.12 show the measured particle size distribution for the fresh bed material and after 100 h of operation. It can be seen, that the bed material originally contained a small mass of fine particles in the size range of 2-15 μm, which could not be detected after the specified duration of fluidization. Additionally, an analytical filter was installed in an isokinetic line in the outlet of the reactor to capture elutriated bed material, which was also analyzed with the laser diffraction particle sizer. All experiments described in this thesis where NWA material was used, were executed with bed material that had been fluidized for more than 100 h prior to the measurements.

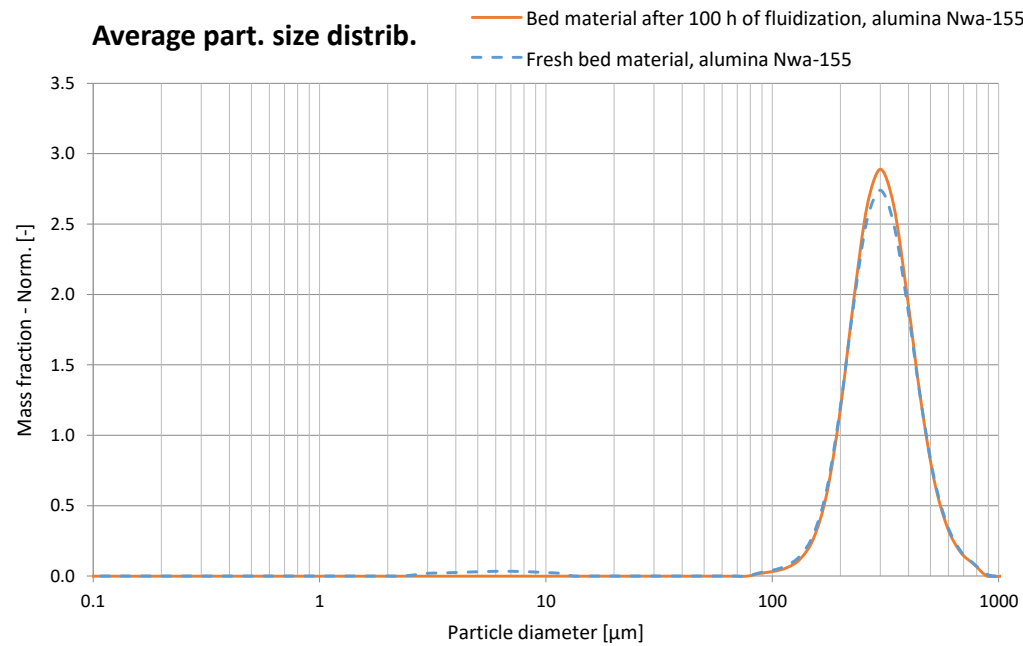


Figure 3.11: Particle size distribution of alumina Nwa-155 particles as delivered and after 100 hours of fluidization.

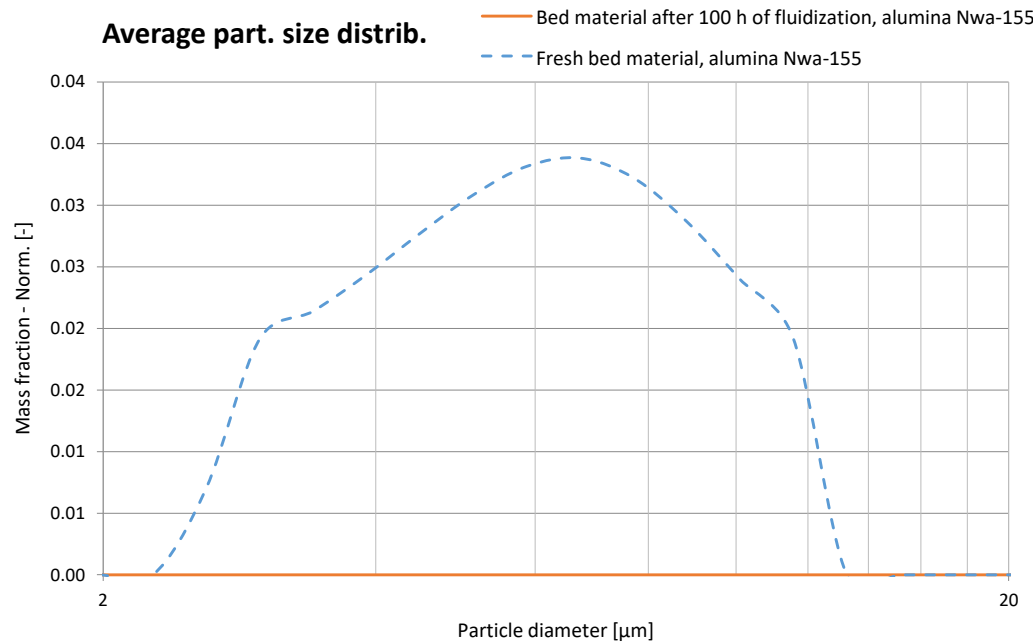


Figure 3.12: Particle size distribution of alumina Nwa-155 particles in the range of 2-15  $\mu\text{m}$  as delivered and after 100 hours of fluidization.

## 4 X-ray measurements

Multiphase flows are omnipresent in process and energy industries as over 99% of the applied reactors in industry branches, such as petroleum processing, energy generation, pharmaceutical production, food processing, waste water treatment, agricultural production, chemical production and biological processes, are multiphase systems [175], [176].

For the design and optimization of multiphase reactor systems, it is necessary to understand their fundamental hydrodynamics and transport phenomena to derive appropriate reactor models [177]–[179]. Hence, precise measurement techniques are required to characterize multiphase systems.

Multiphase flows, particularly fluidized beds, are opaque and therefore require either invasive probe measurements, which are locally constricted and may influence the multiphase flows, or appropriate non-invasive measurements, that are able to distinguish between the phases despite their opaqueness. Tomographic imaging techniques, such as magnetic induction tomography [125], [180]–[182], electrical resistance [183], [184] and capacitance tomography [185], [186], ultrasonic measurements [187], [188] or X-ray and  $\gamma$ -ray tomography [170], [189]–[191], can be applied for this purpose. They have become increasingly available in recent years, as part of the ongoing digitalization of the industry, benefitting from increased availability of powerful computers that are typically required for evaluation of tomographic measurements [192]. A comprehensive review on various fast tomographic imaging techniques was provided recently by Hampel *et al.* [192].

X-ray measurements are well suited for the visualization of fluidized bed flows. They are non-invasive and non-destructive, the scattering of X-ray radiation as it crosses the phase interfaces is negligible [176] and their readiness for densimetric measurements, resulting from more than 120 years of development for medical applications [193], allows the precise determination of the cross-sectional bubble hold-up in fluidized beds.

Non tomographic imaging, such as X-ray radiography, can also be applied to visualize multiphase flows. Due to the fact that the projection of the entire multiphase flow is captured in such images, it is difficult to distinguish between multiple overlapping elements of the flow structure, such as individual bubbles or drops, whereas tomographic reconstructions enable the visualization of the spatial distribution of the phases, given an adequate spatial resolution and number of viewing angles. However, for simple flow structures, such as single bubbles rising in a fluidized bed, such methods are useful as they are readily available and do not require complex and computationally expensive reconstructions.

In this work both X-ray radiography and tomography are applied to visualize BFB flows and to measure individual bubble properties such as their shape, rise velocity, size and radial position.

### 4.1 X-ray attenuation measurements of bubbling fluidized beds

Due to their short wave length in the range of 0.01 – 10 nm and the corresponding energies of 145 eV to 124 keV, X-rays may traverse through long distances of dense material, without being entirely absorbed or scattered. This can be described by the Lambert-Beer law, shown in Equation 4.1. Accordingly, for monochromatic X-rays the intensity  $I$  of the transmitted X-ray radiation depends on the X-ray intensity  $I_0$  before the penetration of the object, the distance  $x$  the radiation travels through the object and the linear attenuation coefficient  $\mu$ , which depends on the density of the material and the wavelength of the radiation.

$$I = I_0 e^{(-\mu x)} \quad (4.1)$$

Based on the assumption of the TFM, which states that fluidized beds consist of two phases, a dense phase representing suspended bed material with a defined voidage and a relative high density and a particle free bubble phase with a significantly lower density, the Lambert Beer law can be applied to calculate the bubble hold-up of a fluidized bed.

The attenuation coefficient can be determined as described in the following. The intensity of X-rays that are transmitted through a defined length  $x_{bed}$  of a bubble free fluidized bed with a superficial gas velocity  $u$ , slightly below the minimum bubbling velocity  $u_{mb}$ , is measured. This intensity is from here on referred to as  $I_{FU}$  (full). Using the same X-ray source, the intensity of X-rays that traversed the empty column, from here on referred to as  $I_{BR}$  (bright), is also measured. Then, the attenuation coefficient can be calculated as follows:

$$\mu = \frac{-\ln \frac{I_{BR}}{I_{FU}}}{x_{bed}} \quad (4.2)$$

In practice, it is not necessary to explicitly determine the attenuation coefficient, as the bubble hold-up for each pathway between X-ray source and detector can be directly determined if the reference intensities  $I_{Fu}$  and  $I_{Br}$  of the bubble free fluidized bed and the empty column are available. Then, the bubble hold-up for a specified pathway through the fluidized bed can be calculated with Equation 4.3, where  $I_{ME}$  is the measured intensity of the BFB.

$$\varepsilon_b = \frac{\ln \left( \frac{I_{ME}}{I_{FU}} \right)}{\ln \left( \frac{I_{BR}}{I_{FU}} \right)} \quad (4.3)$$

However, this approach is only accurate if the X-ray intensities are monochromatic. In reality the applied X-ray radiation often consists of a spectrum of wavelengths and corresponding energies. High energy X-rays are referred to as hard X-rays, whereas the spectrum of X-rays with relative low energies are called soft X-rays. Hard X-rays are absorbed at lower rates than soft X-rays, which leads to an alteration of the X-ray spectrum as the X-rays traverses through the bed material. Consequentially, the attenuation coefficient changes as well [194]. This is referred to as “beam hardening” and requires corrective measures, such as a multipoint calibration as it was applied for the measurements shown in Section 4.3.

## 4.2 X-ray tomography

Tomographic reconstructions of the spatial distribution of the bubble hold-up require X-ray measurements of the fluidized bed from multiple angles. This can be achieved by installing multiple X-ray sources and their associated detector arrays around the column, as it was done in the setup developed by the team of Mudde [170], which was used for the measurements shown in this work. A detailed description of the setup can be found in Section 3.3.1, as well as in publications by Mudde [170], [195]. Alternatively, a moving X-ray source that rotates around the fluidized bed with a sufficient frequency can be used. Examples for this are the X-ray tomography setups of the Helmholtz-Zentrum Dresden Rossendorf, where electron beam guns are used that are rapidly swept across a semicircular metal ring covering 240° to generate X-rays from a moving focal spot [191], [196]–[199]. This method allows frame rates of up to 10 kHz with 240 viewing angles but is restrictive regarding the possible column diameters. Currently, measurements of objects with a maximum diameter of 19.5 cm are possible, while a new setup is under development allowing diameters of up to 40 cm.

The main concern of the methods applied for the measurements shown in this work is that only three viewing angles are available, which restricts the spatial resolution and may cause artifacts. This problem is further discussed in the next section and its impact on the measurements is systematically investigated in a series of tomography simulations shown in Section 4.4.1.

The results of the experiments have been released in previous publications by Maurer *et al.* [133], [168], [200] and Schillinger *et al.* [164], [169], which also included measurements with a smaller column. However, numerous changes have been implemented in the evaluation algorithms that lead to significantly different results. The changes concern the pseudo three-dimensional image reconstruction procedure and are explained in detail in the Section 4.2.3.

### 4.2.1 Tomographic reconstruction of the cross-sectional bubble hold-up

As a first step for the tomographic reconstruction, the line averaged solid fraction needs to be determined from the X-ray attenuation measurements according to the methods described in Section 4.1.1. To account for beam hardening, a seven-point calibration was performed for each of three X-ray source and their associated detector arrays by dividing the column into seven equally spaced sections, which were step-wise filled with bed material for the calibration measurements as shown in Figure 4.1. In this way, the deviation from the Lambert Beer law for the X-ray attenuation can be accounted for. Further details on the calibration procedure can be found in the dissertation by Maurer [70].

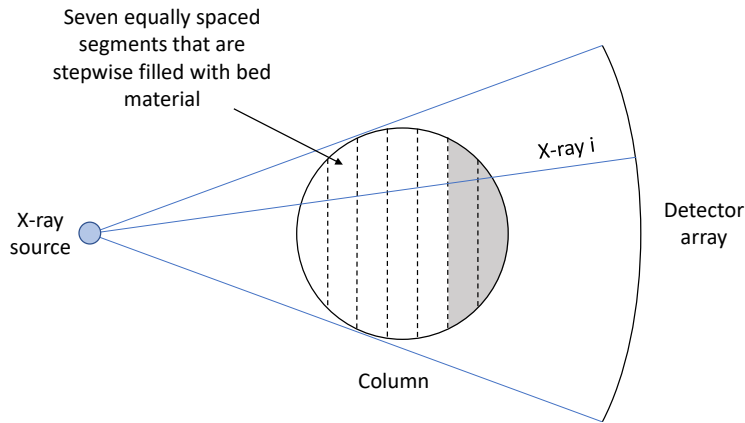


Figure 4.1: Illustration of the seven-point calibration required for tomographic reconstructions of the X-ray measurements

For the measurements with vertical internals the calibration procedure needed to be adapted to account for different attenuation coefficient of the walls of the internals. Maurer [200] proposed a mathematical correction to convert the measured intensities with vertical internals into an intensity profile that would have been measured without the internals. The proposed correction factor  $f_{cor}$  is defined by Equation 4.4, where the intensities without internals is

divided by the intensities with internals, both measured at minimum fluidization. A more detailed description of the seven-point calibration and the correction for measurements with internals can be found in the corresponding publication by Maurer *et al.* [200].

$$f_{cor} = \frac{I_{without\ internals}}{I_{with\ internals}} = \frac{I_0 \exp(-\mu_1 \Delta s)^6 \exp(-\mu_1 \Delta h)^6}{I_0 \exp(-\mu_1 \Delta s)^6 \exp(-\mu_2 \Delta h)^6} \quad (4.4)$$

Either iterative or analytic methods are used to reconstruct the cross-sectional phase distribution from multiple X-ray projections. Filtered back projection is an analytical method that is often applied, as it is relatively fast and less prone for the generation of artifacts. However, it is not well suited for reconstructions from limited projection angles, where it suffers from poor spatial resolution [201]. In such cases algebraic reconstruction techniques (ART) perform better, but they are more complex and computationally expensive. The Simultaneous Algebraic Reconstruction Technique (SART) method is one of the most popular choices and was also used for the reconstructions shown in this work. Applying a SART algorithm reduces what is referred to as salt and pepper noise, which typically occurs with ART algorithms, at the cost of increased computation time [170]. A detailed description of the reconstruction procedure, as it was applied in this work, was provided by Mudde [170], which is summarized in the following.

When the translation from the X-ray attenuation data to the solid fraction for each pathway between X-ray source and detector is established, the tomographic reconstruction through the SART method is possible. For this, the reconstruction grid has to be defined, which represents the spatial resolution of the reconstructed image. Here, a grid resolution of 55 x 55 pixels was chosen following previous publications in their assessment of the trade-off between required computation time and spatial resolution [71], [170]. A solid fraction  $\alpha(x, y)$  that best describes the measured total solid fraction  $p_i$  for each line between detector and X-ray source is reconstructed for each of the pixels of the grid by the SART algorithm. The solid fraction  $p_i$  can be estimated as

$$\tilde{p}_i = \sum_{j=1}^N W_{i,j} \alpha_j \quad (4.5)$$

Here,  $\alpha_j$  is the pixel-based solid fraction and  $W_{i,j}$  the weighting factor, which is the length of the intersection of the ray with the pixel  $j$ , for the  $i$ -th ray transmitted through the bed, as illustrated in Figure 4.2.

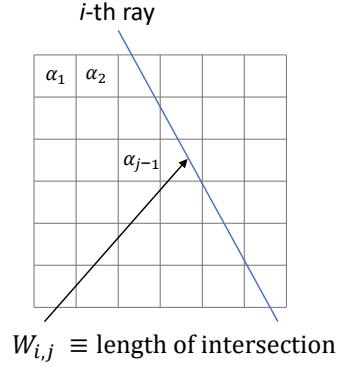


Figure 4.2: Illustration of grid parameters used in the SART algorithm. Adapted from Mudde [170].

The iterative SART algorithm is defined by Equation 4.6, where  $\alpha_j^{n+1}$  is the solid-fraction of the pixel  $j$  for the iterative step  $n + 1$  and  $M$  different rays on  $N$  pixels [170].

$$\alpha_j^{n+1} = \alpha_j^n + \frac{1}{W_{+,j}} \frac{p_i - \tilde{p}_i}{W_{i,+}} W_{i,j} \quad (4.6)$$

with

$$W_{+,j} = \sum_{i=1}^{M \cdot M} W_{i,j} \quad (4.7)$$

$$W_{i,+} = \sum_{j=1}^{N \cdot N} W_{i,j} \quad (4.8)$$

Additionally, the so-called one-step-late (OSL) algorithm [202], shown in Equation 4.9, is added as an further step for each iteration, which effectively removes salt and pepper noise while maintaining sharp edges of larger objects [170].

$$\alpha_{OSL,j}^{n+1} = \frac{1}{1 + \beta \frac{\alpha_{OSL,j}^n - \text{Med}(\alpha_{OSL,j}^n)}{\text{Med}(\alpha_{OSL,j}^n)}} \alpha_j^{n+1} \quad (4.9)$$

Here, the median filter  $\text{Med}(\alpha_j)$  corrects the value of the  $j$ -th pixel by the median of its 3 x 3 pixel neighborhood. The weight of the correction is controlled by  $\beta$  which is set to 0.1 for the reconstruction presented in this work. In this way, the SART algorithm reconstructs a matrix of solid fractions for given attenuation profiles, which can be interpreted as the spatial probability distribution for the positions of the bubbles represented as an inverted gray scale image. This reconstruction procedure has not been changed for the present work, as it has been proven to work reliably in numerous publications [195], [203]–[205].



### 4.2.2 Experimental methods

The X-ray tomography experiments were conducted using the cold-flow model, presented in Section 3.3, and the XR-LD setup introduced in Section 3.3.1. The cold-flow model was placed in the center of XR-LD setup with distances of 71.4 cm between the center of column and the X-ray source and 53.2 cm between the center of column and the X-ray detector array. For all measurements the X-ray energy was set to a maximum level of 150 keV. The data was recorded with a frame rate of 2.5 kHz.

To decrease the required time of the computationally intensive evaluation of the measurements and to reduce the effect of noise, a data set with a reduced frame rate of 250 Hz was generated by averaging 10 sequential measurements. The measurements were conducted over a time frame of two minutes to ensure statistical relevant sample sizes at fluidization numbers of 1.5, 2, 3, 4 and 6 and measurement heights of 6, 9.6, 13.2, 16, 19.7, 23.2, 26, 36, 46 and 56 cm. According to the findings of Rautenbach *et al.* [206] measuring spans of 45 s are required to reliably measure mean bubble rise velocities and 25 s are sufficient for the determination of mean bubble volumes using the same XR-LD setup. The chosen SART reconstruction grid of 55 x 55 pixels corresponds to a spatial resolution of 0.4 cm x 0.4 cm considering the column diameter of  $D = 22.4$  cm.

### 4.2.3 Pseudo three-dimensional image reconstruction

The cross-sectional bubble hold-up images that were reconstructed with the SART algorithm can be stacked into three-dimensional representations, where the horizontal dimensions represent the cross-section of the column at the respective measurement height and the vertical dimension represents the time series of the measurements. This three-dimensional matrix can be processed to extract the properties of individual bubbles.

Since the three-dimensional bubble reconstruction is achieved through stacking of a sequence of two-dimensional slices, this procedure will henceforth be referred to as pseudo three-dimensional reconstruction. Actual three-dimensional reconstructions are only possible with setups that capture two-dimensional projections of the BFB from multiple angles, *e.g.* the XR-AD setup presented in Section 3.3.1. The applicability of this method has been demonstrated through the measurement of an air-filled cylinder of known size, which was pulled upwards through the unfluidized bed with a constant velocity [170].

As a first step for the pseudo three-dimensional reconstruction, the cross-sectional bubble hold-up images are filtered with a median filter applied on the 5 x 5 neighbourhood of each pixel to remove noise. After that, the images are binarized to enable the characterization of the bubble properties. An illustration of the described procedure is shown in Figure 4.3.

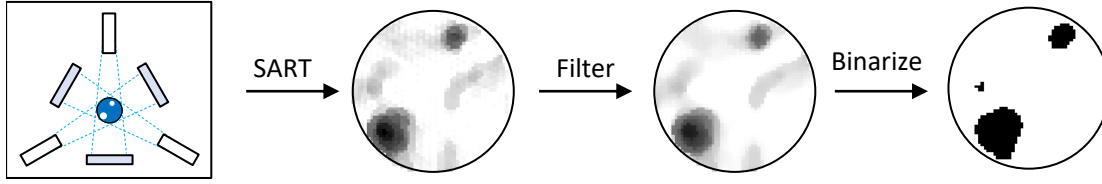


Figure 4.3: Image processing of reconstructed cross-sectional bubble hold-up images.

Previously, a fixed threshold was applied for the binarization, which was determined through the optimization of the tomographic reconstruction of hollow Perspex<sup>®</sup> tubes that represent the bubbles [70]. However, the analysis of the resulting data showed that this would often lead to a significant inconsistency between the bubble hold-up directly derived from the X-ray intensities or via independent measurements and that of the binarized images [133]. Additionally, it often happened that separate individual bubbles would be identified as a single one. These problems would occur more often when multiple bubbles were present in the measurement plane. The issue is a consequence of the limited X-ray detection angles, which is discussed and systematically investigated in Section 4.4. Given the limited data, the SART algorithm cannot always identify the positions of the bubbles unambiguously. In such cases, the reconstructed images can be interpreted as a broadened probability distribution of possible bubble locations with generally lower pixel-wise probabilities than reconstructions of single bubbles would produce. This may lead to situations, where regions of the dense phase are falsely ascribed to the bubble phase, which creates artifact bubbles or merges individual bubbles.

To improve the quality and consistency of the reconstructions, a new method was therefore applied in which the threshold is adapted for the binarization of each individual gray scale image, with the condition that the bubble hold-up of each frame does not change through the binarization. An example of this procedure and the results of the different binarization methods can be seen in Figure 4.4, where the binarization with a fixed threshold results in the merging of two individual bubbles, whereas the adaptive threshold does not. The suitability of this new method is verified systematically by means of tomography simulations in Section 4.4.1.

To retrieve pseudo three-dimensional reconstructions of each bubble, the binarized images are concatenated to form a three-dimensional matrix, where the third dimension thus represents the time steps of the measurements. Individual bubbles and their geometric properties can be identified within these matrices, through the application of the Matlab function *regionprops3*, which identifies and characterizes coherent regions in three-dimensional binary matrices. Since two measurement planes are evaluated, two individual pseudo three-dimensional matrices are available for each experimental setting. A linking algorithm is used to identify the

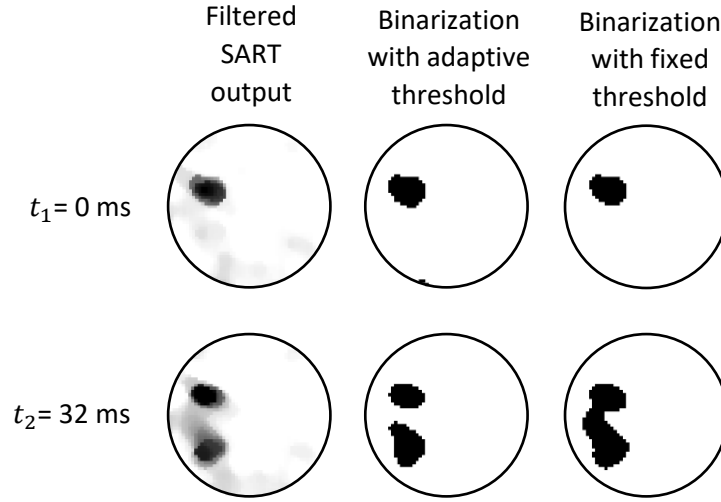


Figure 4.4: Comparison of the reconstruction and binarization of bubbles in the measurement plane. Top: Only a single bubble is present. Bottom: Same measurement 32 ms later, when an additional bubble appeared, resulting in a blurred reconstruction.

same bubble in both matrices. For this, the center of weight of the bubble measured in the lower measurement plane is determined and the matrix representing the upper measurement plane is scanned for bubbles that are within a specified sub-matrix corresponding to a minimum bubble rise velocity of  $0.1 \text{ m s}^{-1}$ , a maximum rise velocity of  $3 \text{ m s}^{-1}$  and a maximum lateral movement of 3 cm. If multiple suitable bubbles were identified, the closest one is linked. Once a bubble has been identified in both measurement planes, its rise velocity  $u_{br}$  is determined. Three methods to calculate the time of flight of the bubbles were applied:

1. The time difference of the centroid of each identified bubble passing through the measurement planes.
2. The time difference between the first moment the bubble entered each measurement plane.
3. Application of a cross correlation method on the horizontal cross section time series of the identified bubble in each measurement plane. With this method, one of the signals is shifted on the time axis until the deviation between the two signals is minimized. The shift of the time series equals the time of flight of the bubble.

The rise velocity  $u_{br}$  can be calculated by dividing the mean distance between the measurement planes by the time of flight. Ultimately, the time of flight of the centroids was used to

determine  $u_{br}$  for the results shown in this thesis, while the other definitions were applied to identify and remove problematic reconstructions due to dynamic bubble events or limitations of the experimental setup. Additionally, the mean of  $u_{br}$  was determined independently from individual bubble reconstructions by applying the cross-correlation method directly on the cross-sectional bubble hold-up time series of both measurement planes. In the following this value will be referred to as  $\hat{u}_{br}$ .

### Determination of the bubble geometry

Once  $u_{br}$  is known for an individual bubble, it can be applied on the bubble geometry to translate its time dimension to the vertical spatial dimension, resulting in the actual geometric description of the bubble. This step was neglected in previous evaluations of the data set, prior to the onset of the work described in this thesis. There, the scale of the vertical dimension has been assumed to be constant, equal to the scale of the horizontal dimensions of the images. This led to erroneous reconstructions, where the rise velocity that would be required to achieve a vertical spatial length equal to the horizontal pixel dimensions would be around  $1 \text{ ms}^{-1}$ , which is significantly larger than most of the measured mean rise velocities, which were in the range of  $0.35 - 1 \text{ ms}^{-1}$  depending on the measurement height and the fluidization number as shown in the experimental results presented in Section 4.3.3. Consequently, a large fraction of the bubbles have been wrongly elongated in previous publications. Overall, bubbles with rise velocities faster than  $1 \text{ ms}^{-1}$  were flattened and slower bubbles were elongated in comparison to their actual shapes. As a result, the volume-equivalent diameters of relatively slow bubbles were increased, whereas those of relatively fast bubbles were decreased leading to significantly distorted bubble size distributions.

Once the vertical dimension of each bubble is determined, the pseudo three-dimensional binary sub-matrix representing that bubble can be translated into a polygon model with the correct geometric dimensions. For this the Matlab function *isosurface* is applied, which generates vertices with uniform horizontal and vertical distances with values of 1 following the structure of the given matrix. The distances between the vertices in each dimension can then be adjusted according to the determined values of the horizontal and vertical dimensions. An illustration of this procedure is shown in Figure 4.5.

Then, the Matlab function *alphaShape* is applied on the polygon reconstruction of the bubble, which creates a bounding volume that envelopes a set of three-dimensional points and allows the direct determination of the surface area and the volume of the polygon. In the next step an ellipsoidal shape is fitted to each bubble with the purpose to simplify the description of bubble shapes and to enable the analysis of how the bubble shape is correlated to other bubble properties, the fluidization number, the measurement height, its radial position and

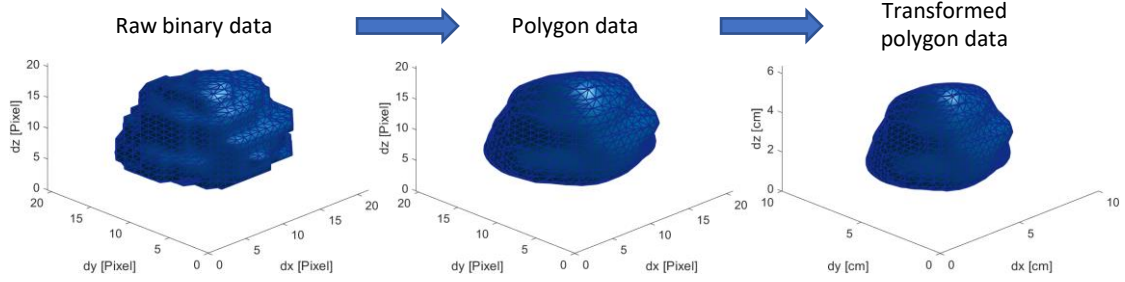
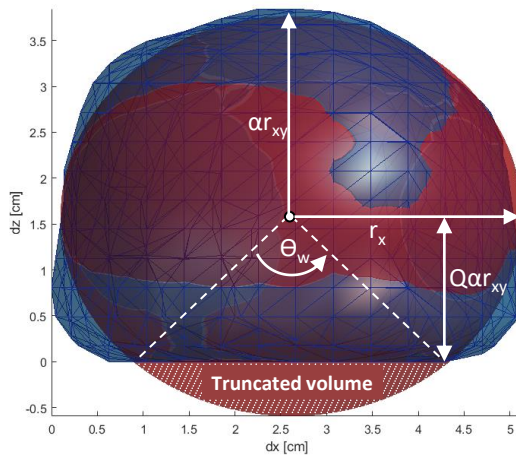


Figure 4.5: Translation of a pseudo three-dimensional binary matrix of an individual bubble into its geometrically correct polygon representation.

so forth. For this, a function called *Ellipsoid fit* [207] was applied, which fits an ellipsoid shape for a given polygon by minimizing the difference of the fitted points from the actual data. Due to the typical spherical-cap shape of bubbles, the bottom part of the fitted ellipsoid often extends beyond the bubble shape. To solve this, the fitted ellipsoids were truncated accordingly. An example of a bubble that was reconstructed following the procedure described above, including the fitted truncated ellipsoid and a summary of their geometric properties can be seen in Figure 4.6.



### Geometric bubble properties

V: Volume                      r: Radius  
A: Surface area                 $\alpha$ : Shape factor  
a: Specific surface area      Q: Truncation factor

### X-Ray tomography reconstruction:

$V_x = 59.18 \text{ cm}^3$   
 $A_x = 117.97 \text{ cm}^2$   
 $a_x = 1.99$

### Fitted truncated ellipsoid:

$V_e = 50.31 \text{ cm}^3$                        $r_x = 2.38 \text{ cm}$   
 $A_e = 104.36 \text{ cm}^2$                     $r_y = 2.69 \text{ cm}$   
 $a_e = 2.07$                                  $r_z = 2.18 \text{ cm}$   
    $\alpha = 0.95$   
    $Q = 0.73$

Figure 4.6: Example of a reconstructed bubble (blue) and the associated fitted ellipsoid (red) together with a description of the geometric bubble properties of the shown bubble.

Note, that the fitting procedure leads to slightly smaller wake angles, than the procedure suggested by Rowe and Partridge [118] as it was described in Section 2.3.2. This is due to the fact, that the fitting is defined by the minimization of the error between all points of the

original data and the fitted shape, which leads to shapes with comparatively reduced truncated volumes and thus smaller wake angles.

For each experimental setting (measurement height  $H$  and fluidization number  $u/u_{mf}$ ), the distributions of a chosen set of bubble properties, which can be found in Table 4.1, are fitted to a selection of 18 commonly used distribution functions. The used distribution functions are: normal, exponential, gamma, logistic, t location-scale, generalized Pareto (GP), uniform, extreme value (EV), generalized extreme value (GEV), Rayleigh, beta, Nakagami, Rician, inverse Gaussian, Birnbaum–Saunders, log logistic, log normal and Weibull. The selected bubble properties were chosen under the assumption that they were sufficient for typical hydrodynamic reactor models as well as for the verification of CFD models. Other important properties such as the surface area and the bubble volume can be directly derived or approximated from the selected parameters.

$u_{br}$ [m/s]	Bubble rise velocity
$d_{b,eq}$ [cm]	Sphere-equivalent bubble diameter
$l:w$ [-]	Aspect ratio length to width
$r_b$ [cm]	Radial position of the bubble in the column

Table 4.1: Experimental settings for the X-ray tomography measurements in the 22.4 cm cold-flow model.

The goodness of fit was rated via the *log likelihood* as well as the *Akaike* criterion. Accordingly, GEV distribution is overall the best suited function to describe the four distributions. To describe the multivariate distributions of various bubble properties, so called t-copulas can be used. They are favorable in scenarios where dependent extreme values are observed in the data [208], which is the case here. A kernel estimator of the cumulative distribution function (CDF) is used to transform the experimental data to the unit square copula scale. Then, the t-copula is fitted to the transformed data via the Matlab function *copulafit*, resulting in a correlation matrix  $\hat{\rho}$  describing the correlations between the bubble properties and the estimated degrees of freedom parameter  $\nu$  for each experimental setting. In this way, a set of distribution and copula function parameters is derived for each of the chosen bubble properties listed in Table 4.1 and each of the experimental settings (measurement height  $H$  and fluidization number  $u/u_{mf}$ ), as presented in Section 4.2.2.

### 4.3 Results of X-ray tomography measurements without vertical internals

The main purpose of the X-ray measurements presented in this section is to establish and verify the tomographic reconstruction methodology in a setup without vertical internals. Then, the results can be compared with correlations from literature which usually do not consider

internals. Another purpose of the experiments is to provide a comprehensive data set of correlated bubble properties that could serve as a benchmark for future CFD simulations. For this purpose, the simpler case without vertical internals is more accessible.

#### 4.3.1 Cross-sectional bubble hold-up

One of the main characteristics of bubbling fluidized beds is the cross-sectional bubble hold-up  $\varepsilon_b$  which describes the bubble phase fraction of the bed cross section at a given height. X-Ray tomography is known to be a precise way to measure not only the cross sectional mean value of the bubble hold-up  $\varepsilon_b$  but also its spatial distribution [209]. Figure 4.7 shows that the values for  $\varepsilon_b$  are fairly consistent over all measured heights for each fluidization number. However, it must be noted that the bubble hold-up measured at lower heights often is lower than that measured at higher heights. This is a deviation from the expectation to find an increased bubble hold-up at lower heights as a consequence of the slower rise velocity of smaller bubbles. The likely reasons for this are that very small bubbles cannot be detected due to the limited spatial resolution and that small bubbles are tendentially reconstructed slightly reduced in size, whereas larger bubbles tend to be reconstructed with slightly increased sizes. The significance of these issues is investigated in detail in Section 4.4.

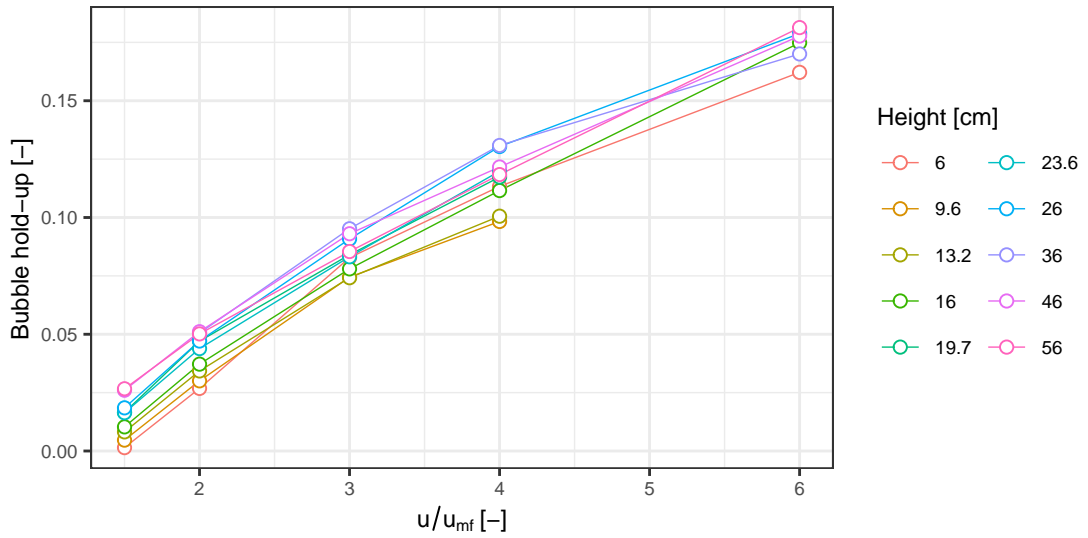


Figure 4.7: Cross-sectional bubble hold-up  $\varepsilon_b$  derived by means of X-ray tomography for various measurement heights and fluidization numbers  $u/u_{mf}$ .

To verify the accuracy of the method and the applied calibration, the values of  $\varepsilon_b$  that were determined via X-ray tomography and averaged over all heights were compared with values that were determined through measurements of the bed expansion in an independent experiment as presented in Figure 4.8. The results show slightly higher values for the estimation from the

bed expansion, which is feasible, since the bed material is classified between the Geldart types A and B and a homogeneous bed expansion could occur before bubbles appear. According to the X-ray measurements,  $\varepsilon_b$  can be described with the polynomial shown in Equation 4.10.

$$\varepsilon_b = -0.059 + 0.059 \frac{u}{u_{mf}} - 0.0032 \left( \frac{u}{u_{mf}} \right)^2 \quad (4.10)$$

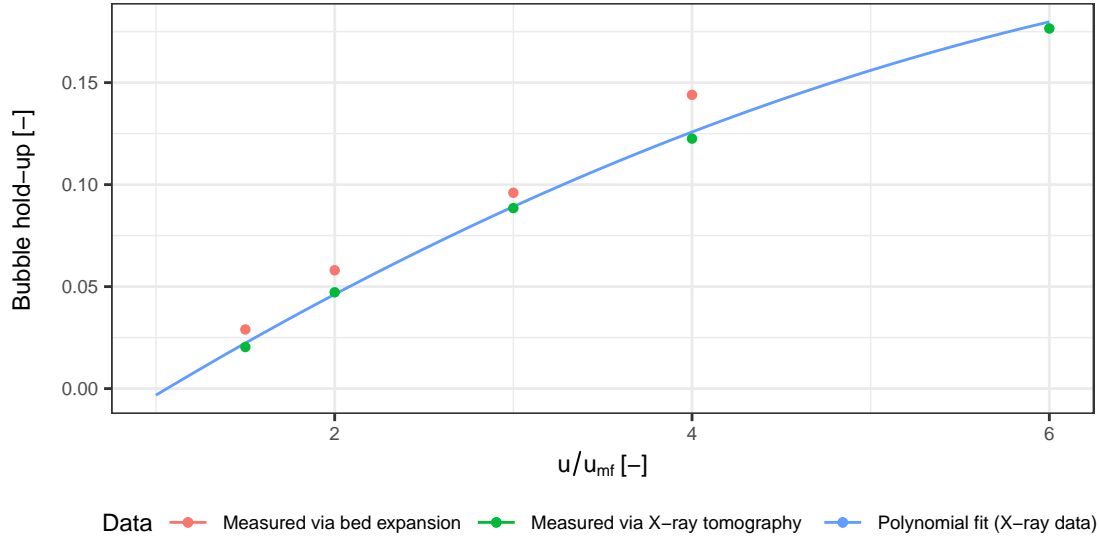


Figure 4.8: Comparison of the cross-sectional bubble hold-up  $\varepsilon_b$  measured with two independent experimental methods: X-ray tomography and measurement of the expanded bed height.

### 4.3.2 Pseudo three-dimensional visualizations

An example for the visual representation of the reconstructed, filtered and binarized BFB at a measurement height of 36 cm and a fluidization number of  $u/u_{mf} = 3$  is given in Figure 4.9, which shows an orthographic and an isometric view of a 3.2 s data sample. Note that the shapes do not necessarily represent the actual bubble shapes as the vertical dimension of the images is the time. Depending on the rise velocity of the individual bubble, the vertical dimension of the actual bubble shapes may be elongated or flattened. The individually reconstructed slices of each bubble are visible with overall seemingly consistent bubble shapes that fit the often observed spherical-cap description for bubbles in fluidized beds.



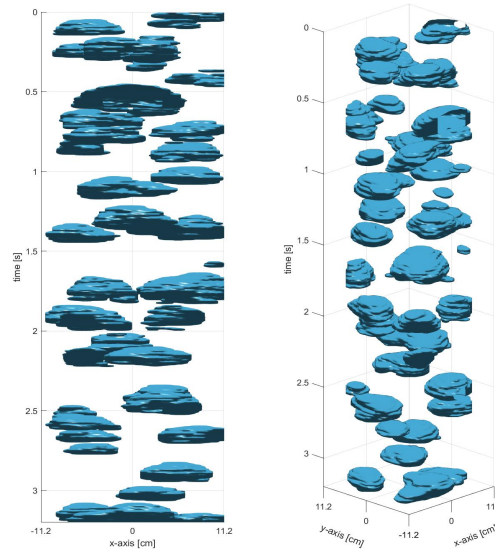


Figure 4.9: 3.2 s sample of reconstructed bubbles that were measured at measurement height of 36 cm and a fluidization number of  $u/u_{mf} = 3$ .

Figures 4.10 and 4.11 show randomly selected 0.9 second samples of the pseudo three dimensional reconstructions together with the corresponding time averaged cross sectional bubble hold-up  $\varepsilon_b$  representing the full two-minute measurements at measurement heights of 6, 16, 26, 36, 46 and 56 cm and fluidization numbers of  $u/u_{mf} = 2$  and 4. The hold-up profiles show that the bubbles are predominantly located close to the wall at the bottom of the column. A possible explanation for this could be bubble and particle flow patterns that typically occur as described in Section 2.3.2 and shown in Figure 2.9. A leakage of gas flow bypassing the gasket between the porous plate and the column is also a plausible explanation. With increasing heights and fluidization numbers, the bubbles move towards the center of the column and become bigger. It appears that there might be a slight maldistribution of the air flow through the porous plate, with a zone of reduced bubble hold-up, which can be seen in the lower left sections of the bubble hold-up images of the lower measurement heights. However, the apparent maldistribution seems not to be significant as  $\varepsilon_b$  is symmetrically distributed at heights of 26 cm and higher. For the measurements at a height of 6 cm one can see an unexpected triangular pattern of  $\varepsilon_b$ . This is likely the result of the triangular arrangement of the X-ray sources and the detector arrays combined with the limited sensitivity for the measurement of small bubbles, which are presumably more affected by beam hardening, X-ray scattering or noise for radiation pathways through the central region of the bed, where the ratio between bubble and dense phase is significantly larger than it would be for bubbles of the same size for pathways closer to the wall. Additionally, it can be seen that many of the bubbles measured at  $H = 6$  cm and  $u/u_{mf} = 4$  appear to be merged together, resulting in shapes that differ from the expected spherical-cap shapes.

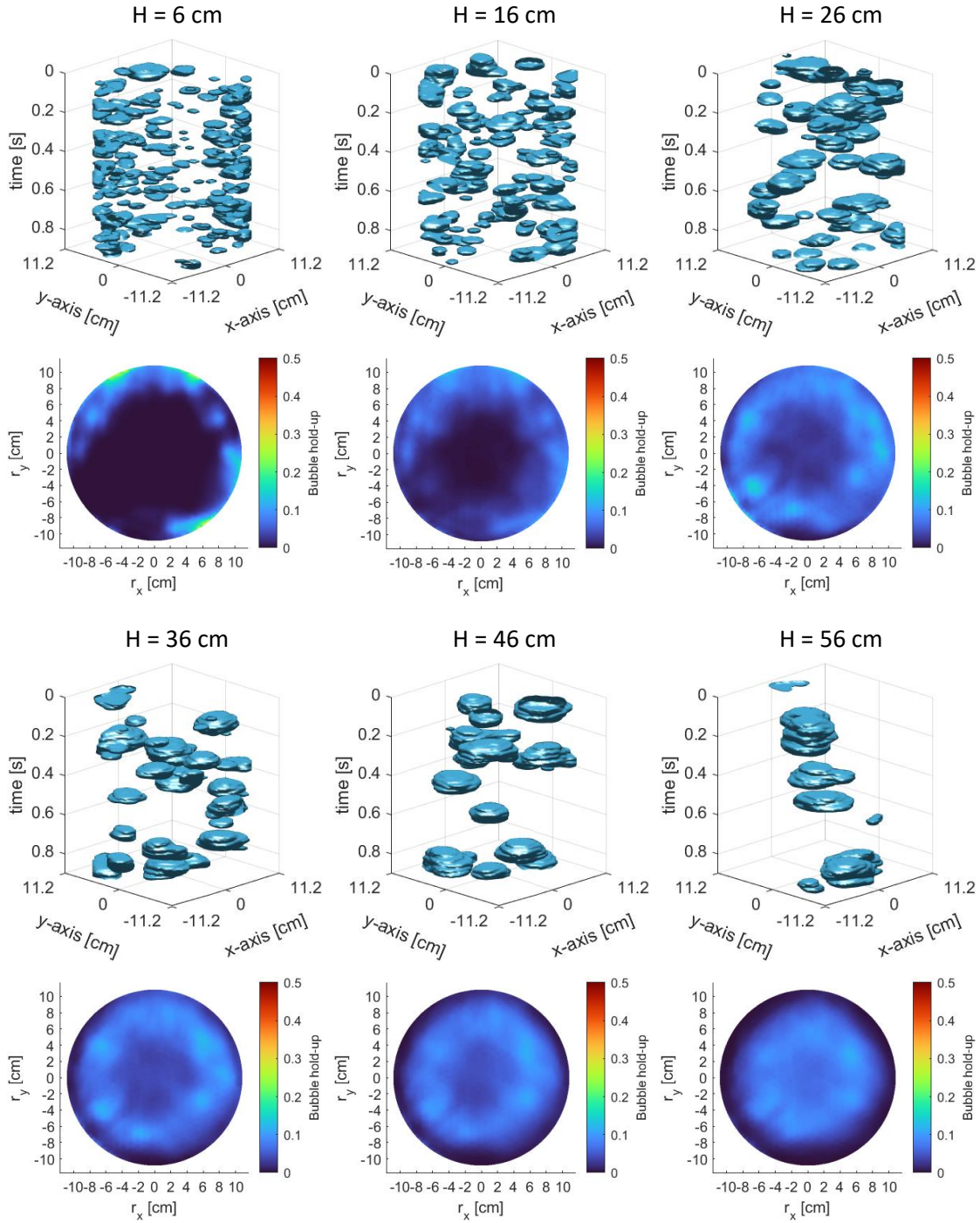


Figure 4.10: Samples of the pseudo three-dimensional reconstructions and the spatial distribution of the respective bubble hold-up for the measurement heights of 6, 16, 26, 36, 46 and 56 cm at a fluidization number  $u/u_{mf} = 2$ .

### 4.3 Results of X-ray tomography measurements without vertical internals

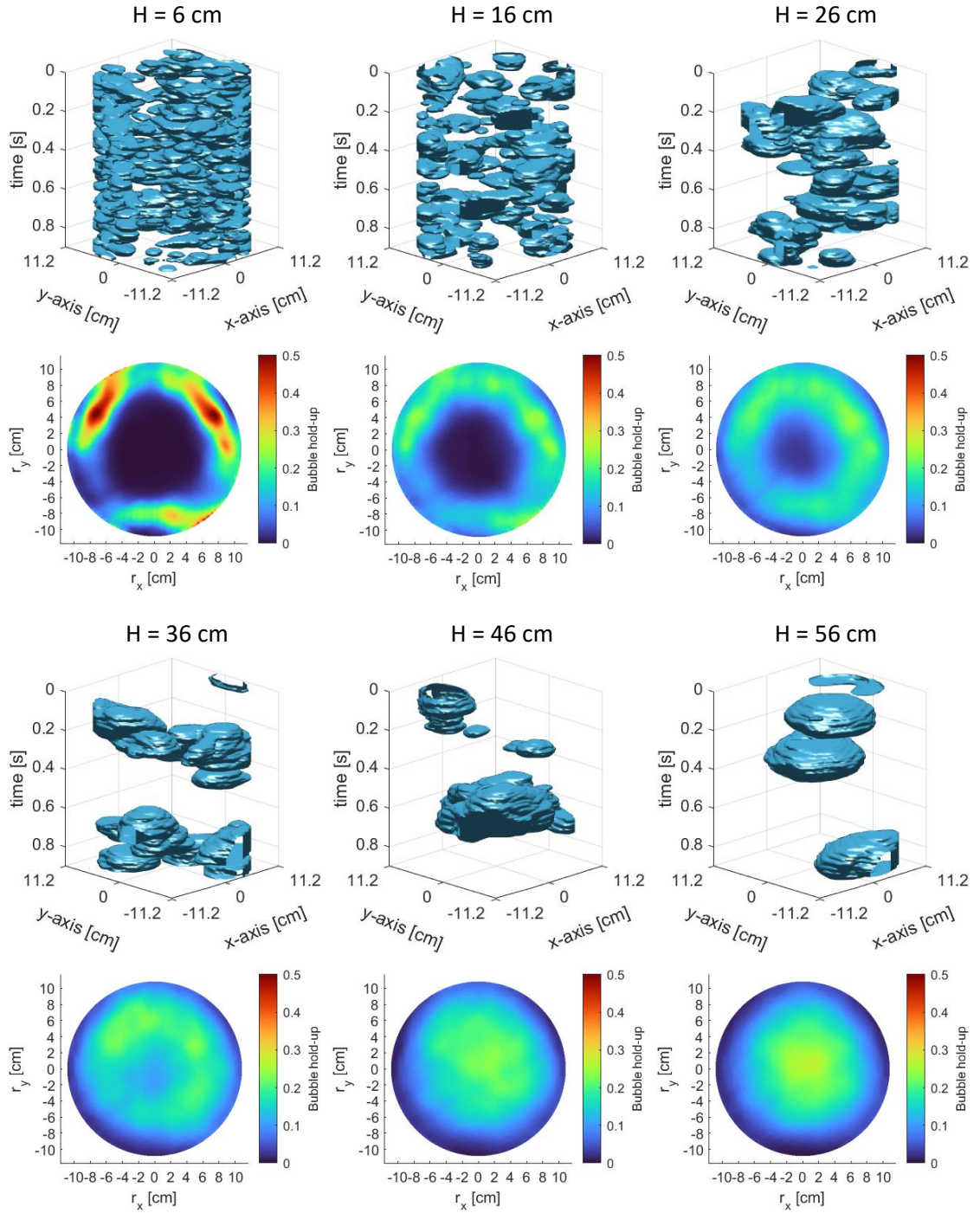


Figure 4.11: Samples of the pseudo three-dimensional reconstructions and the spatial distribution of the respective bubble hold-up for the measurement heights of 6, 16, 26, 36, 46 and 56 cm at a fluidization number  $u/u_{mf} = 4$ .

This problem becomes more apparent in the selected cross-sectional bubble hold-up reconstructions shown in Figure 4.12. It is very likely the result of the limited measurement angles and the many small bubbles that are present at this height, due to which the individual bubble locations cannot be determined unambiguously. By means of tomography simulations, shown in Section 4.4.1, this explanation could be confirmed. Accordingly, all measurements at heights lower than 16 cm were not considered, with measurements at 16 cm still affected by this issue, however not significantly.



Figure 4.12: Selected cross-sectional bubble hold-up reconstructions from a measurement height of 6 cm that are likely the result of limited measurement angles.

### 4.3.3 Statistical evaluation of the measured bubble properties

In total, 105,590 bubbles were reconstructed successfully, representing about 77% of the total bubble hold-up. Unsuccessful reconstructions are those that could not be linked in both measurement planes according to the constraints defined in Section 4.2.3. Following the observation described in Section 4.3.2 that the measurements at heights below 16 cm are likely significantly erroneous, from here on only measurements at heights of 16 cm and above are considered. Additionally, only the measurements at increments of 10 cm are included in the following to preserve the clarity of the presented results. A total of 38,481 bubbles belong to this reduced set of experimental settings. After the filtering according to the methods described in Section 4.4.5 there are 26,753 bubbles left in the reduced data set, which represent 65% of the total measured bubble hold-up for these settings. Unfortunately, the raw data at the height of 36 cm and  $u/u_{mf} = 1.5$  was corrupted and could not be retrieved and therefore is not included in the results. Considering the large number of experimental settings, the missing data does not affect the evaluation.

The summary statistics for the selected experimental settings are shown in Table 4.2. Besides the cross sectional mean bubble hold-up  $\varepsilon_b$ , the summary includes the arithmetic mean, the relative standard deviation (RSD) and the relative standard error (RSE) of various bubble properties. These include the volume equivalent diameter  $d_{b,eq}$ , the bubble rise velocity  $u_{br}$ , the aspect ratio  $l : w$  (length to width), the specific surface areas  $a_b$  and  $a_e$  of the bubble reconstructions and the corresponding fitted ellipsoids, for which the volume weighted means are shown instead of the arithmetic, as well as the number  $n$  of reconstructed bubbles for each setting. Additionally, the mean of the ratio between the reconstructed volumes of the

### 4.3 Results of X-ray tomography measurements without vertical internals

---

individual bubbles for each of the measurement planes, where the larger of the two volumes is divided by the smaller one is listed. This ratio is from here on be referred to as  $V_{b,max}/V_{b,min}$ . The mean values of  $V_{b,max}/V_{b,min}$  show that the deviation between the reconstructed volumes of each measurement plane decreases with the measurement height and fluidization number. This could be another indication for the limitations of experimental methods and will also be discussed in Section 4.4. For all experimental settings except one (height = 6 cm;  $u/u_{mf} = 1.5$ ), all of the mentioned variables had a relative standard error of  $RSE \leq 5\%$  and were therefore considered as statistically representative samples.

H	$u/u_{mf}$	$\varepsilon_b$	Mean ( $d_{b,eq}$ )	RSD ( $d_{b,eq}$ )	RSE ( $d_{b,eq}$ )	Mean $V_{b,max}$ $V_{b,min}$	Mean ( $u_{br}$ )	RSD ( $u_{br}$ )	RSE ( $u_{br}$ )	Mean ( $l:w$ )	RSD ( $l:w$ )	RSE ( $l:w$ )	Mean <sub>vol</sub> ( $a_b$ )	RSD ( $a_b$ )	RSE ( $a_b$ )	n
[cm]	[-]	[-]	[cm]	[-]	[-]	[-]	[m/s]	[-]	[-]	[-]	[-]	[-]	[m <sup>2</sup> /m <sup>3</sup> ]	[-]	[-]	[-]
16	1.5	1.0%	2.2	24%	0.6%	1.34	0.35	26%	0.6%	0.58	36%	0.9%	3.72	21%	0.5%	1599
16	2	3.7%	2.5	29%	0.5%	1.35	0.37	36%	0.7%	0.68	43%	0.8%	4.38	23%	0.4%	2915
16	3	7.8%	3.4	30%	0.6%	1.33	0.50	41%	0.8%	0.88	43%	0.9%	4.95	21%	0.4%	2355
16	4	11.2%	4.3	34%	0.9%	1.31	0.61	45%	1.2%	1.04	47%	1.2%	2.03	22%	0.6%	1496
16	6	17.5%	6.0	41%	1.6%	1.27	0.77	50%	1.9%	1.25	52%	2.0%	1.39	25%	0.9%	690
26	1.5	1.8%	2.6	29%	0.6%	1.28	0.37	28%	0.6%	0.59	33%	0.7%	3.01	24%	0.5%	2070
26	2	4.7%	3.2	29%	0.6%	1.27	0.42	37%	0.7%	0.69	36%	0.7%	2.70	22%	0.4%	2488
26	3	9.1%	4.8	29%	0.7%	1.24	0.57	43%	1.1%	0.95	41%	1.0%	1.90	20%	0.5%	1532
26	4	13.0%	6.4	31%	1.0%	1.20	0.66	49%	1.6%	1.09	41%	1.3%	1.47	21%	0.7%	973
26	6	17.9%	8.9	40%	2.0%	1.18	0.84	44%	2.2%	1.28	44%	2.2%	0.88	23%	1.2%	395
36	2	5.1%	4.0	30%	0.7%	1.21	0.47	41%	1.0%	0.72	36%	0.9%	2.01	22%	0.5%	1718
36	3	9.5%	6.1	31%	1.0%	1.17	0.60	45%	1.4%	0.95	39%	1.3%	1.34	21%	0.7%	963
36	4	13.1%	8.1	34%	1.4%	1.14	0.71	48%	2.1%	1.08	46%	2.0%	1.13	22%	1.0%	538
36	6	17.0%	11.8	34%	2.0%	1.11	0.97	51%	3.0%	1.39	41%	2.5%	0.81	20%	1.2%	282
46	1.5	2.6%	3.4	31%	0.8%	1.21	0.43	35%	0.9%	0.62	33%	0.8%	2.37	24%	0.6%	1540
46	2	5.1%	4.9	31%	0.9%	1.18	0.52	43%	1.3%	0.76	34%	1.0%	1.78	22%	0.7%	1094
46	3	9.3%	7.4	31%	1.3%	1.14	0.67	46%	1.9%	0.96	38%	1.5%	1.25	21%	0.9%	608
46	4	12.2%	9.9	32%	1.7%	1.11	0.81	49%	2.6%	1.18	55%	2.9%	0.97	20%	1.0%	367
46	6	17.8%	14.7	24%	1.5%	1.07	1.00	44%	2.8%	1.50	39%	2.5%	0.70	17%	1.1%	243
56	1.5	2.7%	4.0	30%	0.9%	1.17	0.47	36%	1.1%	0.66	32%	1.0%	2.09	23%	0.7%	1127
56	2	5.0%	5.8	31%	1.1%	1.13	0.58	40%	1.5%	0.80	34%	1.2%	1.37	22%	0.8%	756
56	3	8.5%	9.3	28%	1.4%	1.10	0.75	44%	2.3%	1.05	38%	1.9%	1.05	20%	1.0%	387
56	4	11.8%	11.9	29%	1.7%	1.07	0.88	39%	2.3%	1.22	39%	2.3%	0.83	19%	1.2%	282
56	6	18.1%	16.9	20%	1.4%	1.04	1.01	38%	2.6%	1.66	36%	2.5%	0.61	17%	1.2%	212

Table 4.2: Statistical summary of chosen bubble properties for the measurement heights of 16, 26, 36, 46 and 56 and fluidization numbers of 1.5, 2, 3, 4 and 6.

### 4.3 Results of X-ray tomography measurements without vertical internals

Correlations to predict mean values for bubble properties, mainly the mean bubble diameter and bubble rise velocity, are often used in reactor modeling to calculate various process characteristics, such as the mass transfer between the dense phase and the bubble phase, the heat transfer between the fluidized bed and the reactor walls or inserted heat exchangers or the residence times of both solid and gas phase [54], [68], [210]. In the following, the experimental results are compared to popular correlations from the literature, which according to a literature review by Karimipour *et al.* [68] are well suited for particles of Geldart type B. All selected correlations are presented in Section 2.3.3.

Figure 4.13, shows the comparison between the chosen literature correlations and the probability density of the volume-equivalent bubble diameters  $d_{b,eq}$  and the corresponding bubble rise velocities  $u_{br}$  for all evaluated bubbles belonging to the reduced set of experimental settings defined above. Accordingly, the correlation by Davidson and Harrison, shown in Equation 2.25, describes the mean values of measured bubble rise velocities for the respective bubble diameter very well. However, the experimental data shows a significant variance for this correlation.

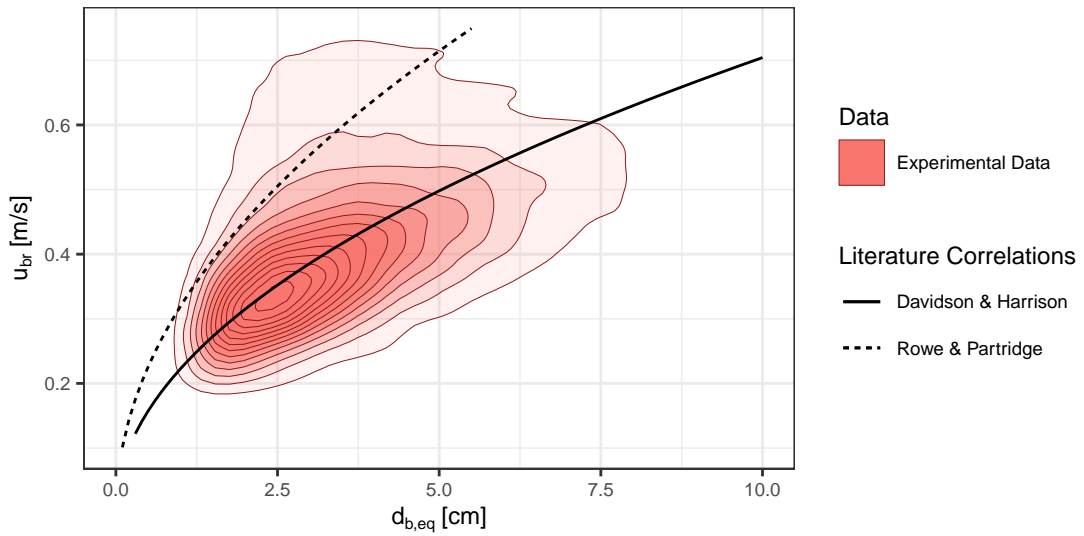


Figure 4.13: Comparison between experimental data measured via X-ray tomography and correlations by Davidson & Harrison [143] and Rowe & Partridge [118] of the correlation between the size and rise velocity of bubbles.

Correlations by Werther [55], Mori & Wen [134] and Darton *et al.* [135] were chosen for the prediction of the bubble diameter. The comparison between the predictions from the literature correlations and the experimental data for the volume-equivalent bubble diameter  $d_{b,eq}$  are shown in Figure 4.14. While the measured bubble diameters are in the range of the correlations by Darton *et al.* and Mori & Wen for  $u/u_{mf} < 2$ , they are generally significantly larger than all investigated correlations predict for higher fluidization numbers. For example,



the deviations of the measured mean of  $d_{b,eq}$  from the predicted values for  $u/u_{mf} = 6$  and  $H = 36$  cm are in the range of about 40-70%, which translates to a deviation of the respective mean bubble volumes between 270% and 490%. The correlations by Mori & Wen and Darton *et al.* show similar gradients to those of the respective experimental data for  $u/u_{mf} \leq 3$  but are less steep for higher values of  $u/u_{mf}$ . Overall, the gradients of the correlation by Mori & Wen are the most comparable to those of the measured data. At heights  $H \geq 46$  cm and  $u/u_{mf} \geq 4$  as well as at  $H = 36$  cm and  $u/u_{mf} = 6$  the mean bubble diameters reach values of 10 cm and more. The bubbles are then in the range of 50% of the bed diameter  $D$  which typically defines the onset of slugging fluidization [73], [105]. It is to be expected that all measured bubbles are influenced by wall effects, as it is said to occur for bubbles with  $d_{b,eq} \geq 0.1D$ , which defines the lower limit of bubbles sizes that can be detected with the X-ray setup [170].

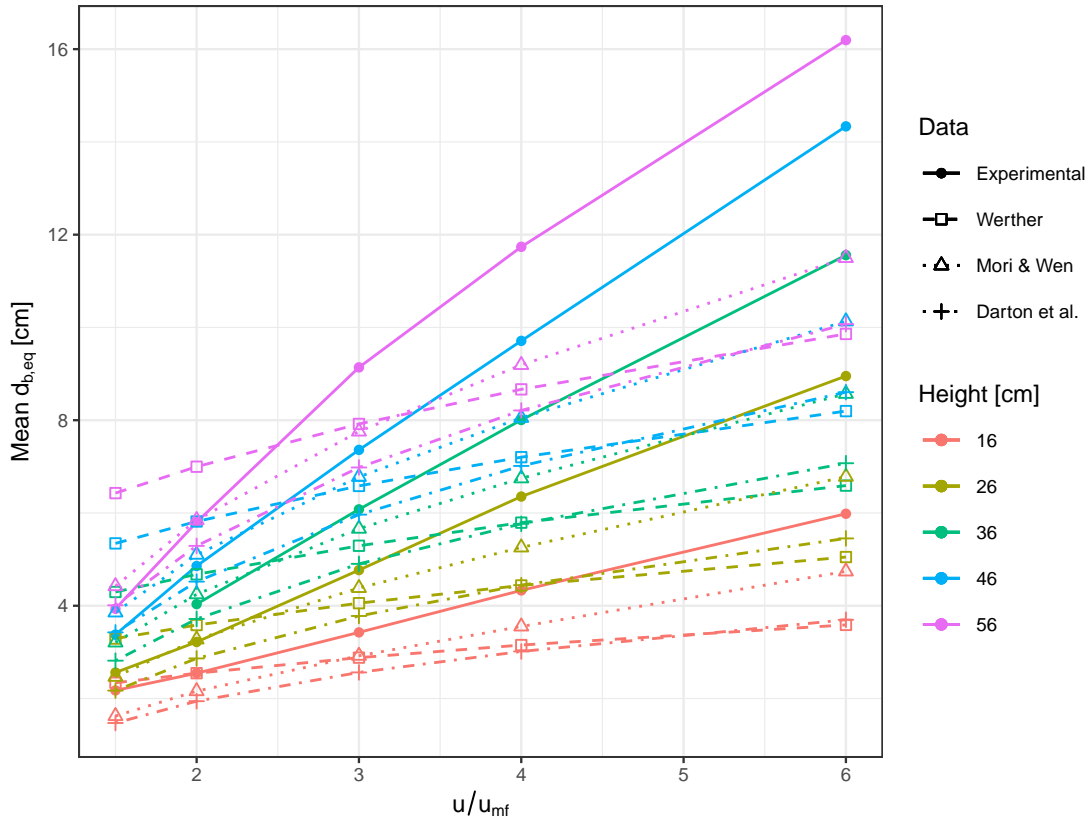


Figure 4.14: Comparison between the mean values of bubble diameters as they were measured via X-ray tomography to the predicted diameters according to literature correlations by Werther[55], Mori & Wen [134] and Darton *et al.* [135].

To compare the measured bubble rise velocities, the bubble sizes determined by the correlations mentioned above were used in combination with correlations that describe the dependency of the rise velocity of a bubble to its volume-equivalent diameter, as it is typically done in hydrodynamic models of fluidized beds [54], [211], [212]. For the prediction of



### 4.3 Results of X-ray tomography measurements without vertical internals

the mean single bubble rise velocity  $u_{br}$ , the correlation by Davidson & Harrison [143] was chosen, as it could be shown above that it describes the measured data well on average. The correlation by Mori & Wen was chosen for the prediction of the mean of  $d_{b,eq}$ , which provided the best match to the experimental data, though it still deviated significantly. In the literature, a distinction is made between the rise velocity  $u_{br}$  of single bubbles in a fluidized bed and the rise velocity  $u_b$  of bubbles in a freely bubbling bed [68], [128] as described in Section 2.3.3. Correlations predicting the rise velocity  $u_b$  are often based on  $u_{br}$  and expanded by an additional term that includes  $(u - u_{mf})$  [56], [73], [122], [213], which can be interpreted as a correction to account for dynamic bubble interactions [144]. Here, the correlations by Davidson & Harrison and Hilligardt & Werther, shown in Equations 2.25 and 2.28 were chosen for the comparison. In Figure 4.15 the experimental data is compared to the respective single bubble rise velocities  $u_{br}$  and the predicted rise velocities  $u_b$  for freely bubbling beds. To improve the clarity of the plot, the data set was further reduced to only include data for the heights 16, 36 and 56 cm.

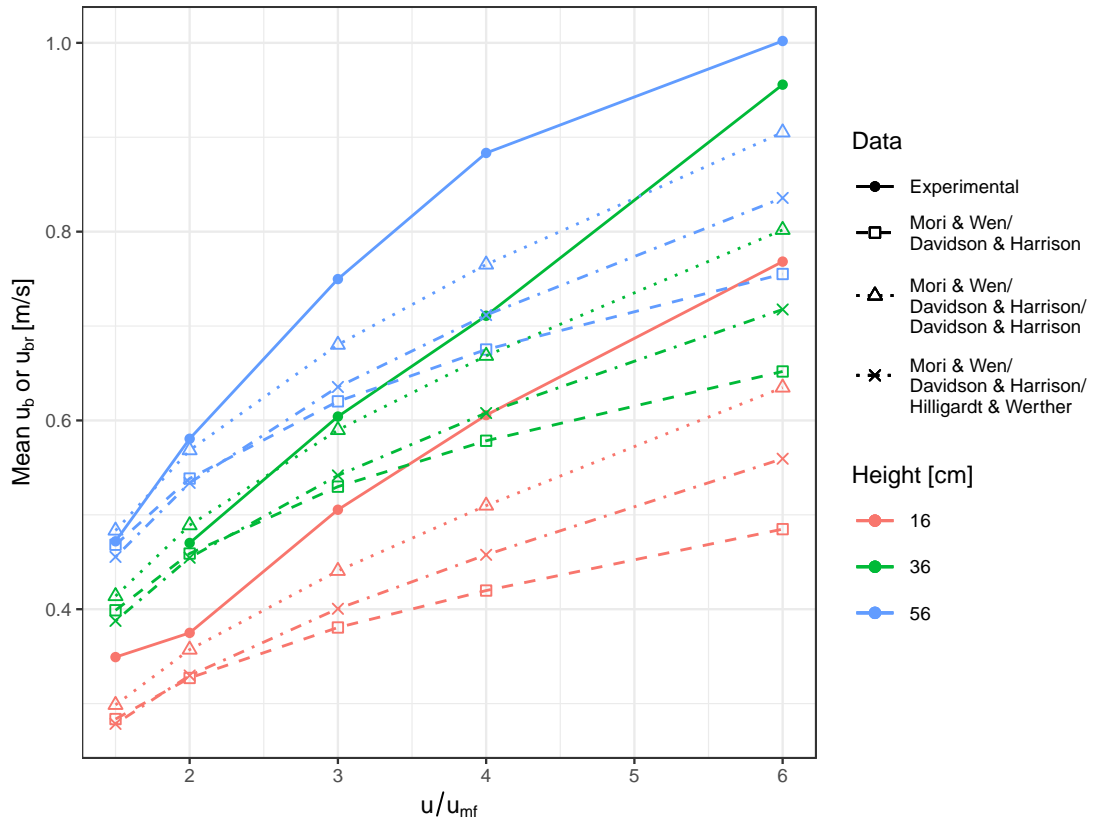


Figure 4.15: Comparison between the mean values of the bubble rise velocities as they were measured via X-ray tomography and predicted single bubble rise velocities according to the combination of the correlation by Mori & Wen that predict the bubble diameter and correlations predicting the rise velocity  $u_{br}$  of single bubbles and  $u_b$  of bubbles in freely bubbling beds.

Here, it is not surprising that the measured rise velocities do not match the predictions from literature correlations well for  $u/u_{mf} > 2$ , considering the deviation that was found between the measured diameters and those predicted from literature which are direct inputs of the rise velocity correlations. The correlation by Davidson & Harrison for the prediction of the rise velocity  $u_b$  in freely bubbling beds deviates the least from the measured values. If the bubble diameters that were measured are used in combination with the correlations to determine  $u_b$ , then there is little deviation between the measured and predicted values of  $u_b$ . This can be seen in Figure 4.16, where a comparison between the measured mean bubble rise velocities and those predicted from the literature correlations are shown in form of a parity plot. Accordingly, the correlations by Davidson & Harrison describe the measured data very well.

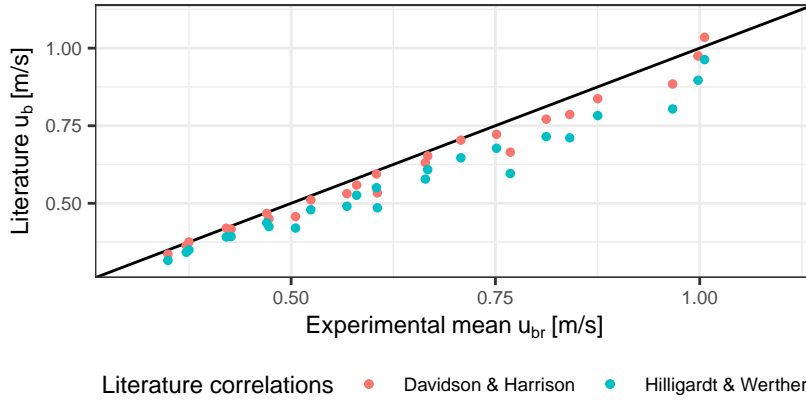


Figure 4.16: Parity plot showing a comparison between the mean values of the bubble rise velocities  $u_B$  as they were measured via X-ray tomography and as they were predicted according to correlations by Davidson & Harrison and Hilligardt & Werther.

In conclusion, it could be shown that the chosen literature correlations are not well suited to predict the mean of the measured values of  $d_{b,eq}$ , whereas the correlation by Davidson & Harrison predicts the mean of the measured bubble rise velocities accurately.

### 4.3.4 Bubble property distributions and their correlations

One of the ambitions of this thesis is to provide correlated distributions of bubble properties instead of simply their mean values, which may improve the accuracy of reactor models. Additionally, such distributions would provide excellent benchmarks for CFD simulations. For the evaluation of the measurements, the focus was put on the equivalent bubble diameter  $d_{b,eq}$ , the bubble rise velocity  $u_{br}$ , the aspect ratio  $l : w$  and the radial bubble position  $r_b$ , because they allow the derivation of most other important bubble phase properties such as the specific surface area  $a$ , the bubble residence time and the spatial distribution of the

### 4.3 Results of X-ray tomography measurements without vertical internals

cross-sectional bubble hold-up  $\varepsilon_b$ . In the following, a selection of scatter plots is presented, which show the results of each individual experimental setting in the reduced range selected in Section 4.3.3 for a combination of the selected bubble properties.

Figure 4.17 shows the scatter plots of the bubble diameter  $d_{b,eq}$  over the bubble rise velocity  $u_b$  for each selected experimental setting. Note the logarithmic scale for  $d_{b,eq}$  to allow a qualitative assessment of the distributions of both large and small bubbles. The mean values from literature correlations that were introduced in Section 4.3.3 and from the experiments are also shown. The comparison of the comparatively broad range of the bubble properties to their mean values indicates that it may not be sufficient to model the hydrodynamics of BFB reactors with just mean values of bubble properties. For instance, for catalytic fluidized bed reactors fast and large bubbles may pose the risk of bypassing reactants through the reactor due to mass transfer limitations while this may not be the case for bubbles with the mean rise velocity and size. The correlation between the shown bubble properties can also be seen, with large bubbles being faster on average than the small ones, as it was described in detail in section 4.3.3.

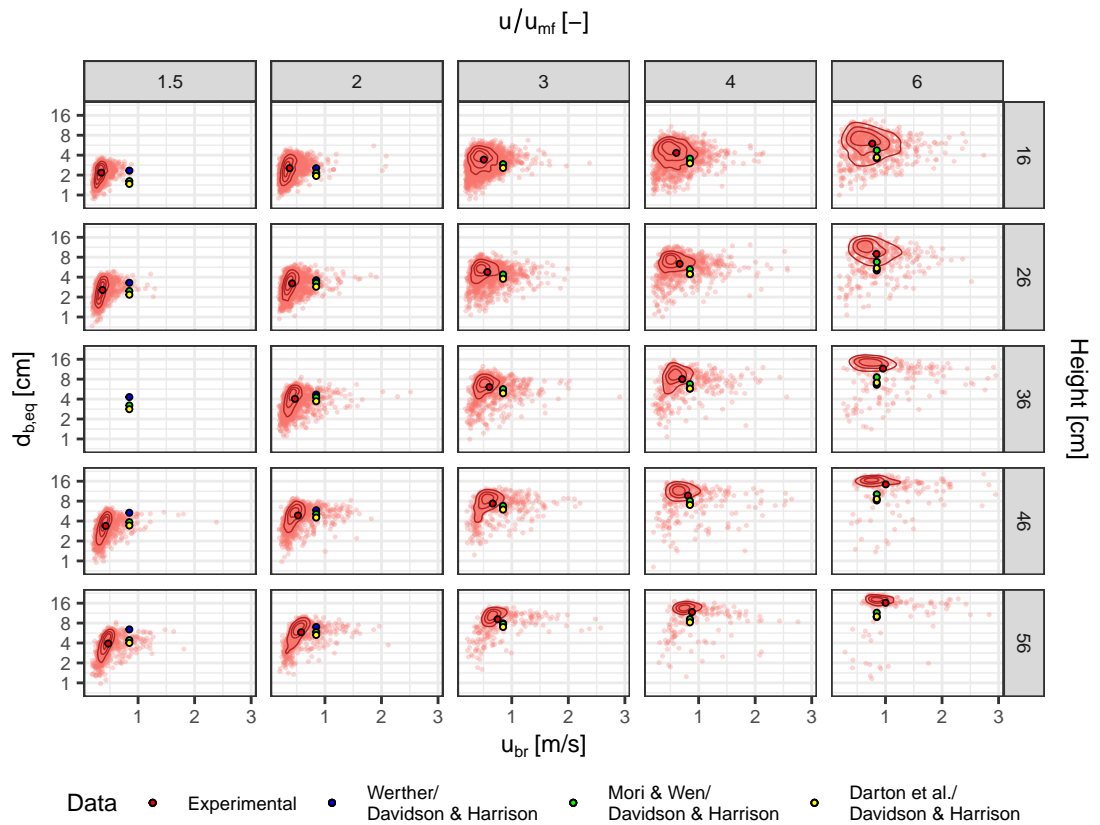


Figure 4.17: Scatter plots including density contour lines of the equivalent bubble diameter  $d_{b,eq}$  over the bubble rise velocity  $u_{br}$  in comparison to mean values predicted by a combination of chosen literature correlations for a selection of experimental settings.

Another important bubble property is the shape of the bubble as previously discussed in Section 2.3.3. Not only does the knowledge of the bubble shape allow the correct calculation of the bubble surface area  $A_b$ , given that its volume-equivalent diameter  $d_{b,eq}$  is known. It is also very important for the measurement of bubble properties with locally constricted methods, such as optical or capacitance probes, where the bubble sizes are derived from pierced chord lengths through statistical methods that require bubble shape assumptions [136], [214]. Also, in case the shape of a bubble correlates with other bubble properties such as its rise velocity, radial position or size, this has to be accounted for in such measurements. Otherwise, there would be a bias towards the properties of oblate bubbles in comparison to elongated ones, which are more likely to be pierced by the probes. This issue is relevant for many of the correlations and experimental data found in literature, where the bubble shapes were often assumed to be constant in general or for a given height and fluidization number [141], [142], [215], [216] and approximated with a variety of shapes such as spherical, spherical-cap, ellipsoidal or truncated ellipsoidal shapes [118], [138]–[140], [217].

In this work, the aspect ratio  $l : w$  is defined by the ratio between the maximum vertical chord length and the circle equivalent diameter of the maximum horizontal cross section of the bubble. According to the measured data, there is a dependency of the mean aspect ratio from the measurement height and the fluidization number as shown in Figure 4.18. The majority of the measured bubble volume exists in shape of elongated bubbles for fluidization numbers of 4 and 6, while the majority is oblate for lower values of  $u/u_{mf}$ . The widely applied assumption of mostly oblate spherical cap shaped bubbles is therefore not suited to describe these results. For instance, Werther proposed a correlation for a shape factor  $\rho$ , as shown in Equations 2.23 and 2.24 in Section 2.3.3, which describes the ratio of the vertical to the horizontal diameter, analogue to the aspect ratio  $l : w$  in this publication. By definition the shape factor  $\rho$  is always less or equal to one. Accordingly,  $\rho$  calculates to values in the range between 0.65 and 0.81 for the selected measurement heights and fluidization numbers of the X-ray tomography measurements.

Further, the scatter plots presented in Figures 4.19 and 4.20 show that there is also a broad spectrum of bubble shapes for each experimental setting and that the aspect ratio of a bubble is correlated to its size and especially to its rise velocity. Considering the measurements at heights and fluidization numbers where wall effects are supposed to occur as described in Section 2.2.3, it is likely that the bubble shapes are influenced by this as well. Additionally, the fact that the settled bed height was 62 cm after fluidization suggests that bubbles in the upper regions of the bed may experience an acceleration towards the bed surface and with that an elongation of their shape, especially in case of large bubbles, as it has been reported to take place [124], [181]. However, it is also known that bubbles experience an elongation in the draft of other bubbles [115], which likely partially explains the variety of observed bubble

### 4.3 Results of X-ray tomography measurements without vertical internals

shapes, given the fact that coalescence frequently occurs which includes such dynamic bubble interactions.

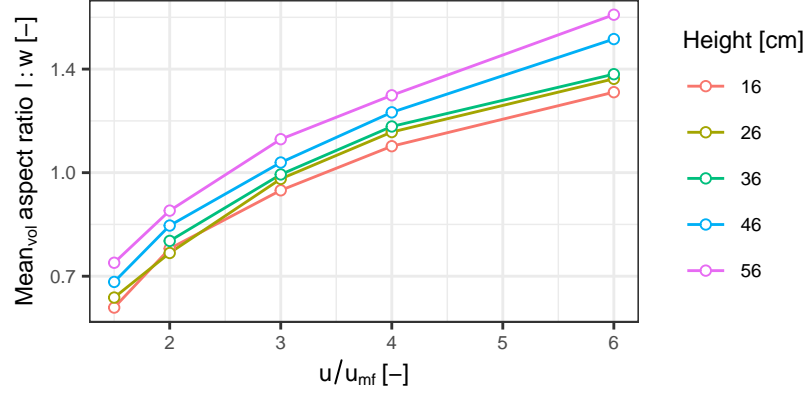


Figure 4.18: Volume weighted mean of the aspect ratio  $l : w$  dependent on the measurement height and the fluidization number.

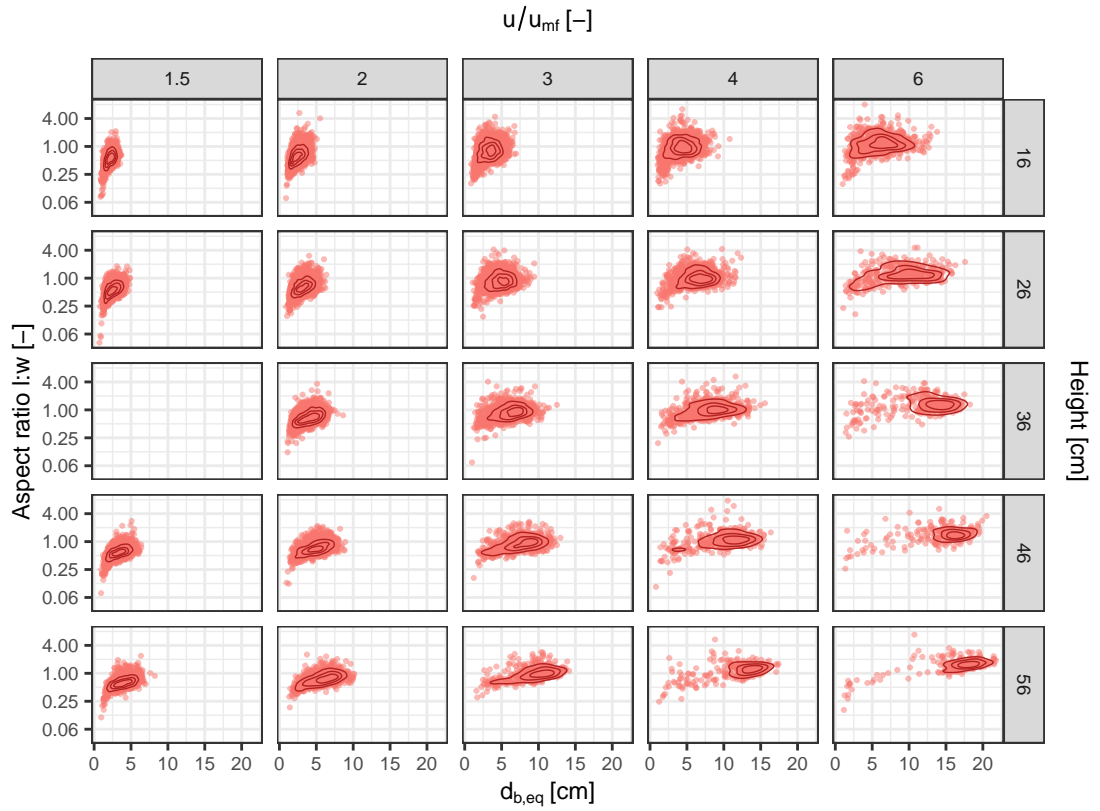


Figure 4.19: Scatter plots including density contour lines of the aspect ratio  $l : w$  over the equivalent bubble diameter  $d_{b,eq}$  for a selection of experimental settings.

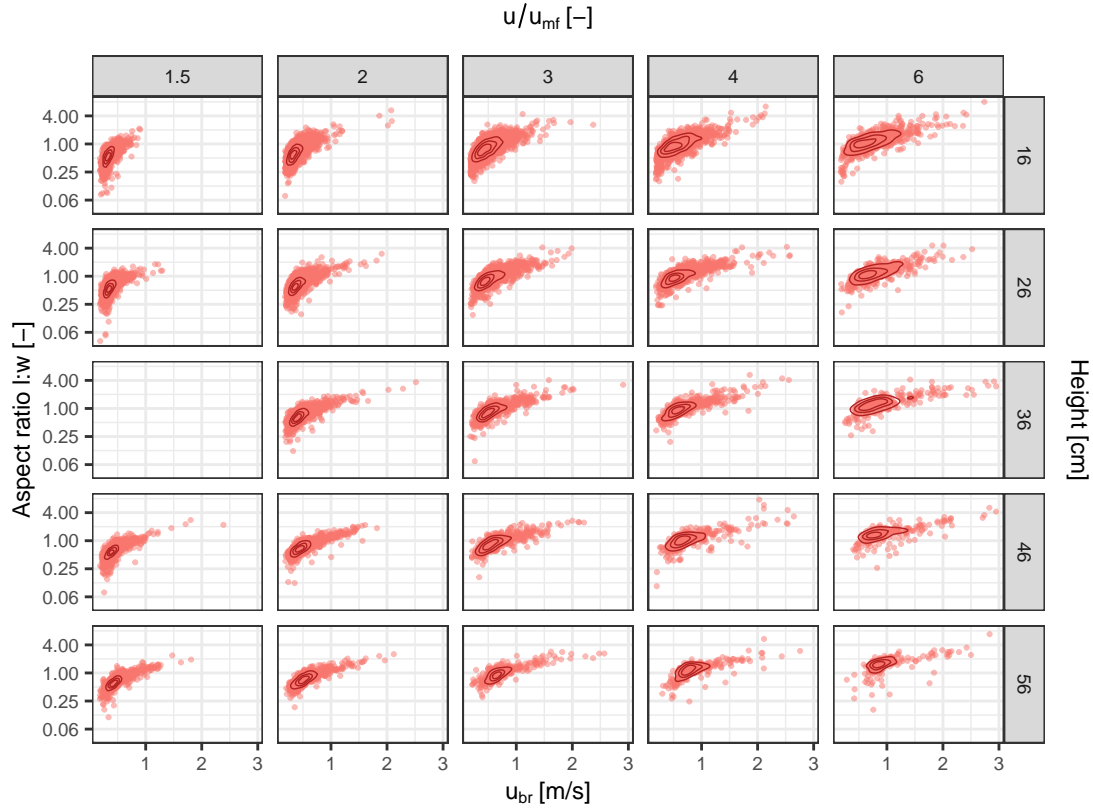


Figure 4.20: Scatter plots including density contour lines of the aspect ratio  $l : w$  over the bubble rise velocity  $u_b$  for a selection of experimental settings.

The assumption of the bubble shape can have significant consequences for the calculation of the specific surface area  $a_b$  of a bubble. Therefore, the measured values of  $a_b$  were compared with those resulting from the typically used assumptions of spherical-cap and hemispherical shapes as well as spheroid shapes according to the shape factor correlation shown in Equation 2.23 by Werther. For this, the measured volume weighted mean of  $d_{b,eq}$  was used and the different shape assumptions were applied on the corresponding bubble volume. The results of this comparison are shown in Figure 4.21. While the hemispherical shape assumption leads to values for  $a_b$  that are up to 3.8 times higher than what was measured, assuming a spheroid shape according to the shape factor proposed by Werther produces values that are up to 2.3 times lower than the measured data. From the considered shapes, the assumption of a spherical-cap shape with a wake angle of  $120^\circ$  resulted in the smallest difference between measured and estimated values of  $a_b$  especially for higher values of  $u/u_{mf}$ . This shape assumption is therefore the most accurate representation for the measured bubbles.

### 4.3 Results of X-ray tomography measurements without vertical internals

In Figure 4.22 a comparison between the volume weighted mean of  $a_b$  derived from the measurements and the corresponding fitted ellipsoidal shapes is shown, which are in good agreement with the measured values of  $a_b$  for lower values of  $u/u_{mf}$  and lower measurement heights. Likely due to the resolution of the reconstructions, only larger bubbles may have a somewhat rough surface area, which may explain the slightly increased values for  $a_b$  in comparison to the fitted ellipsoids, which are modeled perfectly smooth.

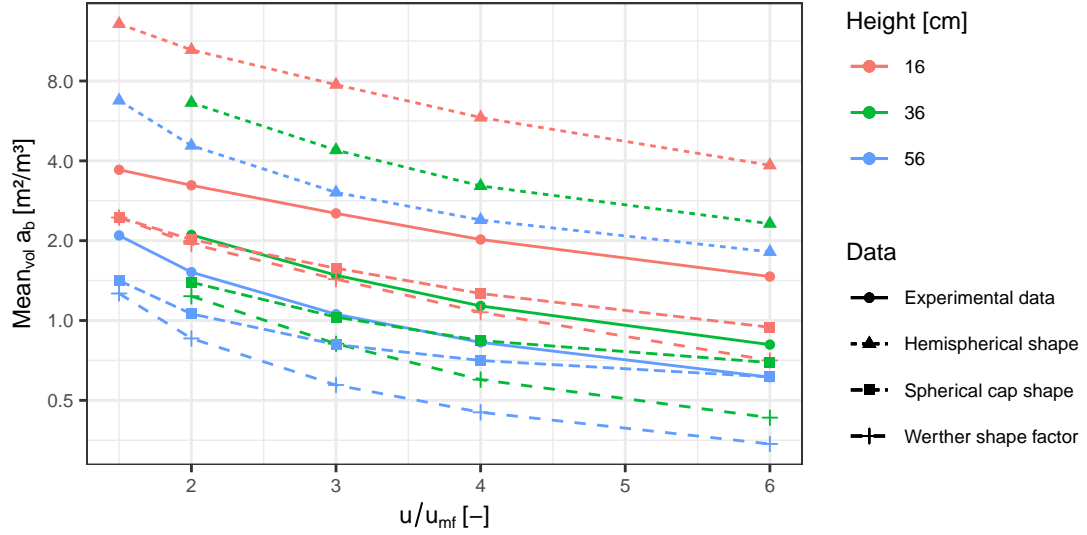


Figure 4.21: Comparison of the measured specific surface areas  $a_b$  and those resulting from typical shape assumptions.

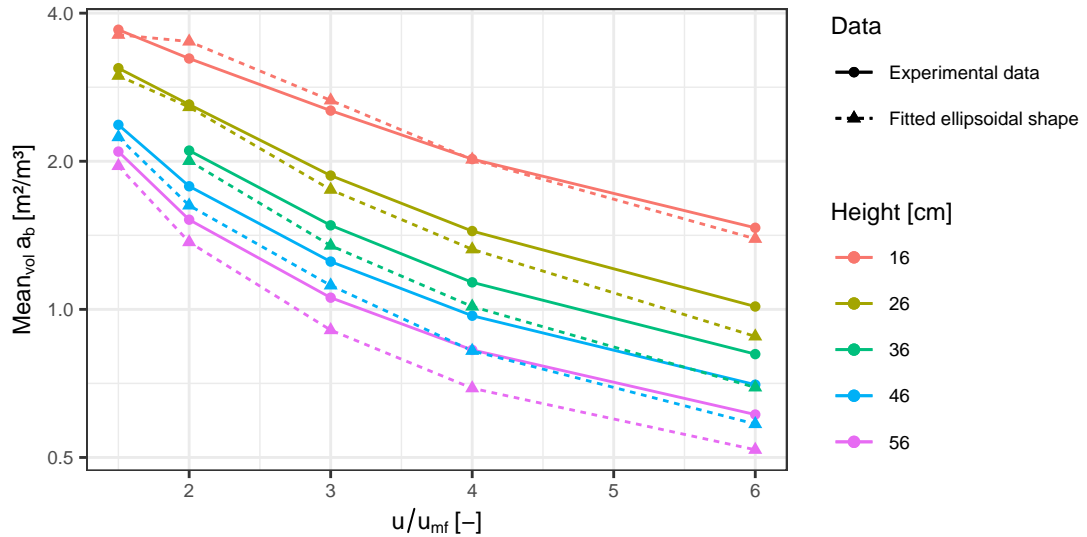


Figure 4.22: Comparison of the measured specific surface areas  $a_b$  and those of the fitted ellipsoids.

The fact that the experimental results show a broad distribution of shapes for a given measurement height and fluidization number that can differ significantly from the presented shape assumptions, further highlights the importance of taking the bubble property distributions in account rather than just their mean values. Knowing the correlated distributions of the bubble volumes, their rise velocities and their shapes allows the calculation of the fraction of the bubble phase volume that is located in bubbles with a certain specific surface area and a certain rise velocity for each experimental setting. For the measured data of this work this is depicted in Figure 4.23, where the cumulative volume of the measured bubbles for each combination of  $a_b$  and  $u_{br}$  is shown. Note that an additional dimension, the radial distribution of the bubble volume, could also be accounted for. The volume weighted mean values of the measurements and the predicted mean values according to the combination of the literature correlations by Mori & Wen for the bubble diameter  $d_{b,eq}$  and by Davidson & Harrison for the bubble rise velocity  $u_b$  together with the spherical-cap shape assumption with a wake angle of  $120^\circ$  are shown as well. Here, the deviation between the predictions from literature correlations and the experimental values are not significant for most experimental settings. This is surprising, considering the large differences that were observed between the means of the measured diameters and rise velocities and those predicted by the respective correlations, as discussed in Section 4.3.3. The broad distributions of  $a_b$  and  $u_{br}$  indicates that the mean values might not sufficiently describe possible mass transfer limitations. For all measurements a significant fraction of the total bubble volume belonged to bubbles with lower values of  $a_b$  and higher values of  $u_b$  than their respective mean values. Implementing these findings in a reactor model could improve mass transfer predictions in comparison to calculations with mean values.

One noteworthy aspect of the methods applied for the presented X-ray tomography measurements is, that the rise velocity of each individual bubble was evaluated and applied to determine the vertical length of the respective bubble. Similar experimental investigations described in literature often apply mean rise velocities of each experiment on the corresponding experimental data to determine the vertical bubble dimensions [218], [219]. Others determine the volume-equivalent bubble diameter completely independently from the rise velocity by measuring the cross section of the bubbles for each frame and averaging cross-sectional diameters over all frames to retrieve the equivalent diameter [220]. A detailed description of their measurements of bubble properties by means of capacitance probes was provided by Werther & Molerus [218], who state: "The fact that the instantaneous rise velocity of a bubble is virtually a stochastic quantity makes the measurement of individual rise velocities pointless. Instead, the local state of fluidization is better described by the mean rise velocity  $u_b$  of the bubbles at the point of the probe." Consequently, the authors derived  $u_b$  through correlation techniques and applied it on all individual signal durations associated with the presence of a bubble at the tip of the probe to determine the distribution of pierced chord



### 4.3 Results of X-ray tomography measurements without vertical internals

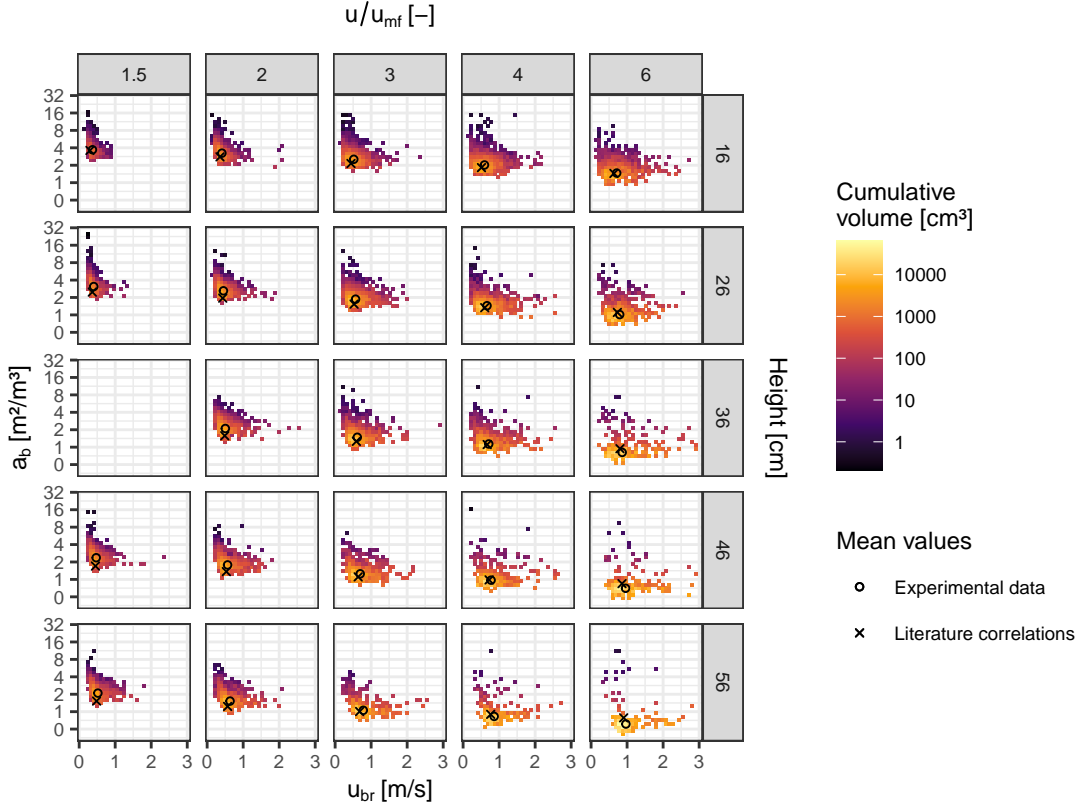


Figure 4.23: Distribution of the cumulative bubble volume respective the specific surface area  $a_b$  and the bubble rise velocity  $u_{br}$  as it was measured by means of X-ray tomography.

lengths. This method would reduce the chord lengths of bubbles that were rising faster than  $u_b$ , while increasing those of bubbles with rise velocities slower than  $u_b$ . Indeed, this will not make a difference for the determination of the mean pierced chord length if the fluctuations in rise velocities were simply due to random stochastic factors.

Potentially, one has to consider the fact that large bubbles rise faster than smaller ones on average, as it has been reported to occur in numerous publications [118], [122], [181], [221] and it has been observed in this work as well. If there was a significant variance in bubbles sizes for a given fluidization number and measurement position than large bubbles would on average be reduced in size, the resulting bubble size distribution should be narrowed and the possibility of fast and large bubbles bypassing reactants may not be identified. A similar problem would occur if there generally was a broad variation of rise velocities. Figure 4.24 shows the resulting normalized probability densities of  $d_{b,eq}$  for each of the two described methods. It can be seen that the deviations between both methods are negligible in most cases. Only for  $u/u_{mf} \geq 4$  the application of mean bubble rise velocities for the size determination leads to broadened bubble size distributions rather than a narrowed one as expected.

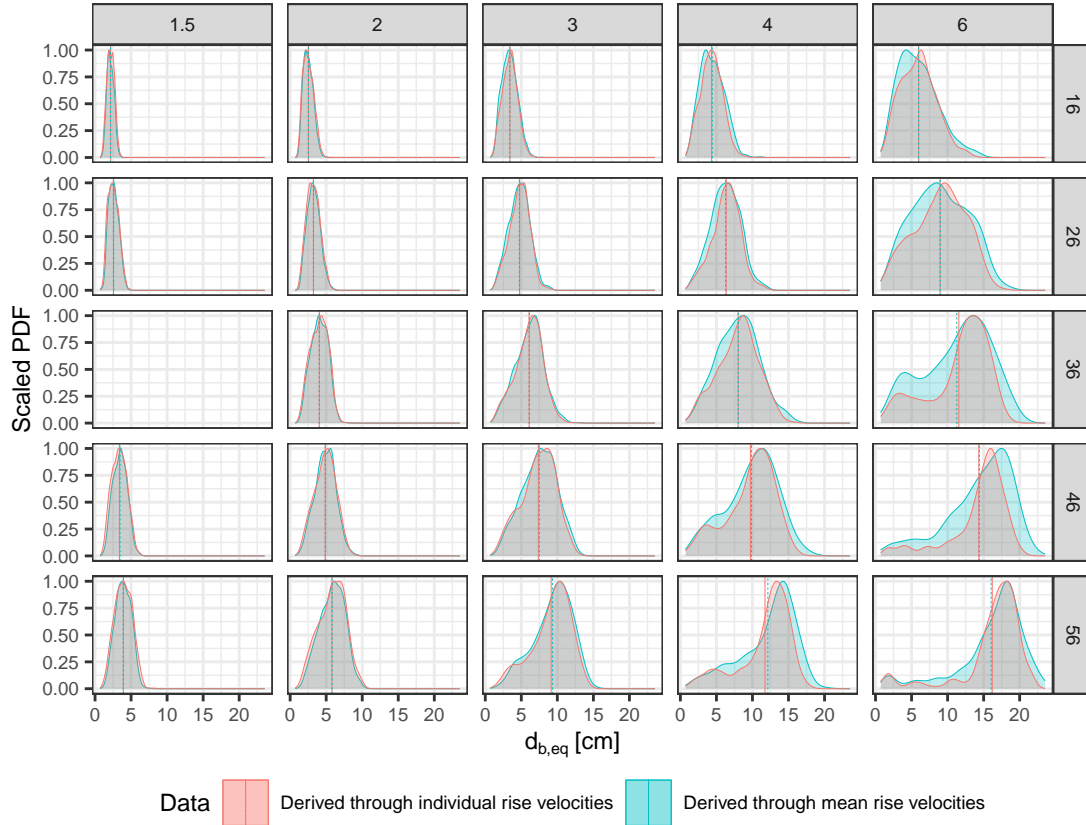


Figure 4.24: Comparison between the normalized probability density distributions of  $d_{b,eq}$  derived through the application of the mean bubble rise velocity  $u_b$  and of the individual bubble rise velocities  $u_{br}$  for the determination of the vertical lengths of the bubbles.

#### 4.3.5 Fitted correlated bubble property distributions

According to the methods described in Section 4.2.3, GEV distribution functions were fitted to the measured bubble property distributions for each experimental setting and t-copula functions were fitted to account for the correlation between the bubble properties. The resulting set of parameters can be found in the Appendix A. In the following, samples from the fitted correlated distributions are compared to the experimental data for four exemplary settings (Heights: 16 and 36 cm, Fluidization numbers: 2 and 4). The comparison of the respective bubble property distributions is shown in the form of probability density contour plots in the Figure 4.25. Overall, the fitted distributions match the experimental data including their correlations very well. As indicated by the analysis of the scatter plots of the experimental results in Section 4.3.4, the linear correlation matrices  $\hat{\rho}$  describing the t-copulas show a strong correlation between the volume-equivalent bubble diameter, bubble rise velocity and shape of the bubbles. The fitted distributions can be used to generate large samples for Monte Carlo simulations as it was done in the present work for the tomography simulations shown

### 4.3 Results of X-ray tomography measurements without vertical internals

in Section 4.4.1. Additionally, they can serve as a basis for the development of a statistical model that represent the experimental results and allow the interpolation for other settings. CFD models can be validated directly with the experimental data or with larger data samples generated with the fitted set of correlated distribution functions presented in this section.

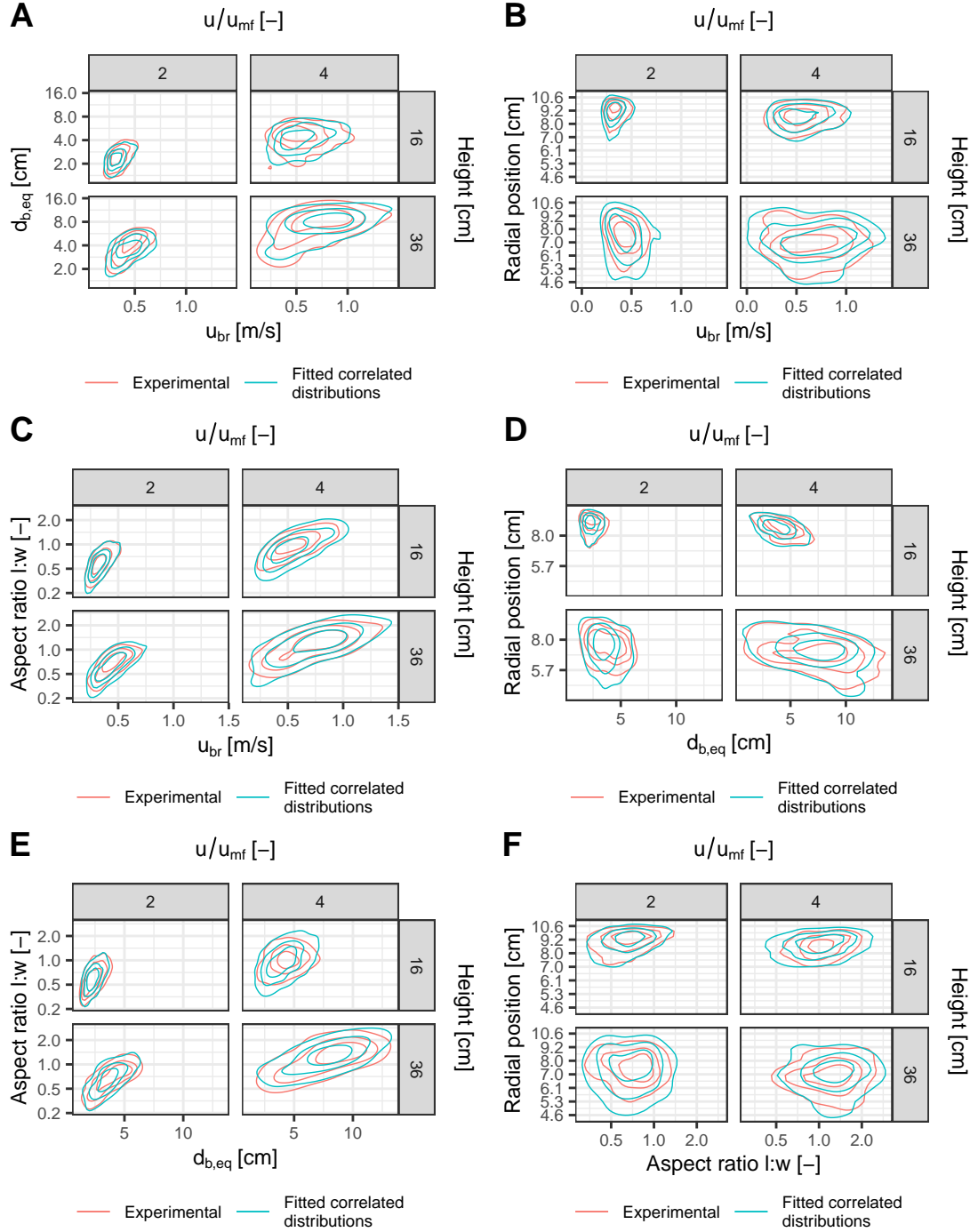


Figure 4.25: Comparison between fitted correlated distributions and the experimental data.

### 4.4 Verification of the applied X-ray tomography methods

In this section, different approaches to assess the limitations of the experimental methods applied in this work as well as the feasibility of the results are presented, based on which appropriate post-processing steps are derived.

#### 4.4.1 Tomography simulations

The simulation of X-ray intensity profiles of known solid fraction distributions can be a helpful tool to quantify the limitations of the applied X-ray tomography reconstruction methods. Given a defined ground truth for the spatial distribution of artificially generated phantom objects that represent bubbles in a fluidized bed as well as the spatial arrangement of the setup, then the Lambert Beer law can be applied to calculate the corresponding X-ray attenuation profiles for each detector, as described in Section 4.2.1. The resulting X-ray intensity profiles for the six detector arrays can then be reconstructed and evaluated with the methods described in Sections 4.2.1 and 4.2.3.

In Section 4.4.2, simulations of the reconstructions of single frames of randomly distributed bubble shapes that were sampled systematically are shown and evaluated to investigate the limitations of the experimental setup for the static case. Additionally, an algorithm, referred to as *3D-Bubblesampler*, which generates randomized pseudo three-dimensional bubbles, where the vertical dimension represents the time, was applied for pseudo three-dimensional tomography simulations. In that case, the bubbles were sampled from fitted distribution functions of the correlated bubble properties, as they were presented in Section 4.3.5, for the two measurement planes. This study is shown in Section 4.4.4.

Similar tomography simulations concerning the same experimental setup have been conducted by other authors. Yang *et al.* [222] investigated the performance of two reconstruction algorithms. He compared the SART algorithm with the Adaptive Genetic Algorithm (AGA) by means of tomography simulations of specific constellations of two or three phantom bubbles and concluded that the SART algorithm produced more accurate reconstructions at comparatively high resolutions but was more susceptible for noise. Mudde *et al.* [189] simulated the reconstruction of the two-dimensional bubble hold-up in a fluidized bed with a diameter of 40 cm. The authors investigated the influence of noise and the spatial resolution for different arrangements of one or two bubbles in close proximity with one another or the wall for two fan beam configurations consisting of either five or three X-ray sources and detector arrays. They decided that the reconstructions using only three sources was poor and focused on the case with five sources for which they confirmed a temporal resolution of 10 ms and a spatial resolution of 10 mm. Additionally, they found that noise significantly influenced the

measurements due to the short sampling time of 10 ms. In later studies conducted at higher frame rates it could be shown, that by averaging 10 sequential measurements the effect of the noise could be reduced considerably [170].

Among others, the XR-LD setup has been used to measure bubble property distributions of freely bubbling fluidized beds [223]–[225] including publications [133], [164], [168], [169], [200] that are based on the data set, which is also evaluated in this work. However, to the best of our knowledge, the limitations of the system concerning the measurement of multiple bubbles that are present in the measurement plane simultaneously, has not been investigated systematically yet.

One of the main issues of the experimental setup is what is referred to as limited data problem in CT applications [226]. Due to the fact, that only three detector arrays and thus only three observation angles are available for each measurement plane, the location of bubbles cannot always be determined with sufficient certainty. This may cause the misinterpretation of individual independent bubbles as a single larger one or the occurrence of artifacts that may erroneously be interpreted as bubbles. To investigate the magnitude of these issues, a systematic series of tomography simulations was conducted.

##### 4.4.2 Two-dimensional tomography simulations

A set of images that represent the cross-sectional distribution of bubbles, from here on referred to as phantoms, in a virtual measurement plane, was randomly generated with a systematic variation of the phantom bubble hold-up  $\varepsilon_{b,ph}$  and the mean cross-sectional phantom bubble diameter  $d_{b,ph}$ . Analogue to the measured RSD of  $d_{b,eq}$  shown in Table 4.2, the RSD for each generated distribution of  $d_{b,ph}$  was set to 25%. For each combination of  $d_{b,ph}$  and  $\varepsilon_{b,ph}$  a statistically representative sample sizes of 100 images was generated. The selected values of  $d_{b,ph}$  are 2, 3, 4, 6, 8 and 12 cm, which were chosen according to the measured mean values of  $d_{b,eq}$  shown in Table 4.2. At a height of 56 cm and a fluidization number  $u/u_{mf} = 6$  the measured time resolved cross-sectional bubble  $\varepsilon_b$  hold-up peaked at values of around 0.4. Hence, the  $\varepsilon_{b,ph}$  was varied with values between 0 and 0.4.

The tomography simulation algorithm was applied on the phantom images and the resulting distributions of the diameters of the reconstructed phantom bubbles were compared with the original images. Some typical examples of successful and incorrect reconstructions are shown in Figure 4.26. It can be seen that the quality of the reconstructions depends on the number of bubbles and the way they are aligned in relation to the detector angles. The top row of the figure shows an example for an erroneous reconstruction of many small bubbles, where the SART algorithm is unable to determine the bubble locations, leading to significantly wrong positions, shapes and sizes of the reconstructed objects. In the second row, an example

of three bubbles being specifically aligned in relation to the detector angles can be seen, which lead to the generation of artifacts that may be wrongly interpreted as bubbles. The third row shows that multiple medium sized bubbles can be reconstructed well, although the individual shapes are slightly distorted. With increasing diameters and thus a reduced number of individual bubbles, the ability of the algorithm to reconstruct images at even larger hold-ups improves, as can be seen in the bottom row of the figure.

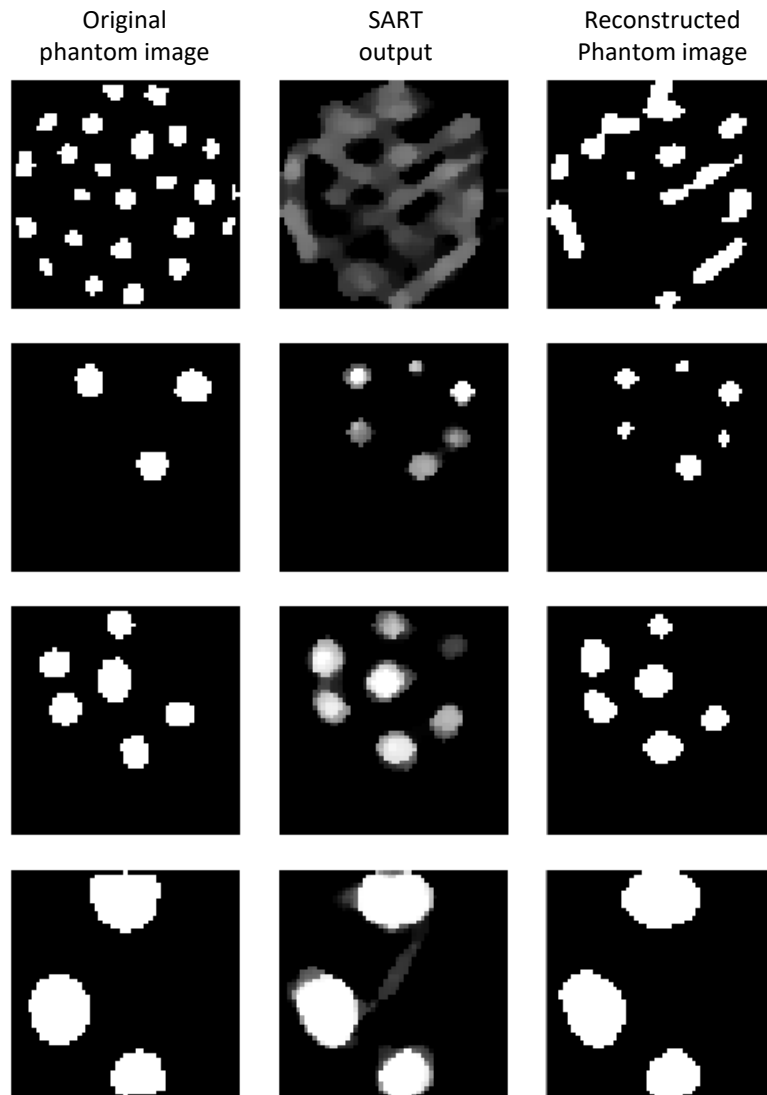


Figure 4.26: Comparison between original phantom images, the simulated output of the SART algorithm and the resulting binarized reconstructed image for typical faulty reconstructions (top two rows) and typical successful reconstructions (bottom two rows).

It could also be shown that the reconstruction procedure leads to reduced diameters of the reconstructed bubbles in comparison to the original phantom bubble diameters, if they were smaller than 2.5 cm. Very small bubbles would often times not be recognized at all.

Large bubbles however, would often be reconstructed slightly increased in size. One example for each of these cases can be seen in Figure 4.27.

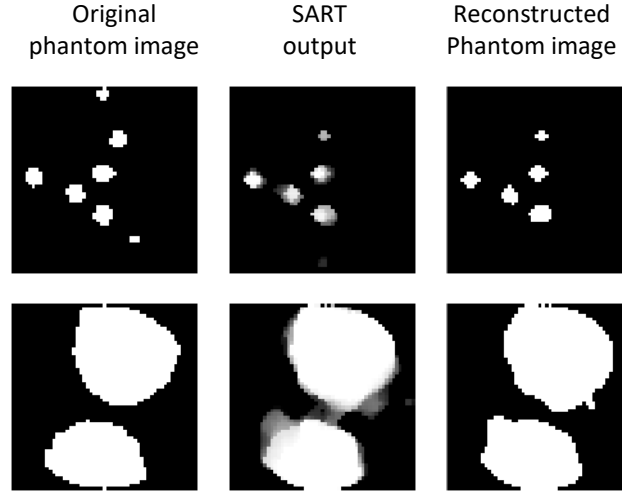


Figure 4.27: Comparison between original phantom images, the simulated output of the SART algorithm and the resulting binarized reconstructed image showing one example of the typical size reduction occurring for the reconstruction of small phantom bubbles (top row) and the slightly increased size of a reconstructed larger bubbles (bottom row).

These phenomena also influence the overall reconstructed mean cross-sectional bubble hold-up as can be seen in Figure 4.28, which shows the ratio between the bubble hold-up of the original phantom images and that of the reconstructed images in dependency of the mean of  $d_{b,ph}$  averaged over all samples. If mostly smaller bubbles  $\leq 2.5$  cm are being reconstructed,  $\varepsilon_{b,ph}$  is reduced through the reconstruction, while it is increased slightly when bubbles that are larger than 2.5 cm are reconstructed.

The complete results of the simulations are shown in Figure 4.29 in form of probability density distributions of the diameters  $d_{b,ph}$  of the original phantom data and their reconstructions for each category of mean bubble diameters and bubble hold-up.

In the figure, the effect of the limited data problem can be seen. Often, the algorithm is not able to correctly reconstruct bubbles when there are too many individual bubbles present in the measurement plane. In those cases, the variance of the distributions increases with the mean typically shifting towards larger bubble sizes, as individual bubbles are merged together through the reconstruction. Therefore, the bubble size distribution for settings with larger bubble hold-ups can only be reconstructed well if the mean diameter implies a small number of individual bubbles. For the mean values of  $d_{b,ph}$ , there is a significant deviation between original images and their reconstructions for settings with bubble hold-ups of  $\varepsilon_{b,ph} \leq 0.3$ . Besides that, the mean diameters of the reconstructions match the original data very well. If the simulation results are compared to the experimentally determined time averaged

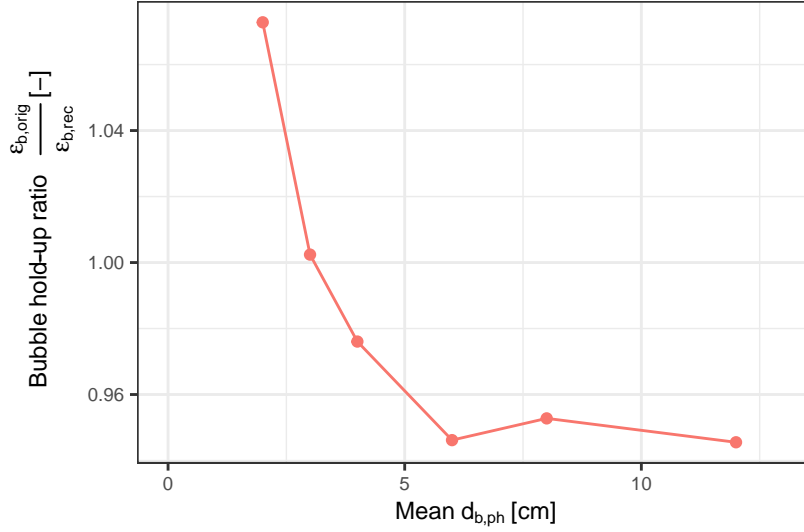


Figure 4.28: Ratio between the hold-up of the original phantom images and that of the reconstructed images in dependency of the mean  $d_{b,ph}$  of the phantom bubbles.

cross-sectional bubble hold-ups and the corresponding mean diameters at the different measurement heights, as presented in Section 4.3.3, than the reconstruction quality can be estimated for each setting. In this way it can be determined that for any measurement heights of 26 cm and above, the bubble size distributions can be reconstructed well, while the height of 16 cm can be rated as a borderline case. For instance, at  $u/u_{mf} = 1.5$  and 2 the measured hold-up is typically below 5%, while the mean bubble sizes are in the range of 2 - 6 cm for all measurement heights  $\geq 16$  cm. It can therefore be assumed that the measured distributions are likely correct for these settings. At  $u/u_{mf} = 3$  and above however, it is likely that the measured distribution at 16 cm is affected more noticeably from the limited data problem. Generally speaking, with lower bubble hold-ups or with higher measurement heights, where bubbles typically are larger and less in number, the quality of the reconstructions increases. Note that the experimentally measured bubble property distributions shown in Figures 4.17, 4.19 and 4.20 in Section 4.3.4 show larger variances at lower measurement heights, which could be explained this way. However, the general trends for the mean values, the variance as well as the correlations between different bubble properties are consistent throughout all shown experimental settings.

#### 4.4.3 Dynamic bubble events

While the method shown in Section 4.4.2 is a suitable tool to analyze the limited data problem for the static case, additional efforts may be necessary to investigate how the highly dynamic situation in a bubbling fluidized bed affects the measurements. Bubbles of different sizes,



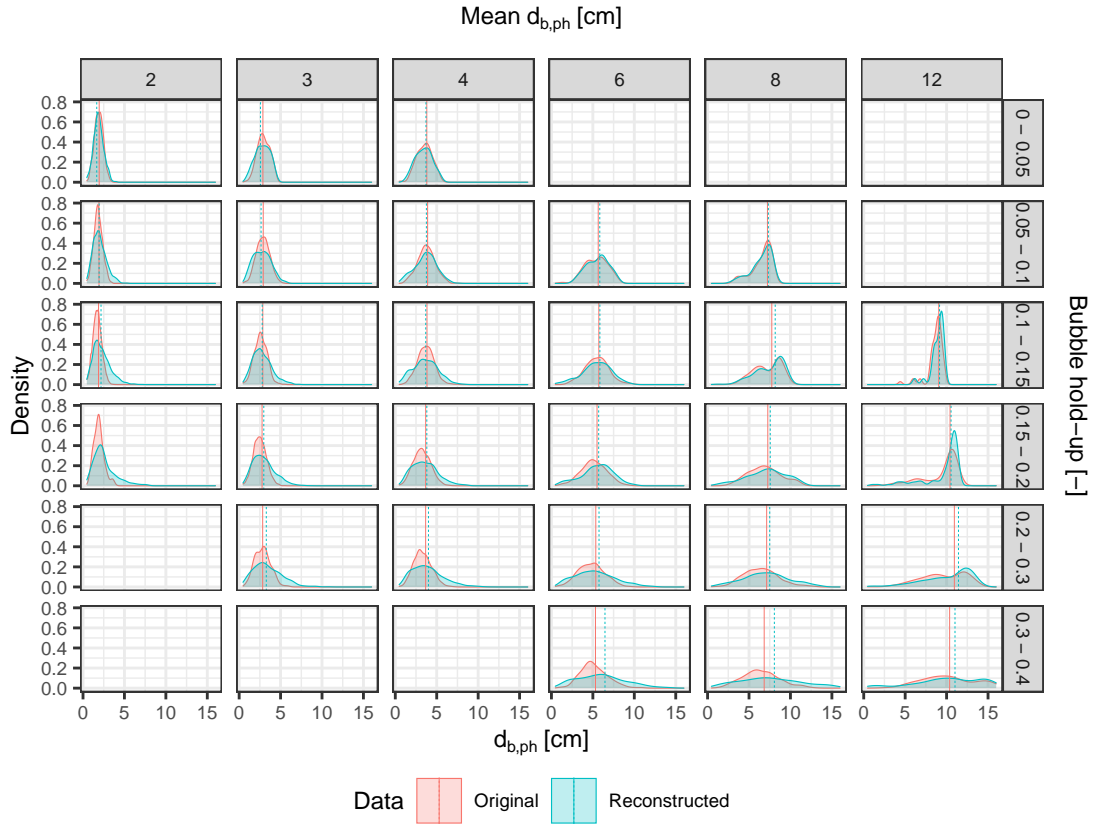


Figure 4.29: Probability density plots showing the comparison between the distributions of original sampled bubble phantoms and their reconstructions for various mean bubble diameters and bubble hold-ups.

with different rise velocities entering and leaving the measurement planes at different times may increase the potential of independent bubbles being connected through an erroneous reconstruction at some point in time. Figure 4.30 shows a case, which is possibly a failed reconstruction due to the alignment between bubbles and detectors. However, in other cases the reconstructions appear to show bubbles that potentially are coalescing while rising through the measurement planes as can possibly be seen in the example shown in Figure 4.31.

Such uncertain and potentially highly dynamic bubble events highlight a drawback of the described reconstruction method and a potential source for false reconstructions, which is the dependency of the vertical bubble dimension on the measured bubble rise velocity. If bubbles change their shape and/or rise velocity during the measurement, which may occur especially during coalescence or breakage events but also due to erroneously merged bubbles as a result of the limited data problem described above, it could lead to a false determination of their rise velocity. Affected bubble events therefore need to be identified and removed from the data set, leaving only the ones that were sufficiently stable and consistent during the measurement.

Settings:  $u/u_{mf} = 3.33$ , height = 26 cm, Bubble ID = 542  
 $u_{br} = 0.56$  m/s,  $r_x = 9.82$  cm,  $r_y = 10.69$  cm,  $r_z = 3.07$  cm

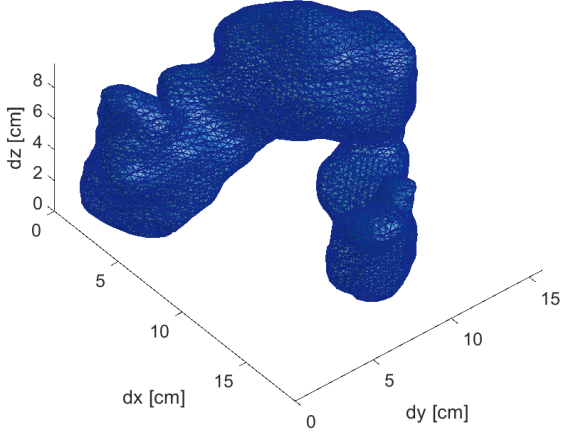


Figure 4.30: Three-dimensional reconstruction of a bubble that is possibly an example of an erroneous reconstruction resulting from the limited data problem.

Settings:  $u/u_{mf} = 3.33$ , height = 26 cm, Bubble ID = 1302  
 $u_{br} = 0.33$  m/s,  $r_x = 2.91$  cm,  $r_y = 7.59$  cm,  $r_z = 3.27$  cm

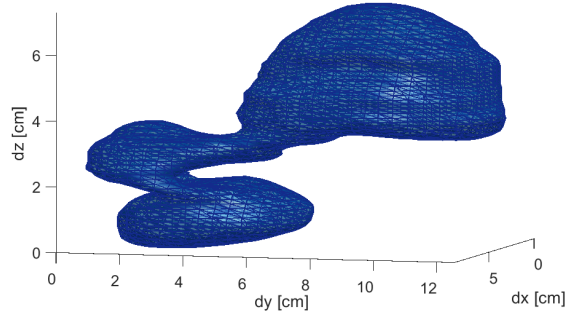


Figure 4.31: Three-dimensional reconstruction that is possibly showing the coalescence of two or three bubbles.

### 4.4.4 Pseudo three-dimensional tomography simulation

One way to investigate parts of the issues described above is to expand the tomography simulation studies by also implementing the time dimension. The *3D-Bubblesampler* algorithm, as it was introduced in Section 4.4.1, was applied to create two sets of phantom data. For this, two three-dimensional matrices containing only zero entries were generated. Note, that the horizontal dimensions of these matrices represent the spatial dimensions of the measurement plane, while the vertical dimension represents the time steps of the measurement. Next, a random sample from a given bubble property distribution is generated, in which the bubble geometry is represented with a binary matrix, where values of one represent the bubble phase. This sub-matrix is then placed at a random vertical position within the matrix representing the lower measurement plane, under the condition that there is no overlap with other bubbles. If the bubble cannot be placed anywhere within 1000 iterations, the next sample is generated. Each bubble that is placed in this way, is also placed in the matrix representing the upper measurement plane corresponding to its rise velocity and assuming no lateral movement and no change of velocity or shape. Bubbles may exhibit a broad range of rise velocities, which can lead to bubbles overlapping in the upper measurement plane.

While this approach certainly falls short to fully capture the highly dynamic situations in fluidized beds, it is useful to verify the ability of the applied pseudo three-dimensional reconstruction methods to distinguish between individual bubbles with various rise velocities and

spatial arrangements. Additionally, the simulations allow to compare the performance of the reconstruction algorithm applying the adaptive threshold, as it was introduced in Section 4.2.3 in comparison to using a fixed threshold as it was previously done. For the results shown in this work, the phantom data was sampled from the fitted distributions presented in Section 4.3.5.

Samples of the original experimental data, the generated phantom data and the corresponding reconstructions with both discussed methods are shown in Figure 4.32 for measurement heights of 26 and 46 cm and fluidization numbers of 2 and 4. The color coding in the following figures is as follows: Blue indicates experimental data, orange indicates phantom data, green indicates reconstructed data that was binarized with an adaptive threshold, while data that was reconstructed with a fixed threshold is shown in purple.

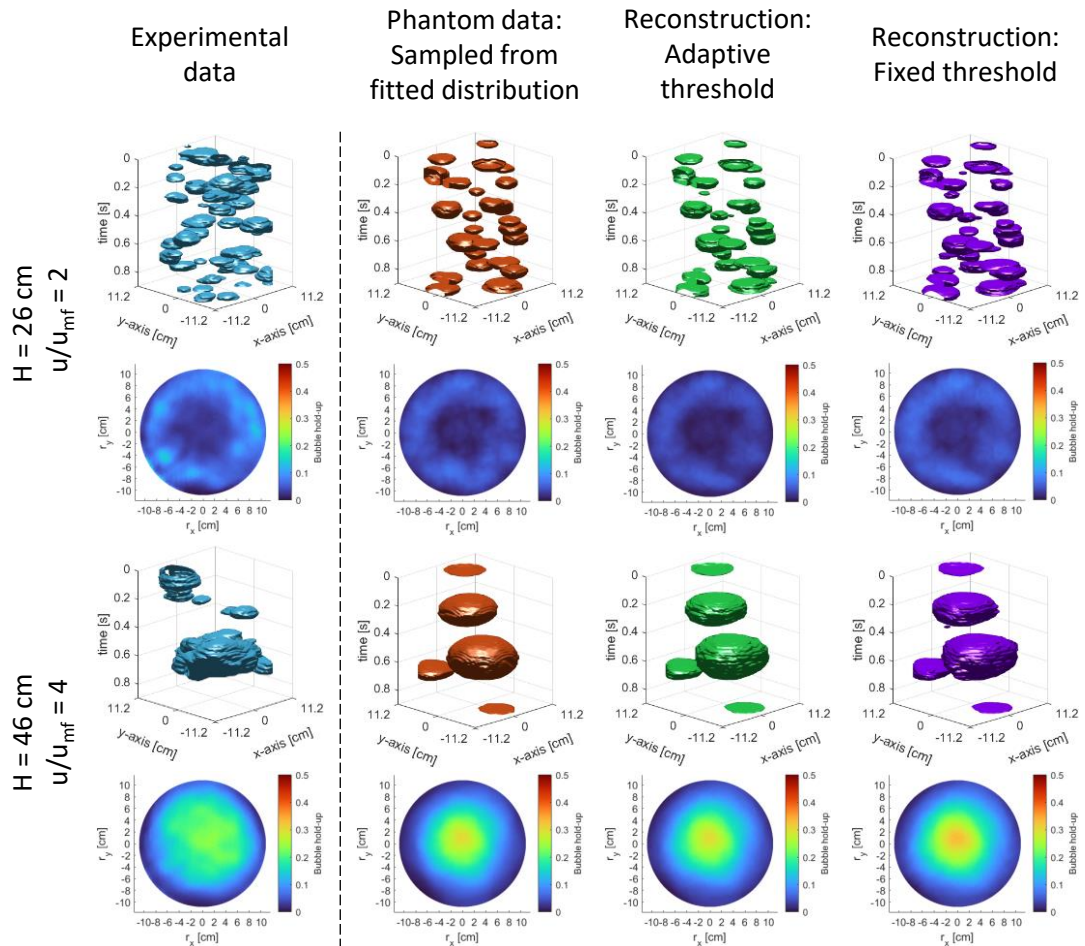


Figure 4.32: Comparison between 0.9 s samples of the pseudo three-dimensional visualizations and the corresponding bubble hold-up data of the experimental data, the used samples from the fitted distributions and the reconstructions of the X-ray tomography simulations for two exemplary experimental settings.

Overall, the reconstructed shapes and the bubble hold-ups agree well with those of the original phantom samples. As expected from the results of the two-dimensional tomography simulations presented in Section 4.4.2, the reconstruction of single large bubbles appears to be more accurate than those that are measured as part of a swarm of bubbles that passes the measurement plane simultaneously. For the latter, some small artifacts were generated, some bubbles appear to have merged, while others were not reconstructed at all. However, these cases do not seem to significantly influence the reconstructed bubble distributions overall. The reconstructions that were binarized with a fixed threshold appear to have a slightly increased rate of generated artifacts and the mean cross-sectional hold-ups are also slightly increased. Furthermore, the pseudo three-dimensional data that was generated from the fitted distributions appears to represent the experimental data well.

To evaluate the applicability of the overall presented tomography methodology, the resulting bubble property distributions of the sampled phantom data and the corresponding reconstructions have to be compared with the original experimental data. Figure 4.33 shows the correlated probability density distributions of the chosen bubble properties and their correlations, as they were suggested in Section 4.3.4.

Generally, the sampled and reconstructed data represent the experimental findings very well. The differences resulting from the individual experimental settings far exceed the comparatively small differences between experimental data, sampled phantom data and the corresponding reconstructions for a given setting. There is a slight difference between the experimental data and the sampled phantom data, with the distributions of the latter showing marginally broader variances. However, it is more important to note that the reconstructed distributions accurately represent their ground truth, that being the phantom data, especially when the adaptive threshold was applied. One difference between the different data sets is the distribution of the aspect ratio. The aspect ratios of the phantom samples are more likely to be oblate in comparison to the experimental data and the corresponding reconstructions tend to be even more flattened. Some of these deviations between the experimental data and the phantom data may be explained by the way the pseudo three-dimensional representations were generated. For example, if a fast bubble, which tends to be elongated, gets merged with a slow bubble, which tends to be oblate, then the impact of the fast bubble, which counter-intuitively is relatively flattened in the pseudo three-dimensional representation, on the properties of the newly formed bubble is insignificant in comparison to that of the oblate slow bubble, which exists far longer in the measurement plane as it is elongated in the time dimension. Since the velocity of the bubble is determined by the time of flight of its center of weight, it will be much closer to the value of the slow bubble, due to its comparatively large pseudo three-dimensional volume.

#### 4.4 Verification of the applied X-ray tomography methods

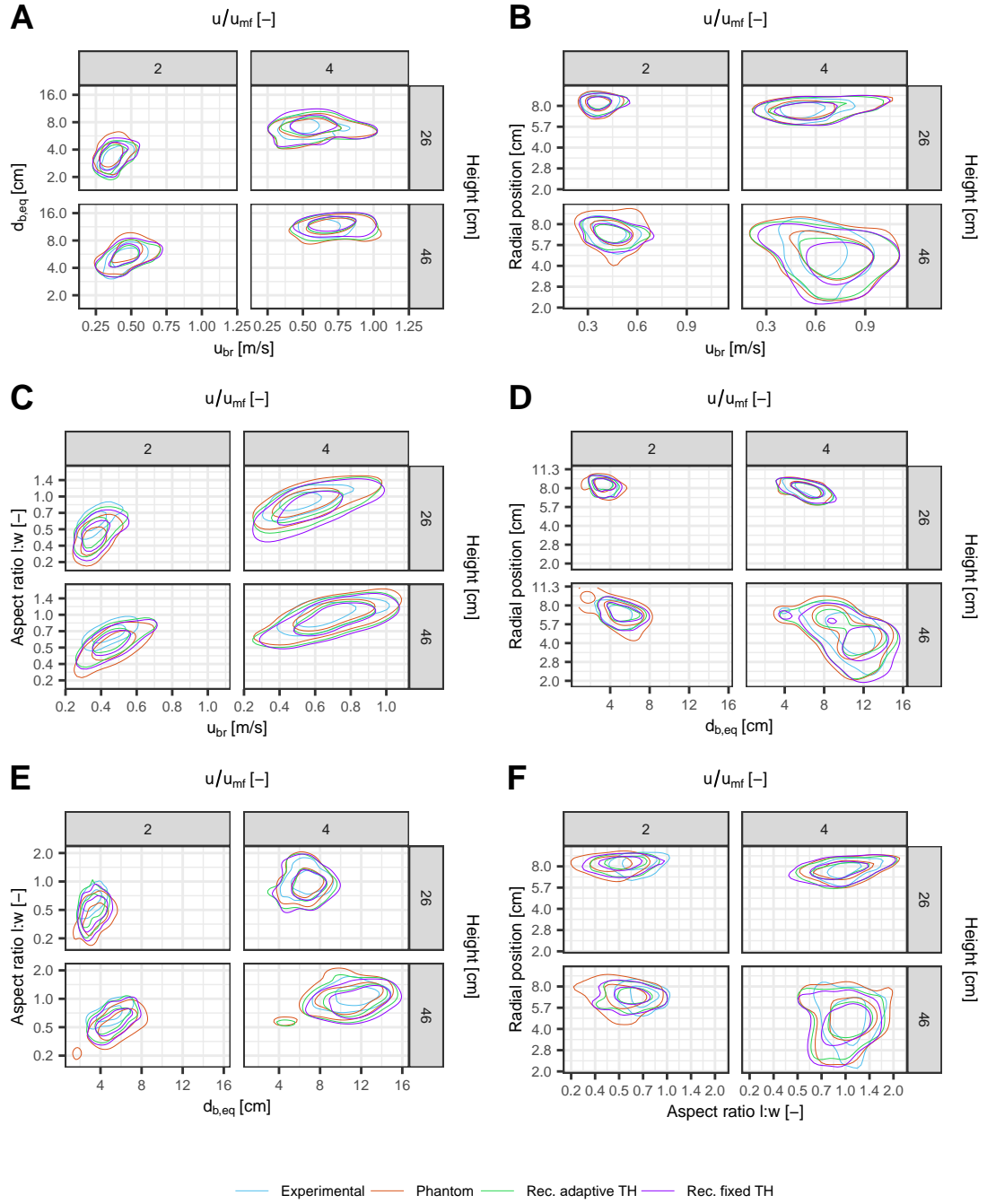


Figure 4.33: Probability density contour plots comparing the experimental data with the sampled data from distribution functions that were fitted to the experimental data and their simulated tomographic reconstructions where a fixed threshold and a adaptive threshold were used.

This would explain the slightly increased percentage of oblate bubbles for the phantom data and more so for the reconstructions as bubbles that are close to each other are more likely to get merged through the reconstruction.

### 4.4.5 Post processing of the X-ray tomography measurements

Two filtering methods were applied in this work to account for the identified limitations of the experimental methods. First, the three different definitions of the rise velocity, as they were described in 4.2.3 were compared. Any bubble for which the difference between any of the three velocity definitions exceeded more than 30% were removed from the results. For the second filter, the ratio  $V_{b,max}/V_{b,min}$  between the larger and the smaller reconstructed bubble volume between the upper and lower measurement planes, as it was introduced in Section 4.2.3, were compared. Figure 4.34 shows the median of  $V_{b,max}/V_{b,min}$  for all experimental settings.

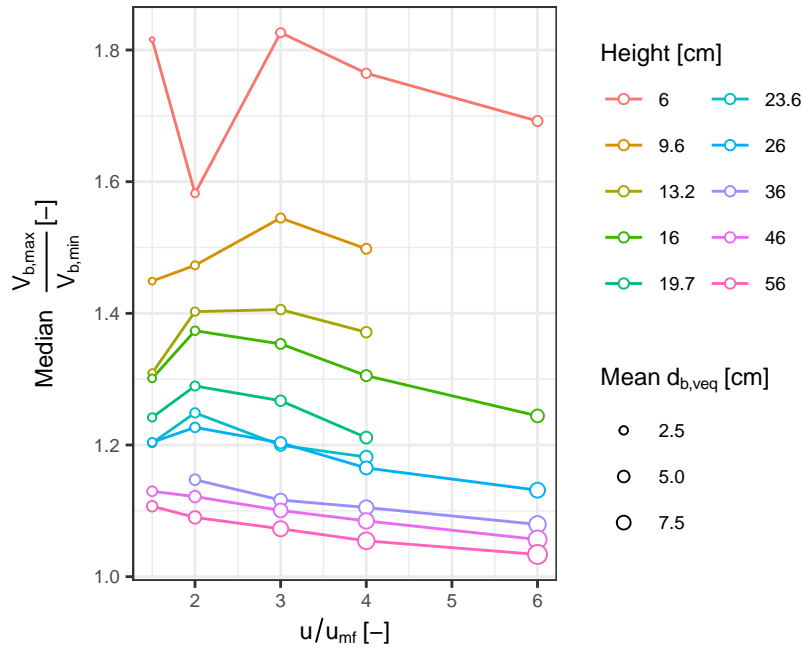


Figure 4.34: Median of the ratio of reconstructed bubble volumes  $V_{b,max}/V_{b,min}$  for all experimental settings.

The data indicates that the problem occurs more at lower heights and lower values of  $u_{mf}$ . Small values for  $V_{b,max}/V_{b,min}$  will always occur due to the dynamic behavior of the bubbles, which may result in shape transformations or a change of the rise velocity during the measurement. However, larger values for  $V_{b,max}/V_{b,min}$  are more likely to represent erroneous reconstructions. It was decided that bubbles for which the reconstructed bubble volumes differed by more than 100% between the two measurement planes were removed from the

data set. This may appear to be a rather generous threshold but one has to consider that a doubling of the volume only leads to a 26% increase of the equivalent diameter  $d_{b,eq}$ . The potential error is also further halved by using the average volume between the lower and upper measurement plane for the calculation of  $d_{b,eq}$ . Additionally, this filter method mostly affects the lower spectrum of the measured bubble sizes with equivalent diameters in the range of two to three cm, for which the accuracy of the experimental setup and the described tomography reconstruction methods is known to be limited anyway, independent of the bubble dynamics.

It is challenging to determine the threshold values for the proposed filters systematically, as it remains unclear how to automatically estimate the goodness of reconstructions, which would be necessary given the several ten thousand bubbles that were reconstructed and evaluated. Additionally, it has to be avoided that such filtering leads to biased results. Ultimately, the filtering thresholds were selected through manual examination of randomly sampled pseudo three-dimensional reconstructions, which were filtered as a result of systematically step wise adjusted threshold values. To assess the effect of the filtering on the resulting bubble property distributions, the unfiltered data needs to be compared with the distributions resulting from different filtering thresholds. Figure 4.35 shows the resulting probability density distributions for two different filter settings. Filter 1 corresponds to the thresholds described above, while Filter 2 is set with more drastic values. Here, any bubbles for which the rise velocity definitions differ by more than 10% or the ratio  $V_{b,max}/V_{b,min}$  exceeds the value 1.25 are excluded. The unfiltered data set consists of 38,481 bubbles for the chosen measurement heights. Filter 1 reduces the number of bubbles to 26,675 and Filter 2 only leaves 12,864 bubbles. While Filter 2 removes roughly two thirds of bubbles, the resulting distributions do not change significantly. As expected, small bubbles are affected more often. It was therefore concluded that while it is necessary to filter the data to remove the impact of significantly erroneous reconstructions, it is not useful to drastically reduce the database by further filtering.

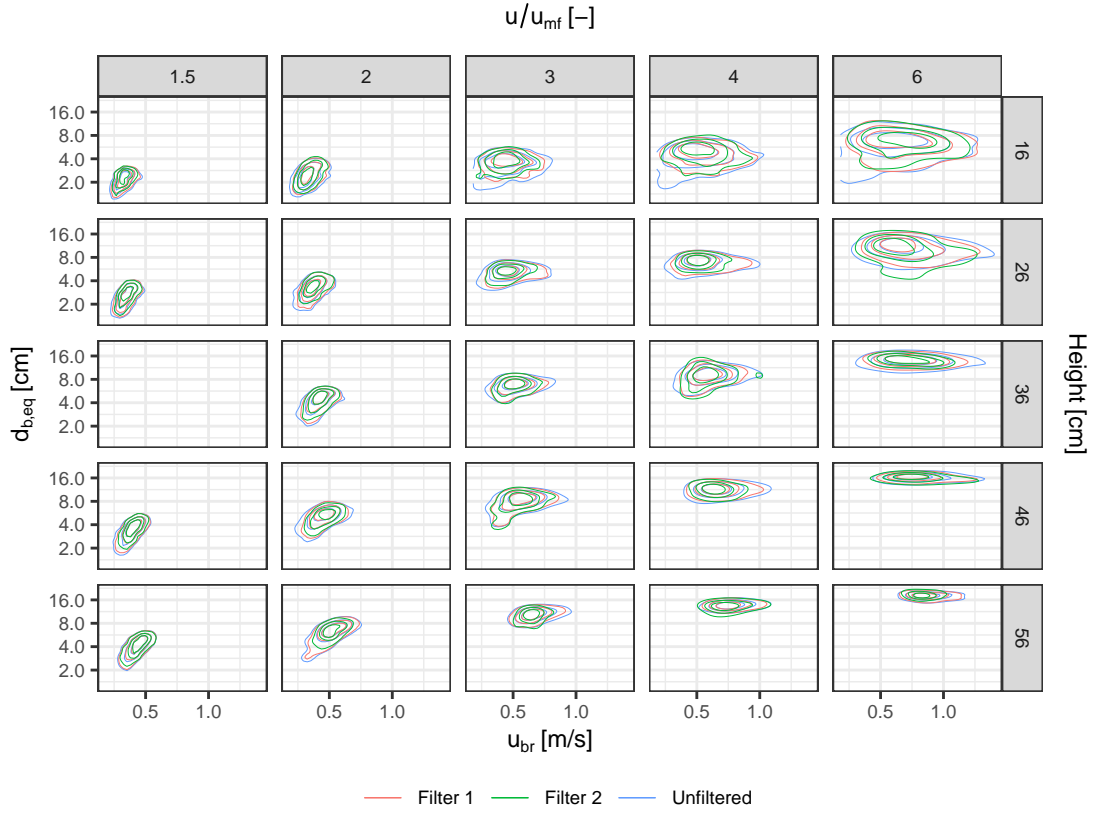


Figure 4.35: Comparison of the impact of different filter settings for the X-ray tomography data without internals.

## 4.5 Results of X-ray tomography measurements with vertical internals

After the X-ray tomography methods have been established and the limitations of the methods have been identified, in the following section the results of the measurements including vertical internals are compared to the case without internals. The implementation of the vertical internals may present additional challenges for the tomographic reconstructions, as it could be shown in Section 4.4.2 that the SART algorithm is less accurate if many small bubbles are present in the measurement plane. Considering the presence of vertical internals, it is to be expected that bubble interactions are more restricted leading to less coalescence and thus smaller bubble sizes on average as well as to more complex shapes of the individual bubbles around the internals. Additionally, the attenuation of the X-rays through the bed cannot be considered to be linear anymore, given that the density of the bed is not homogenous due to the presence of vertical Perspex<sup>®</sup> internals that are filled with packed bed material. Maurer [70] suggested a mathematically derived correction factor, as shown in Equation 4.4, to account for the presence of vertical internals under the assumption, that difference



#### 4.5 Results of X-ray tomography measurements with vertical internals

in densities between the bed and the internals filled with particles is small. Alternatively, the measurements with vertical internals could have been calibrated by the seven-point calibration method presented in Section 4.2.1, which would have required considerable efforts given the irregular circular arrangement of the internals. The SART algorithm has also been expanded for the reconstruction of measurements with vertical internals in the work of Maurer. By implementing a constraint that the solid fraction at pixels where internals are present are set to a value representing the dense phase in each iteration step, it would be assured that no bubble hold-up would be assigned at the positions of the vertical internals. However, the evaluation of the data showed that this often did not work as intended. While the local bubble hold-up would be reduced significantly at the designated positions of the internals, it still was not zero and the bubble phase could be assigned to these positions through the binarization. To overcome this, the positions of the internals were additionally accounted for during the pseudo three-dimensional reconstruction procedure. In previous works, any bubble hold-up that was located at a designated position of an internal was removed from the binarized image. Considering the fact that about 30 % of the cross-section of the bed consists of internals, this would lead to a significant reduction of the bubble hold-up and individual bubble sizes. For the present work, the positions of the internals were accounted for prior to the binarization step. The images were then binarized with an adaptive threshold, as it is described in detail in Section 4.2.3, which maintained the originally measured bubble hold-up. The problem can be seen in Figure 4.36, where two individual reconstructions of the measurements with internals at a height of 36 cm and  $u/u_{mf} = 3$  are shown.

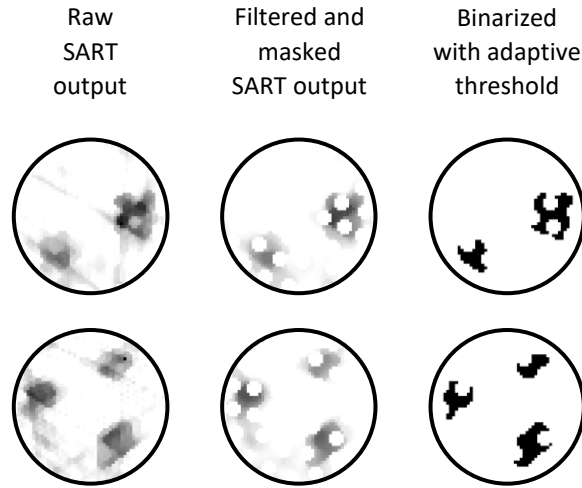


Figure 4.36: Samples of binarization procedure of tomographic reconstructions of X-ray measurements with Internals at a  $H = 36$  cm and  $u/u_{mf} = 3$ .

In the top row of the figure, bubble formations that appear to be wrapped around several internals can be seen. Here, the implementation of the internals seems to work reasonably

well, though theoretically it is possible that several individual small bubbles have been reconstructed as single bubbles. The bottom row shows a case, where the internals were located at locations, which the SART reconstruction had assigned to the bubble phase. Regarding the limitations of the applied X-ray tomography methodology, as they were established in Sections 4.4.2 and 4.4.4, it becomes clear that the spatial resolution of the setup is not sufficient to distinguish between clusters of individual small bubbles rising in close proximity to one another in between the internals and large single bubbles that are wrapped around the internals. In case these bubble formations were clusters of small bubbles, it is likely that their individual volumes communicate and are somewhat connected, as they rise in a compact formation with the same rise velocity. However, considering that such clusters of small bubbles would have significantly larger surface areas, which could influence mass transfer rates in comparison to individual single bubbles representing the same volume, underlines the necessity to further investigate the issue. For the mass transfer, one also has to account for the fraction of the bubble surfaces that are in direct contact with the internals and therefore are not available for mass exchange with the dense phase. The problem of the limited spatial resolution and viewing angles becomes more obvious for higher gas velocities as can be seen in Figure 4.37, where two reconstructions of the measurements at a height of 36 cm and  $u/u_{mf} = 6$  are shown. Here, the broadly distributed gray-scale values produced by the SART algorithm indicate a reduced certainty of the exact spatial distribution of the bubble hold-up, which ends up being assigned to the most probable areas that include positions where internals would be present.

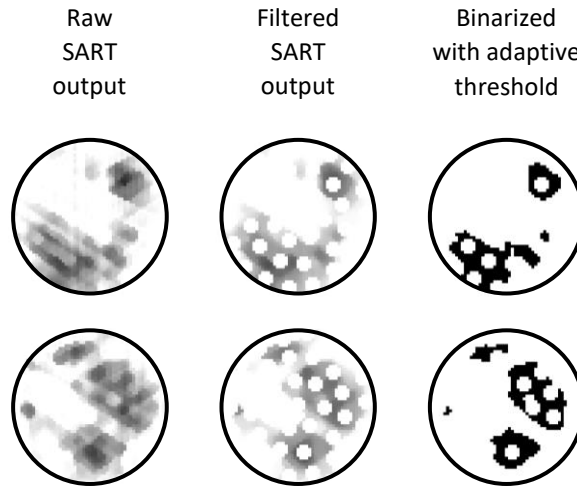


Figure 4.37: Samples of binarization procedure of tomographic reconstructions of X-ray measurements with Internals at a  $H = 36$  cm and  $u/u_{mf} = 6$ .

In general, the bubble size distributions that were reconstructed with inserted internals show significantly smaller values of  $d_{b,eq}$  in comparison to the measurements without internals. Given the fact, that the reconstruction of small bubbles is less accurate and more likely to

be impacted by artifacts and considering the impact of the internals mentioned above, a reduced reliability of the measurements with internals must be assumed and an independent verification of the results is necessary. For the interpretation of the results presented in the following, the mentioned concerns have to be considered.

### 4.5.1 Cross-sectional bubble hold-up

In Section 4.3.1 it was established that the XR-LD setup is able to measure the cross-sectional bubble hold-up well, with slightly smaller values than what was estimated from the measurement of the bed expansion. A small overprediction was observed for the reconstruction of large individual bubbles, whereas small bubbles would be reduced in size through the reconstruction which lead to reduced values of  $\varepsilon_b$ . In Figure 4.38, a comparison between the measured cross-sectional bubble hold-up averaged over all measurement heights for the case with and without internals is shown. It can be seen that a considerably smaller hold-up was measured when internals were present. Analogous to the measurements without internals, the bubble hold-up was additionally estimated via the measurement of the bed expansion. Note, that the measurement of the expanded bed height with internals must be regarded as an estimate, because at lower fluidization numbers the bed height was not very uniform and therefore the margin for error is increased for relatively small increases of the bed height. Overall, the measured bed expansion is slightly higher than the X-ray measurements of the bubble hold-up in both cases with and without internals.

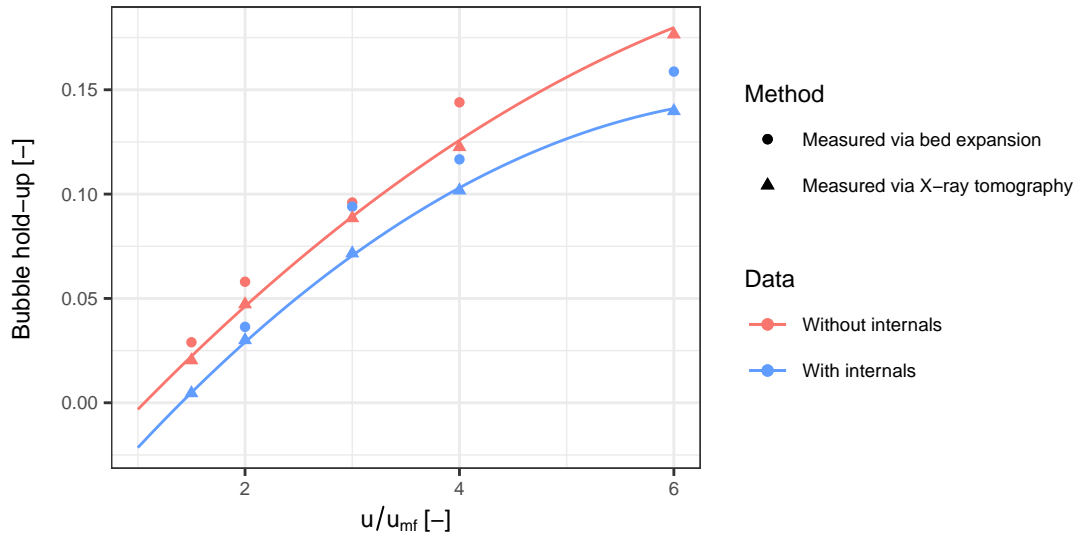


Figure 4.38: Comparison of the cross-sectional bubble hold-up  $\varepsilon_b$  measured with two independent experimental methods, X-ray tomography and measurement of the expanded bed height, for the cases with and without vertical internals.

It is known that the measured mean bubble rise velocities decrease when internals are present in comparison to the measured values without internals [133]. This could also be verified in the analysis of the data for the present work shown in Section 4.5.3 and was additionally confirmed by independent single bubble experiments presented in Section 4.5. Reduced rise velocities usually indicate that the hold-up should increase due to the longer dwell times of the bubbles. It is therefore surprising that the overall bubble hold-up was reduced through the presence of internals, which suggests that more gas flows through the dense phase than in the case without internals. Potentially this can be explained by the considerably larger wall surface area that the fluidized bed is in contact with, which may stabilize the bed resulting in an increase of minimum bubbling velocity  $u_{mb}$  as it was confirmed in numerous measurements that the minimum fluidization velocity  $u_{mf}$  is not affected by the presence of internals.

### 4.5.2 Pseudo three-dimensional visualizations

Figure 4.39 shows a comparison between the tomographic reconstruction of a 3.2 s sample without internals on the left side and with internals on the right side for a measurement height of 26 cm and a fluidization number of 3. The internals are not shown but their impact on the bubble sizes and their shapes is visible. It can be seen that the presence of internals leads to a significant reduction of the bubble sizes in comparison to the case without internals.

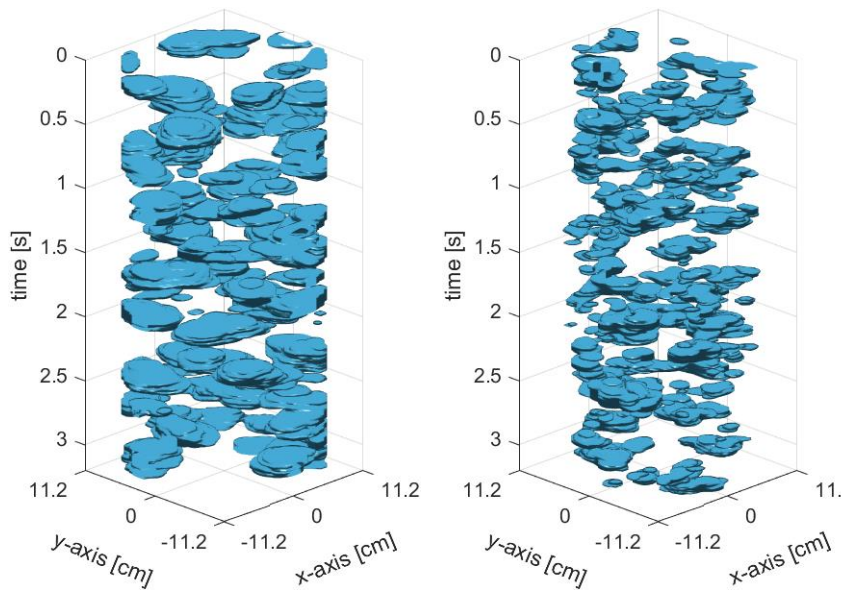


Figure 4.39: 3.2 s sample of reconstructed bubbles that were measured at a measurement height of 26 cm and a fluidization number of  $u/u_{mf} = 3$ . The left image shows the case without internals and the right the case with vertical internals present.

#### 4.5 Results of X-ray tomography measurements with vertical internals

---

Figures 4.40 and 4.41 show comparisons of 0.9 s samples of reconstructed data and their corresponding time averaged cross sectional bubble hold-ups for the measurements with and without internals for two fluidization numbers and three measurement heights. Analogous to the observation described above, the presence of internals leads to a reduction of the bubble hold-up and of the bubble size. The shape of the bubbles appear more irregular with internals. The positions of the internals are easy to recognize in the time averaged visualizations of  $\varepsilon_b$ , which show similar patterns to those measured without internals. Areas with increased hydraulic diameters, as defined by Equation 2.37, appear to show increased local bubble hold-ups in comparison to areas, where the spacing between the internals or between the internals and the wall is smaller. The presence of internals seems to restrict the movement of bubbles towards the center of the column with increasing heights and fluidization numbers.

In Figure 4.42 the evolution of the cross-sectional hold-up for a measurement height of 56 cm and all investigated gas velocities is shown for the measurements without internals (row A) and with internals (rows B and C). For the measurements with internals, two cases of the binarized SART output are shown. For the images shown in row B the positions of the internals were not masked prior to the binarization, whereas row C shows images that were binarized after accounting for the positions of the internals under the constraint to maintain the overall bubble hold-up resulting in a increase of the bubble hold-up between the internals. While the hold-up is more gradually distributed for the case without internals, more abrupt transitions between regions of high and low local bubble hold-ups can be seen for the case with internals. This may imply, that the internals restrict the lateral movement of the bubbles or reduce their tendencies to coalesce in lateral direction, and that the bubbles are more likely to move in preferential vertical leading to a reduction of the overall coalescence rate.

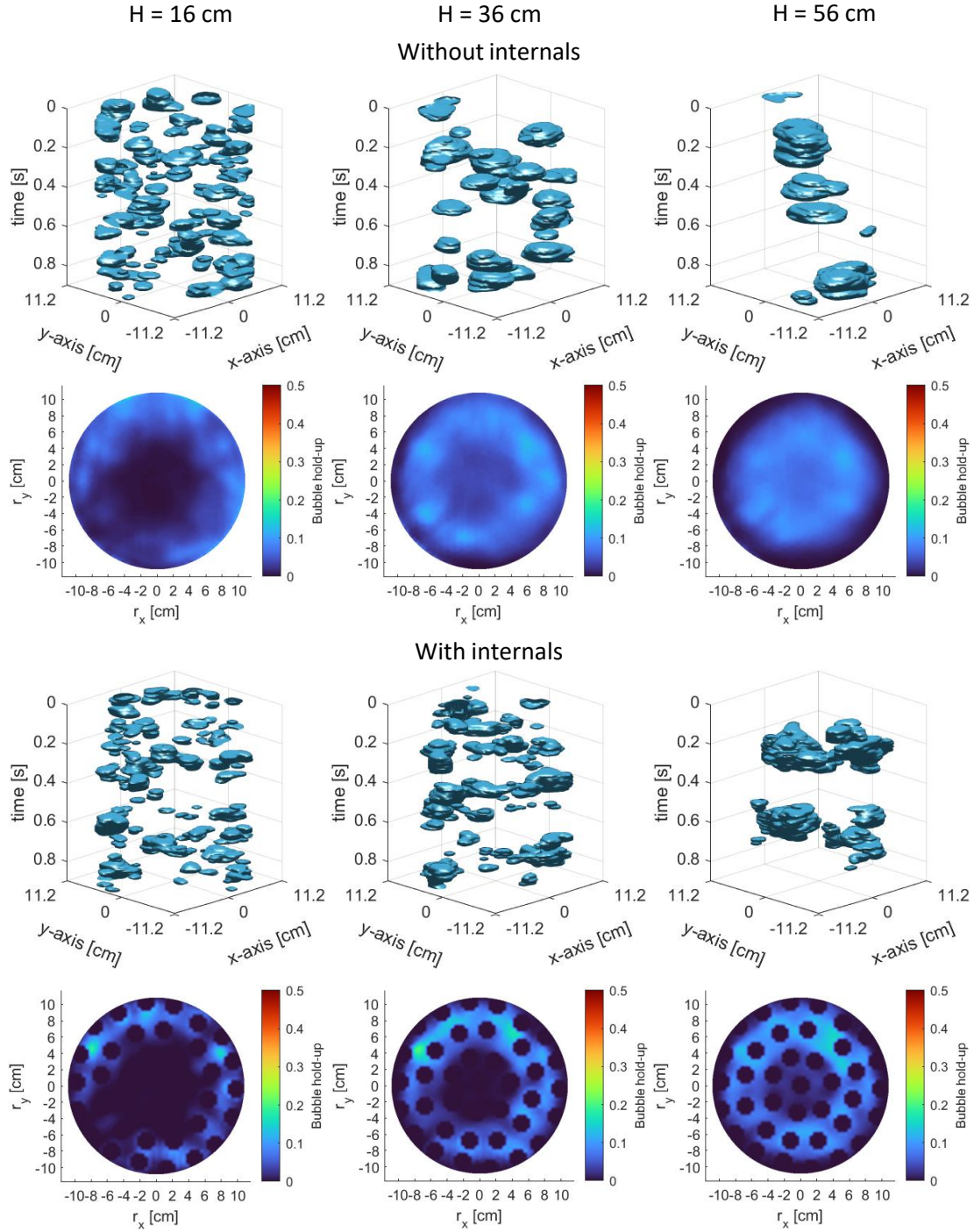


Figure 4.40: Comparison of samples of the pseudo three-dimensional reconstructions and the spatial distribution of the respective bubble hold-up for the measurement heights of 16, 36 and 56 cm at a fluidization number  $u/u_{mf} = 2$ .

## 4.5 Results of X-ray tomography measurements with vertical internals

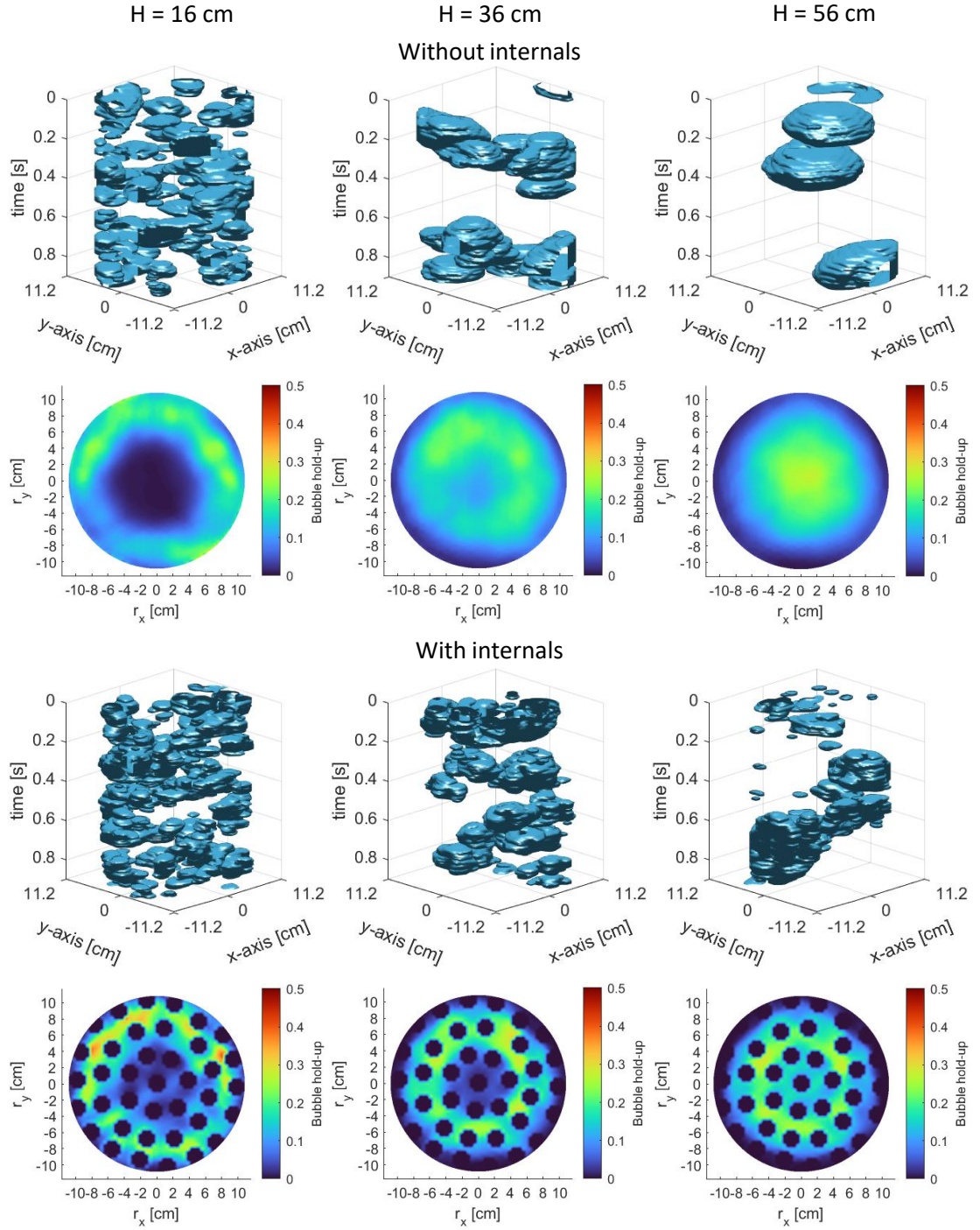


Figure 4.41: Comparison of samples of the pseudo three-dimensional reconstructions and the spatial distribution of the respective bubble hold-up for the measurement heights of 16, 36 and 56 cm at a fluidization number  $u/u_{mf} = 4$ .



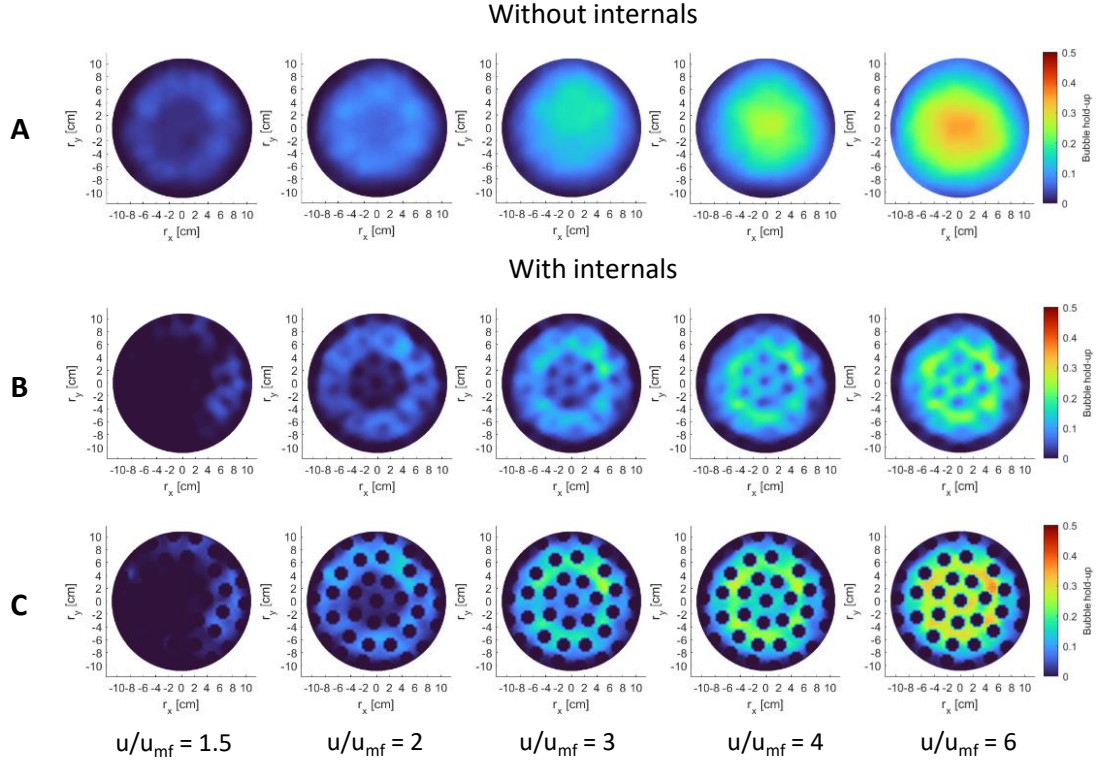


Figure 4.42: Comparison of the evolution of the bubble hold-up measured with (B,C) and without internals (A), for increasing values of  $u/u_{mf}$  at a measurement height of 56 cm. For the images shown in row B, the positions of the internals were not masked prior to the binarization, whereas row C shows images that were binarized after accounting for the positions of the internals under the constraint to maintain the overall bubble hold-up.

#### 4.5.3 Statistical evaluation of the measured bubble properties

A total of 28,494 bubbles were reconstructed from the measurements with internals, which is about 25% less than the 38,481 that were reconstructed for the same experimental settings without internals. After the filtering of the data according to the methods described in 4.4.5, there are 13,858 bubbles left, which is about 50% of the original data. The summary statistics are formatted analogous to those presented in Table 4.2 in Section 4.3.3 and are shown in Table 4.3. No bubbles were reconstructed for the measurement at a height of 16 cm and  $u/u_{mf} = 1.5$ , and only five bubbles were reconstructed for the measurement height of 26 cm and the same fluidization number, which can therefore not be considered statistically representative and are consequently excluded from the results.



## 4.5 Results of X-ray tomography measurements with vertical internals

H [cm]	$u/u_{mf}$ [-]	$\varepsilon_b$ [-]	Mean ( $d_{b,eq}$ ) [cm]	RSD ( $d_{b,eq}$ ) [-]	RSE ( $d_{b,eq}$ ) [-]	Mean $\frac{V_{b,max}}{V_{b,min}}$ [-]	Mean ( $u_{br}$ ) [m/s]	RSD ( $u_{br}$ ) [-]	RSE ( $u_{br}$ ) [-]	Mean ( $l:w$ ) [-]	RSD ( $l:w$ ) [-]	RSE ( $l:w$ ) [-]	Mean ( $a_b$ ) [ $m^2/m^3$ ]	RSD ( $a_b$ ) [-]	RSE ( $a_b$ ) [-]	n [-]
16	2	1%	1.88	25%	1%	1.39	0.30	33%	1%	0.77	42%	2%	4.78	32%	1%	725
16	3	4%	2.62	32%	1%	1.36	0.37	43%	1%	1.07	51%	1%	3.52	26%	1%	1619
16	4	7%	3.29	37%	1%	1.33	0.44	47%	1%	1.26	53%	2%	2.98	22%	1%	1097
16	6	11%	4.07	46%	2%	1.33	0.60	56%	3%	1.61	59%	3%	2.48	21%	1%	491
26	2	1%	2.29	30%	2%	1.44	0.37	49%	3%	0.93	56%	3%	3.77	29%	2%	345
26	3	4%	3.35	34%	1%	1.43	0.51	57%	2%	1.33	60%	3%	2.81	24%	1%	530
26	4	6%	4.25	38%	2%	1.44	0.64	54%	3%	1.64	58%	3%	2.36	22%	1%	433
26	6	9%	5.14	42%	3%	1.42	0.78	57%	4%	1.98	61%	4%	2.04	23%	1%	246
36	1.5	0%	2.10	23%	2%	1.37	0.28	22%	2%	0.56	32%	2%	4.29	23%	2%	214
36	2	3%	2.85	31%	1%	1.31	0.34	37%	1%	0.87	40%	1%	3.25	23%	1%	1228
36	3	6%	4.07	36%	1%	1.27	0.49	47%	2%	1.19	46%	1%	2.47	21%	1%	929
36	4	7%	4.85	39%	1%	1.27	0.62	50%	2%	1.48	51%	2%	2.15	20%	1%	694
36	6	10%	5.82	48%	2%	1.22	0.79	51%	3%	1.83	56%	3%	1.79	24%	1%	366
46	1.5	0%	2.38	25%	2%	1.32	0.30	34%	2%	0.73	38%	2%	3.75	23%	1%	263
46	2	3%	3.25	32%	1%	1.27	0.36	38%	1%	0.89	41%	1%	2.96	21%	1%	1044
46	3	6%	4.76	39%	1%	1.24	0.54	50%	2%	1.25	51%	2%	2.15	22%	1%	687
46	4	8%	5.77	43%	2%	1.22	0.64	50%	2%	1.45	52%	2%	1.86	22%	1%	514
46	6	10%	6.82	51%	3%	1.24	0.80	51%	3%	1.81	56%	3%	1.62	23%	1%	291
56	1.5	1%	2.50	29%	2%	1.34	0.27	36%	2%	0.68	41%	2%	3.68	23%	1%	324
56	2	3%	3.48	37%	1%	1.27	0.35	43%	1%	0.85	42%	1%	2.79	23%	1%	814
56	3	6%	5.12	42%	2%	1.22	0.51	56%	3%	1.23	59%	3%	2.07	23%	1%	467
56	4	8%	6.28	45%	2%	1.23	0.65	51%	3%	1.49	52%	3%	1.75	22%	1%	355
56	6	10%	8.40	46%	3%	1.19	0.79	45%	3%	1.87	51%	4%	1.50	19%	1%	177

Table 4.3: Statistical summary of chosen bubble properties for the measurement heights of 16, 26, 36, 46 and 56 and fluidization numbers of 1.5, 2, 3, 4 and 6 with internals present.

The measured rise velocities with internals present are reasonably well described by the correlation by Davidson & Harrison [143], given in Equation 2.25. This can be seen in Figure 4.43, which shows the probability density of  $u_{br}$  and  $d_{b,eq}$  of all evaluated bubbles independent from the fluidization number or the measurement height. For the measurements with internals, there is a shift towards slower velocities, especially for smaller bubbles, in comparison to the correlation by Davidson & Harrison and the data measured without internals.

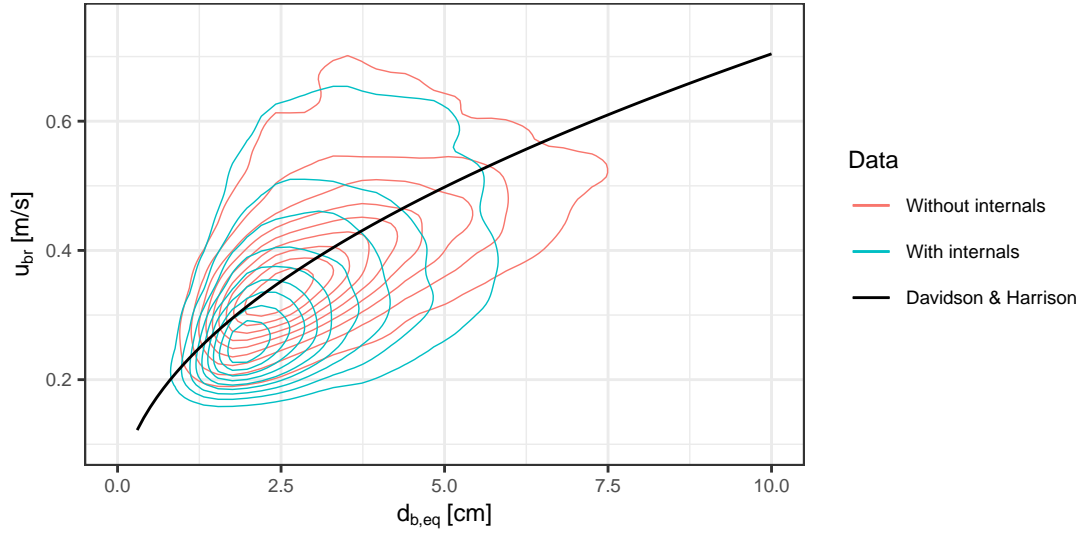


Figure 4.43: Comparison between experimental data measured via X-ray tomography with and without internals and the correlation by Davidson & Harrison [143] for the correlation between the size and rise velocity of bubbles.

A notable difference in comparison to the measured data without vertical internals is the significant reduction of bubble sizes, as shown in Figure 4.44. The gradients of the bubble sizes in dependency of the fluidization number is similar to those measured without internals for fluidization numbers of up to 4. From there on, the gradients appear less steep. It is possible that the internals reduce the degree of freedom for the lateral movement of the individual bubbles and with that, their likelihood to coalesce with other bubbles would decrease as well. The arrangement of the internals could lead to preferential pathways for the bubbles in areas, where the spacing between the internals is wider than in others. This could result in less friction between the wall and the dense phase and facilitate the fluidization locally. One also has to consider the tube spacers that were installed at two heights inside the fluidized bed, as shown in Section 3.3, which may split bubbles and thus the mean bubble diameter decreases. This was observed to occur during the single bubble measurements presented in Section 4.5. Note, that the shown position of the tube spacers in Figure 3.6 does not necessarily represent the configuration used in the experiments evaluated in this section, since the tube bundle fixation was overhauled since then and the original state was unfortunately not documented.

#### 4.5 Results of X-ray tomography measurements with vertical internals

It is also possible that the quality of the reconstructions is affected by the presence of the internals and the corresponding heterogeneous density distribution within the bed. There could be pathways between X-ray source and detector, where the density deviates significantly from what it would be without internals. In that case, it could be that single bubbles are reconstructed as multiple individual ones when parts of it are not recognized. A similar effect could occur through the placement of the internals after the tomographic reconstruction, which may separate individual bubbles into multiple ones. However, the magnitude of the difference in the mean bubble size measured with and without internals is significant and the visualizations presented in Figures 4.40 and 4.41 show clearly distinguishable bubble shapes, which on average are smaller than those measured without internals, especially considering the volume that is occupied by internals. The impact of erroneous or corrupted reconstructions is therefore assumed to not be significant and unlikely to explain the reduced bubble sizes.

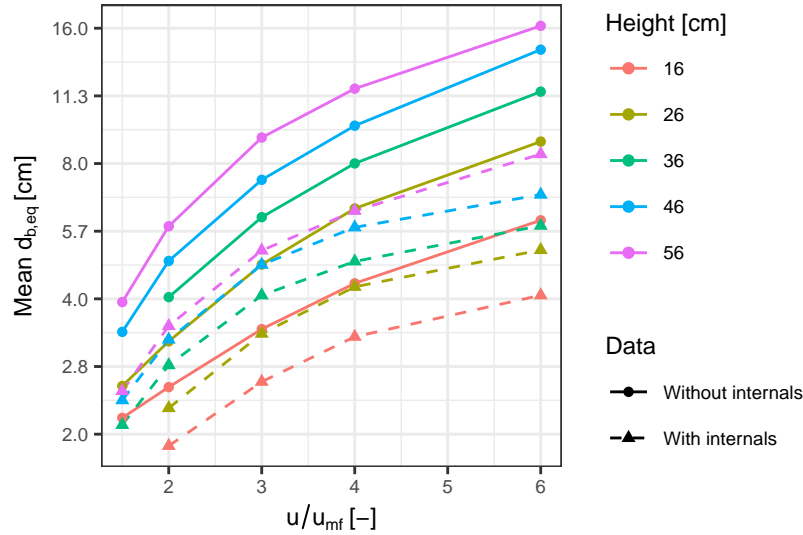


Figure 4.44: Comparison between the mean values of volume-equivalent bubble diameters as they were measured via X-ray tomography with and without internals.

The mean rise velocities of the bubbles are also significantly lower than those measured without internals as shown in Figure 4.45. Interestingly, the rise velocities at measurement height of 16 cm are substantially lower than those at all other measurement heights, which show very little variance for each fluidization number. In general, the gradients of the mean values of  $u_{br}$  in relation to  $u/u_{mf}$  appear to be very similar to those from the measurements without internals. The rise velocities at heights between 26 and 56 cm with internals are in between those measured at heights between 16 and 26 cm without internals. This aligns well with the measured bubble diameters at the respective heights with and without internals, as shown in Figure 4.44, which can be seen as an additional indication for the correctness of the

reconstructed bubble sizes, given the correlation between the size and the rise velocity of a bubble.

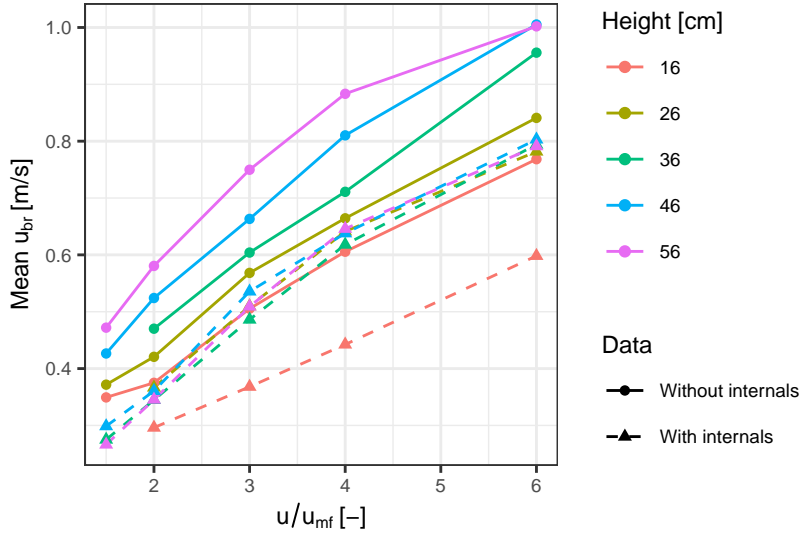


Figure 4.45: Comparison between the mean values of bubble rise velocities as they were measured via X-ray tomography with and without internals.

In Figure 4.46, the comparison of the aspect ratios measured with and without internals can be seen. Generally, the bubble shapes are more elongated when internals are present with similar gradients in relation to  $u/u_{mf}$ . Interestingly, the bubbles measured with internals at a height of 26 cm are more elongated on average than those measured at higher heights for most gas velocities, which is a deviation of the trend of the measurements without internals. For all heights  $\geq 36$  cm the mean aspect ratio appear to not change for a given value of  $u/u_{mf}$ .

### 4.5.4 Bubble property distributions and their correlations

The comparison of the mean values of the bubble properties measured with and without internals clearly demonstrates the significant influence the internals have on the hydrodynamics of the BFB. However, as elaborated in Section 4.3.4, mean values alone may not be sufficient for the description of the hydrodynamics within the catalytic BFB reactors. Broad variances of rise velocities and bubble sizes may impose mass transfer restrictions that potentially could not be determined from the respective mean values. For the scope of this work, in consideration of the optical probe measurements in the pilot plant GanyMeth presented in Section 5.3, a special focus was put on the accurate description of the bubble property distributions and their correlations, especially concerning the bubble shapes.

In Figure 4.47 the correlated density distributions of the volume-equivalent diameters  $d_{b,eq}$  and the bubble rise velocities  $u_{br}$  measured with and without internals are shown for each

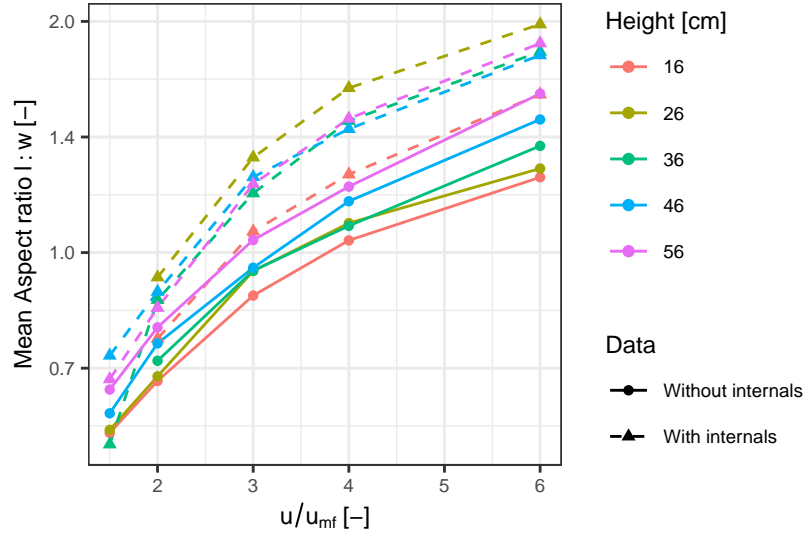


Figure 4.46: Comparison between the mean values of bubble aspect ratios as they were measured via X-ray tomography with and without internals.

combination of  $u/u_{mf}$  and the measurement height. It can be seen that in all cases the maximum diameters of the bubbles measured with internals are below the maxima of those measured without internals. The distributions measured with internals at higher heights and fluidization numbers are also much broader in comparison to those measured without internals. At most heights, a significant fraction of the bubbles measured with internals have volume-equivalent diameters in the range of 2 - 4 cm, whereas the measurements without internals show much more narrow size distributions for  $u/u_{mf} \geq 3$ . A clear correlation between  $d_{b,eq}$  and  $u_{br}$  can be seen for both data sets.

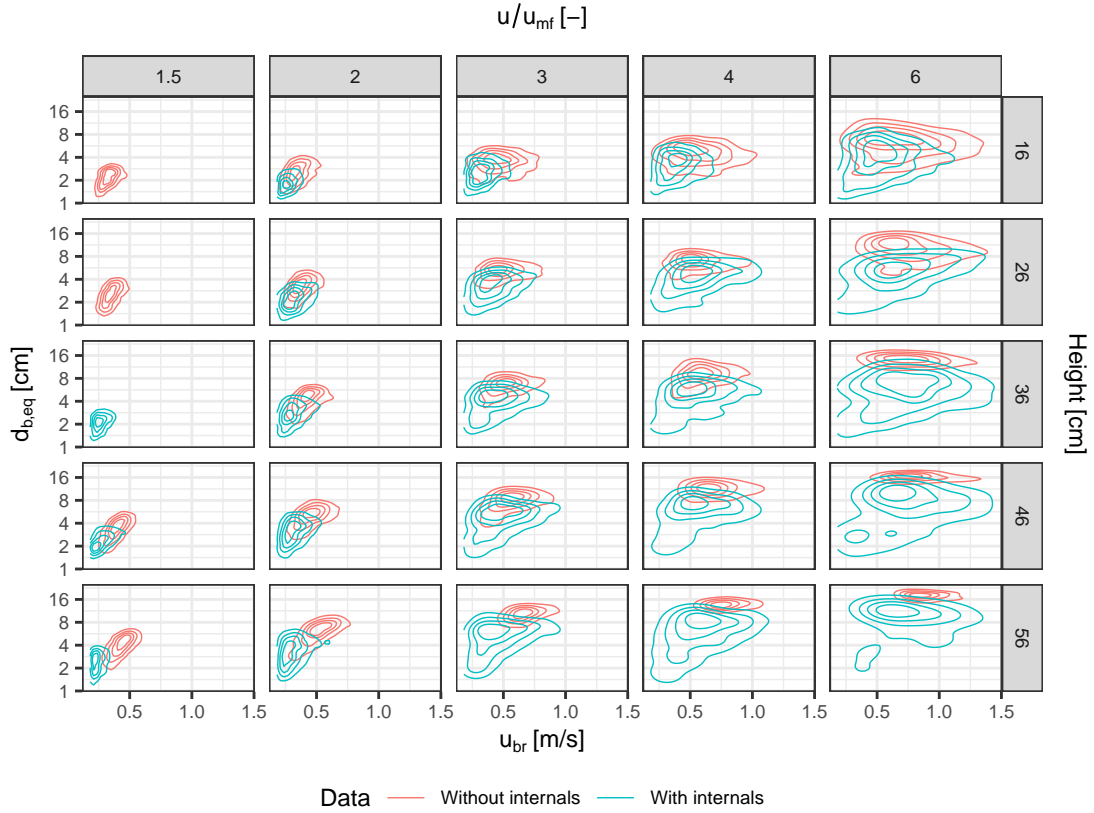


Figure 4.47: Density contour plot of the equivalent bubble diameter  $d_{b,eq}$  over the bubble rise velocity  $u_{br}$  for X-ray measurements with and without vertical internals

Figure 4.48 shows comparisons of the correlated density distributions of the aspect ratio  $l : w$  and the rise velocity  $u_{br}$  between the measurements with and without internals. In both cases, a clear correlation between  $u_{br}$  and the aspect ratio can be seen, which appears to be more pronounced and to have a steeper gradient for the data measured with internals. For the case with internals comparatively higher values for  $l : w$  are measured for a given value of  $u_{br}$ .

## 4.5 Results of X-ray tomography measurements with vertical internals

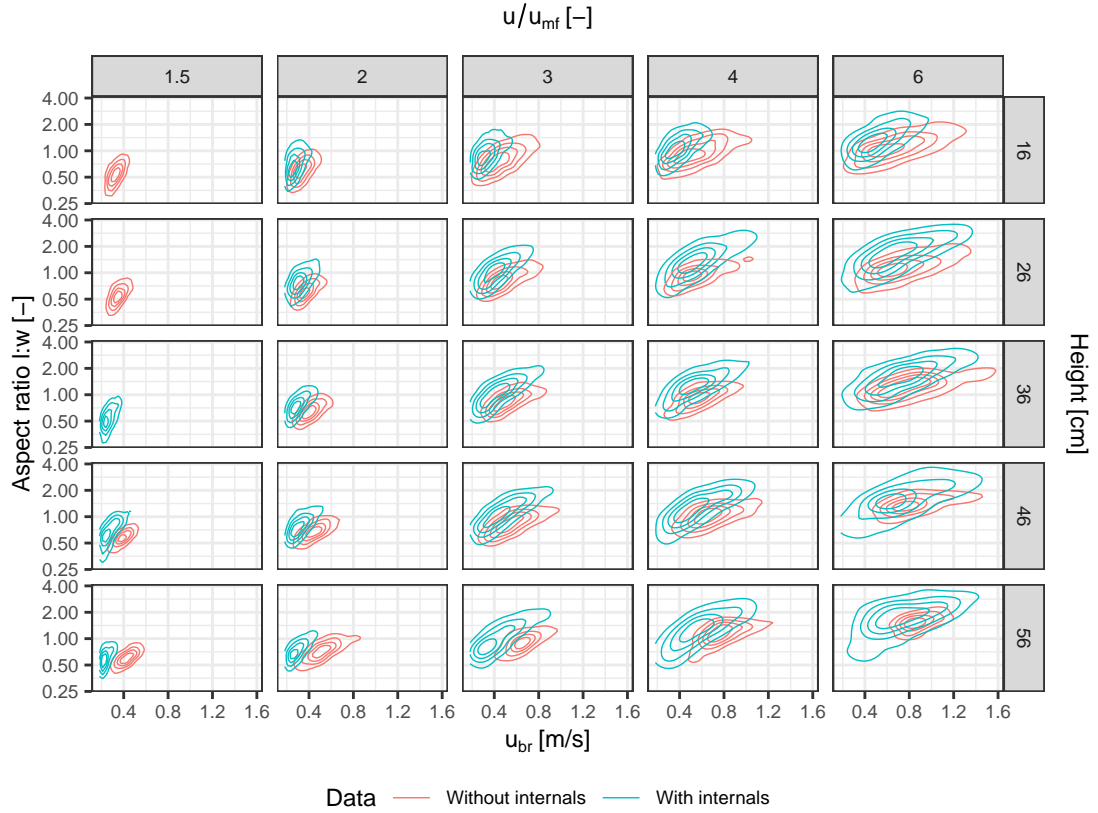


Figure 4.48: Density contour plot of the bubble aspect ratio  $l : w$  over the bubble rise velocity  $u_{br}$  for X-ray measurements with and without vertical internals.

As mentioned before, one concern of catalytic BFB reactors is the possible breakthrough of reactants in bubbles. Figure 4.49 shows the cumulative volume of bubbles with a defined rise velocity and specific surface area for the measurements with internals, analogous to Figure 4.23 shown in Section 4.3.4 for the measurements without internals. The mean values of both cases, with and without internals, are shown as well. One can see that the comparatively decreased bubble sizes lead to significantly increased specific surface areas. There are also less critical bubbles that are fast and large in comparison to the measurements without internals. However, one still has to consider that about 30% of the cross section consists of internals and therefore also roughly 30% of the bubble surface areas are in contact with the internals and consequently do not participate in the diffusive mass transfer between the bubbles and the dense phase.

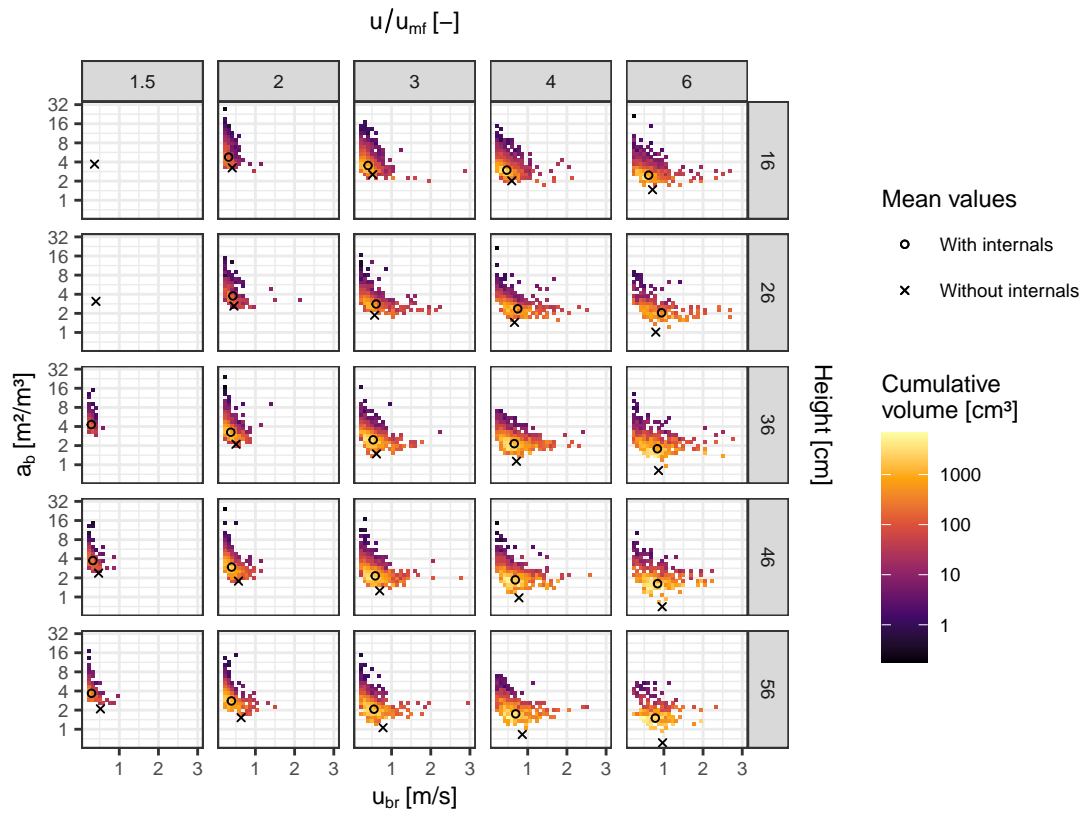


Figure 4.49: Distribution of the cumulative bubble volume respective the specific surface area  $a_b$  and the bubble rise velocity  $u_{br}$  as it was measured with internals by means of X-ray tomography including mean values of the measurements with and without internals.



## 4.6 X-ray radiography measurements

One obvious shortcoming of the X-ray tomography experiments described in Sections 4.2, 4.3 and 4.5 is the restriction of the XR-LD setup to one-dimensional measurements of the transmitted X-ray intensities and the corresponding two-dimensional tomographic reconstructions of cross-sectional bubble hold-up. A three-dimensional reconstruction of individual bubbles is only possible by means of stacking the individual reconstructed cross sections of a bubble and applying the measured rise velocity for the determination of the vertical length of the reconstructed slices of the bubble. While this may be sufficient for bubbles that rise statically through the measurement planes without changing their shapes and rise velocities, it could be problematic for more dynamic bubbles and could lead to a distortion of the reconstructed bubble properties, as it was described more detailed in Section 4.4.3.

One of the findings of the evaluation of the tomographic measurements was that there is a broad variance of bubble shapes which are correlated to the rise velocity of the bubble with elongated bubbles typically being faster than oblate ones. Given the fact that the vertical dimension of each reconstructed bubble is directly proportional to its measured rise velocity, due to the applied pseudo three-dimensional reconstruction method, there is the risk of an artificial correlation between the rise velocity and the bubble shape. If the rise velocity of a bubble was overestimated, this would lead to an elongation of its shape, whereas an underestimation would flatten the bubble vertically. The observed range of shapes and its correlations to other bubble properties was determined to be a relevant finding for the measurements with optical probes in the pilot plant GanyMeth, as the transformation of the measured chord-lengths to bubble size distributions depends on the assumed bubble shape [136], [214].

Additionally, through a detailed series of tomography simulations presented in Sections 4.4.2 and 4.4.4, it could be shown that the limited available angles of the XR-LD setup may generate artifact bubbles or falsely merge individual bubbles through the reconstruction. It was demonstrated that this problem would only affect the measured bubble property distributions if many small bubbles were present and that the effect is probably negligible for the majority of the measurements. This is especially the case for the determination of the mean values of the bubble sizes. However, this was only investigated in detail for the measurements without internals and solely by means of simulation. The measurements with internals are more likely to be affected by this problem due to the significantly smaller bubble sizes in comparison to the measurements without internals. The simulations also could not account for other possible issues such as beam hardening, noise, dynamic bubble interactions and the heterogeneous density distribution when vertical internals are inserted in the bed.

To elucidate the above mentioned uncertainties and to verify the results from the X-ray tomography measurements, additional X-ray measurements were conducted with the XR-AD setup described in Section 3.3.1, which allows the observation of the dynamic behavior of entire bubbles as they rise towards the surface by means of X-ray projections. Additionally, synchronized measurements with optical probes were conducted to allow the direct comparison of the two measurement techniques and thus to verify the optical probe evaluation methods that were developed in this work.

For the experiments presented in this section, alumina particles of the type NWa that can be considered an intermediate between Geldart Type A and B particles, as described in Section 3.4, were used as bed material. Air at ambient conditions was used as the fluid for the fluidization in the cold-flow model as it was described in Section 3.3. The experiments include measurements of BFBs or individually injected bubbles and were either conducted with three area detectors arranged around the column or with just two area detectors in place when the optical probe was inserted. In Figure 4.50, different variants of the experimental setup are shown. Sub-figure (A) shows the setup with internals inserted and all three detectors (1) in place around the column. Sub-figure (B) shows the inserted optical probe (2) as well as one of the bubble injection ports (3), that connects one of the solenoid valve of single bubble injection setup presented in Section 3.3.2 to a vertical nozzle inside the column that can be moved radially. A second identical bubble injection nozzle is installed on the opposing side.

### 4.6.1 X-ray radiography calibration and evaluation

For the measurements presented in this section a two-point calibration was carried out, which was shown to be sufficient in unpublished independent experiments at TU Delft, where results of two-point calibrations were compared with results of 15-point calibrations.

However, the evaluation of the data showed that this assessment was likely not applicable for the used materials. For the experiments shown in this work, the exact determination of the bubble hold-up is not necessary, nonetheless it is important to discuss the applicability of the used method for future measurements or the further evaluation of the data shown in this work.

According to the Lambert Beer law, as described in Section 4.1, the bubble hold-up for each pathway between X-ray source and detector can be calculated with reference measurements of the transmitted X-ray intensities  $I_{BR}$  through the empty column and  $I_{FU}$  through the column filled with bed material at minimum fluidization as shown in Equation 4.3.

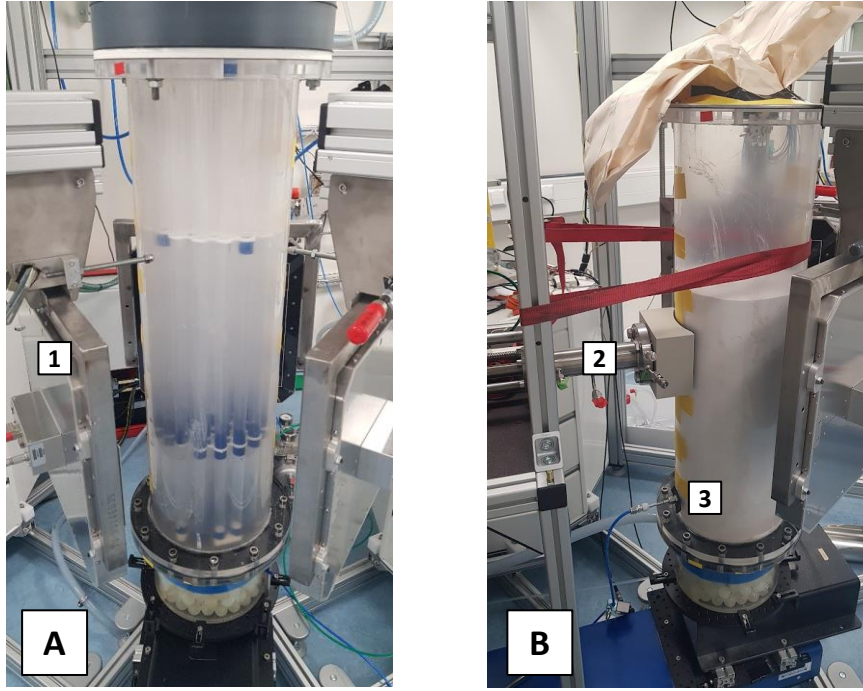


Figure 4.50: Images of the experimental setup showing the cold-flow model with inserted vertical internals and three X-ray area detectors (1) in Sub-figure (A) and with the optical probe (2) inserted, one of two bubble injection ports (3) that is connected to an external air supply, without vertical internals and two X-ray area detectors in Sub-figure (B).

$$\varepsilon_b = \frac{\ln\left(\frac{I_{ME}}{I_{FU}}\right)}{\ln\left(\frac{I_{BR}}{I_{FU}}\right)} \quad (4.3)$$

By applying the measured hold-up on the corresponding depth of the bed for the given pathway between detector and X-ray source, the horizontal length of the bubble phase can be determined. For measurements that include vertical internals, it is not feasible to calculate the depth of the bed for any X-ray pathway geometrically the way it can be done easily for the simple case without internals. However, the bed depth can be calibrated from the reference images. Given the reference images of the column, empty and filled with bed material both with and without internals, as shown in Figure 4.51, then the bed depth can be calculated as described in the following.

The transmitted X-ray intensity profile for the case with internals is given by Equation 4.11, where the attenuation coefficient  $\mu_B$  and the bed depth  $\Delta B_{Int1}$  are unknown.

$$I_{FU,INT1} = I_{BR,INT1} e^{-\mu_B \Delta B_{Int1}} \quad (4.11)$$

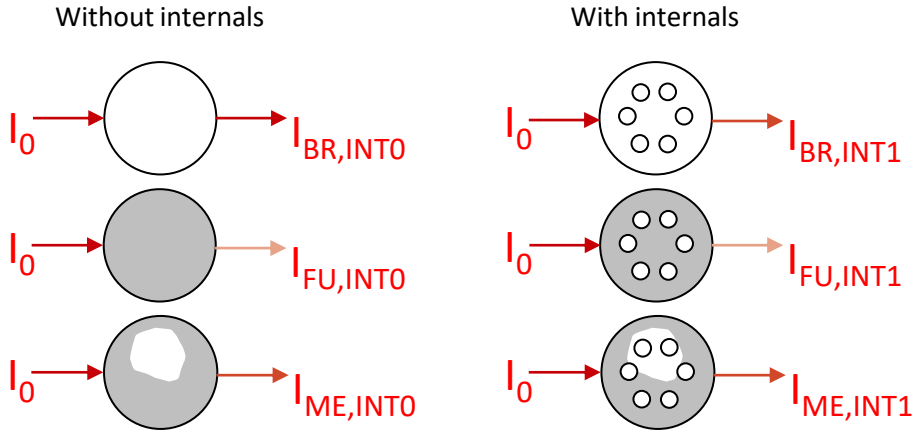


Figure 4.51: Illustrations of the X-ray intensity attenuation measurements of the references for the two-point calibration and measurements of bubbles for the cases with and without internals.

The analogous equation for the case without internals allows the calculation of the attenuation coefficient  $\mu_B$  since the bed depth is known, as shown in Equation 4.12.

$$\mu_B = \frac{-\ln \frac{I_{FU,INT0}}{I_{BR,INT0}}}{\Delta B_{Int0}} \quad (4.12)$$

Then the bed depth with internals can be calculated by inserting Equation 4.12 into Equation 4.11:

$$B_{Int1} = \frac{-\ln \frac{I_{FU,INT1}}{I_{BR,INT1}}}{\mu_B} \quad (4.13)$$

An example of the application of the calculated bed depth to determine the depth of a single bubble with and without internals is shown in Figure 4.52. In the top row a case without internals is shown, whereas the bottom row shows an example with internals. The images on the left side show the profile of the bubble hold-up for a single bubble, the images in the middle show the calculated bed depth profile and the images on right show the resulting bubble depths of the same images as shown on the left. For the given example without internals, the horizontal width of the bubble measures 9 cm, while the maximum calculated bubble depth is only about 5.5 cm. This observation cannot be explained by an asymmetry of the bubble, as the same observation was made from all viewing angles for all injected bubbles. It is also unlikely that particles within the bubble phase are responsible for this deviation between the measured width and depth of the bubbles as it would mean that for the given case roughly 40% of the bubble phase consists of particles. It was thus concluded that the Lambert Beer law

based on a two-point calibration is not applicable to describe the attenuation of X-rays for the given setup, likely due to beam hardening or X-ray scattering. Therefore, any radiographic images presented in the following that show the bubble depth profile will not include the color-coding legend, as it was shown that the calculated bubble depth is not accurate. A possible way to achieve a multi-point calibration is to use the measured data for the single bubble injections presented in Section 4.6.4. The X-ray attenuation could be calibrated for each size class of injected bubbles, so that the mean bubble depth equals the mean bubble width that was determined by means of image processing. Considering the several hundred bubbles that were measured from two or three angles for each of the five different volume-equivalent diameter classes in the range of 2 - 10 cm, the achievable calibration should be statistically robust. However, for the evaluation of the experiments shown in this work, the determination of the bubble depth was not relevant and such a calibration was therefore not attempted.

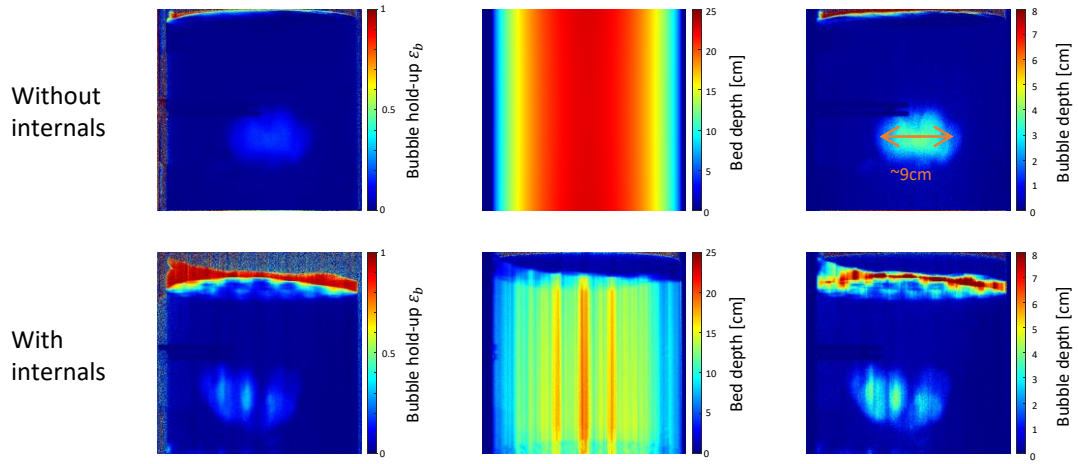


Figure 4.52: Images that show the bubble hold-up profile on the left, the bed depth profile of the bed without bubbles in the middle and the corresponding bubble depth profile on the right for the cases without internals in the top row and with internals in the bottom row.

### 4.6.2 X-ray radiography measurements of bubbling fluidized beds

Comprehensive measurements of the BFB regime were conducted for measurement times of two minutes and each combination of the measurement heights, frame rate and the fluidization numbers, as shown in Table 4.4. The experimental settings are the same as those from the measurements with the XR-LD setup presented in Sections 4.2, 4.3 and 4.5. Each of the frame rates represents a different height of the field of view. Measurements taken at full resolution show a section of the bed with a height of about 24 cm.

Fluidization number $u/u_{mf} [-]$	1.5, 2, 3, 4, 6
Height of detector center [cm] (200 Hz and 85 Hz measurements)	16, 26, 36, 46
Height of detector center [cm] (22 Hz measurements)	10, 30, 49.2

Table 4.4: Experimental settings for the BFB experiments with the XR-AD setup

Images taken at increased frame rates of 85 and 200 Hz show vertically cropped sections of the bed, with heights of 7.1 cm and 1.6 cm respectively.

The main objective of these measurements was to provide data that will allow the direct comparison between the pseudo three-dimensional reconstructions, the actual three-dimensional reconstructions once they are available and the projected images themselves. Currently, the three-dimensional reconstruction from the projected radiographic data is not feasible, due to the substantial computational effort that is required for the reconstruction. Only a pseudo three-dimensional reconstruction of the data, based on the methods described in Sections 4.2.3, is possible. Nonetheless, the radiographic images allow a qualitative assessment of the dynamic evolution of the bubbles within BFB at the given settings as well as a manual estimation of bubble properties. All images presented in this section were taken at a height of 30 cm for the center of the detector in relation to the gas distributor plate.

Figure 4.53 shows images of the BFB with and without internals that were measured for increasing fluidization numbers. For the images with internals, the white dashed line indicates the height of the surface from the reference image, above which the data is not calibrated.

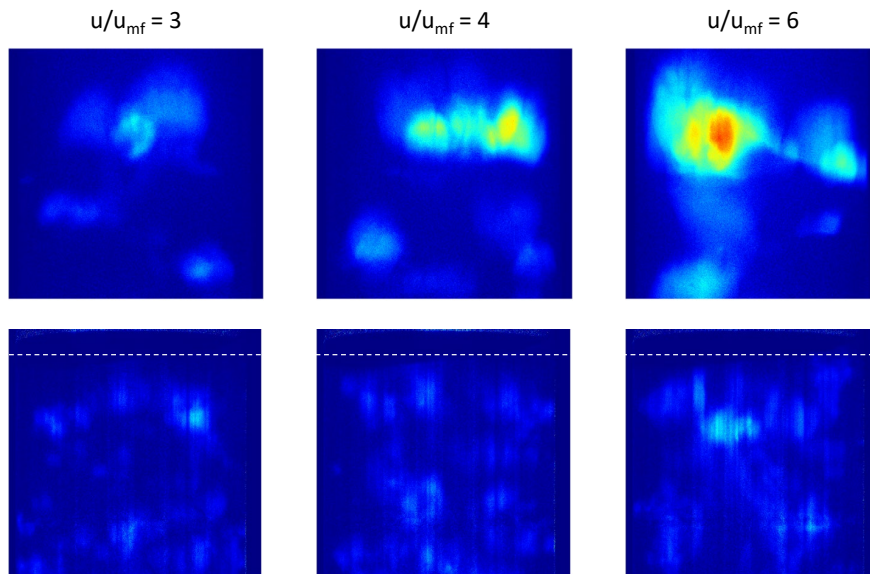


Figure 4.53: Sample radiographs of BFBs with and without internals for  $u/u_{mf} = 3, 4$  and  $6$

While the bubble size distributions from the measurements without internals consists of relatively few large bubbles, there are many small bubbles in comparison when internals are present.

To evaluate the dynamic evolution of bubbles within BFB, time series of images captured at  $u/u_{mf} = 3$  are shown in Figure 4.54. For the images without internals, shown in the top row, one can see bubbles of various sizes, shapes and rise velocities. Throughout the time series, multiple coalescences can be seen, where the lower of two coalescing bubbles elongates as it accelerates towards the upper one. The interpretation of the time series captured with internals present is more challenging, due to the many small bubbles that overlap in the field of view and the presence of the verticals that interfere the visual appearance of the bubbles, making it difficult to distinguish between clusters of small bubbles and large individual bubbles. The visual evaluation confirms that the mean bubble rise velocity is reduced significantly when internals are present. To provide an example, one bubble has been tracked manually for each time series in the figure to determine its rise velocity. For the shown case, a bubble rising in a bed without internals, which is marked with a green dot, rises with an average rise velocity of  $0.43 \text{ m s}^{-1}$ , whereas the bubble from the measurements with internals, which is marked with a yellow dot, rises with a velocity of  $0.24 \text{ m s}^{-1}$ .

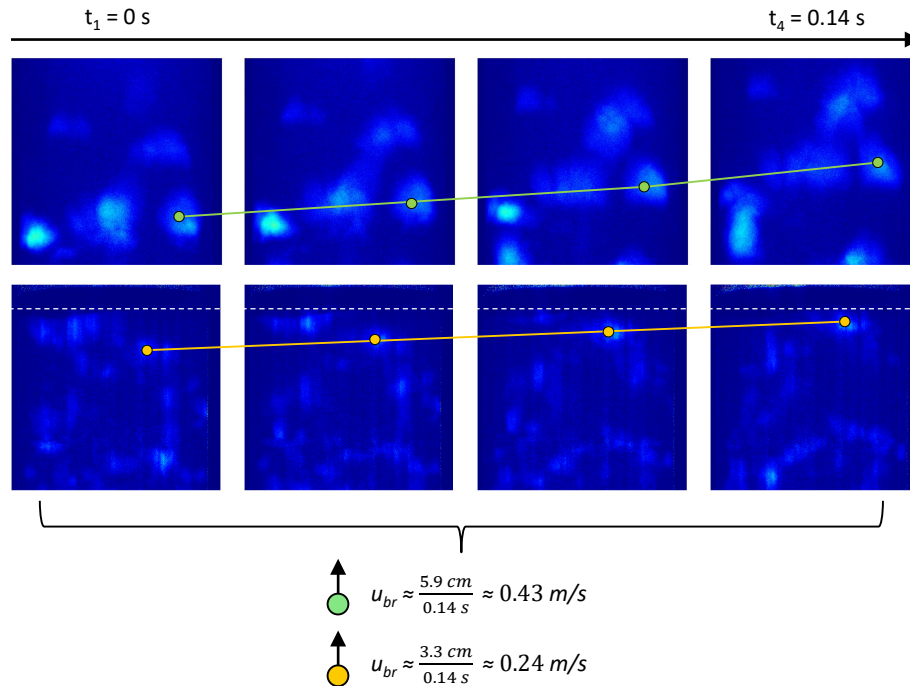


Figure 4.54: Time series showing rising bubbles a BFB with and without internals. The images include an illustration of the tracing of individual bubbles for the manual determination of their rise velocities.



An example of a highly dynamic bubble interaction in a BFB without internals can be seen in Figure 4.55. The bubble on the left side, which is marked with a yellow dot, appears to just have coalesced and is rising steadily henceforth with a rise velocity of approximately  $0.45 \text{ m s}^{-1}$ . On the right side of the images, a highly dynamic series of bubble interactions that involves multiple coalescing bubbles can be seen. One of the involved bubbles, marked with a green dot, travels with a velocity of  $1.05 \text{ m s}^{-1}$  throughout the coalescence event, during which it distorts significantly. Such examples of bubble interactions demonstrate the highly dynamic situation within BFBs and indicate the importance of accounting for broad distributions of bubble sizes and rise velocities rather than just their mean values. Given the frequency at which coalescence occurs in BFB reactors, such events are not rare and effect the mass transfer between the bubble and the dense phase [126].

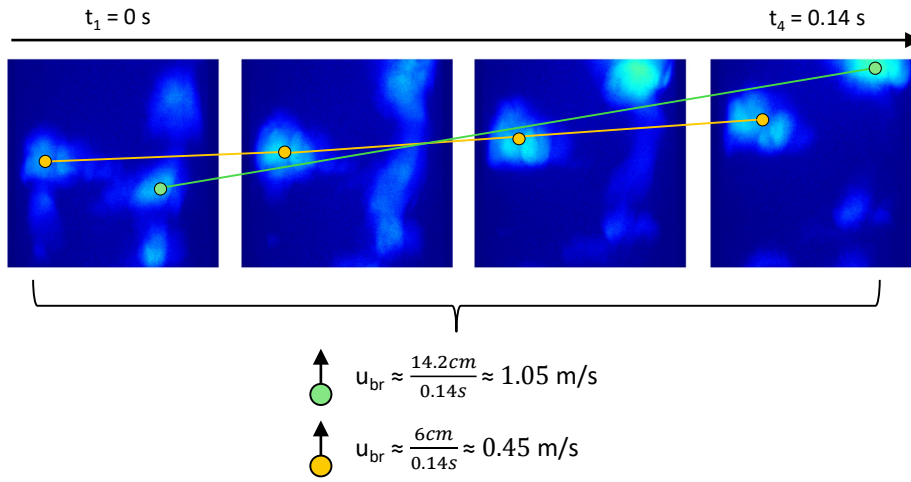


Figure 4.55: Time series showing dynamic bubble interactions including tracing of individual bubbles, one of which is actively coalescing in the shown images, for the manual determination of their rise velocities.

A manual evaluation of the projected bubble sizes was performed for the measurements at fluidization numbers of 3 and 4, in which individual bubbles were measured in randomly selected frames that were captured at a height of 30 cm above the distributor plate. For this, only bubbles that were clearly distinguishable were selected and their volume-equivalent diameter was determined assuming a symmetric bubble shape. A selection of corresponding images, including the measured bubble diameters and markings of the heights 26 and 36 cm above the distributor plate, can be seen in Figure 4.56. For a sample size of 52 bubbles at  $u/u_{mf} = 3$  and 29 bubbles at  $u/u_{mf} = 4$ , the mean values of  $d_{b,eq}$  were 5.9 cm and 9.1 cm respectively.



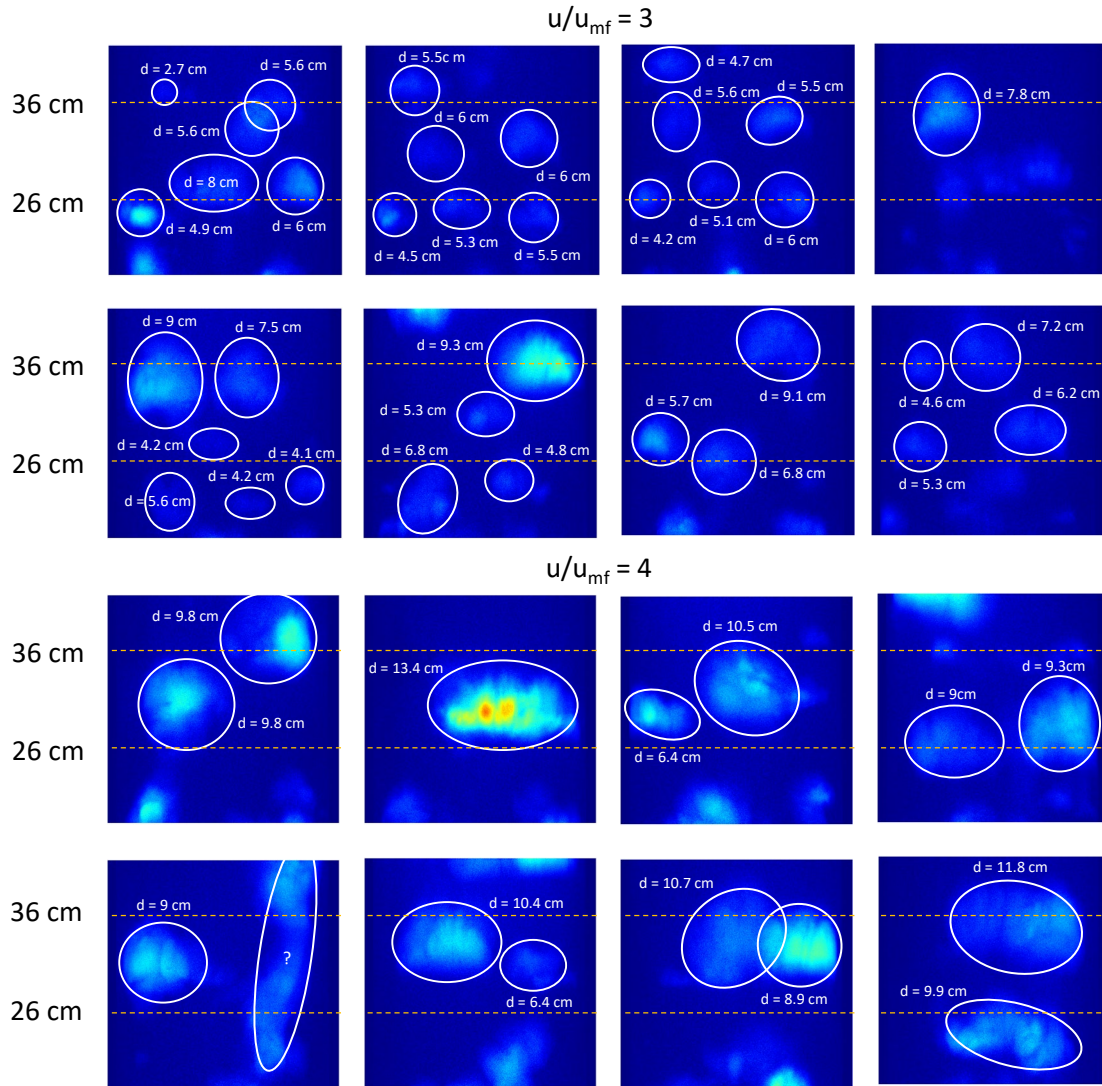


Figure 4.56: Manual determination of the bubble size distribution from radiographic BFB measurements.

A comparison between the manually measured bubble diameters and the results from the X-ray tomography measurements shown in Section 4.3.4 is given in Figure 4.57. It can be seen that the evaluated data, which represents a field of view from 18 to 42 cm above the distributor plate, lies in between the expected range of mean  $d_{b,eq}$  for measurement heights of 36 and 46 cm as measured by means of X-ray tomography. The manually determined bubble diameters are therefore slightly larger than expected for  $u/u_{mf} = 4$ . Possible reasons for this could be the small sample size or an overestimation of the bubble sizes through the simplified manual measurement with hand drawn ellipsoids.

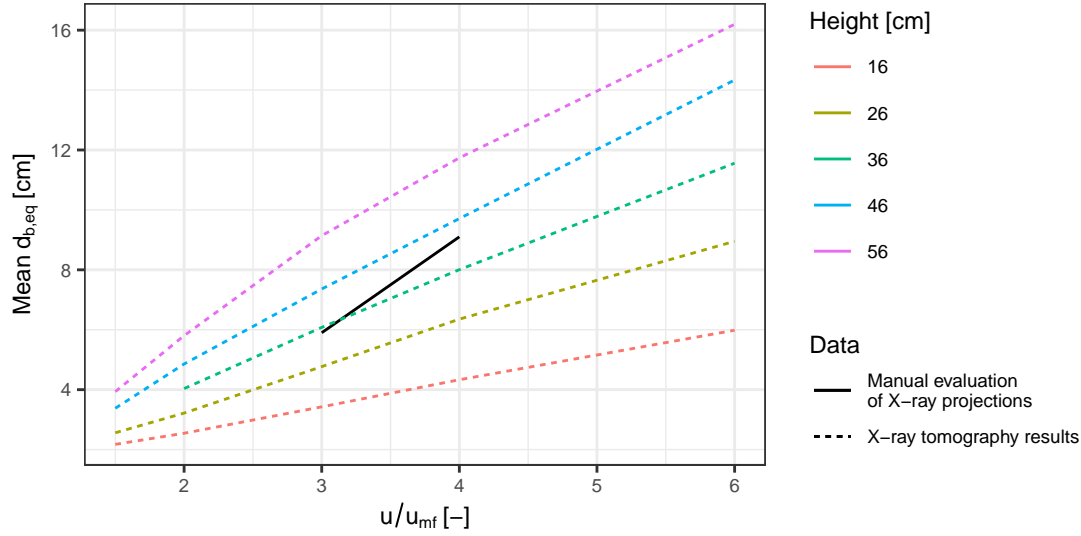


Figure 4.57: Comparison of the mean  $d_{b,eq}$  measured by means of X-ray tomography and manually evaluated from X-ray radiograms.

Note, that the manual evaluation of the X-ray radiographic images presented in this section can only serve as a approximated assessment of the data, considering the small sample sizes and the limited accuracy of the manual measurements. Nonetheless, the application of X-ray radiography allowed the independent verification of previous findings and provided additional observations of the dynamics within BFB that support the speculated reasons for the observed range of bubble sizes, shapes and rise velocities, which appear to be mainly the result of highly dynamic bubble interactions. A detailed manual evaluation of the BFB with vertical internals was not feasible due to the large number of individual bubbles that were overlapping and the visual interference cause by the internals. This further highlights the limitations of the applied methods for measurements with internals.

#### 4.6.3 X-ray radiography measurements of injected bubbles

One way to overcome the challenging measurement of the hydrodynamics within BFBs is the injection of single bubbles into a fluidized bed that is not bubbling yet. Then, the size, shape, rise velocity and trajectory of individual bubbles can easily be measured by means of readily available image processing tools and a tomographic reconstruction is not necessary. By injecting two bubbles with defined spatial and temporal distances, the complex interaction of bubbles can be studied in a controlled, reproducible and systematic manner. Controlled bubble injections with defined volumes are especially useful for measurements when vertical internals are inserted in the bed, as the visual interference caused by the internals as well as the heterogeneous density distribution make the interpretation of freely bubbling beds

challenging. Another important application of bubble injections in the scope of this work is the independent verification of the evaluation of the optical probe measurements. The measured bubble properties can be directly compared, by synchronizing optical probe measurements with X-ray radiographic measurements of the injected bubbles. Additionally, the projected images allow the assessment of how the probe influences the bubble. The setup used for the experiments shown in this section allows the injection of stable bubbles with volume-equivalent diameters between 2 and 10 cm, through one or two available injection nozzles that can be positioned anywhere on a central horizontal chord through the cold-flow model at a height of approximately 10 cm above the distributor plate. A detailed description of the setup is provided in Sections 3.3 and 3.3.2.

### Image processing

For the evaluation of the measurements, an algorithm has been written that identifies the bubble in the projection image and tracks its center of weight, shape and size for each frame and each viewing angle. An example of the applied image processing steps, which are explained in detail in the following, can be seen in Figure 4.58.

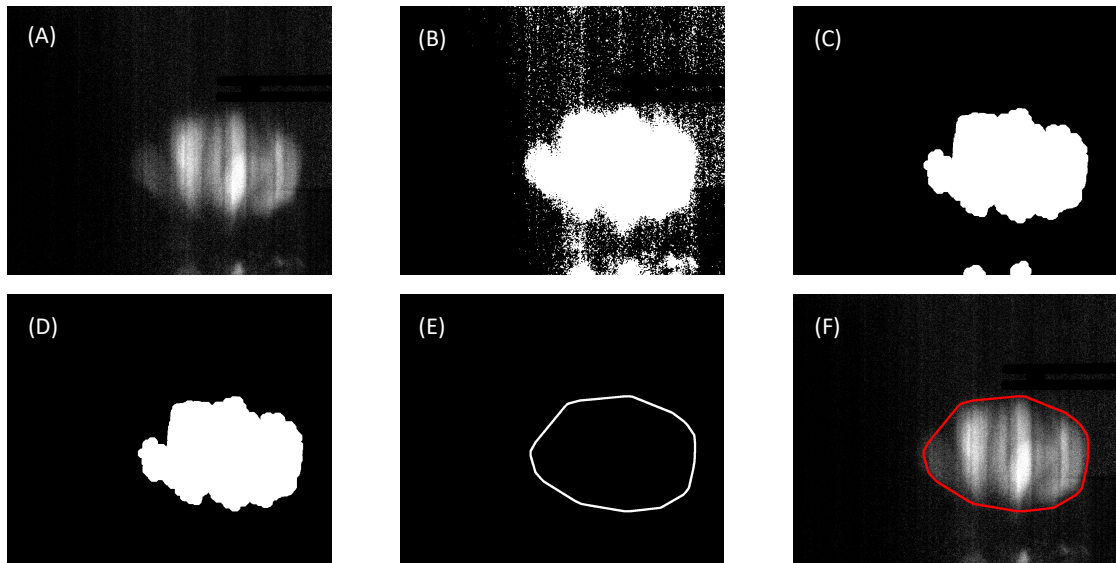


Figure 4.58: Binarization of an X-ray radiogram of a single injected bubble in a fluidized bed with internals

First, a Gaussian filter is applied on the bubble depth image, which was retrieved through the calibration with reference images according to the methods described in Section 4.6.1, to reduce the salt-and-pepper noise. Then, the image is binarized with a fixed threshold, which often would produce an image, in which the bubble would be clearly identifiable within a significant amount of salt-and-pepper noise. Furthermore, for the measurements with

internals, the binarization would sometimes lead to situations, where a cluster of multiple bubbles would be identified instead of a single one. While it is possible, that the injected bubble would split into multiple small bubbles, it appears less likely that this is usually the case here, as the overall shape of the supposed cluster and its rise velocity stays steady while rising towards the surface. This issue would mostly appear for the smaller bubbles that are more likely impacted by the visual interference of the internals, whereas the larger ones could clearly be identified as single bubbles in most cases. To overcome these binarization issues, additional image processing steps had to be applied.

A series of morphological manipulations of the image was performed using the Matlab function *bwmorph*. The binary image was first eroded, which essentially means that a defined thickness of the outermost layer of pixels of each object representing the bubble phase, would be erased. In this way, any small disconnected objects would be removed from the binary image. After that, the image is dilated again, which effectively means that a layer of pixels with a defined thickness equal to that what was removed earlier will be added again to each object representing the bubble phase, so that the remaining objects approximately match their original shapes. The result of this morphological operation is shown in Figure 4.58 (C). If any other objects are left in the image that are significantly smaller than the expected bubble size, then they are removed from the image.

In the next step, the bubble is visualized by the convex hull that surrounds the single binarized object that is the bubble. For this, the Matlab function *bwconvhull* was used. Note that this step only serves for visualization purposes. The geometric properties, such as the center of weight, the total projected area, and the minor and major axis of the bubble are then determined by applying the Matlab function *regionprops* on the binarized images for all viewing angles. The mean of each bubble property is retrieved by averaging its values over all frames for a given time step. Frames in which multiple bubbles were detected are either a sign for a bubble that split into multiple bubbles or a failed binarization and the respective bubble properties are excluded from the evaluation. For the measurements that included optical probes, the bubble properties are only evaluated as long as the bubble is still below the optical probe, which would conceal the projection of the bubble.

### Experimental methods and settings

The volume of an injected bubble is proportional to the opening time of the valve. By injecting bubbles in short intervals and including a vessel as a pressure reservoir, the pulsed flow is dampened so that a semi-steady flow rate is established up-stream of the pressure vessel that can be measured with a MFC.

In this way the mean volume  $\bar{V}_b$  of an injected bubble can be determined as shown in Equation 4.14, where  $\dot{V}$  is the measured flowrate,  $\Delta t$  is the total measurement time and  $n$  is the number of injections.

$$\bar{V}_b = \frac{\dot{V} \Delta t}{n} \quad (4.14)$$

Additionally, the bubble volumes were determined by means of image processing as described above. A comparison between the applied methods to determine the volumes of the injected bubbles is shown in Figure 4.59. In addition to the two methods already described, the bubble volumes that were also determined through the integration of the bubble depth that was calculated from the X-ray attenuation profile as described above.

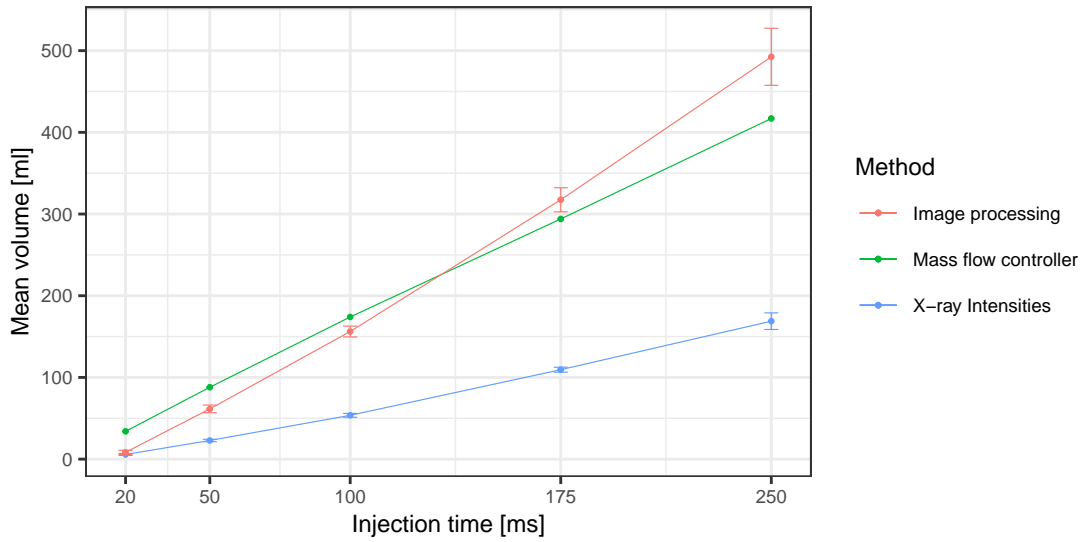


Figure 4.59: Comparison of the injected bubble volumes as measured by means of radiographic image analysis and mass flow controller.

One can see, that the values determined through the measured mass flows are proportional to the injection times. The volumes that were determined through the measurement of the projected areas match those measured with the MFC reasonably well, whereas the integration of the bubble depth results in values that significantly deviate from the others. This was to be expected due to the supposed beam hardening or X-ray scattering effects. For small injection times  $t \leq 100$  ms, the bubble volumes determined through the projections are smaller than those resulting from the measured mass flow. The reason for this could be that some of the injected air dissipates into the dense phase, which is not bubbling yet indicating that additional air may flow through the dense phase. For injection times  $t \geq 175$  ms the opposite is the case, and the projected areas slightly overestimate the bubble sizes. A possible explanation

## Chapter 4. X-ray measurements

could be that the evaluation of binarized projections does account for particles within the bubble. The wake of a bubble typically intrudes centrally into the bottom of the bubble, as it has been described in Section 2.3.2. This means that the part of the wake volume that is inside of the bubble, will be assigned to the bubble phase through the evaluation of the projected area. The same is true for particles that rain through the bubble, which seemed to occur more often in larger bubbles. For the results presented in the following the bubble volume determined through the projected area will be used.

The five selected injection times represent bubbles with volume-equivalent diameters that are shown in Table 4.5. Sample images that show the corresponding X-ray projections for each listed injection time, taken from the measurements that included the optical probe, are shown in Figure 4.60.

$\Delta t_{injection}$ [ms]	Mean $d_{b,eq}$ [cm]	Count $n$ [-]
20	2.44	56
50	4.89	57
100	6.68	54
175	8.46	46
250	9.75	47

Table 4.5: Volume-equivalent bubble diameters per injection time.

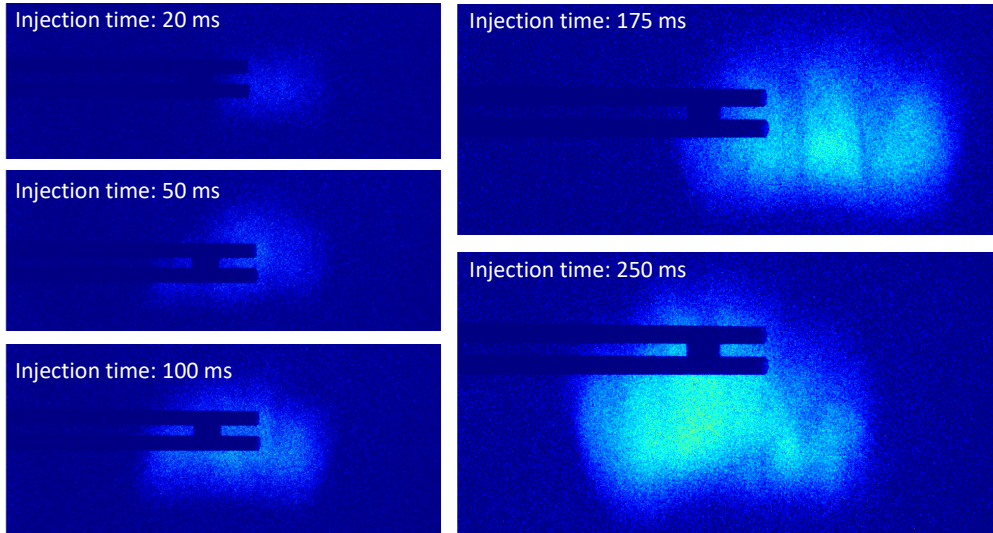


Figure 4.60: Radiograms of bubbles that were injected over a specified duration.

For each injection time, the measurements were conducted over a period of 60 s for the case without internals and 180 s for measurements with internals with 1 s gaps in between the injections to ensure that no bubble interactions would occur. The measurements were carried out with and without optical probes present. The optical probe was inserted at a height of



40 cm above the distributor plate to enable the bubble to stabilize after the injection and prior to measurement via the optical probe. The bed height of the fixed bed was 53 cm. Additional measurements with an increased fixed bed height of 63 cm were carried out for selected settings with internals to investigate, if the proximity of the optical probe to the bed surface would influence the measurements. All measurements shown in the following were carried out at the same superficial gas velocity  $u$  that was set slightly above  $u_{mf}$  to ensure a fluidized bed that is not bubbling yet.

### 4.6.4 Results of the X-ray radiography measurements of single injected bubbles

Measuring the properties of single bubbles with defined volumes that are not influenced by dynamic flow patterns found in freely bubbling beds in statistically representative sample sizes allows a systematic analysis of the influence of the internals on the properties of the bubbles. Additionally, the high-resolution projection images allow a qualitative analysis of the dynamic evolution of a bubble as it rises and possibly interacts with the internals or the optical probe. Figure 4.61 shows a comparison between the time series of two bubbles that were injected over a period of 250 ms, which have a volume-equivalent diameter of roughly 10 cm, with and without internals present, measured at a frame rate of 22 Hz.

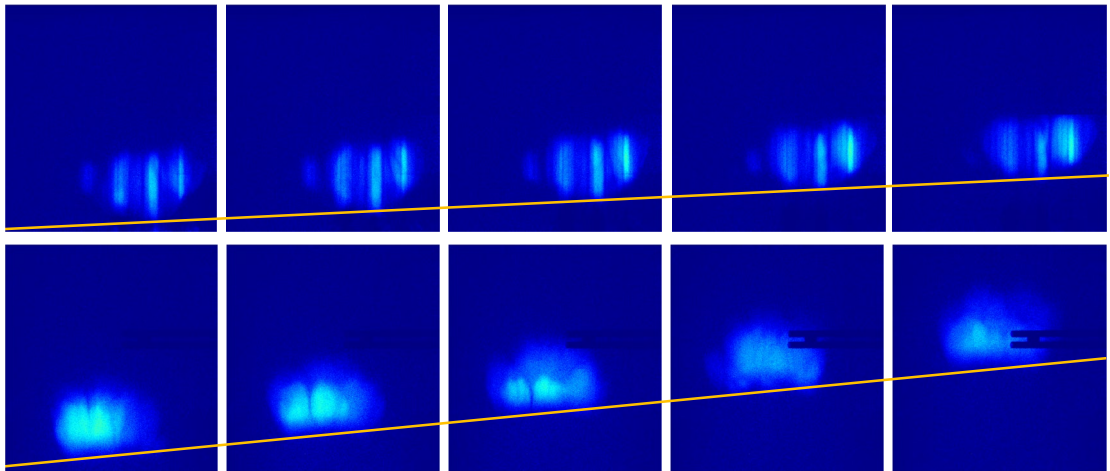


Figure 4.61: Time series captured at 22 Hz of two bubbles that were injected for 250 ms with internals, shown in the top row, and without internals, shown in the bottom row.

One can see, that the bubble with internals present seems more irregularly shaped. The vertical pattern of the internals are clearly visible and the bubble appears as if it consists of multiple cylindrical shaped volumes. As stated before, it remains unclear if this appearance is solely a visual effect or if this indeed shows a cluster of multiple elongated bubbles that are steadily communicating with one another and thus behave similar to a single bubble. Answering this question might be relevant for the calculation of the mass transfer between the

bubble and the dense phase given the fact that the specific surface area would be significantly increased if it indeed was a cluster of bubbles. The Figure also shows the difference in rise velocities, which is indicated by the different gradients of the straights that connect the bottom of the bubbles in each frame.

It is important that the injected bubbles are stable and reproducible to ensure statistically representative measurements of the properties of bubbles with a defined volume. Figures 4.62 and 4.63 show five time series each of the radiographic images of bubbles that were injected for 100 and 250 ms respectively, which were randomly selected and measured at a frame rate of 22 Hz. The inserted optical probe is also visible. One can see that the projected areas and the rise velocities of the bubbles do not deviate significantly. The bubbles show some variations in their shapes and stability and occasionally appear to partially split before quickly coalescing again. In some cases, particles can be seen raining through the bubbles. This alleged instability of bubbles appears to occur more frequently for the larger bubbles. Some interference of the bubble by the optical probe can also be seen, especially for larger bubbles. An example for this is shown in the bottom row of Figure 4.63, where the probe seems to initiate a temporal collapse of the bubble roof, through which particles rain through the bubble.



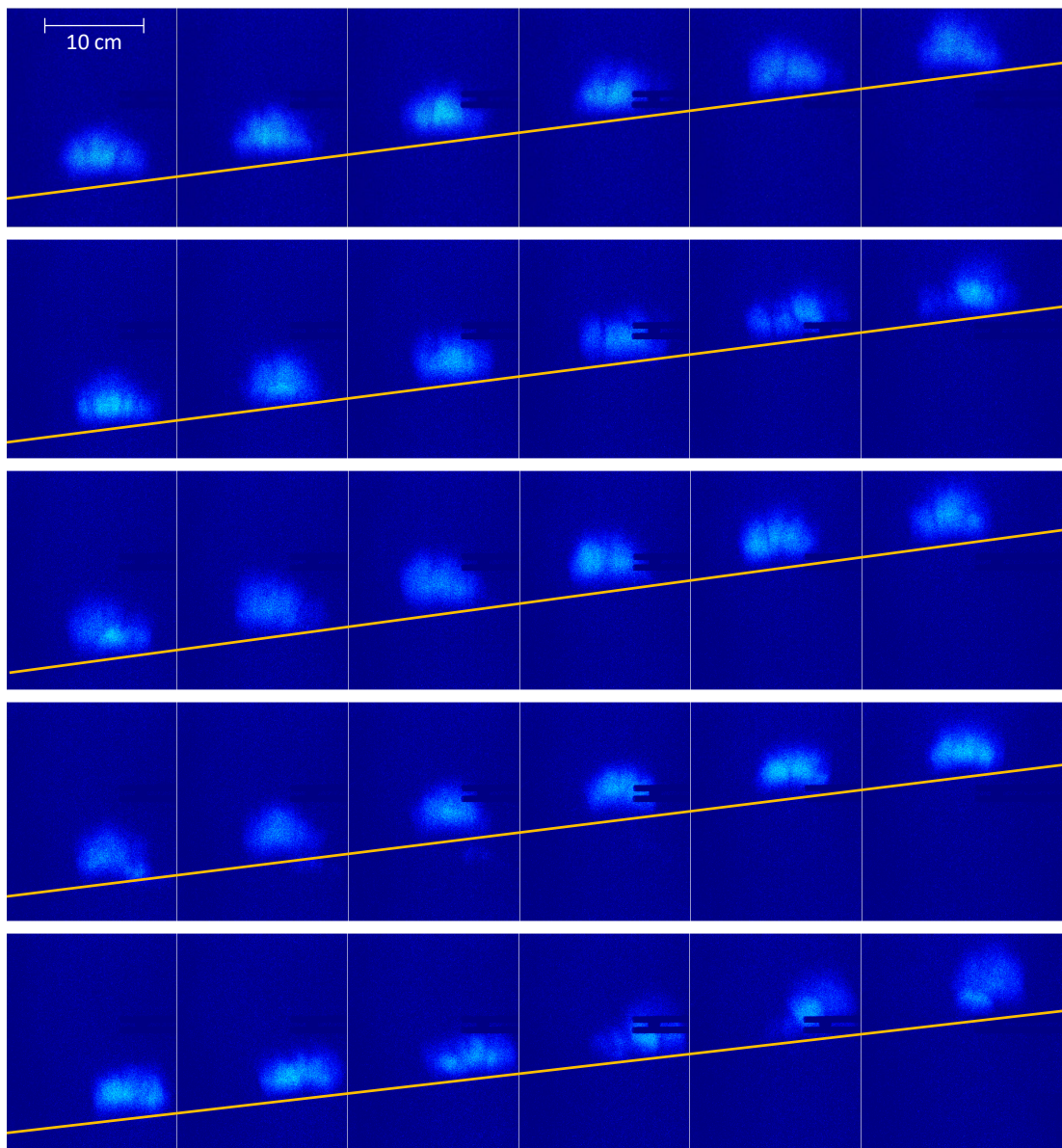


Figure 4.62: Time series of radiograms captured at 22 Hz of bubbles that were injected for 100 ms with inserted optical probe.

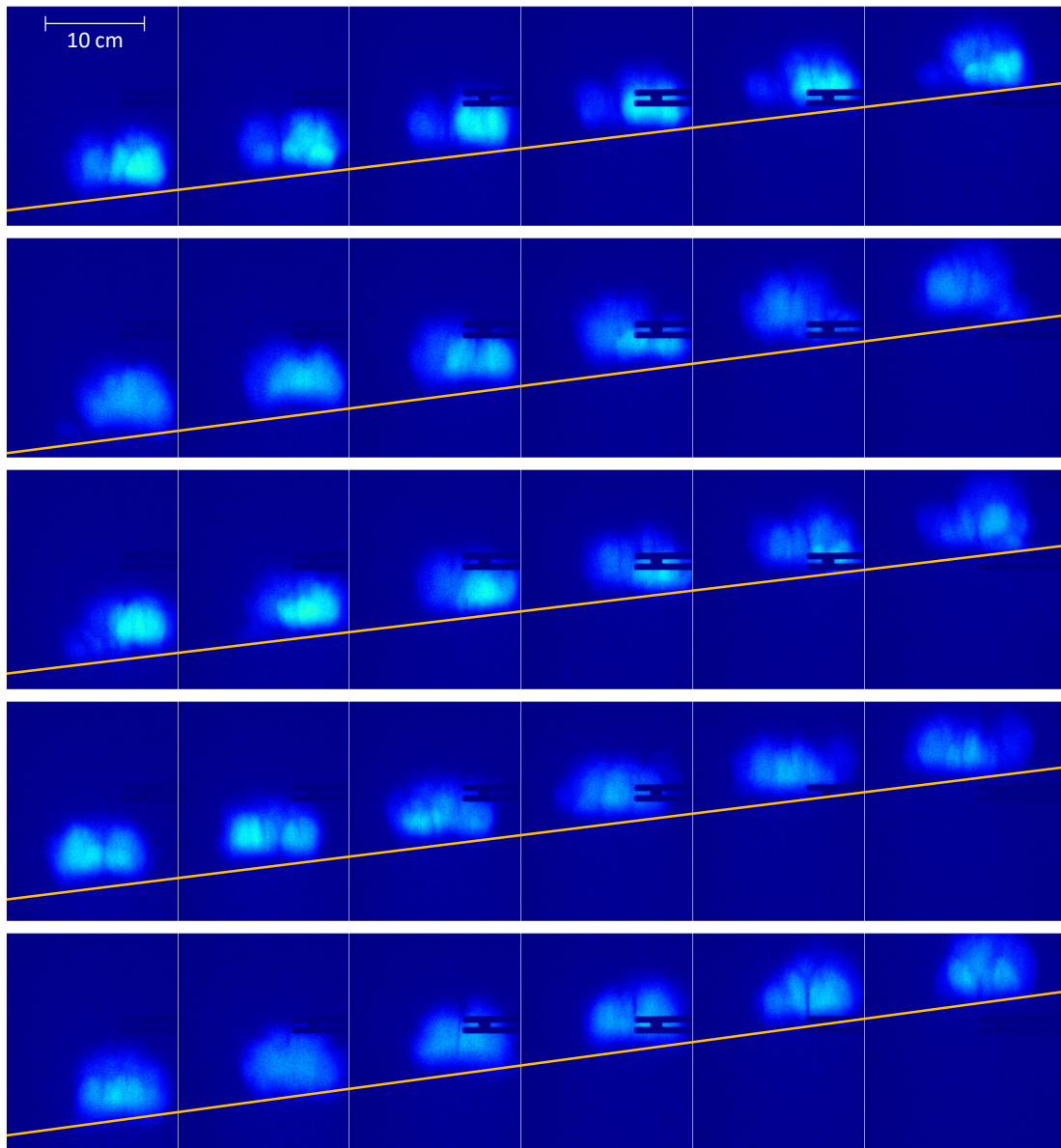


Figure 4.63: Time series of radiograms captured at 22 Hz of bubbles that were injected for 250 ms with inserted optical probe.

The measurement of injected bubbles with internals involved several additional challenges. The bubbles often split as they pass the tube spacer, which was presented in Section 3.3, Figure 3.2. This can be seen in Figure 4.64, which shows three time series of bubble injections over 100, 175 and 250 ms respectively with a reduced frame rate of 11 Hz. After the injection, the small and medium sized bubbles quickly stabilize as they approach the tube spacer, which is positioned at a central height in the figure. The bubbles adapt flattened shapes and appear to briefly stagnate below the tube spacer before splitting into multiple, dynamically interacting and distorted bubbles. The severeness of the disturbance of the bubble flow by the tube spacer depends on the bubble size. While the bubbles that were injected for 100 ms appear to stabilize soon after the interaction, this is not the case for bubbles that were injected over 175 ms, which were affected the most out of all tested injection times. The bubbles that were injected over 250 ms appeared to be less influenced as they often quickly re-coalesced after passing the tube spacer. Depending on the specific injection time, this interaction could lead to a broad variance of bubble sizes, shapes and rise velocities at the height at which the optical probe was placed.

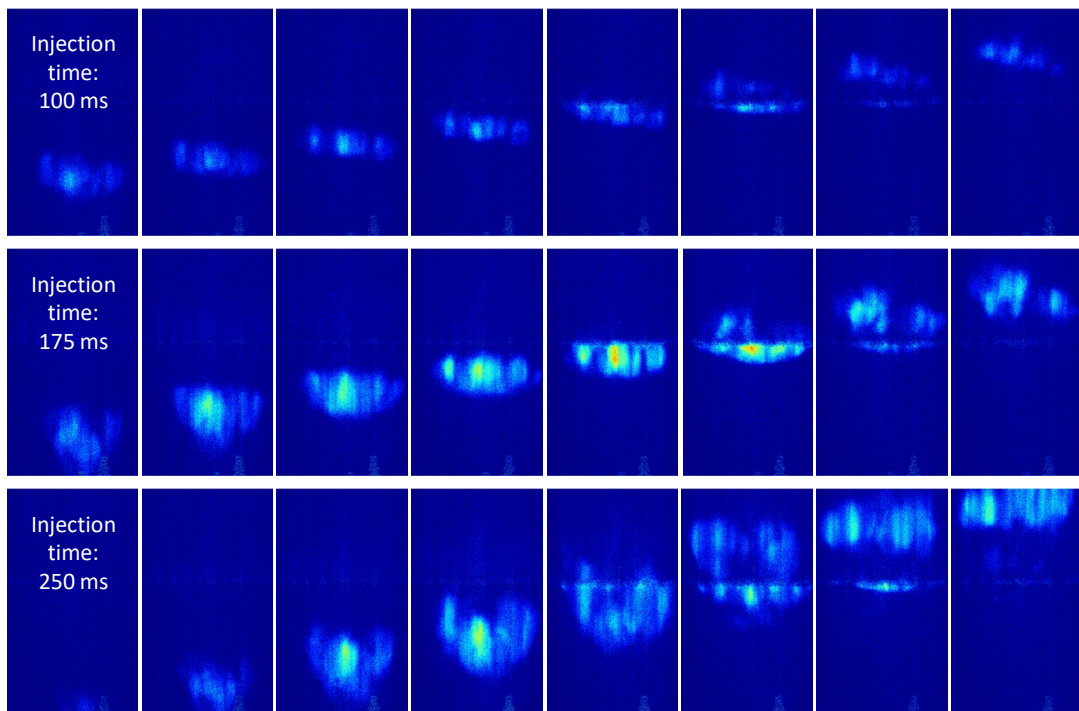


Figure 4.64: Time series of radiograms captured at 22 Hz showing the interaction between the tube spacer and bubbles that were injected for specified times.

Furthermore, the presence of internals makes it is also more difficult to assess the influence of the probe on the pierced bubble, as the internals distort the view. Details, such as the raining through of particles as it could be seen in Figures 4.62 and 4.63 for the case without internals, could not be observed with internals present.



The bubble sizes for injection times  $t \leq 175$  ms also appeared significantly smaller than those for the same injection times without internals, while the projected area of bubbles that were injected over a duration of 250 ms were comparable to those measured without internals. Theoretically, the projected areas of bubbles with a defined volume should appear approximately 20% larger when internals are present due to the volume that is occupied by the internals.

Therefore, it can be assumed that a larger fraction of the injected air dissipates into the dense phase for the case with internals and the validity of a direct comparison of the bubble properties for a given injection time is questionable especially for the shorter injection times. This assumption matches the observation that the bubble hold-up is reduced for a given fluidization number when internals are inserted as it was presented in Section 4.5.4. A comparison of the projections of bubbles that were injected for 100 and 250 ms for the cases without internals and with internals is shown in Figure 4.65.

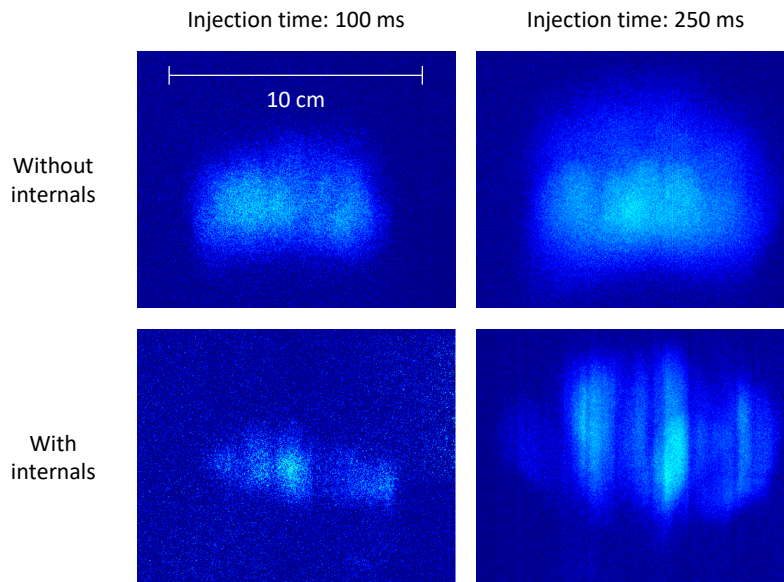


Figure 4.65: Comparison of the projected areas of bubbles that were injected for 100 and 250 ms with and without internals present.

Figure 4.66 shows five time series of X-ray projections showing rising bubbles that were injected for 250 ms each in fluidized bed with internals. The bed height was increased to 63 cm to avoid surface effects on the bubbles as they pass the probe. Note that the frame rate of the time series have been reduced to 11 Hz, to show the entire interaction between bubble and optical probe in a reasonable number of frames.

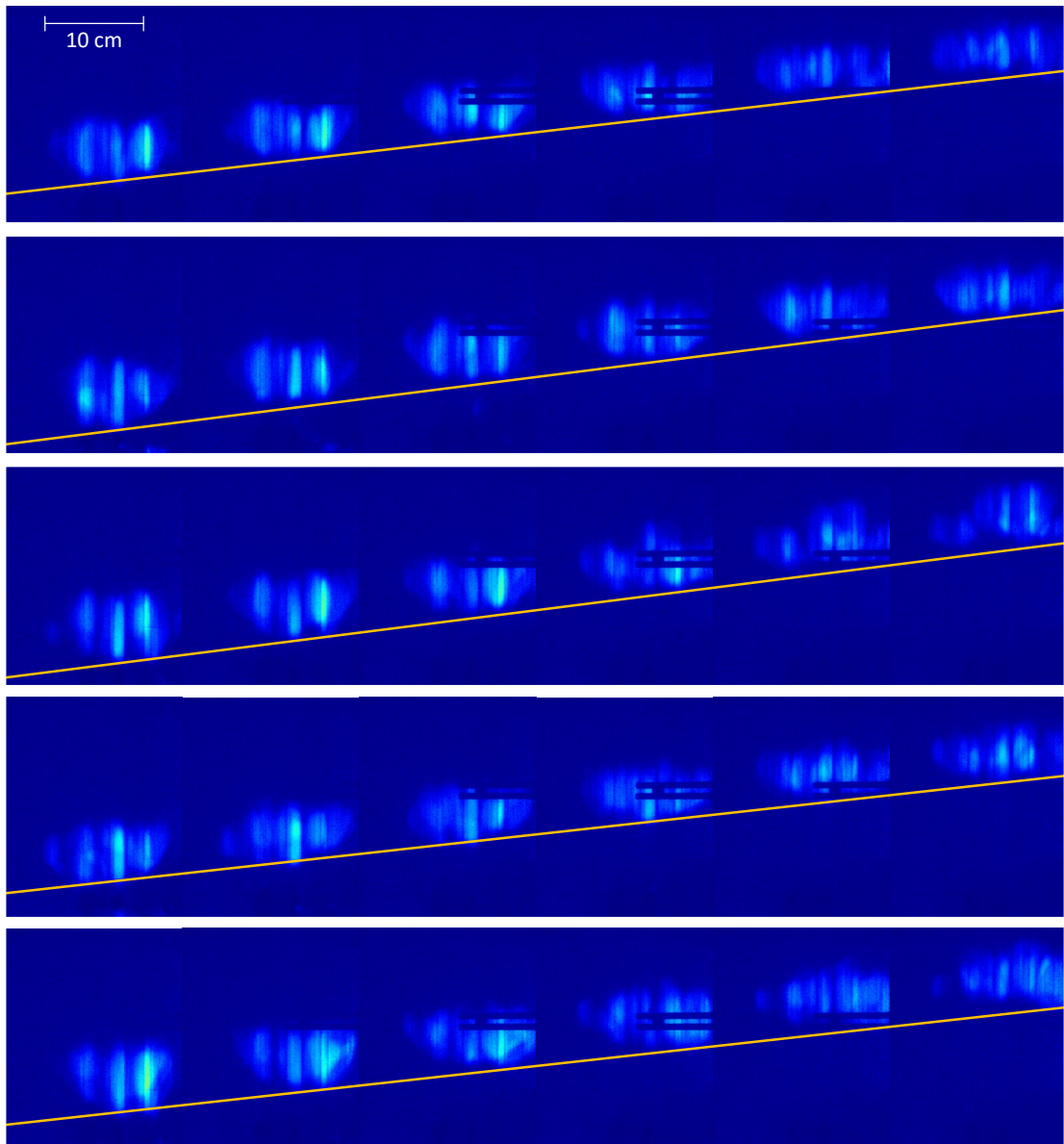


Figure 4.66: Time series of radiograms captured at 11 Hz of bubbles that were injected for 250 ms with inserted optical probe and inserted verticals.

It can be seen that the bubbles have not fully stabilized yet after they have passed through the tube spacer and change their shape as they rise. Interestingly, the bubbles seem significantly flattened, ultimately reaching an almost squared-nosed slug-like appearance, in comparison to the similar sized bubbles without internals present as shown in Figure 4.63. This is unexpected considering that the results of the tomographic reconstructions presented in Section 4.5.4 showed that the bubbles appeared elongated on average when internals were present in comparison to the measurements without internals.

A possible reason for this could be that the observed distortion of the X-ray attenuation profile, as it was discussed in Section 4.6.1, also affects the X-ray measurements that were conducted with the XR-LD setup and the corresponding tomographic reconstructions. This could potentially cause a misinterpretation of single flattened bubbles as multiple elongated ones.

Another feasible explanation could be that the smaller bubbles are mostly elongated as they rise in between the internals. As the bubbles grow through coalescence and reach sizes that extend around multiple internals, they might eventually change their shape to more flat, slug-like appearances. The reason for this could be, that the degrees of freedom for the displacement of the particles above the bubble is reduced due to the presence of internals. This could also increase the chance of particles raining through the bubble and thus causing it to split, which could partially explain the comparatively reduced rate of bubble growth when internals are present.

Therefore, it is possible that the conflicting results between X-ray tomography and radiography show different stages of the bubble growth and that locally restricted slugging may occur when vertical internals are inserted in the fluidized bed. This hypothesized fluidization regime will henceforth be referred to as local slugging.

In four of the five shown time series, which were randomly selected, the optical probe does not appear to influence the bubble flow, while it is debatable for the remaining time series shown in the third row where the bubble appears to split after it passes the probe.

The situation is different for smaller bubbles, which are significantly influenced by the probe. This can be seen in Figure 4.67, where five time series of injections over 100 ms are shown for a fluidized bed with the height of 63 cm. Note, that the bubble is unstable when it enters the frame after it had just passed the tube spacer, causing it to split into multiple bubbles and then re-coalescing as described above. Consequently, the bubbles show a dynamic range of shapes as they rise towards the probe. Their rise velocities however are stable until they reach the probe, at which point they accelerate significantly. After the bubble has passed the probe, it continues to rise with the same velocity it had before it reached the probe. This can be explained by the Venturi effect caused by the narrowing of the free cross section, through which the gas flows, by the probe.



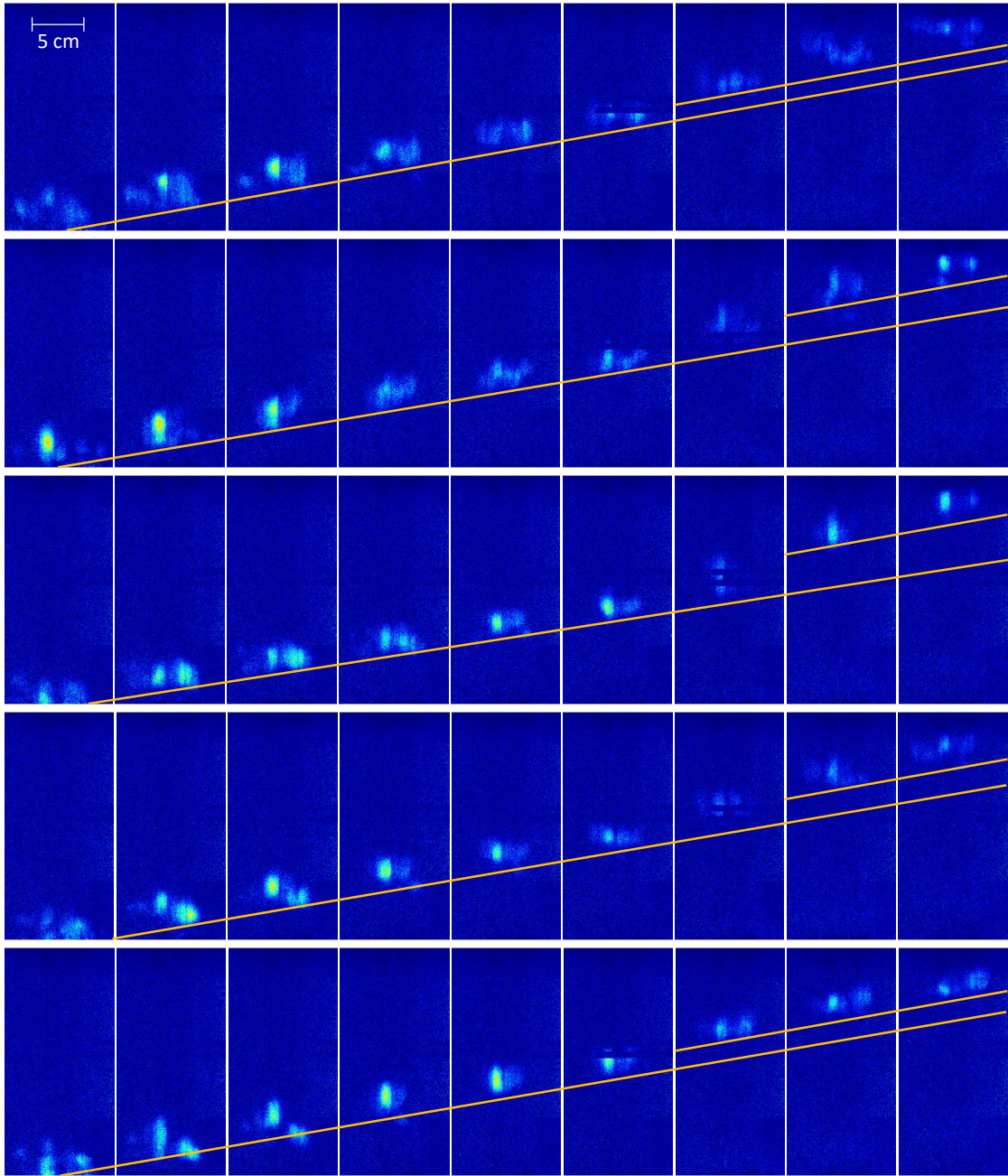


Figure 4.67: Time series of radiograms captured at 11 Hz of bubbles that were injected for 100 ms with inserted optical probe and inserted verticals.

Only injections for 100 and 250 ms were conducted with a bed height of 63 cm. For all other measurements, the bed height was 53 cm. Unfortunately, this significantly influenced the measurements, as all bubbles that were injected for times  $t \geq 20$  ms experienced an additional acceleration towards the surface and with that an elongation of their shape during their measurement with the optical probe. This problem was not predicted during the preparation

of the experiments, as only through the X-ray images it became clear that a path length of around 20 cm was not enough for the bubbles to stabilize after the injection and the influence of the tube spacer was underestimated. With an injection point at about 10 cm above the distributor plate, the optical probe had to be installed at a height of 40 cm and there was not enough bed material available to account for the increased probe height. Only for the measurements with internals, the bed height could be increased. However, to keep the measurements with and without internals comparable, most measurements with internals were carried out at the same bed height of 53 cm.

### Measured bubble properties

Figure 4.68 shows the rise velocities  $u_{br}$  and the respective volume-equivalent bubble diameters  $d_{b,eq}$  of single injected bubbles that are categorized by injection time measured with and without internals present.

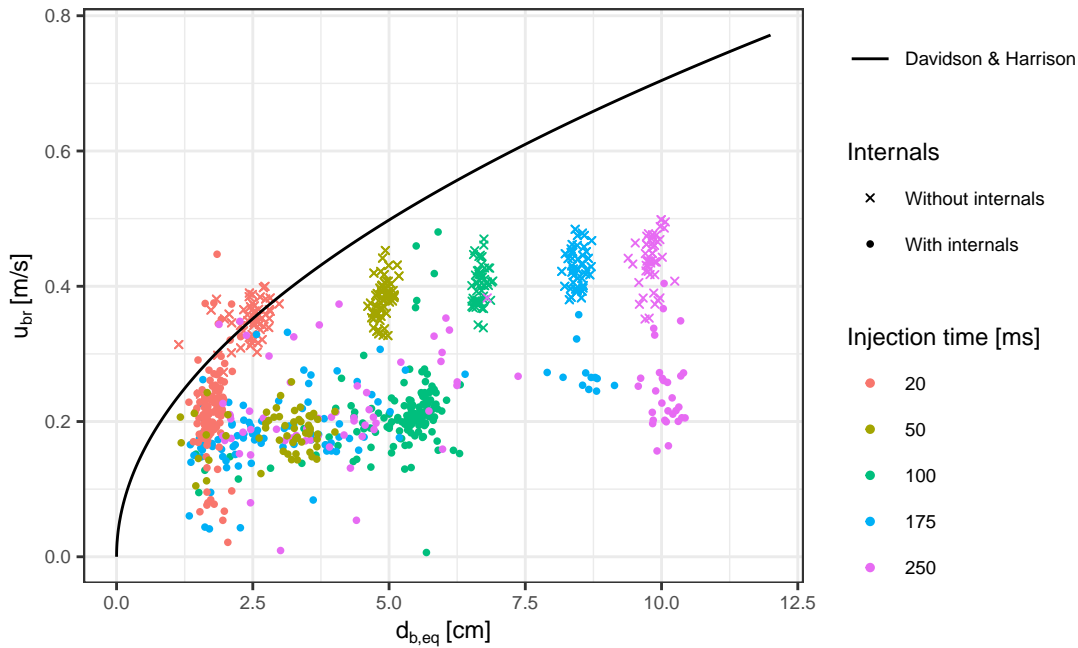


Figure 4.68: Volume-equivalent diameters  $d_{b,eq}$  and rise velocities  $u_{br}$  of injected bubbles with and without internals in comparison to the correlation proposed by Davidson & Harrison [143].

The injections without internals show narrow size distributions, verifying the accuracy of the injection mechanism and the reproducibility of the presented experiments. While there is a correlation between  $d_{b,eq}$  and  $u_{br}$ , it is inadequately described by the correlation proposed by Davidson & Harrison [143], which was introduced in Section 2.3.3, Equation 2.25 and was proven to describe the situation of a BFB in the same experimental setup as used here well, as



presented in Sections 4.3.3 and 4.5.3. Here, the measured correlation is significantly weaker. For the measurements with internals present, the rise velocities are for most cases roughly half of what they are without internals present for a given bubble size. Additionally, one can see that the size distributions are comparatively broad and outliers are frequent. Especially the bubbles that were injected for 175 ms show a comparatively large variance and are significantly smaller than their expected size range in most cases. Bubbles that were injected for 250 ms also show a broadened distribution with about two thirds of the bubbles significantly reduced in size, while the remaining third is close to the expected size range 10% above the volume-equivalent diameters that were measured without internals. The smallest class of bubbles that were measured, corresponding to an injection time of 20 ms, appear to be more stable with a comparatively narrow size distribution. The measured size distributions for injection times  $t \leq 100$  ms are reasonably stable and generally consist of smaller sizes when internals are present in comparison to the case without internals. This further supports the observation that a fraction of the injected air dissipates into the dense phase for the case with internals. The comparatively broad distributions of bubble sizes for the injections with internals are most likely the result of the disturbance caused by the tube spacer, as it was described in above, which has to be considered for all shown results of the measurements with internals present.

One important finding of the X-ray tomography measurements presented in Sections 4.3.4 and 4.5.4 was the correlation between the rise velocity and the aspect ratio of a bubble. This is especially important for the present work, considering the relevance of the shape assumption for the evaluation of the optical probe measurements. However, it has to be considered that the vertical length of the pseudo three-dimensional tomographic reconstructions that led to this correlation are directly proportional to their measured rise velocity. Any bubble, for which the rise velocity would be overestimated, would be elongated in comparison to its actual shape and vice versa. It is therefore useful, to confirm this finding with an independent method, such as the one presented in this section. In Figures 4.69 and 4.70, the aspect ratios  $l : w$  and the corresponding rise velocities  $u_{br}$  from the single injection bubble measurements as well as those retrieved from the tomographic reconstructions are presented for measurements with and without internals. The data from the tomography measurements includes bubbles from all experimental settings but was filtered to only include bubbles with rise velocities  $u_{br} \leq 1 \text{ ms}^{-1}$  and volume-equivalent diameters  $d_{b,eq} \leq 10 \text{ cm}$  to ensure the comparability of the two data sets. For the case without internals, shown in Figure 4.69, it is evident that the two independent measurements agree well. Only for the bubbles that were injected for 20 ms, no correlation between shape and rise velocity is apparent. The aspect ratios of the injected bubbles are in the range of 0.5 to 0.8 with a mean value of 0.62, which agrees well with reported values from literature for similar measurements [69], [141].

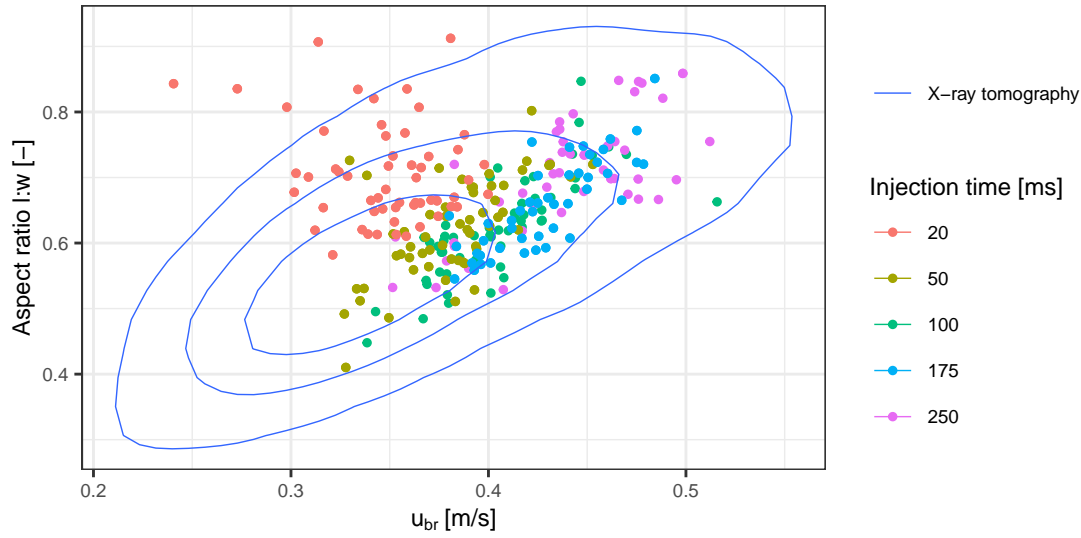


Figure 4.69: Aspect ratios  $l : w$  and rise velocities  $u_{br}$  of injected bubbles in a fluidized bed without internals in comparison to the results of the X-ray tomography measurements.

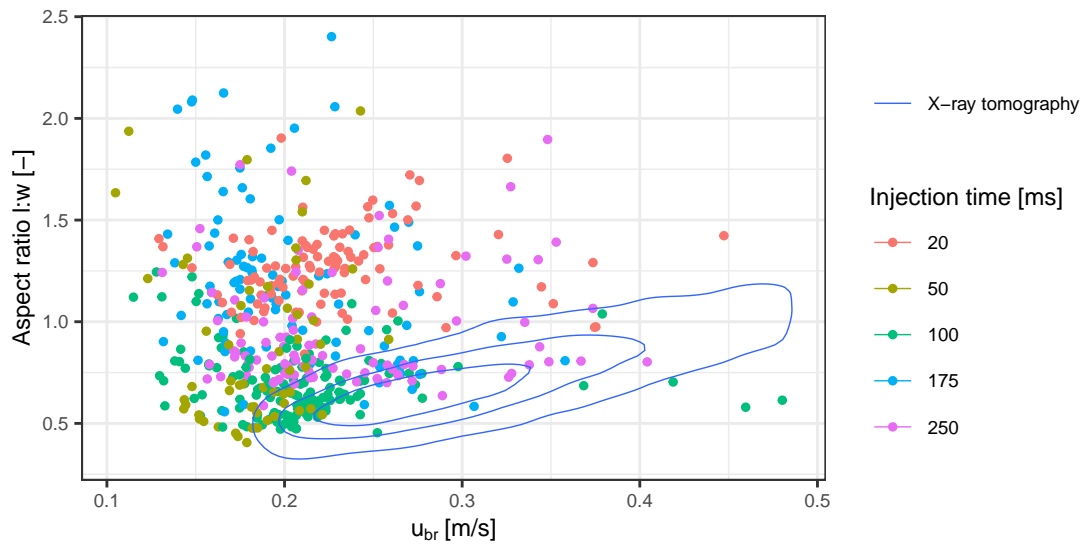


Figure 4.70: Aspect ratios  $l : w$  and rise velocities  $u_{br}$  of injected bubbles in a fluidized bed with internals in comparison to the results of the X-ray tomography measurements.

For measurements with internals, shown in Figure 4.70 there is a broad distribution of aspect ratios for the injected bubble that do not appear to be correlated to the rise velocity and are mostly outside of the range that was measured via X-ray tomography. This is not surprising, considering the unstable and dynamic situation of the bubbles that are actively splitting and re-coalescing in the region above the tube spacer, where the measurements were conducted.

Additionally, it is possible that smaller bubbles appear more elongated than they are, due to the visual interference caused by the internals.

### Verification of optical probe measurements

Another main purpose of the experiments conducted with the XR-AD setup was the verification of the optical probe measurements and the evaluation methodology that was developed in the scope of this work. The technical details of the optical probes can be found in Section 3.2 and the applied algorithms for the evaluation of the measurements are described in detail in Chapter 5, where the experiments under pressure in the pilot plant GanyMeth are presented. To summarize, the optical probes measure the presence of a bubble at vertically aligned points, with a distance of 1 cm. In this way the rise velocity and with that the pierced chord length of the bubble can be determined. For the determination of the rise velocity, a cross correlation technique is applied which also provides an assessment of how well the signals of the lower and upper probe correlate, which is used to filter measured chord lengths that likely represent bubbles that were pierced at the outer edges, where any lateral movement significantly influences the measured bubble properties. The average pierced chord length  $\bar{l}_{chord}$  for a convex body is given by Equation 4.15, where  $V$  is the volume and  $A$  is the surface area of the body [227].

$$\bar{l}_{chord} = 4VA \quad (4.15)$$

For a spherical or ellipsoidal body this results in a relation between the vertical diameter  $d_{b,vert}$  and  $\bar{l}_{chord}$  as shown in Equation 4.16. A detailed mathematical derivation of the equation can be found in the dissertation by Schillinger [71].

$$\bar{l}_{chord} = d_{b,vert} \frac{2}{3} \quad (4.16)$$

For the results from the X-ray projection image processing, the measured values of  $d_{b,eq}$  as well as  $d_{b,vert}$  are shown. In Figure 4.71, the distributions and the mean values of the chord lengths measured by means of optical probes and those of the volume-equivalent and vertical diameters that were determined through X-ray projection image processing are shown for each category of injection times. The mean values of the measured pierced chord lengths were scaled according to Equation 4.16 to estimate  $d_{b,vert}$ .

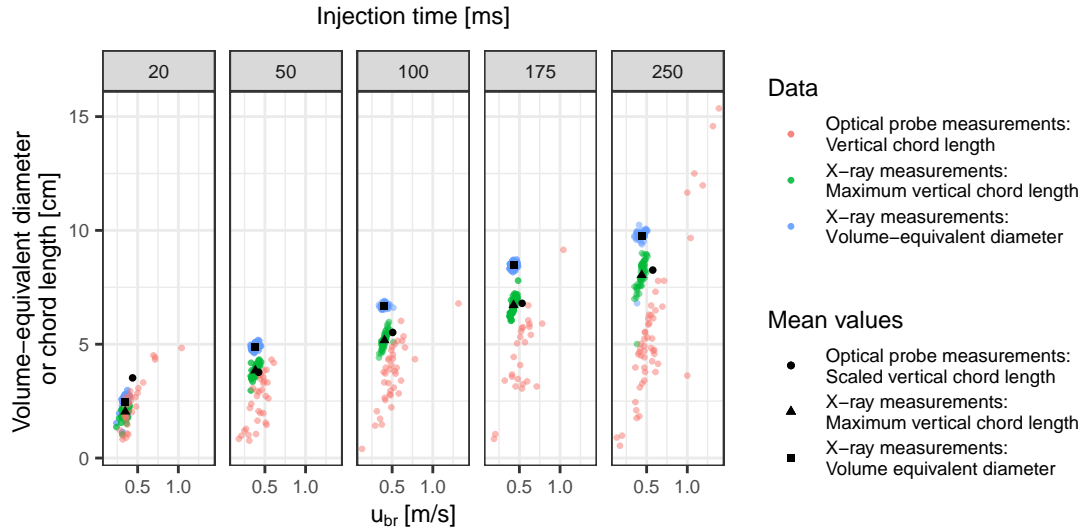


Figure 4.71: Comparison between pierced chord lengths measured by means of optical probes and the corresponding volume-equivalent and vertical bubble diameters determined by means of image analysis of X-ray radiograms.

It can be seen that rise velocities which were obtained by means of the optical probe were on average faster and show larger variances than those obtained from the X-ray projections. The measured chord lengths are also distributed more broadly in comparison to those measured via X-ray.

Broad distributions of chord lengths that are smaller than the actual vertical diameters of the bubbles were to be expected, considering that the bubbles will not always be pierced centrally and that the projected image overestimates the vertical diameter on average. However, there are a few outliers that are almost twice the length of the vertical diameter obtained through X-ray. These are the result of erroneous measurements of the rise velocity, which directly impact the determination of the chord lengths proportionally. There are also outliers with relatively short chord lengths and slow rise velocities that can be explained in the same way. Once again, this highlights the issue of the direct dependency of a measured bubble dimension, in this case the pierced chord length, from the measured rise velocity as it was already discussed for the X-ray tomography measurements. One could argue that erroneously determined rise velocities are stochastically distributed and thus even out on average. Considering one of the ambitions of this work, to determine bubble property distributions rather than mean values to enable the identification of critical fast and large bubbles, this could potentially cause misinterpretations of the data.

The synchronized measurements allow the direct comparison of the measurement of individual bubbles with optical probes and X-ray detectors. Some of the X-ray images were captured with a reduced vertical resolution at an increased frame rate of 85 Hz. While these settings did not allow the image processing with the methods described above, due to the limited field of view that is obstructed by the optical probe, they are useful for the visual analysis of the bubbles that were measured with significantly increased rise velocities by the optical probes. Figure 4.72 shows a time series of a bubble, which was injected for 250 ms, where the optical measurements resulted in a rise velocity of  $u_{br} = 1.04 \text{ m s}^{-1}$  and a corresponding chord length of 9.7 cm. The images include time stamps, indicating when the optical probe registered the bubbles for the first and last time as well as a time stamp that marks the moment the bubble has traveled 2.5 cm with  $u_{br} = 0.53 \text{ m s}^{-1}$ . Accordingly, the optical probe overestimated  $u_{br}$  significantly, which consequently lead to an overestimation of the chord length that should be in the range of 6 cm. In Figure 4.73, the corresponding normalized voltage signals of the optical probe are shown together with the shifted signal of the upper probe according to the applied cross-correlation method that was used to determine the rise velocity. The voltage signals appear to correlate very well, but one can see that the time difference between when the two probes first detect the bubble deviate from the time difference between the moments the probes last detect the bubble. Feasible explanations for this could be that the bubble was pierced peripherally, that it was changing its shape during the measurement or that it was moving laterally. A more thorough analysis of the optical probe signal evaluation is presented in Section 5.2.3, where this issue is discussed in further detail.

The results for the measurements with internals are shown in Figure 4.74 for the sake of completeness. As expected, the dynamic and unstable situation of the bubbles during the measurement and their acceleration towards the surface make the interpretation of the results useless.

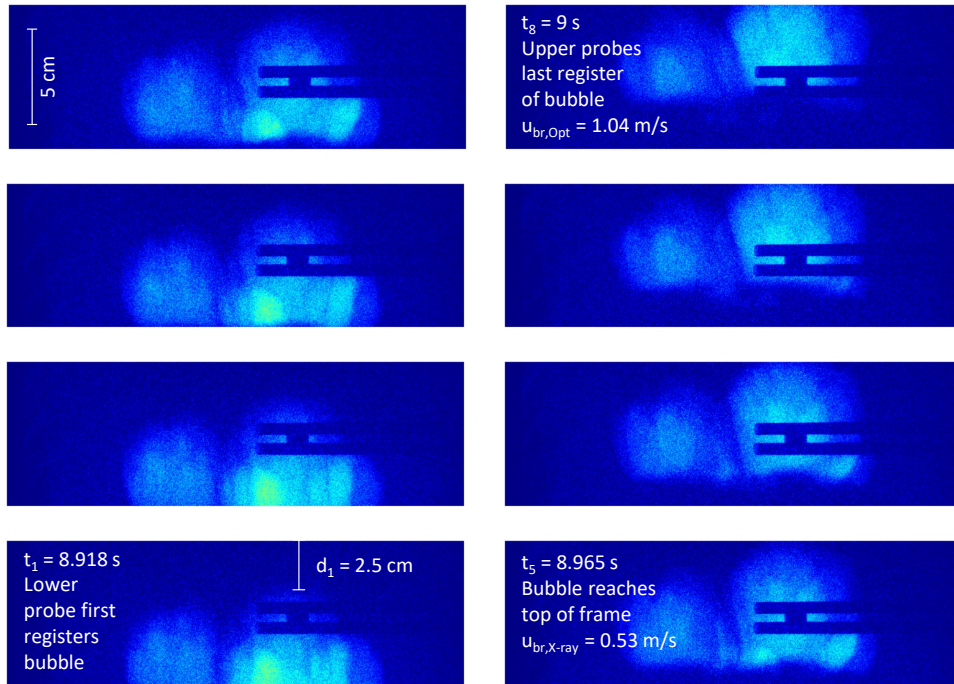


Figure 4.72: Time series of radiograms showing a bubble that is being measured by the optical probe including timestamps of the optical probe registered the bubble and a manual evaluation of the rise velocity.

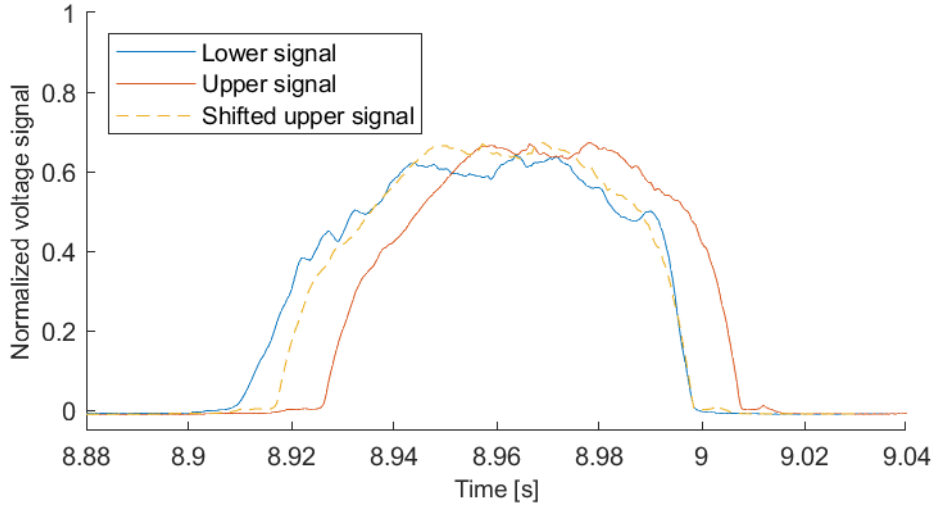


Figure 4.73: Normalized voltage signals of the optical probe for the measurement of the rising bubble shown in Figure 4.72.

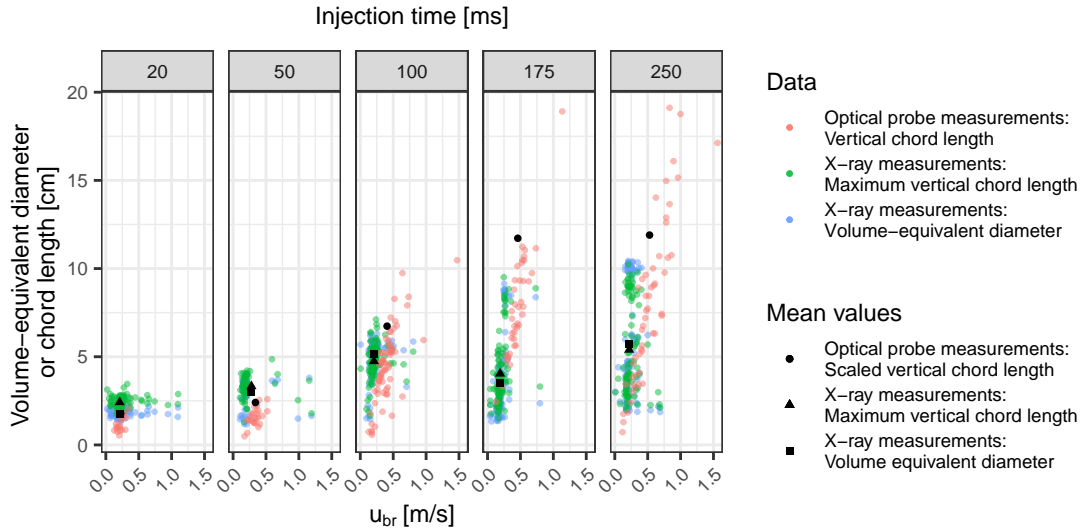


Figure 4.74: Comparison between pierced chord lengths measured by means of optical probes and the corresponding volume-equivalent and vertical bubble diameters determined by means of image analysis of X-ray radiograms with internals present.

#### 4.6.5 X-ray radiography measurements of controlled bubble interactions

The bubble injection setup allows the precisely timed consecutive injection of multiple bubbles through the same nozzle or the second available nozzle. Both nozzles can be freely positioned on a central line inside the column with the injection point positioned at a height of roughly 10 cm above the distributor plate. In this way dynamic bubble interactions can be studied in a controlled and reproducible manner. Bubbles of defined volumes can be injected in defined spatial and temporal distances and observed by means of X-ray radiography. The availability of three viewing angles enables a three-dimensional tomographic reconstruction of the dynamic bubble interaction. An algorithm that would allow this is currently under development in a collaboration between the Technical University Delft and the Dutch national research institute Centrum Wiskunde Informatica (CWI). The evaluation of such measurements is also possible by means of image processing, similar to the methods described in Section 4.6.3. However, additional adaptations of the respective algorithms are required to track multiple bubbles and recognize the coalescence, which will be implemented in the future. Considering the limited field of view, only the interaction of comparatively small bubbles with injection times in the range of 100 ms can be captured in this manner as bigger bubbles will not be completely within the frame throughout the interaction. Nonetheless, a qualitative assessment through visual examination of such measurements is very useful to confirm assumptions that were made about the hydrodynamics within BFB for the evaluation of the X-ray tomography and optical probe measurements in the scope of this thesis or to explain some of the observations.

Additionally, the data could serve as a precise benchmark for CFD simulations, where the highly controlled settings and the high resolution images from multiple angles would allow an accurate comparison between the simulation and the measurements. All measurements presented in the following were captured at full resolution with a frame rate of 22 Hz and the center of the detectors positioned at height of 40 cm above the distributor plate. The images show bubbles that were injected through the same nozzle.

In Figure 4.75, randomly selected time series of two bubbles that were consecutively injected for 100 ms with a time gap of 150 ms in between the injections are shown. The top and the bottom rows show bubbles that were fairly stable throughout the interaction, whereas the upper bubble in the time series shown in the middle row split before the coalescence. For the more stable situations in the top and bottom row of the figure, one can see that the upper bubble rises with a steady velocity and maintains the typical spherical cap shape until the moment the bubbles coalesce. However, the lower bubble accelerates and elongates significantly as it approaches the upper bubble. Similar observations have been made by Boyce *et al.* who conducted comparable experiments for which a rapid magnetic resonance imaging (MRI) setup was applied [125]. The controlled coalescence of bubbles that were injected for 250 ms with a time gap of 300 ms is presented in Figure 4.76 in form of three randomly selected time series that show different stages of the coalescence. Again, the upper bubble does not appear to be affected prior to the coalescence, while the lower bubble accelerates and elongates. Due to the comparatively larger sizes of the bubbles one can see more details of the dynamics of the coalescence. Especially in the time series shown in the middle row of the figure, it seems like rigorous mixing of the dense phase and bubble phase takes place for a brief moment. The same time series also shows that the lower bubble has split during its approach towards the upper bubble and a second coalescence follows the first.

The described examples demonstrate the highly dynamic nature of coalescence events. Given the rate at which the mean bubble diameters grow, in respect to the height within the bed, indicates the high frequency at which coalescence occurs, which are known to be the main mechanism responsible for bubble growth in BFB [73]. The acceleration and elongation of bubbles within the drag of other bubbles likely explains part of the fast and elongated bubbles that were measured via X-ray tomography as presented in Sections 4.3.4 and 4.5.4.

While accelerated bubbles pose the risk of bypassing reactants through a catalytic BFB reactor due to their decreased residency time, it is known that coalescences and dynamic bubble interactions in general enhance the mass transfer significantly.



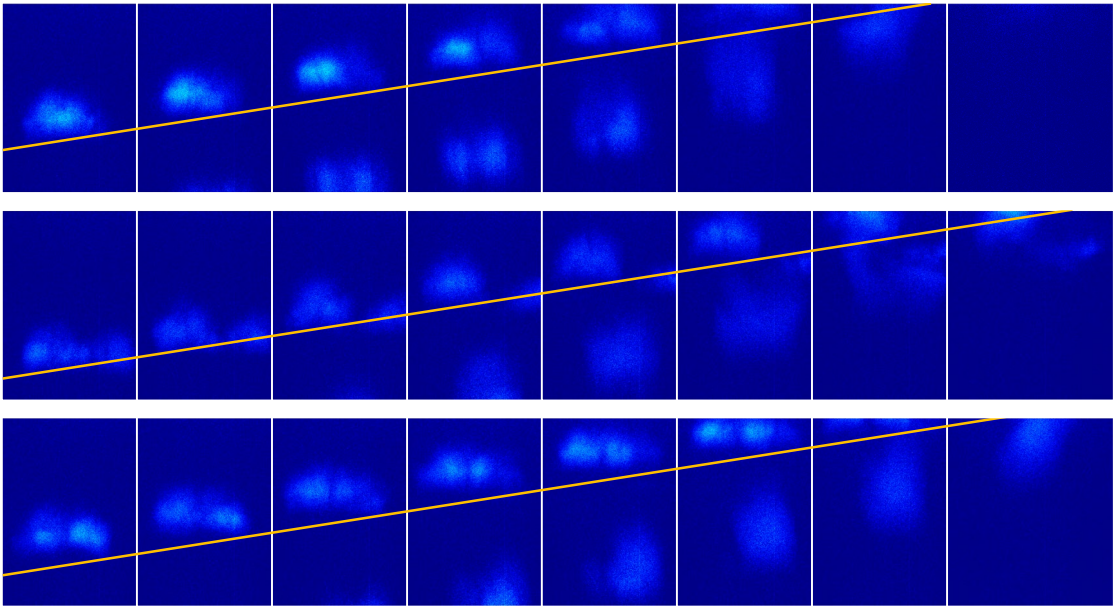


Figure 4.75: Time series of radiograms showing the dynamic interaction between two bubbles that were injected for 100 ms each through the same nozzle, with a time gap of 150 ms in between the injections.

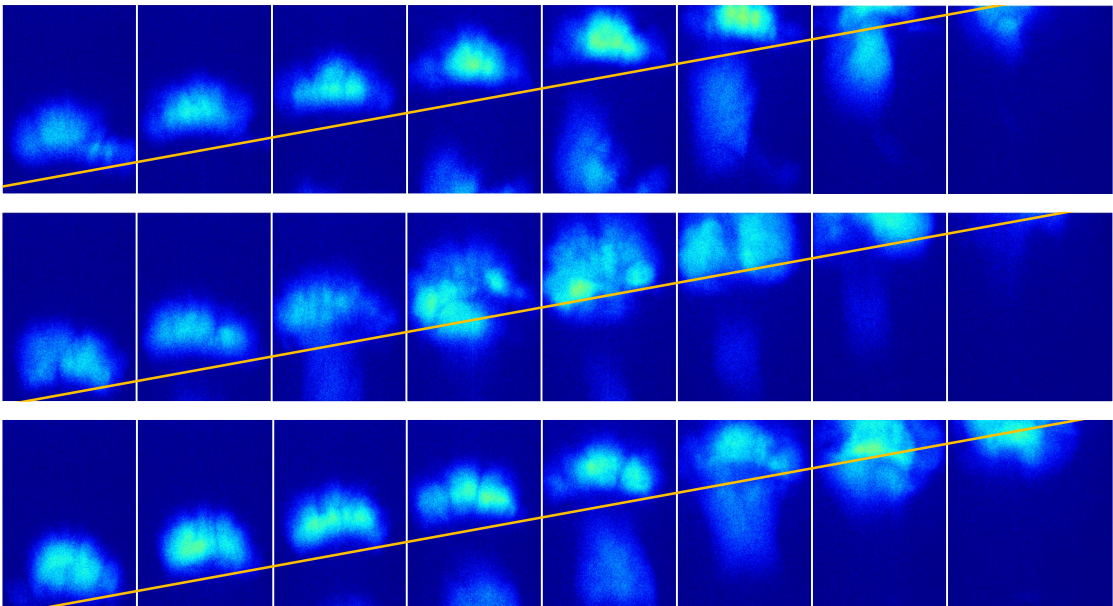


Figure 4.76: Time series of radiograms showing the dynamic interaction between two bubbles that were injected for 250 ms each through the same nozzle, with a time gap of 300 ms in between the injections.

The reason for this is an increase of the throughflow which consequently increases the convective mass transfer [126], [127] as well as an enhancement of the interface diffusive mass transfer [126] through the intensified circulation of the gas within the bubble and the fast replacement of particles within the boundary layer of the bubble due to its fast velocity.

It is therefore not trivial to derive the risk of bypassing reactants from the bubble size and rise velocity distributions that were measured through X-ray tomography, as bubbles that may be considered critical due to their fast rise velocity could actually be bubbles that are actively coalescing and thus show increased mass transfer rates. To account for the increased mass transfer due to dynamic bubble interaction Sit & Grace [126] suggest an enhancement factor of 1.32 for the mass transfer coefficient in BFBs.

## 5 Hydrodynamic measurements at the GanyMeth pilot plant

Fundamental hydrodynamic characteristics of BFB reactors can be measured in cold-flow models of the reactor. However, some aspects, such as the influence of elevated pressures and temperatures, and of reactive conditions, which in the case of the methanation reaction cause a significant volume contraction of the reacting gases, cannot be investigated in such model reactors. The flow patterns and general hydrodynamic properties are also influenced by the measurement height within the bed. *e.g.* fluidized beds may be freely bubbling at lower heights and reach a slugging state at higher heights after bubble sizes reach certain diameters in the range of the column diameter by means of coalescence. Therefore, a pilot plant reactor is required, which allows the safe operation and measurements at reactive conditions and increased bed heights.

For the fluidized bed methanation research in the TCP group at PSI, a pilot plant, referred to as GanyMeth, has been constructed, at which such measurements can be performed. In the GanyMeth plant, X-ray measurements are not feasible, due to the steel walls of the reactor. To enable hydrodynamic measurements under reactive conditions at temperatures of up to 400 °C and pressures of up to 12 bar, an optical measurement system was developed that can sustain such environments. A detailed description of the GanyMeth plant and the optical probes that were used, can be found in Sections 3.1 and 3.2. Note, that all stated reactor pressures refer to their absolute value henceforth.

In this chapter, the influence of the pressure as well as of the Geldart type of the bed material are investigated by means of optical probe measurements. First measurements with increased pressures of up to 5 bar have been conducted prior to this work by Schillinger *et al.* [72]. One of the observations the author reported was a significant deviation between measurements that were conducted by means of X-ray tomography in the cold-flow model and the optical probe measurements in the pilot plant at comparable measurement heights and otherwise identical conditions. A comparison of the results is shown in Figure 5.1, where the colored areas indicate

deviations between the two methods. As a possible explanation, the author suggested that elongated bubbles, marked in green, would result in small values of  $d_{b,eq}$  in comparison to the respective chord length, whereas flattened bubbles, marked in yellow, would lead to chord lengths that are smaller than the corresponding values of  $d_{b,eq}$ .

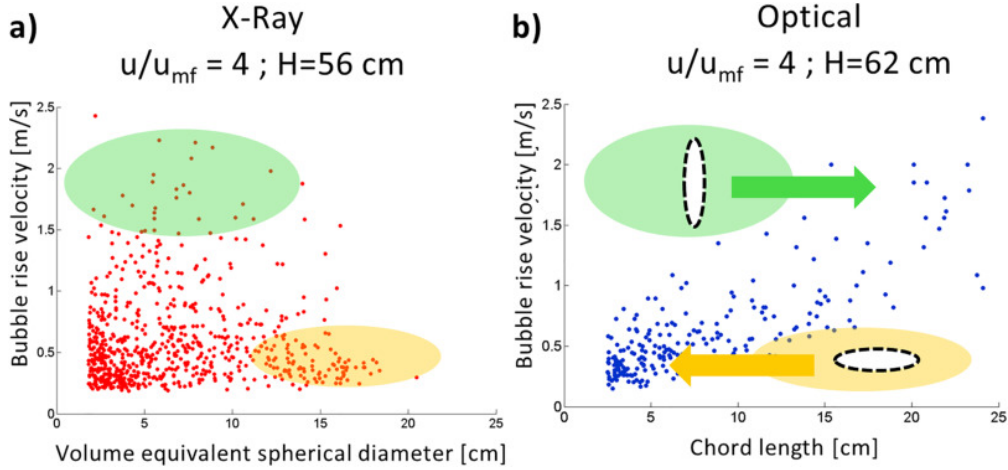


Figure 5.1: Results from previous publications, showing a comparison of distributions of bubble properties (bubble rise velocity and volume equivalent diameters) obtained via X-ray tomography reconstructions in a model reactor (a) and with optical probe measurements in a pilot plant of the same geometric dimensions (b) at similar experimental settings (fluidization number  $u/u_{mf} = 4$  and measurements heights of 56 cm for the X-ray measurements and 62 cm for the optical measurements). Illustration from Schillinger *et al.* [72]

As stated in Section 1.4, the investigation of this contradiction is one of the main research questions of the present work and led to a detailed overhaul of the X-ray tomography evaluation methods as presented in Chapter 4. Consequently, the methodology of the optical probe measurements are investigated in similar detail in the following.

Optical probes allow the local measurement of the rise velocity and the pierced chord length of bubbles as well as general bubble hold-up at a specified point within the reactor. The one-dimensional nature of such measurements is advantageous on the one hand, as it allows the precise localization of the measured bubble properties within the reactor. On the other hand, it is constrictive as only pierced chord lengths are measured and complex statistical transformations are necessary to estimate the distribution of the volume-equivalent diameter from a measured chord length distribution. It is also necessary to measure at multiple heights and radial positions within the fluidized bed to obtain a matrix of data points that is representative for the asymmetric flow patterns that are typically found in BFBs. Optical probes are inserted in the fluidized bed and therefore may influence the local flow. For the given situation within the GanyMeth pilot plant, where the optical probe is inserted in between vertical heat exchanger tubes, the influence can be significant due to the local narrowing of the

cross sectional area. In Section 4.6.3, it could be shown that bubble with volume-equivalent diameters  $d_{b,eq}$  in the range of approximately 4-5 cm accelerate significantly, as they pass the optical probe, while larger bubbles with  $d_{b,eq} \approx 10$  cm appear to not be influenced. There are also uncertainties about the influence of the vertical internals on the shape of the bubble, as the evaluation of the X-ray tomography and radiography measurements presented in Chapter 4 produced partly inconsistent results. The X-ray tomography measurements showed that bubbles were typically elongated when internals are present in comparison to measurements at the same height and fluidization numbers without internals. In contrast, the X-ray projections of single injected bubbles in a fluidized bed with internals show a flattened appearance in comparison to those that were measured without internals present. These uncertainties require further investigations in the future to verify some interpretations made in this chapter, specifically about the possible onset of slugging or local slugging fluidization.

### 5.1 Review on the influence of the pressure on the hydrodynamics in fluidized beds

It is well known that the pressure can significantly influence the hydrodynamics in fluidized beds. Based on the ideal gas law, the density of the gas is proportional to the pressure, while the change of the viscosity of the gas with the pressure is negligible in comparison. Accordingly, an increase in pressure increases the drag forces exerted on the particles. The implications of increased pressures on the fluidized bed are manifold but are not yet fully understood and seemingly conflicting observations have been reported. For Geldart type A particles, it has been observed that the fluidization becomes smoother with increasing pressures and that the gas velocity  $u_{mb}$  at which bubbling occurs as well as the bed expansion is increased [228]–[231]. Some authors found that particles, which behave like Geldart type B material under ambient conditions, exhibit smooth and homogeneous fluidization at elevated pressures, therefore behaving more like Geldart type A material [95], [228], [232]. Sobreiro & Monteiro [233] observed both a decrease and increase of  $u_{mb}$  with the pressure for different types of particles.

The properties of the bubbles may also change with the pressure. It is often reported that the bubble sizes decrease with increasing pressures [223], [229], [234]–[236] and that the size decrease is more significant for smaller particles [234], [235]. However, some researchers found that Geldart type B powders do not show an influence of the pressure on the bubble sizes [237]. Kawabata *et al.* [238] observed, that the bubble volumes do not change with the pressure but that the bubbles flatten in shape, which may explain why some authors measured decreasing bubble sizes if they measured pierced chord lengths. It has also been reported that the bubble sizes may first increase and then decrease with the pressure or vice versa for a

given bed material [228], [236], [239], [240]. For the influence of the pressure on the bubble rise velocities, the reports are also inconsistent. While some authors reported an increase of the rise velocities with the pressures [241], others stated the opposite [242] and some observed both an increase and a decrease of the rise velocity for the same bed material, depending on the pressure levels [236], [239], [240].

A comprehensive summary of reported findings was provided in the review by Shabanian *et al.* which addresses the influence of the pressure, the temperature and interparticle forces on the hydrodynamics in fluidized beds [243].

The many conflicting reports on the influence of the pressure on fluidized bed characteristics, which can have significant impacts on the performance of catalytic BFB reactors and the fact that no studies on the influence of the pressure on the hydrodynamics of BFB reactors with vertical internals could be found in the literature, initiated the experimental investigations presented in this chapter.

## 5.2 Preparation of the measurements

To ensure accurate and statistically robust measurements, comprehensive efforts were made for the development of the experimental methodology. This included a complete overhaul of the electronic components of the optical probe sensor system, a detailed revision and adaptation of the algorithms that were applied for the evaluation of the raw data, cross verification with independent X-ray measurements as they were presented in Chapter 4 as well as several series of preliminary measurements to perform the design of experiments.

### 5.2.1 Overhaul of the electronic components of the optical sensor system

A series of first preliminary measurements revealed several concerns towards the data quality. There was a broad variance of the baseline voltage, which corresponds to complete reflection of light for the 12 sensor outputs, some of which were close to the maximum measurable voltage of the data acquisition hardware resulting in low signal to noise ratios and cut off signals. The measurements showed unsteady baselines and unstable fluctuating signals when a bubble was detected with significant variations of the signal quality between lower and upper sensor head of the optical probe. Consequently the signal deviated significantly from an ideal semi-binary signal that would be desired for the measuring a two phase system. Initially, it was uncertain, whether these issues were caused by hydrodynamic effects, such as particles raining through the bubbles, lateral movement of the bubbles or fluctuating distances between the probe and the opposing edge of the bubble. Additionally, the data showed considerable noise in general which required proportional filtering and smoothing of the signals.

Consequently, the electronic components of the optical probe sensor system were revised in a systematic manner. A new voltage divider was installed, so that the maximum voltage signal could no longer surpass the maximum voltage the data acquisition system can measure. Potentiometers were installed through which the voltages powering the laser sources and thereby the laser intensity could be adjusted for each laser diode individually. This allowed the calibration of the baseline, to account for variances of the optical pathway leading from the laser source through the glass fibers to the probe head into the bed and reflected back through glass fibers to the optical sensor. A test bench, referred to as Optimus, was built to test various combinations of chosen laser sources and photo sensors for the measurement of the reflected light from a white disc, which included gaps of defined width and was rotated in specified velocities to simulate the measurement of ideal bubbles of certain sizes and rise velocities. For the optical coupling, capsules were designed to house the laser and photo diodes, and to fix the end of the glass fiber bundles in direct contact to the respective diode with a screw mechanism. The setup is shown in Figure 5.2.

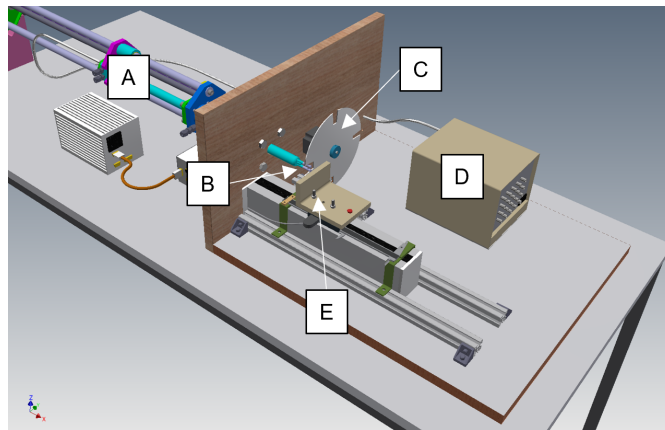


Figure 5.2: Illustration of the Optimus test bench. A: Optical probe including entire optical pathway; B: Lower and upper sensor head; C: Rotating disc with gaps; D: Electronic components of the sensor system; E: Linear guide for possible bubble depth simulations.

The tests showed, that the selected photo sensors could measure the simulated bubbles with rise velocities of up to  $5 \text{ ms}^{-1}$  precisely. It could also be shown that the fluctuation of the baseline voltage comes from the variation of the reflective properties of the rotating disc. This can be seen clearly in Figure 5.3, which shows a sample measurement taken at simulated rise velocity of  $3.7 \text{ ms}^{-1}$ , where the fluctuation of baseline is repeated precisely with every rotation. Furthermore the amount of noise could be reduced significantly, while the signal to noise ratio was increased significantly through the application of a more powerful laser.

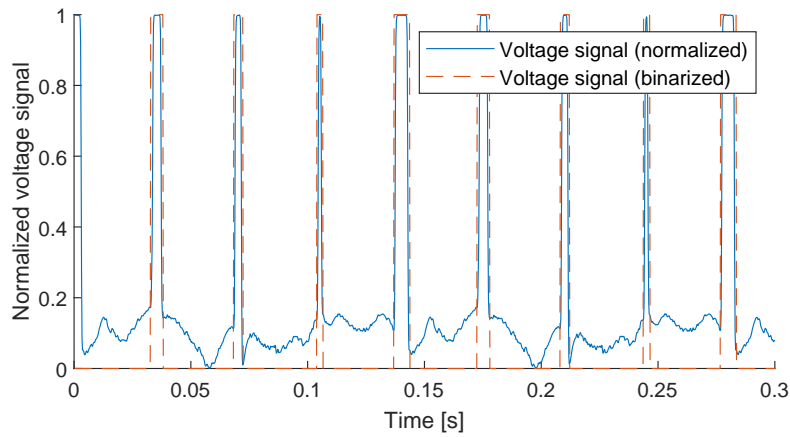


Figure 5.3: Sample of the normalized and binarized voltage signal for a measurement at the Optimus test bench with a simulated rise velocity of  $3.7 \text{ m s}^{-1}$ .

### 5.2.2 Revision of the evaluation algorithm

In the dissertation by Schillinger [71], an algorithm for the evaluation of the optical probe measurements at the GanyMeth plant was developed. In a first step, the signal is binarized to distinguish between dense phase and bubble phase. Figure 5.4 shows the binarization steps, which are briefly explained in the following. A more detailed description can be found in the dissertation by Schillinger [71].

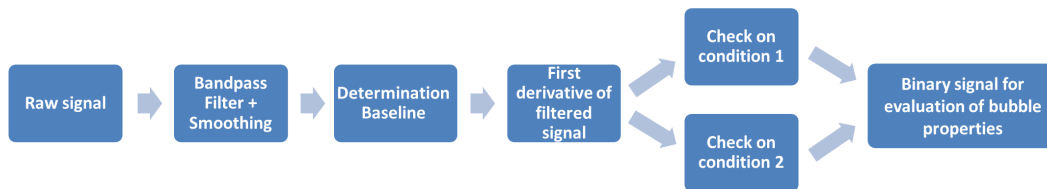


Figure 5.4: Process scheme to convert the raw signal of the optical sensors into a binary signal, Illustration from Schillinger [71].

### Description of the original algorithm

In a first step, a band pass filter and subsequent smoothing of the signal is applied on the raw voltage signal to remove low frequencies, corresponding to a drift of the baseline, and high frequent measurement noise. Then, a histogram analysis of the signal is performed to determine the baseline of the signal through the voltage bin that is found most often in the signal. For the identification of the beginning and the end of bubble events, two conditions were defined that have to be fulfilled. The first condition states that the first derivative of the signal must exceed a specified threshold to be considered a possible beginning of a bubble



event and must be lower than a second negative threshold to define the possible end of a bubble event. The second condition is that the start and end of bubble events have to be close to the baseline. Otherwise any sharp fluctuations of the signal that are not close to the baseline and therefore clearly represent the measurement of the bubble phase would interrupt the definition of a single bubble. The corresponding sections of the signals between identified start and end points of bubble events are then set to a value of one for binarized signal. In the following, the terms "lower" and "upper" signal will be used to refer to the signals that correspond with to the lower and upper sensors that are coupled vertically in a fixed distance for each optical probe.

After the signal has been binarized, the identified bubble events are linked by pairing any bubble event from the lower binary signal with the bubble event from the upper binary signal that is the closest in the time series after the lower signal bubble event. The rise velocity is then determined through the time difference between the onset of the bubble event in the lower and the upper binarized signal and the distance of 10 mm between the two measurement points. Once the rise velocity of a bubble event is available, it is applied on the mean duration of the bubble event in the lower and upper signal to receive the pierced chord length.

### **Identified issues within the original algorithm**

In reality, a precise definition of the start and end of a bubble is not feasible, due to the random fluctuations of the reflective properties of the bed material, random density fluctuations within the dense phase, and the superimposed noise that affects the signal and requires filtering which also affect the definition of the starting point of the bubble. These factors can lead to an arbitrary random shift of the definition of the start of the signals, which is biased towards shifting the signals in a way that favors an increase of the rise velocity rather than a decrease. This is because a shift of the signals in a way that would increase the resulting rise velocity by a certain factor would require a shift by less time steps than a reduction of the rise velocity by the same factor would need. Therefore, this method would on average overestimate the rise velocity and in consequence also overestimate the resulting pierced chord lengths. This shift is often significant, as can be seen in the example signals presented in Figure 5.5, where the definition of the start and end of the bubble event in the lower and upper signal cannot be clearly determined and appear arbitrarily shifted. In this case, the start and end points of the bubble event were identified in a way that lead to the upper binary signal beginning before the lower binary signal, which clearly does not represent the order of the voltage signals that show the expected order of events.

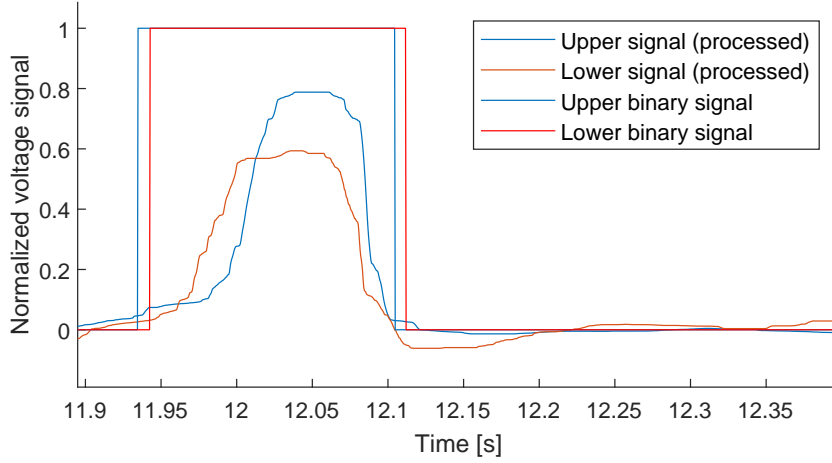


Figure 5.5: Normalized lower and upper voltage signals of a measured bubble that are filtered and smoothed, and the corresponding binarized signals. The shown measurement was performed prior to the overhaul of the electronics and the evaluation algorithm.

### Revision of the algorithm

A much more robust way to determine the rise velocity of a measured bubble is the application of a cross-correlation technique. This was implemented as follows. After the start and end points of bubble events have been identified according to the methods described above, the corresponding lower and upper signal sections of each identified bubble event are extracted and evaluated individually. After the lower and upper signal sections have been normalized, their correlation is determined according to Equation 5.1, where  $x$  is the normalized lower signal,  $y$  is the normalized upper signal,  $\bar{x}$  and  $\bar{y}$  are their respective mean values, and  $\sigma_x$  and  $\sigma_y$  are their respective standard deviations.  $X_{cor}(\delta)$  is calculated for all values  $\delta \in [1, n]$ , which determines the shift of the upper signal by  $\delta$  time steps. For a perfectly correlated signal, the value of  $X_{cor}$  becomes 1.

$$X_{cor}(\delta) = \frac{\frac{1}{n} \sum (x_i - \bar{x})(y_{(i+\delta)} - \bar{y})}{\sigma_x \sigma_y} \quad (5.1)$$

The corresponding rise velocity can then be calculated according to Equation 5.2, where  $d_{sensors}$  is the distance between the measurement points of the lower and upper signal,  $f$  is the measurement frequency and  $\delta_{max}$  is the number of time steps the upper signal has to be shifted to maximize  $X_{cor}(\delta)$ .

$$u_{br} = \frac{d_{sensors} f}{\delta_{max}} \quad (5.2)$$

Two examples that show the normalized upper and lower voltage signals as well as the shifted upper signal resulting from the application of this method are shown in Figure 5.6 and 5.7.

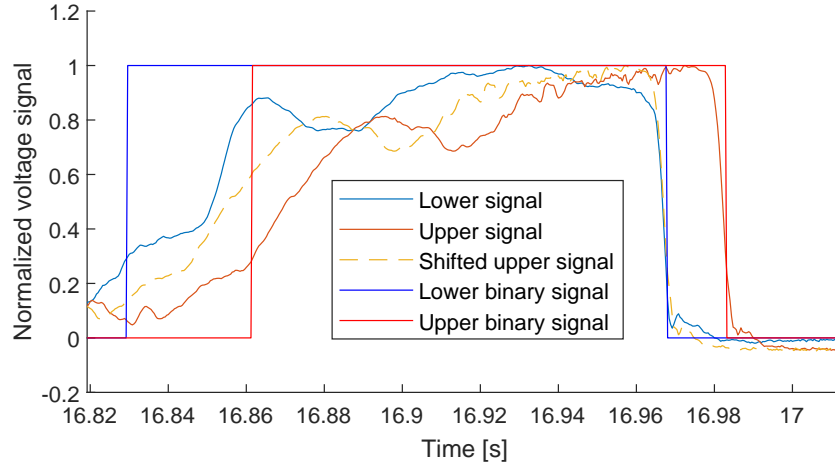


Figure 5.6: First sample showing normalized voltage signals from the measurement of a bubble and the shifted upper signal resulting the application of the cross correlation method for the determination of  $u_{br}$ .

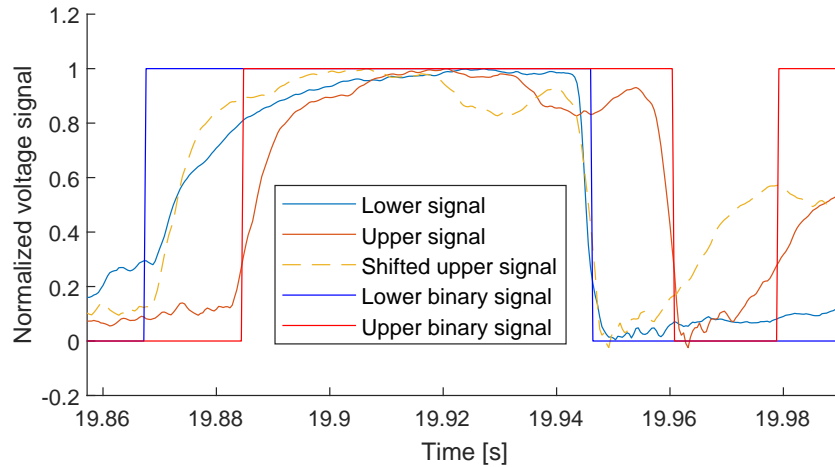


Figure 5.7: Second sample showing normalized voltage signals from the measurement of a bubble and the shifted upper signal resulting the application of the cross correlation method for the determination of  $u_{br}$ .

Both examples show a comparatively high correlation between the upper and lower signal at the end of the identified bubble events, whereas their starting points are not very well defined and correlate less. This is especially true for the sample shown in Figure 5.6. The reason for the differing signal quality at the start and at the end of a bubble event could be explained by the spherical cap shape that is typical for bubbles in fluidized beds and which was also observed by means of X-ray radiography for the given bed material, as shown in Section 4.6.4. The bubble is first pierced in the spherical curved upper part of the bubble,

leading to a delayed onset or more irregular shape of the signal. When the bubble end passes the probe, the descend is abrupt due to the comparatively flattened bottom of the bubble. This is shown in Figure 5.8, where the position of the probe relative to the bubble is illustrated for consecutive time steps.

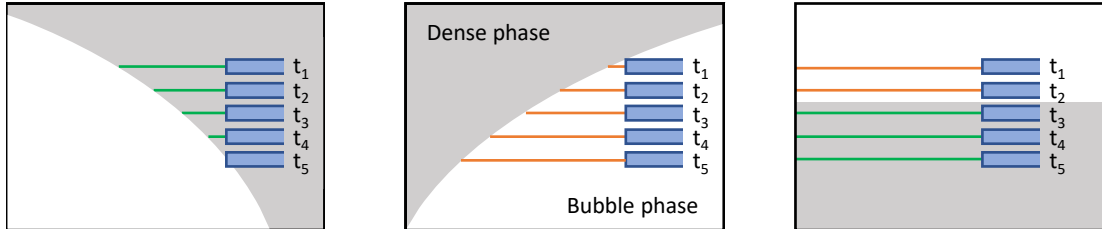


Figure 5.8: Illustration of the beginning and end of the measurement of a bubble by means of an optical probe.

One can argue that the end of a bubble event is better suited for the measurement of the rise velocity as it is less affected by lateral movement of the bubble, fluctuations of the bubble shape and shorter in duration. The application of the proposed cross correlation method, ensures that the rise velocity is determined accordingly, especially when it is applied on the first derivatives of the signals rather than the signals themselves, given the steep slopes of the signals at the end of a bubble event.

Other authors have also applied such cross correlation methods [132], [142], [244] for similar measurements, however the technique is usually applied on the entire duration of signals to determine the mean rise velocity, which is then applied on the duration of the individually identified bubble events to calculate the mean pierced chord length. In this work however, in analogy to the evaluation of the X-ray tomography measurements, the rise velocity of each bubble is determined individually. As mentioned before in the discussion of the X-ray tomography results, it could be argued that the rise velocity of an individual bubble is merely a stochastic quantity. However, the correlation between the rise velocity and the shape as well as the size of the bubble that was measured by means of X-ray tomography as presented in Sections 4.3 and 4.5 has to be considered here. As stated before, for the transformation of pierced chord length distributions to the corresponding distributions of the volume-equivalent bubble diameters, knowledge of the shape of the bubble is crucial and ignoring these correlations or only applying them on the measured mean values would distort the transformed distributions.

### 5.2.3 Limitations of the optical probe sensor system

For the determination of individual bubble rise velocities with optical probes, one has to consider the limitations of such one-dimensional measurements of complex dynamic multi-

phase flows. For instance, lateral movement of bubbles can cause false measurements of the rise velocity, when the lower and upper probe pierce the bubble at different radial positions of the bubble. Additionally, the bubble may experience dynamic transitions during the measurement, such as the change of its shape and rise velocity as well as bubble splitting and coalescence, as it was discussed in Section 4.4.3 and shown to occur during dynamic bubble interactions in the X-ray radiographic measurements presented in Sections 4.6.2 and 4.6.5.

Both, the measurement of bubbles that were pierced sideways during lateral movement of the bubble and the measurement of dynamic bubble events as described above would typically result in different dwell times for the lower and upper sensor. This could be identified by determining the ratio  $\tau$  between the difference of the lower and upper signal duration of a bubble event  $\Delta t_{Signal}$  and their mean  $\bar{t}_{Signal}$ , as defined by Equation 5.3, for each individual bubble. The value of  $\tau$  is in the range between 0, corresponding to no differences in the lengths between the lower and upper signal, and 2, corresponding to the border case of infinite differences between the lower and upper signal lengths. The case  $\tau = 1$  means that one of the signals double the length of the other.

$$\tau = \frac{\Delta t_{Signal}}{\bar{t}_{Signal}} \quad (5.3)$$

Additionally, the lower and upper signals would differ qualitatively for such events. The maximized correlation  $X_{cor}$  between the lower and the shifted upper signal would be lower in comparison to bubbles that transited the probe solely in vertical direction with a steady rise velocity and shape.

A filter was applied, to remove any measured bubble from the data set, according to specified thresholds for  $X_{cor}$  and  $\tau$ . Figure 5.9 shows distributions of the measured chord lengths and rise velocities for all investigated radial positions and heights for a pressure of 1.14 bar. Further details on the experimental settings can be found in Table 5.5 in Section 5.2.5.

Each subplot corresponds to different ranges of  $X_{cor}$  and  $\tau$  and shows the count density of the bubble properties. The color coding signifies the overall count of bubbles in each subplot. The distribution shown in the bottom left of the figure represents bubbles with the lowest  $X_{cor}$  and the maximum  $\tau$ , whereas the distribution in the top right represents bubbles that are the least affected. One can see that the count density of unaffected bubbles is comparatively high and that small and slow bubbles appear to be affected more by reduced data quality, which indicates that lateral movement and piercing of the bubbles close to their edges is indeed the likely cause, as it is more likely to occur for bubbles that are small in comparison to the probe dimensions.

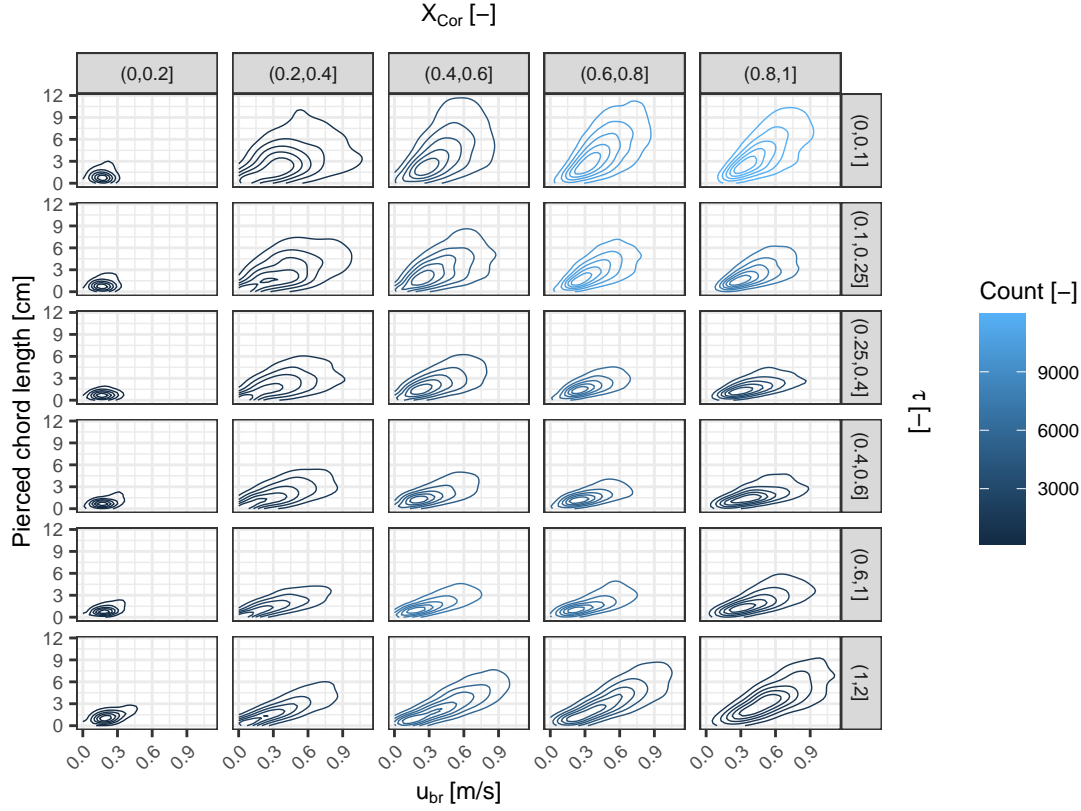


Figure 5.9: Density distributions of the measured pierced chord lengths and rise velocities of the bubbles, categorized by specified ranges of  $X_{Cor}$  and  $\tau$ .

To further quantify the limitations of the optical probes, a Monte Carlo study was performed to investigate the impact of the lateral movement on the ratio of the pierced chord lengths between the lower and upper sensor. A number of 1,000 symmetrical bubbles were simulated for each specified category of  $d_{b,horiz}$  in the range of 0.1 to 15 cm. For each bubble, a random point  $P_{lower}$  was sampled as the location, where the lower sensor head pierced the bubble. Then the point  $P_{upper}$  was determined by sampling a random angle and a random distance  $r_{lm}$  for the lateral movement, which was sampled from the distributions that were measured by means of X-ray tomography in the experiments shown in Section 4.5.4 for the given range of bubble sizes. This procedure is illustrated in Figure 5.10.

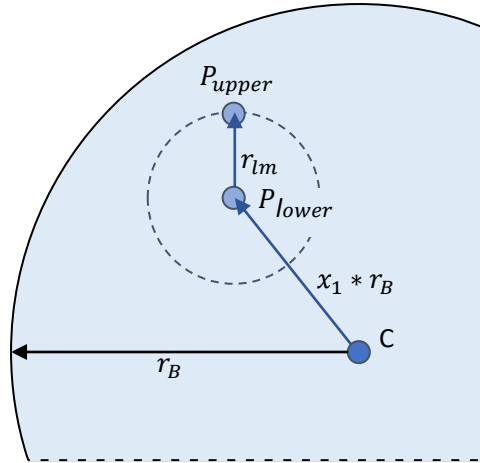


Figure 5.10: Determination of pierced chord lengths of the lower and upper sensor according values of the lateral movement measured via X-ray tomography.

A sample distribution of measured lateral movements and the corresponding results of the Monte Carlo simulations are shown in Figures 5.11 and 5.12. The results match the observation that smaller bubbles with horizontal diameters  $d_{b,hORIZ} < 5$  cm are significantly more affected and thus further support the explanation that lateral movement is the likely cause. Given the steep gradient of  $\tau$  for bubbles with  $d_{b,hORIZ} < 2.5$  cm evidences that the optical probes are not suited for the measurements of bubbles in this horizontal size range as their measured rise velocity and chord lengths is likely distorted significantly.

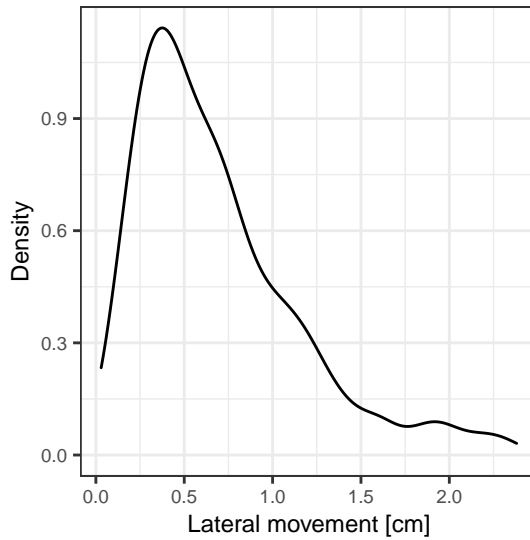


Figure 5.11: Distribution of lateral movement for all bubbles measured at height of 36 and  $u/u_{mf} = 4$  by means of X-ray tomography.

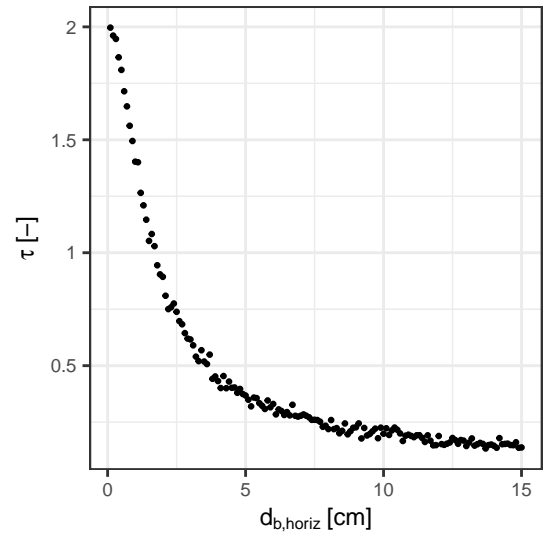


Figure 5.12: Mean values of  $\tau$  resulting from the Monte Carlo simulation of the pierced chord lengths for lateral moving bubbles.

To avoid such distortions of the measurements, any measured bubble for which  $X_{cor} < 0.6$  or  $\tau > 0.25$  were removed from the data set for the results presented in this chapter. This significantly reduced the number of evaluated bubbles. For the NWa bed material, a total of 1,136,262 bubbles were measured. After the filtration, 256,929 bubbles were left in the data set. A comparison between the filtered and unfiltered distributions of the measured bubble rise velocities and the corresponding pierced chord lengths for a pressure of 1.14 bar is shown in Figure 5.13.

It can be concluded that the optical probes are not well suited for the measurement of small and slow bubbles, which are filtered disproportionately. However, considering the scope of the experimental investigations of this work, where the main concern is a possible mass transfer limitation between the bubble phase and the dense phase, such bubbles have no significant impact.

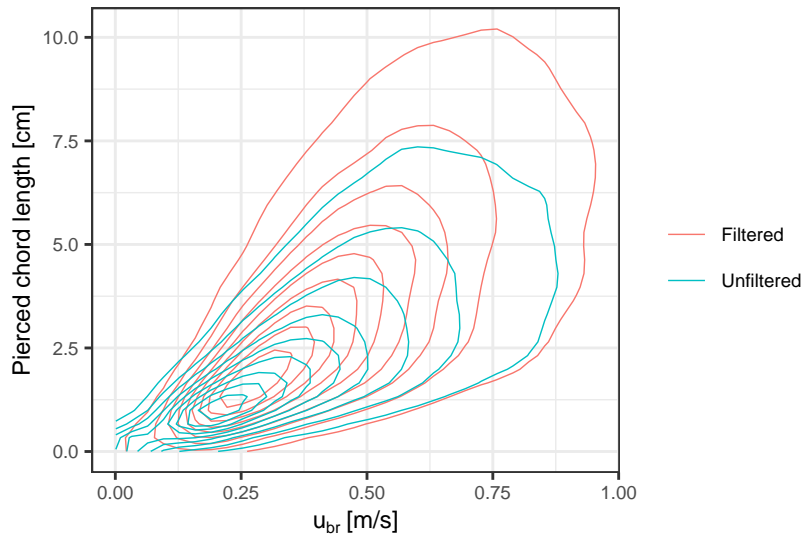


Figure 5.13: Comparison of the count density of the filtered and the unfiltered data set of all bubbles that were measured for a pressure of 1.14 bar

### 5.2.4 Estimation of geometric bubble property distributions from optical measurements

The goal of the hydrodynamic investigations presented in this chapter is to obtain the spatial distributions of the bubbles and their properties within the BFB reactor for a given pressure and fluidization number, which will then be used for the development of a reactor model for the prediction of the mass and energy balances. For this, the knowledge of chord lengths is not sufficient and the spatial distributions of volume-equivalent diameter and rise velocities are required.



Many authors have investigated the relationship between chord length and bubble size distributions and developed mathematical methods to obtain bubble size, volume or area probability density functions (PDFs) from the measured chord length distributions. Commonly applied techniques can be divided into parametric, non-parametric and maximum entropy estimation methods [245], [246]. In most parametric methods, the measured chord length PDFs are approximated with distribution functions such as the Gamma or Rayleigh function and complex backward transformations are applied to retrieve the underlying bubble geometry PDFs, for which the type of the distribution function has to be known before [214], [217]. The non-parametrical approaches do not require the a priori knowledge of the chord length or bubble geometry PDFs for the backward transformation [136], [139], [247]–[249]. The proposed maximum entropy estimation methods are based on the maximum entropy principle by Jaynes [250] and claim to overcome many of the shortcomings of previously proposed methods as they do not require the use of a backward transform or a constant bubble shape assumption [245], [251].

Rüdisüli *et al.* published a detailed analysis of the methods described above, for which Monte Carlo simulations were conducted to investigate the applicability of the methods for the simulated measurements of given bubble size distribution in the cross-section of a fluidized bed by intrusive probes [246]. The author describes the shortcomings of the investigated methods, stating that they suffer from numerical instabilities, scarcity of adjustable model parameters and the requirement of a priori knowledge of the distribution types and bubble shapes. Additionally, the simplistic assumptions of a homogeneous bubble shape based on an ellipsoid model and a uniform cross-sectional spatial bubble distribution are criticized. The study concludes, that for the conducted Monte Carlo simulations none of the investigated methods produced indisputably good results and none managed to clearly outperform the simple approach of approximating the mean bubble size by the mean measured chord length.

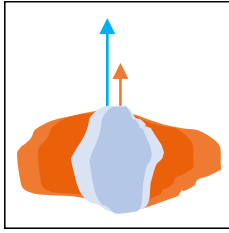
The observations from the X-ray tomography measurements described in Sections 4.3.4 and 4.5.4 of this work, further support this criticism. It could be shown that there are broad variances of the bubble shapes, which are correlated with the respective bubble sizes and rise velocities. Further, a non uniform spatial distribution of the bubbles across the bed cross section was measured. These observations have to be accounted for.

Considering the statements of Rüdisüli *et al.* and the results of the X-ray tomography measurements, a new and comparatively simple approach was developed for the evaluation of the optical probe measurements in this chapter.

For the estimation of the geometric properties of the measured bubble chord lengths, the following aspects are accounted for in the evaluation of the optical probe measurements shown in this chapter:

1. Correlation between the shape and other bubble properties
2. Ratio between mean pierced chord length and vertical diameter of the pierced bubble
3. Probability of the bubble being pierced by the optical probe
4. Weighting of the measured bubble properties according to the radial probe position to account for the heterogeneous spatial distribution of the bubble hold-up

### Correlation between the shape and other bubble properties



It was shown that the aspect ratio  $l : w$  of a bubble is correlated to its rise velocity and diameter. The optical probes measure the rise velocity as well as the vertical pierced chord length of the bubble. Since both these properties are correlated to the aspect ratio, it is feasible to estimate the bubble shape from the optical probe measurements.

In Figures 5.14 and 5.15, the density distributions of  $d_{b,vert}$  and  $u_{br}$  in dependence of the aspect ratio  $l : w$  are shown for all bubbles that were measured by means of X-ray tomography as they were presented in Sections 4.3.4 and 4.5.4.

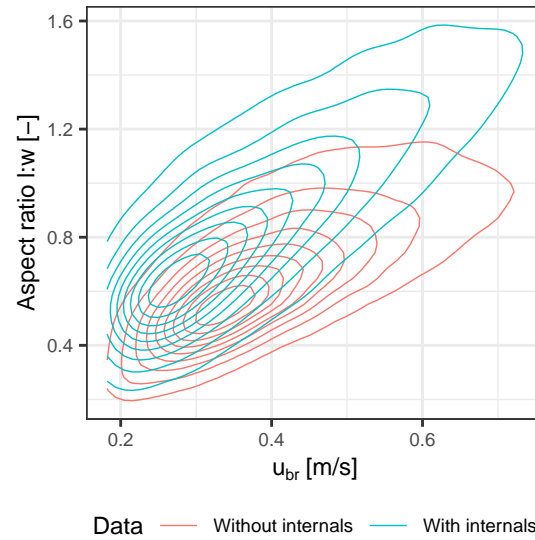
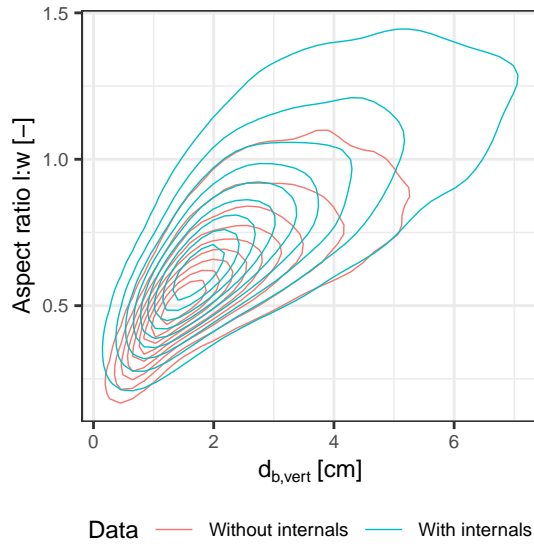


Figure 5.14: Contour plots showing the probability densities of the vertical diameters  $d_{b,vert}$  and the aspect ratios  $l : w$  of all bubbles measured via X-ray tomography after filtering, with and without internals.

Figure 5.15: Contour plots showing the probability densities of the rise velocities  $u_{br}$  and the aspect ratios  $l : w$  of all bubbles measured via X-ray tomography after filtering, with and without internals.

One can see that both,  $d_{b,vert}$  and  $u_{br}$  are approximately linearly correlated with  $l:w$ . It is therefore reasonable to fit the correlation function by applying multiple linear regression (MLR). The resulting functions are shown in Equation 5.4 for the case with internals and Equation 5.5 for the case without internals.

$$l:w = 0.07 + \frac{1.38u_{br}}{m/s} + \frac{0.082d_{b,vert}}{cm} \quad (5.4)$$

$$l:w = 0.18 + \frac{0.98u_{br}}{m/s} + \frac{0.041d_{b,vert}}{cm} \quad (5.5)$$

To assess the applicability for the case with internals, the correlation was applied on the experimentally determined values of  $d_{b,vert}$  and  $u_{br}$  from the X-ray tomography measurements. The resulting values of  $l:w$  were plotted in comparison to the measured values as shown in Figure 5.16. For low fluidization numbers and low measurement heights, the correlation does not reflect the broad variance of the measured aspect ratio distribution. However, for the majority of the shown settings, the correlation performs well.

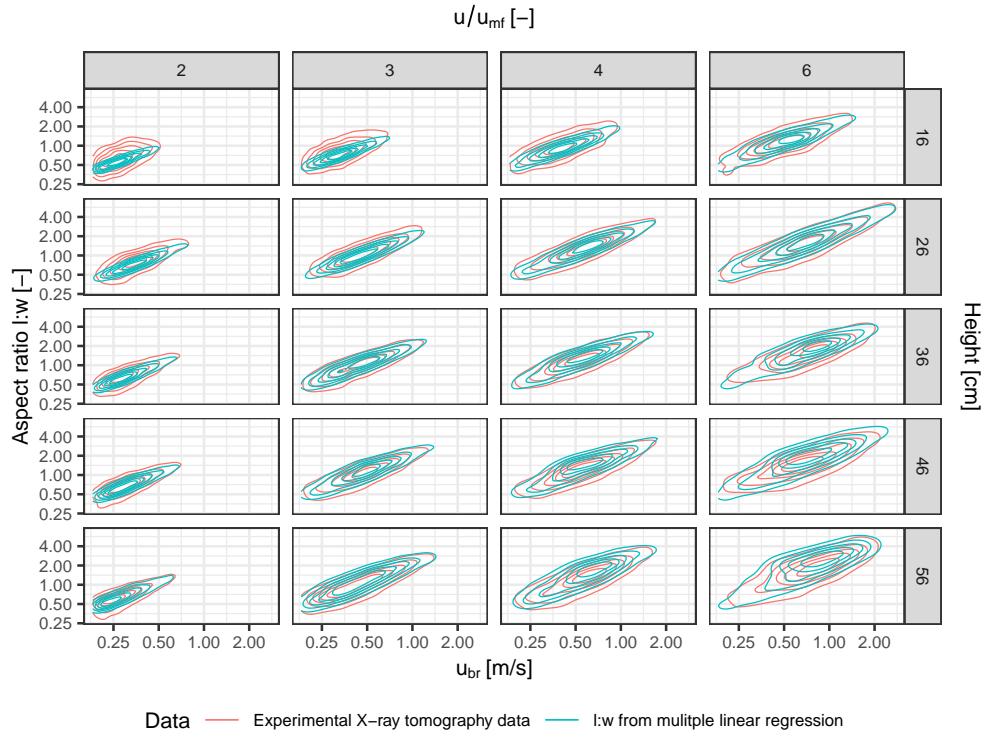
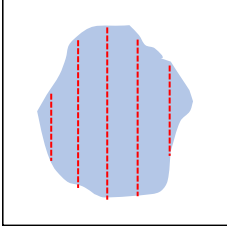


Figure 5.16: Comparison between the measured aspect ratios and those determined through the application of Equation 5.4.

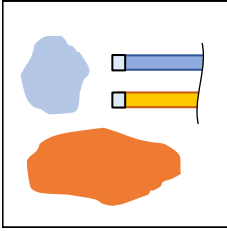
### Ratio between mean pierced chord length and vertical diameter of the pierced bubble



It has to be considered that the pierced chord length does not represent the vertical length of the bubble on average. As discussed previously in Section 4.6.4, the mean pierced chord length  $\bar{l}_{chord}$  equals  $2/3$  of the vertical diameter  $d_{b,vert}$  of the bubble, given its symmetry. Through synchronized X-ray radiography and optical probe measurements it could be shown that this ratio can indeed be

applied on the measured pierced chord lengths to retrieve  $d_{b,vert}$  if a statistically sufficient number of measured chord lengths is available.

### Probability of the bubble being pierced by the optical probe



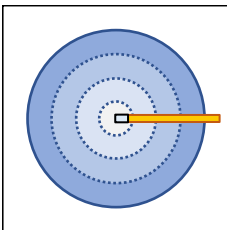
It is necessary to account for the probability of the probe to pierce bubbles of certain sizes and shapes, otherwise the measurements would over-represent large and flat bubbles and their associated properties. This is relevant in consideration of the broad distributions of bubble sizes and aspect ratios that were measured and especially because of the described correlation between shape and

rise velocity, which would not be represented accurately if their hit probabilities were not accounted for. The measurement of the rise velocity allows the approximation of the aspect ratio  $l : w$  as described above. Then the hit probability  $P$  can be estimated with Equations 5.6 and 5.7, where  $D$  is the bed diameter,  $n_{int}$  is the number of internals and  $d_{int}$  is the diameter of the internals. The measurement of each individual bubble can thus be weighted accordingly.

$$d_{b,horiz} = \frac{1.5l_{chord}}{l : w} \quad (5.6)$$

$$P = \frac{d_{b,horiz}^2}{D^2 - n_{int}d_{int}^2} \quad (5.7)$$

### Weighting to account for radial measurement position



The measurements also have to be weighted according to their radial positions, to account for the heterogeneous spatial distribution of the bubble hold-up. As shown by means of X-ray tomography in Section 4.5.4, the time averaged cross-sectional bubble hold-up is distributed rotationally symmetrical. Therefore, measurements at a defined radial position are representative for all points on the same

radius. To account for the increasing perimeter of represented points within the bed with increasing radial measurement positions, the measurements have to be weighted according to Equation 5.8, where  $W$  is the weighting factor,  $r$  is the radial position of the probe,  $\delta_{Int}$  is the sum of the intersections with internals on the circle with the radius  $r$  and  $R$  is the inner radius of the reactor.

$$W(r) = \frac{2\pi r - \delta_{Int}}{2\pi R} \quad (5.8)$$

### 5.2.5 Design of experiments

It is crucial to design the experiments carefully to minimize the risks of systematic errors, to understand and account for the limitations of the applied methods, and to optimize the execution of the experiments accordingly with the goal to obtain statistically robust results with verified methods. After the functionality of the sensor systems and the evaluation algorithms had been confirmed, a series of preliminary measurements was conducted to establish the experimental settings for the extensive measurements that were planned.

#### Influence of the reflector extension

One open question was, if the reflector extensions at the end of each optical probe, shown in Section 3.2, Figure 3.5, would influence the measurements. Therefore one of the extensions was removed and a series of measurements at four heights, using two probes, one with and one without the reflector extension, were conducted over a time period of two hours to minimize the RSE of the measurements, so that they are comparable. The fluidization number was set to 1.6, as it was assumed that small bubbles are more likely to be influenced than larger ones. The distributions of the measured pierced chord lengths and rise velocities are shown in Figure 5.17 and the summary statistics are shown in Table 5.1. Ideally, measurements with and without the reflector extension should have been conducted at the same height. Nonetheless, the measurements at  $H = 107$  cm clearly show that the distributions are affected by the reflector extension, as they are shifted towards small diameters and slower rise velocities in comparison to the measurement without the reflector extension at a lower height, which contradicts the well documented growth of the bubble diameters with the height in the bed. This is further evidenced by the comparatively reduced time averaged bubble hold-up that was measured at the height of 107 cm and the overall significantly reduced number of detected bubbles for the probes with the reflector extension, which can be seen in Table 5.1.

Consequently, the reflector extensions were removed from all probes except one, to enable measurements with catalyst material that will likely require the reflector attachment. It was

## Chapter 5. Hydrodynamic measurements at the GanyMeth pilot plant

Height [cm]	Reflector	$\epsilon_b$	Mean $l_{chord}$ [cm]	RSD $l_{chord}$	RSE $l_{chord}$	Mean $u_{br}$ [m/s]	RSD $u_{br}$	RSE $u_{br}$	$n$
62	With	1.5%	1.51	51%	3%	0.23	30%	2%	295
82	Without	5.4%	2.68	64%	2%	0.35	49%	2%	1019
107	With	3.1%	2.26	59%	3%	0.27	51%	3%	408
137	Without	7.9%	4.12	66%	2%	0.47	59%	1%	1890

Table 5.1: Summary statistics of the preliminary measurements with and without reflector attachment at  $u/u_{mf} = 1.6$  over 2 h each.

decided to place the probe with the reflector extension at the height of 107 cm, which is the second top measurement position, as the preliminary studies have shown that the bubble properties change less drastically at higher positions in the bed.

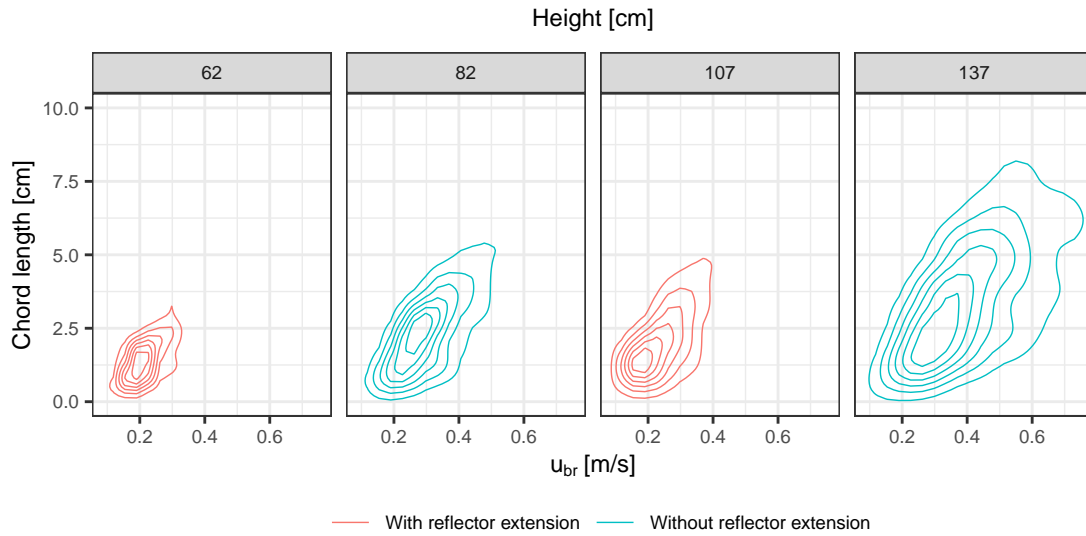


Figure 5.17: Comparison of preliminary measurements with and without reflector attachment conducted at  $u/u_{mf} = 1.6$  over 2 h each.

### Optimization of experimental methods

To optimize the time efficiency of the experiments, a series of measurements was performed to assess the possibility of measuring with multiple optical probes simultaneously. For this, measurements with just one probe and all probes simultaneously inserted were conducted at heights of 62 and 107 cm at  $u/u_{mf} = 2.4$  over a time period of 2 hours each. The results are shown in Figure 5.18 and Table 5.2, which show that measurements with all probes inserted are virtually identical to those where just one probe was used. Accordingly, the efficiency of the experiments can be increased significantly by measuring with all six probes inserted simultaneously.

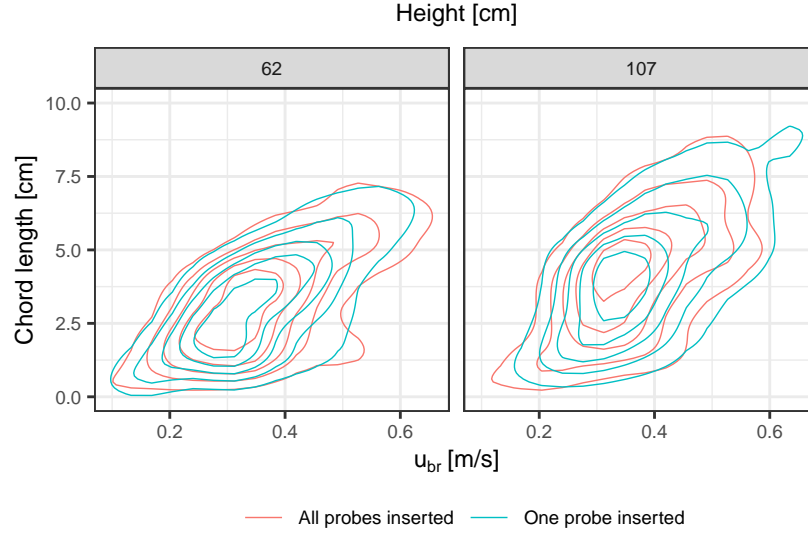


Figure 5.18: Comparison of preliminary measurements with a single probe and with all probes inserted at  $u/u_{mf} = 2.4$  over 2 h each.

Height [cm]	Probes inserted	$\varepsilon_b$	Mean $l_{chord}$ [cm]	RSD $l_{chord}$	RSE $l_{chord}$	Mean $u_{br}$ [m/s]	RSD $u_{br}$	RSE $u_{br}$	$n$
62	All	9.7%	3.53	60%	2%	0.40	47%	1%	1041
62	One	9.3%	3.49	61%	2%	0.40	51%	2%	1007
107	All	11.1%	5.35	69%	2%	0.45	57%	2%	927
107	One	11.1%	5.15	66%	2%	0.46	53%	2%	1080

Table 5.2: Summary statistics of preliminary measurements with a single probe and with all probes inserted at  $u/u_{mf} = 2.4$  over 2 h each.

The required measurement times for each experimental setting were estimated through an extensive series of long term preliminary studies. The measurements were conducted over a period of two hours at a radial position of 63 mm for fluidization numbers  $u/u_{mf} \in [2; 3; 4; 6; 8; 10]$  at a reactor pressure of 1.14 bar. The RSE of the measured pierced chord lengths and rise velocities was determined for each combination of measurement height and  $u/u_{mf}$ , which allowed the calculation of required measurement time for an acceptable RSE of 5%. Since the measurements were conducted with all probes inserted simultaneously, the measurement time for each setting had to be chosen according to the measurement position that required the longest measurement time. The measurement times that were estimated in this manner are listed in Table 5.3. For the measurements with the SCCa material, the order of required measurement times for each fluidization number is reversed in comparison to the required settings for the NWa material. The reason for this is that the SCCa material is classified as Geldart Type A, for which the minimum bubbling velocity  $u_{mb}$  is higher than  $u_{mf}$ . Therefore the onset of bubbling is comparatively delayed and consequently the bubbles

Bed material	Unit	$u_{mf}$					
		2	3	4	6	8	10
NWa	[s]	600	600	600	900	900	1200
SCCa	[s]	1200	900	900	600	600	600

Table 5.3: Estimated required measurement times for each fluidization number and bed material.

at lower heights and low values of  $u_{mf}$  are too small to be measured properly. This leads to relatively large fractions of the bubbles being removed through the filtering at these settings and longer measurement times are required therefore.

### Determination of the minimum fluidization velocity

The values of  $u_{mf}$  were determined for each pressure individually, according to the methods described in Section 2.2.2, to account for a possible influence of the pressure as it has been reported that an increase of the pressure leads to a decrease of  $u_{mf}$  in several studies [238], [252]–[255]. For most of the selected pressures, the procedure was repeated at least once, due to observed deviations of the measured  $u_{mf}$  for a given pressure. Especially the values of  $u_{mf}$  that were measured for a pressure of 2 bar differed significantly, while no differences in the execution of the measurements or the quality of the data were apparent. In Figure 5.19, measured pressure drop curves are shown for a selection of pressures, including two repeated measurements. A closer view of the typical turning points of the curves, which indicate the onset of fluidization, is shown in Figure 5.20 for the same data, where the deviations between the measurements can be seen clearly. The resulting values for  $u_{mf}$  are listed in Table 5.4.

Pressure [bara]	$u_{mf}$ [cm/s]	$u_{mf}$ [cm/s]
	(NWa material)	(SCCa material)
1.14	2.98	0.96
2	3.58	0.84
3	3.33	0.78
4.5	3.49	0.82
6	3.31	1.03
9	3.28	1.01
11	3.21	0.89

Table 5.4: Measured values of  $u_{mf}$ .

The correctness of listed values is debatable, given the deviations that were observed for repetitions of the pressure drop measurements, the generally limited accuracy of the method and expected decrease of  $u_{mf}$  with increasing pressures. Nonetheless, it was decided to proceed with  $u_{mf}$  values for each pressure as they were measured.



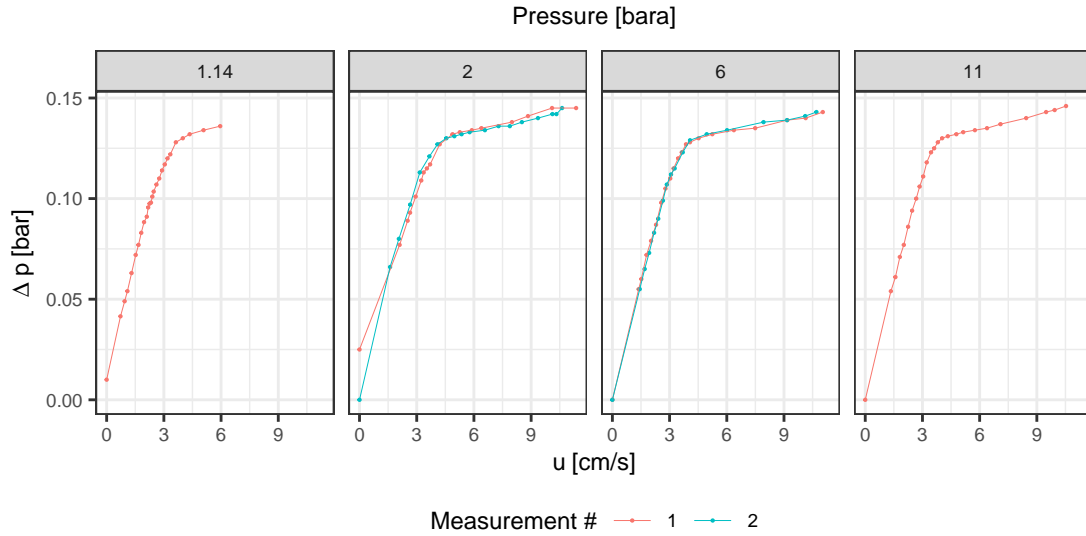


Figure 5.19: Pressure drop curves measured for several pressures in the GanyMeth pilot plant with NWa bed material.

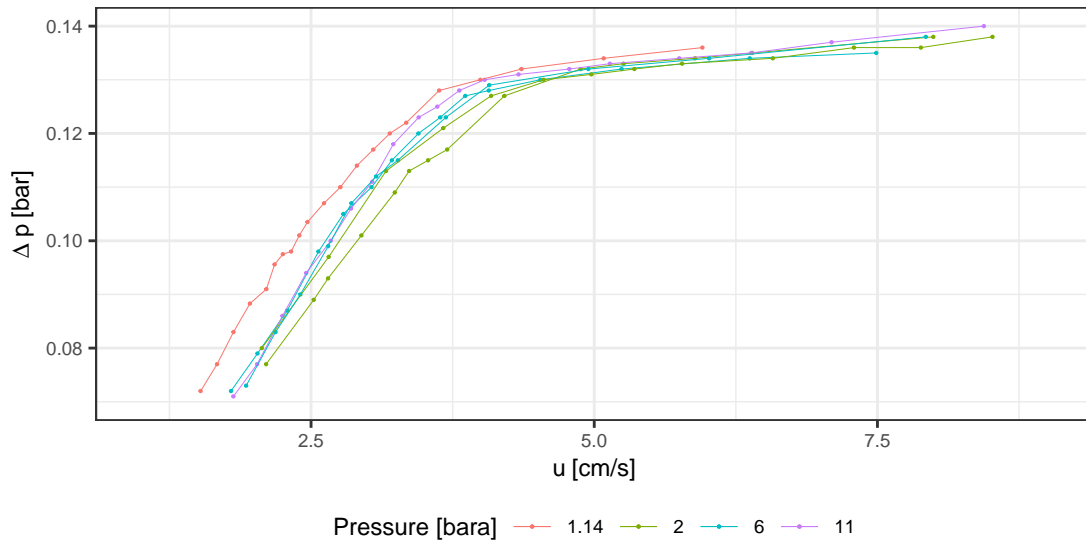


Figure 5.20: Detail of the pressure drop curves, showing the onset of fluidization, measured for several pressures in the GanyMeth pilot plant with NWa bed material.

For future measurements, a more reproducible and automated method should be developed for the determination of  $u_{mf}$ . Alternatively, the value of  $u_{mf}$  that was measured at 1.14 bar could be used as the reference for all measurements as it has been measured numerous times resulting in the same value previously and has been applied in several previous publications and for all X-ray measurements that were presented in this thesis.

### 5.3 Results of the measurements in the pilot plant GanyMeth

The experimental settings of the optical probe measurements in the GanyMeth pilot plant presented in this section are shown in Table 5.5. Note, that for a pressure of 11 bar and NWa bed material, the maximum fluidization number that the plant could be operated at is  $u/u_{mf} = 8$ . In total, measurements at 2988 individual settings were carried out with durations between 10 and 20 minutes each, according to the required measurement times listed in Table 5.3 at a measuring frequency of 5000 Hz.

Absolute pressure [bar]	1.14, 2, 3, 4.5, 6, 9, 11
$u/u_{mf}$ [-]	2, 3, 4, 6, 8, 10
Heights [cm]	17, 32, 62, 82, 107, 137
Radial positions [mm]	18, 31, 47, 63, 79, 94
Bed material	NWa (Geldart A/B) and SCCa (Geldart A)
Settled bed height [cm]	170 (NWa bed material), 160 (SCCa bed material)

Table 5.5: Experimental settings of the optical probe measurements in the GanyMeth pilot plant.

A total of 1,136,262 bubbles were measured using the NWa bed material and 761,749 using the SCCa material. After the filtering of the data according to the methods described in 5.2.3, there are 256,929 (22.3%) bubbles left from the measurements with the NWa material and 156,218 (20.5%) from the measurements with the SCCa material.

#### 5.3.1 Cross verification between the X-ray and optical probe measurements

An important and unique aspect of the present work is the possibility to compare several different techniques for the measurement of bubble properties in fluidized beds and to cross-verify the results thereby. Each of the methods shown in this work, namely X-ray tomography, X-ray radiography and optical probe measurements, have their own advantages and shortcomings. The uncertainties of each method would be significantly reduced if it could be demonstrated that each method leads to the same results for measurements with the same experimental settings.

#### Comparison of the measured bubble hold-up

Since the measurements of  $\varepsilon_b$  is virtually binary and does not require any further interpretation or processing, they can be considered to be the most accurate of the determined bubble phase properties. This also holds true for the X-ray tomography measurements of the hold-up, which were presented in Section 4.5.1 for the case with internals. Therefore, the measured cross-sectional mean values of  $\varepsilon_b$  are well suited to compare the different measurement techniques on a fundamental level. In Figure 5.21, a comparison between the bubble hold-ups that

### 5.3 Results of the measurements in the pilot plant GanyMeth

were measured by means of optical probes, X-ray tomography and bed expansion is shown. Here, the local bubble hold-ups that were measured with the optical probes in the GanyMeth pilot plant were weighted according to Equation 5.8 and averaged over the measurement heights 17, 32 and 62 cm. This was done to keep the measurements comparable with the X-ray tomography measurements, which were averaged accordingly over the measurement heights of 16, 26, 36 and 56 cm. Likewise the bed expansion was measured in a bed with a settled height of 55 cm. Both, the X-ray and bed expansion measurements were conducted in the cold-flow model with internals present that match the geometry of the GanyMeth pilot plant. The figure shows similar trends for the bubble hold-up in dependence of  $u/u_{mf}$ . However there is an offset between the curves for each measurement technique. For the comparison between the optical probe measurements with the X-ray measurements, the offset is almost precisely 0.04 for each fluidization number, whereas the hold-up measured via bed expansion is in between the other two measurement techniques.

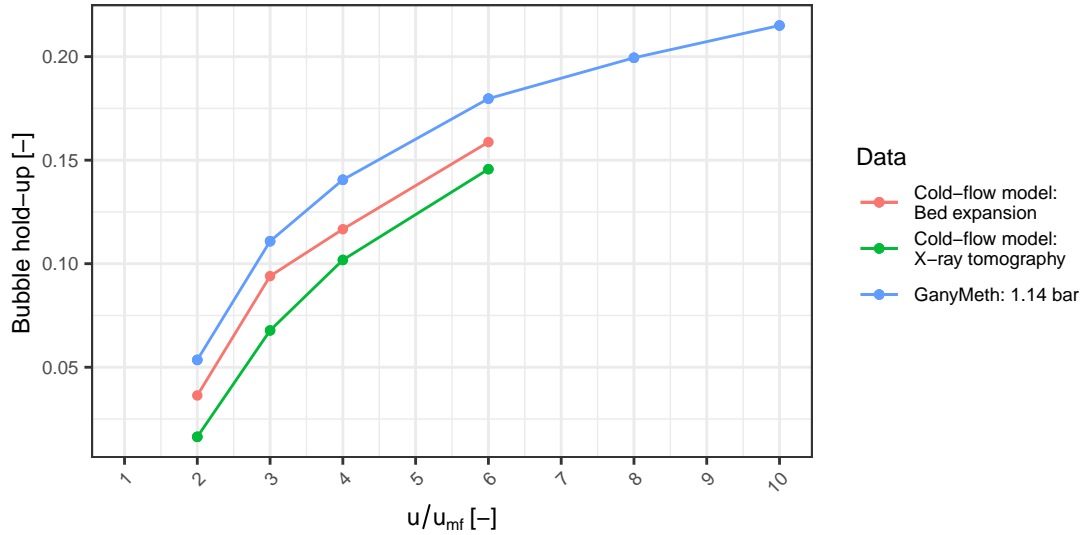


Figure 5.21: Comparison of the mean cross-sectional bubble hold-up, measured with optical probes in the pilot plant GanyMeth and via X-ray tomography in the cold-flow model, and averaged over comparable measurement heights. The estimation of the bubble hold-up via the measurement of the bed expansion in the cold-flow model is also shown.

One possible explanation for the offset could be that the X-ray measurements underestimate the hold-up. This is plausible, as beam hardening or X-ray scattering possibly affects the X-ray measurements, as discussed in Section 4. Additionally, it could be shown by means of tomography simulations, that small bubbles are reconstructed reduced in size, as presented in Sections 4.4.2 and 4.4.4. On the other hand, in Section 5.2.1 it could be demonstrated that the optical probes are highly sensitive towards fluctuations of light intensities and may therefore slightly overestimate the bubble hold-up, as approaching bubbles may reduce the

intensity of the reflected light even before the bubble is actually pierced. Ultimately, one has to consider that the distinction between the bubble phase and the dense phase is in fact not perfectly binary. There are zones around bubbles with reduced particle densities and particles frequently rain through the bubble phase. Generally speaking, the bubble hold-up cannot exceed the values that result from the bed expansion. Therefore it is likely that the optical probes overestimate the hold-up, while it is probably slightly underestimated by the X-ray measurements.

### Comparison of the measured bubble property distributions

The measurement of bubble property distributions is the central topic of this thesis and comprehensive efforts were undertaken for the development of the experimental methodologies, both for the X-ray measurements shown in Chapter 4 and the optical probe measurements presented in this chapter.

Figure 5.22 shows the pierced chord length and rise velocity distributions that were measured in the GanyMeth pilot plant at a pressure of 1.14 bar, where the chord lengths are scaled according to Equation 4.15 in comparison to the vertical bubble diameter and rise velocity distributions measured by means of X-ray tomography at comparable experimental settings. The optical probe data was filtered according to the restrictions of the X-ray tomography data, which means that any bubbles with  $u_{br} < 0.18 \text{ ms}^{-1}$  were removed to make the data sets comparable. Furthermore, the measured pierced chord lengths were weighted according to their radial position, as described by Equation 5.8 and scaled by a factor 1.5 to account for statistical ratio between mean chord length and vertical bubble diameter according to Equation 4.16.

There is an excellent match between the compared data sets which can be considered as strong evidence for the correctness of the data, given that the measurements were conducted with two independent methods.

Furthermore, the volume-equivalent diameters and with that the hit probabilities from the measured pierced chord lengths can be estimated according to the other methods that were derived in Section 5.2.4, through the application of Equations 5.4 and 5.7. However, it turned out that implementing the reduced hit probabilities of bubbles with comparatively small horizontal diameters impaired the match between the data that was measured via X-ray tomography and the resulting volume-equivalent diameters from the processed optical probe data. The comparison between the resulting volume-equivalent diameters, without considering the hit probabilities, with the X-ray tomography results are shown in Figure 5.23, whereas Figure 5.24 shows the case where the hit probabilities have been accounted for.

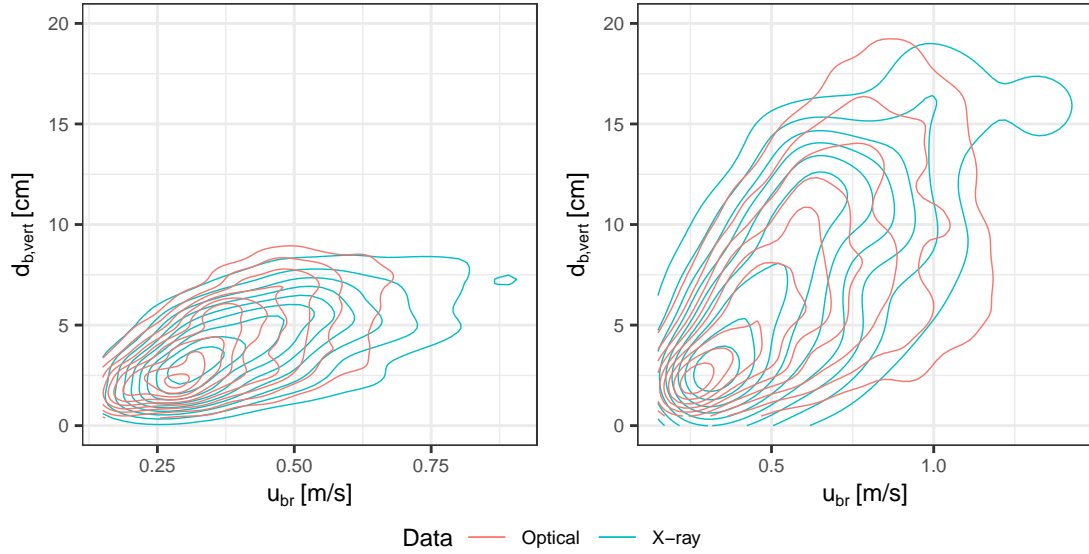


Figure 5.22: Comparison of the pierced chord lengths and rise velocities measured with optical probes in the GanyMeth pilot plant with the vertical bubble diameters and rise velocities measured by means of X-ray tomography at height. The figure on the left shows measurements from a height of 32 cm (optical) or 36 cm (X-Ray) at  $u/u_{mf} = 3$ . The figure on the right shows measurements from a height of 62 cm (optical) or 56 cm (X-Ray) at  $u/u_{mf} = 4$ .

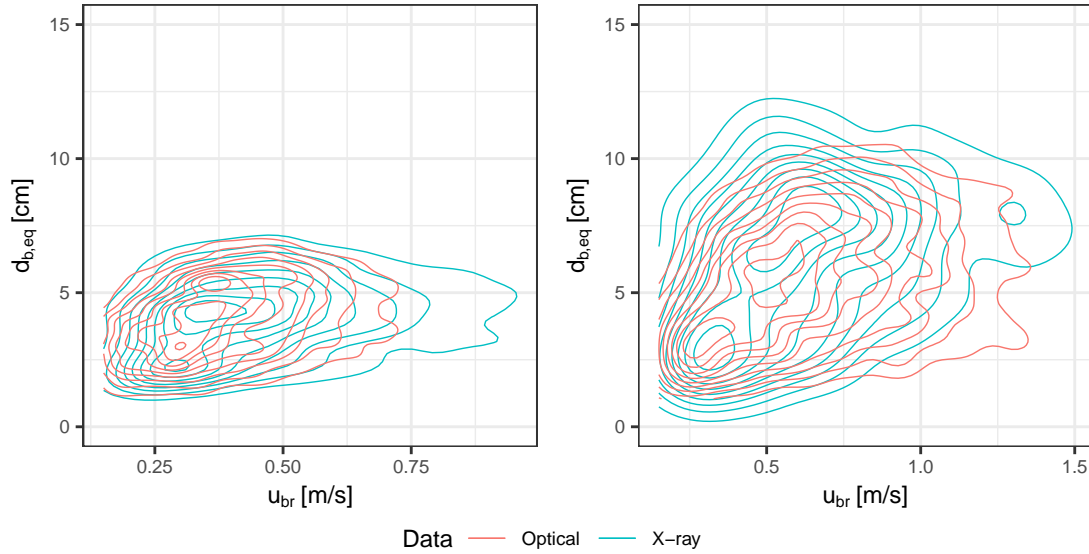


Figure 5.23: Comparison of the estimated volume-equivalent diameters and rise velocities measured with optical probes in the GanyMeth pilot plant (without accounting for the hit probabilities) with the volume-equivalent diameters and rise velocities measured by means of X-ray tomography. The figure on the left shows measurements from a height of 32 cm (optical) or 36 cm (X-Ray) at  $u/u_{mf} = 3$ . The figure on the right shows measurements from a height of 62 cm (optical) or 56 cm (X-Ray) at  $u/u_{mf} = 4$ .

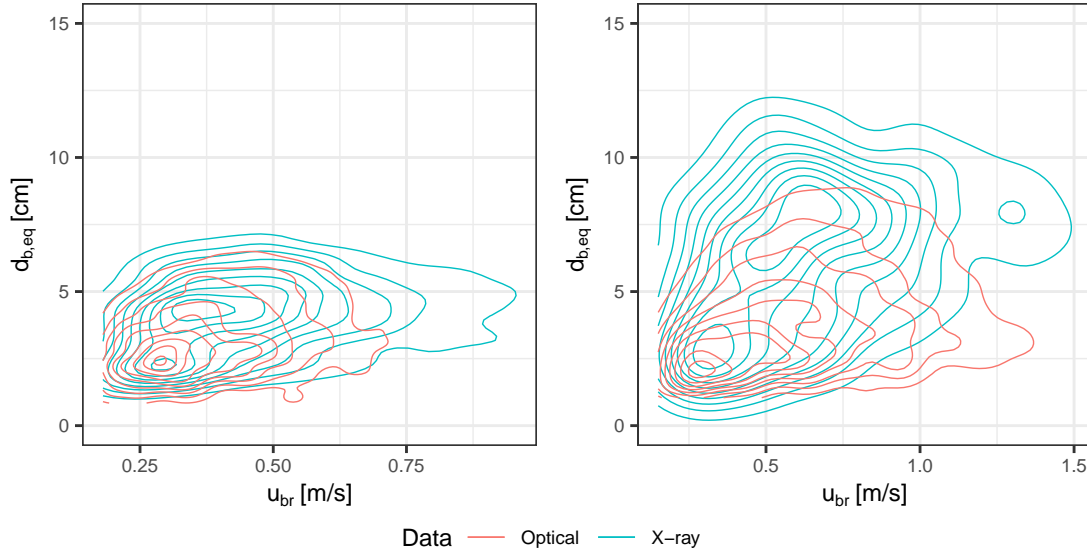


Figure 5.24: Comparison of the estimated volume-equivalent diameters and rise velocities measured with optical probes in the GanyMeth pilot plant (with accounting for the hit probabilities) with the volume-equivalent diameters and rise velocities measured by means of X-ray tomography. The figure on the left shows measurements from a height of 32 cm (optical) or 36 cm (X-Ray) at  $u/u_{mf} = 3$ . The figure on the right shows measurements from a height of 62 cm (optical) or 56 cm (X-Ray) at  $u/u_{mf} = 4$ .

If the hit probabilities are ignored, the match between the two data sets is very good. The reason for the worsening of the match when hit probabilities are included has not been understood so far. It is plausible that the X-ray tomography measurements suffer from a low spatial resolution and small bubbles are falsely merged with larger bubbles through the reconstruction.

The results of this comparatively simple approach to retrieve geometric bubble property distributions from the chord length distributions demonstrate its feasibility and usefulness, especially in comparison to what the results would be if a uniform bubble shape was assumed. In that case, the original shape of the measured chord length distributions would be preserved and the density of large and fast bubble would be over estimated. Further investigations are required to verify and improve the method, which should include appropriate Monte Carlo simulations and the application of the back transformation methods that were briefly introduced in Section 5.2.4.

### 5.3.2 Measured cross-sectional bubble hold-up

Optical probes allow the precise local determination of the local bubble hold-up  $\varepsilon_b$ . Given a sufficient resolution of measurement points, the spatial distribution of the bubble hold-up

can be derived as well. In Figures 5.25 to 5.28, the measured values of  $\varepsilon_b$  that were averaged over the cross section through the radial position weighting of the measurements via Equation 5.8 and averaged over all measurement heights are shown for all investigated reactor pressures in separate figures for each type of bed material.

#### NWa bed material

For fluidization numbers  $u/u_{mf} \leq 3$  there are only small differences in the measured hold-up for different pressures, whereas the hold-up increases significantly with increasing pressures for higher values of  $u/u_{mf}$ . At the maximum measured fluidization number  $u/u_{mf} = 10$ , the bubble hold-up that was measured at a reactor pressure of 9 bar is more than double of that measured at 1.14 bar. A possible explanation for this increase of the hold-up at elevated pressures could be a reduced stability of the bubbles, caused by a reduction of the bubble throughflow which would otherwise stabilize the bubble roof. Consequently the bubbles split more frequently, as it has been described to occur for BFB reactors when the pressure is increased [256]. Due to the splitting of the bubbles, they are smaller in size on average and therefore rise with comparatively reduced velocities, which increases the overall bubble hold-up. Another possible explanation could be an earlier transition of the fluidization regime from bubbling to slugging or local slugging fluidization with increased pressures. Bubbles with flattened slug-like shapes rise with comparatively slow velocities, which would increase their dwell time and with that the value of  $\varepsilon_b$ . Such a decrease of transition velocities at which fluidization regime transitions occur have been reported for increasing pressures by other authors before for fluidized beds without internals [257], [258].

Figure 5.26 provides a more detailed impression as it shows the hold-up profiles over the reactor heights for each pressure. One can see that the hold-up is not equally distributed over all heights and that the shapes of the hold-up profiles for each pressure depend on the fluidization number. At a pressure of 6 bar for example, the hold-up increases with the height for low fluidization numbers, whereas it decreases with the height at higher values of  $u/u_{mf}$ . At some pressures, for example at 4.5 bar, the hold-up is reduced at intermediate heights for certain fluidization numbers. One reason for these observations could be that fluidized beds typically are divided into regions with different characteristic particle flow patterns that are often described as gulf like streams and which may influence the local bubble motion and with that their local residence times. The location of these regions within the BFB reactor may shift vertically in dependence of the pressure and  $u/u_{mf}$ . Another reason could be a transition between different flow regimes. As mentioned above, a transition from the BFB regime to a slugging regime is plausible, which could reduce the bubble hold-up at heights right below the onset of slugging fluidization, as the bubbles there would accelerate towards the comparatively slow slugs and coalesce with them.

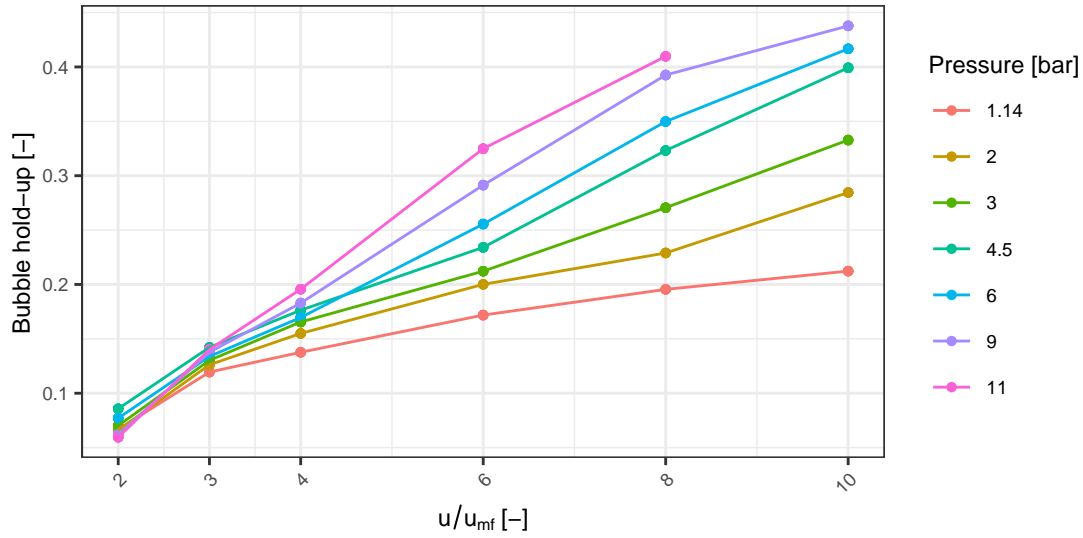


Figure 5.25: Bubble hold-up measured with optical probes averaged over all measurement positions for all measured pressures and the NWa type bed material.

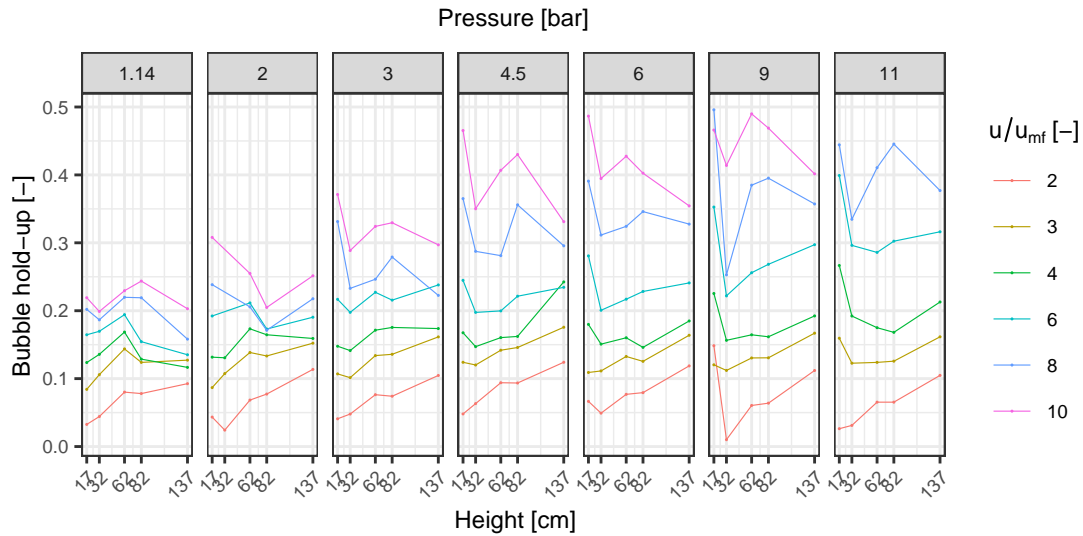


Figure 5.26: Bubble hold-up measured with optical probes averaged over all radial positions for all measured pressures, height positions and the NWa type bed material.

### SCCa bed material

The bubble hold-up, which was measured with SCCa particles as bed material and averaged over all measurements positions, is shown in Figure 5.27. Overall, the influence of the pressure on the hold-up appears to be similar to that observed for the NWa material. The measured bubble hold-up is generally about 50% lower than that of the NWa powder, which is most likely a result of the increased minimum bubbling velocity  $u_{mb}$  and the corresponding delayed



onset of bubbling fluidization that is typical for the fluidization of Geldart type A particles. For a pressure of 1.14 bar, the measured hold-up deviates from the general trend, showing higher values than other measurements at increased pressures for most fluidization numbers, especially for  $u/u_{mf} \leq 3$ . This could be explained by an increase of  $u_{mb}$  and the corresponding delayed onset of the bubbling fluidization, which is known to occur for Geldart A type material at increased pressures [228]–[231].

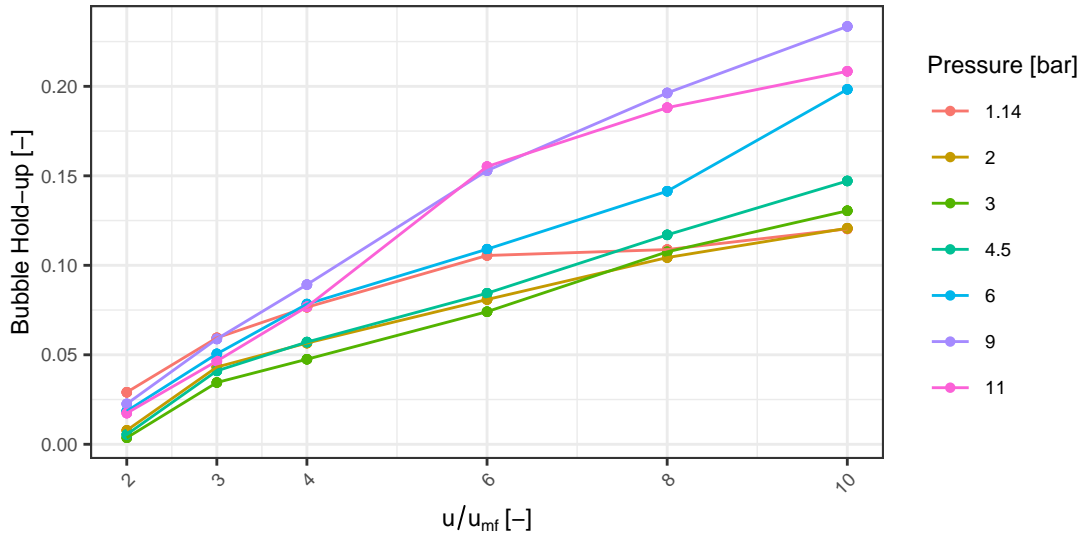


Figure 5.27: Bubble hold-up measured with optical probes averaged over all measurement positions for all measured pressures and the SCCa type bed material.

Figure 5.28 shows the cross-sectional bubble hold-ups as they were averaged for each height, fluidization number and pressure for the SCCa material. For pressures  $\leq 2$  bar one can see, that the hold-up at height of 17 cm increases with the pressure and  $u/u_{mf}$ , especially for  $u/u_{mf} \geq 6$ , and drops seemingly abrupt at the next measurement height of 32 cm. The height at which the hold-up reaches its minimum appears to shift upwards with increasing pressures and fluidization numbers, which can be seen for pressures  $\geq 6$  bar. Again, these findings may indicate an influence of the pressure on the transitioning between fluidization regimes or particle circulation patterns.

#### 5.3.3 Measured mean bubble properties

It is known, that the pressure can significantly influence the bubble properties, but reports found in literature are often conflicting and to the best of our knowledge, no studies on the influence of the pressure on BFB with vertical internals were published.

It could be shown, that it is possible to transform the measured distributions of pierced chord lengths to the corresponding volume-equivalent bubble diameter distributions for ambient

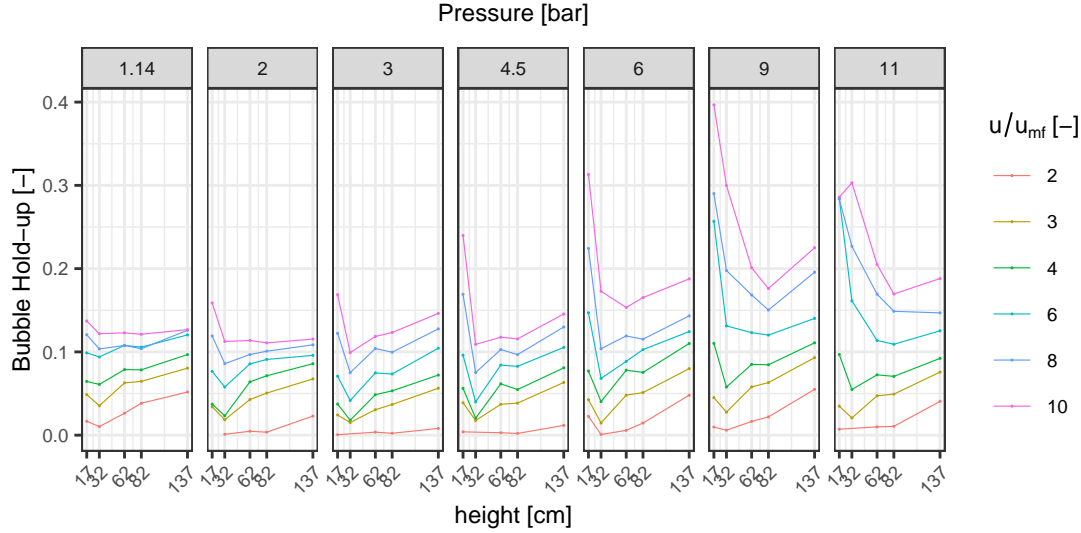


Figure 5.28: Bubble hold-up measured with optical probes averaged over all radial positions for all measured pressures, height positions and the SCCa type bed material.

pressures. However, it was decided to only present the measured chord lengths in this section, as it was not verified, whether the applied correlation for the estimation of the bubble shape from the rise velocity is valid at elevated pressures and heights above those at which the X-ray measurements were conducted. Additionally, it is also plausible that a transition from bubbling fluidization to a slugging regime occurs, in which case the developed methods are also not verified and less likely to be applicable.

For the mean values of the measured bubble rise velocities, two variants were determined:

1. The arithmetic mean of all rise velocities that were measured for each individual bubble.
2. The mean rise velocity determined through the application of the cross-correlation method on the entire lower and upper signals, which is henceforth referred to as  $u_{b,CC}$ .

### Measured pierced chord lengths for the NWa material

In Figure 5.29, the chord lengths that were measured for the fluidization of NWa bed material are shown for each pressure and measurement height categorized by  $u/u_{mf}$ . For a pressure of 1.14 bar, one can see that the mean chord lengths increase with increasing values of  $u/u_{mf}$ , but reach a maximum at about 8 cm at  $u/u_{mf} = 6$ . A further increase of the fluidization number leads to decreasing chord lengths at higher heights. At a pressure of 2 bar, the measured chord lengths appear to not be influenced for  $u/u_{mf} \leq 4$  but then drop abruptly for a further increase of the fluidization number in comparison to what was measured at 1.14 bar. This

trend continues for higher pressures, with earlier and seemingly less abrupt declines of the mean pierced chord lengths with increasing pressures and fluidization number. Eventually the chord lengths appear to reach a relatively stable value for all measurement heights with values in the range of 5 cm.

One explanation for these observations could be, that a maximum stable bubble size is eventually reached where the coalescence and bubble splitting rates have reached an equilibrium. A reduction of the measured pierced chord lengths could also be explained by a flattening of the bubble shapes with increasing pressures, as it has been reported to occur by Kawabata *et al.* [238]. However, the stated suppositions would not explain the observation that the chord lengths first peak and then drop again with increasing fluidization numbers for the lower pressures. A possible reason for these observations could be the onset of slugging or local slugging fluidization, for which the bubble shapes could change significantly to what is often referred to as squared-nosed slugs. As described in Section 4.5, when internals are present such bubble shapes could exist, even without necessarily covering the complete cross section.

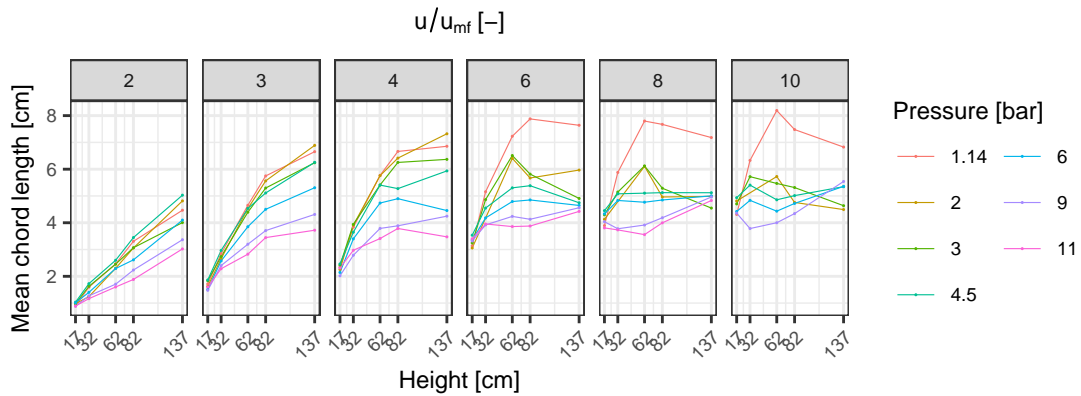


Figure 5.29: Mean pierced bubble chord lengths measured with optical probes averaged over all radial positions for all measured pressures, height positions and the NWa type bed material.

#### Measured rise velocities for the NWa material

In Figure 5.30, the measured rise velocities for the NWa material is shown for a reduced selection of pressures to preserve the clarity of the plot. One can see, that mean values of  $u_{br}$  match well with  $u_{b,CC}$ , which is determined from cross-correlating the entire lower and upper signal for most settings. For higher measurement heights and fluidization numbers, the two methods deviate more, especially for a pressure of 1.14 bar. The reason for these deviations are not clear but the filtering of the data could be excluded, as the unfiltered data showed the same deviations. For the following analysis of the rise velocities, the values that were measured for each bubble individually will be used.

The sub-figures show that the rise velocities increase with the height for  $u/u_{mf} = 2$  and all pressures. For a pressure of 1.14 bar and increased fluidization numbers, the mean rise velocity appears to reach a maximum value of around  $0.8 \text{ m s}^{-1}$  before it drops. The rise velocity profile appears to not change with increasing fluidization numbers in the range of  $u/u_{mf} \geq 6$ . For higher pressures, the maximum value of the mean rise velocity is significantly faster at values around  $1.1 \text{ m s}^{-1}$  and is reached at higher fluidization numbers of  $u/u_{mf} \geq 8$  and at a higher height. At a pressure of 9 bar, the rise velocities are lower over most heights for all  $u/u_{mf} \leq 4$  in comparison to the other shown pressures. With a further increase of the  $u/u_{mf}$  however, the rise velocity profiles of the pressures 4.5 and 9 bar become increasingly similar.

These observations are somewhat surprising, as the measured chord lengths are significantly smaller at 4.5 and 9 bar in comparison to those measured at 1.14 bar for all heights and fluidization numbers. This led to the assumption that the bubbles are either reduced in size or flattened, or that there potentially could be a transition to the slugging regime. However, for all these explanations, one would expect comparatively slower rise velocities for the corresponding higher pressures.

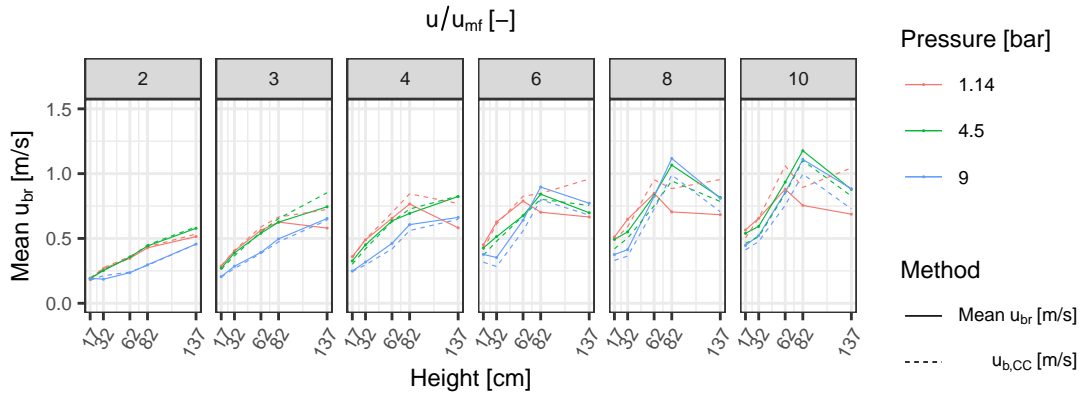


Figure 5.30: Mean bubble rise velocities measured with optical probes averaged over all radial positions for all measured pressures, height positions and the NWa type bed material.

### Measured pierced chord lengths for the SCCa material

The chord lengths that were measured with SCCa material are shown in Figure 5.31. Similar to the measurements with the NWa material, a maximum chord length appears to be reached at a measurement height of 137 cm and  $u/u_{mf} = 6$  for a pressure of 1.14 bar. An increase of the pressure leads to a reduction of the measured chord lengths in comparison to the measurements at 1.14 bar. At a height of 32 cm and  $u/u_{mf} \geq 3$ , the chord lengths are relatively increased for the pressures  $\geq 6$  bar and decreased at a height of 62 cm, whereas all other pressures show a comparatively consistent bubble growth with the measurement height

and fluidization number. For the fluidization numbers  $u/u_{mf} \geq 6$  and heights above 62 cm, the influence of the pressure is clearly visible, with decreasing chord lengths for increasing pressures.

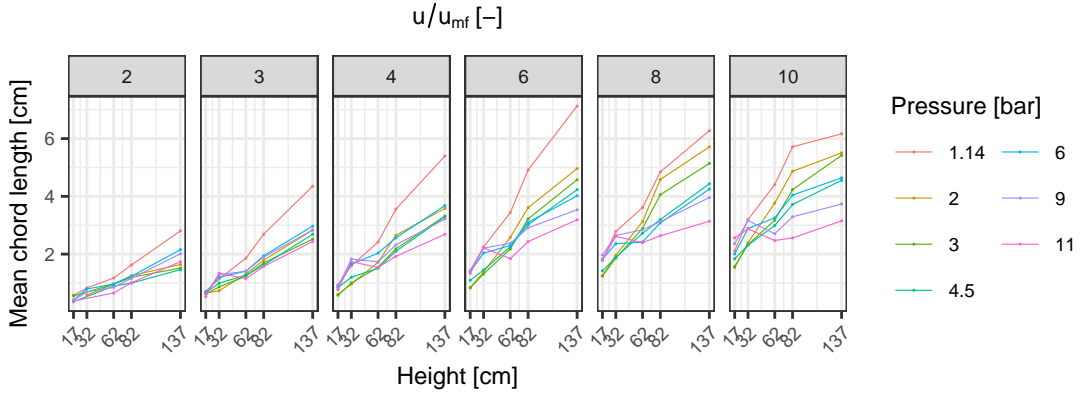


Figure 5.31: Mean pierced bubble chord lengths measured with optical probes averaged over all radial positions for all measured pressures, height positions and the SCCa type bed material.

Plausible reasons for the observations could again be the reduction of the bubble stability with the pressure, whereas no clear indications of a transition to a slugging regime are apparent.

#### Measured rise velocities for the SCCa material

In Figure 5.32, the measured rise velocities for the SCCa powder are shown.

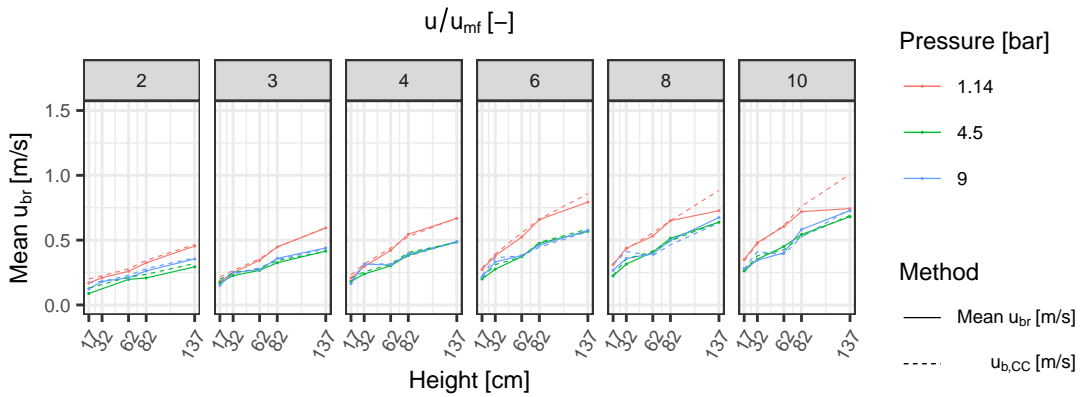


Figure 5.32: Mean bubble rise velocities with optical probes averaged over all radial positions for all measured pressures, height positions and the SCCa type bed material.

For most settings, the mean values of  $u_{br}$  match  $u_{b,CC}$  precisely. Only at  $u/u_{mf} \geq 6$ , there is a deviation between the two methods for a pressure of 1.14 bar. An increase of the pressure above 1.14 bar leads to reduced rise velocities. Interestingly, the differences between the

rise velocities profiles were insignificant between the measurements at elevated pressures in comparison to the measurements at 1.14 bar.

## 6 Discussion, conclusions and outlook

At Paul Scherrer Institute (PSI), a bubbling fluidized bed (BFB) reactor is under development for a methanation process as part of a Power-to-Gas (PtG) concept. Methanation is a strongly exothermic reaction, for which BFB reactors are well suited, as the bubbles cause an intensive particle circulation which leads to virtually isothermal conditions over the entire bed height. For the purpose of removing the reaction heat from the system, the reactor design includes a vertical heat exchanger tube bundle. While the bubbles are beneficial for the cooling of the reactor, they pose the risk of reducing the methane yield if reactants are bypassed through the reactor within bubbles, if these become too big and rise too fast.

Comprehensive techno-economic studies have been conducted in consideration of the conflict between the availability of renewable energies and the energy demands at different time-scales for an all-year operation of the upgrading process [51], [61]. Among others, the studies highlighted the possibilities and requirements of part load operation of the PtG process chain.

It is therefore necessary to conduct detailed hydrodynamic investigations to determine the mass flow limitations of the process for different operation scenarios and to reduce the risks involved with the scale-up of chemical reactors. A particular focus was put on studying the influence of the vertical tube bundle on the hydrodynamics, as only a few reports on BFB reactors with vertical internals are available in literature. A pilot plant BFB reactor, referred to as GanyMeth, has been constructed in a scale that will allow the measurement of various hydrodynamic details and their influence on the reactor performance under reactive conditions. For this purpose, an optical probe sensor system has been developed at PSI. Additionally, several series of X-ray measurements have been conducted in a cold-flow model of the reactor to investigate the hydrodynamics with and without internals and to support the development of the evaluation methodology for the optical probe experiments by means of cross verification of measurements at similar experimental settings.

### 6.1 Achieved results

Several unique aspects characterize the hydrodynamic investigations presented in this thesis. Three independent methods, namely X-ray tomography, X-ray radiography and optical probe measurements have been applied to measure bubble properties for the same bed material and the same reactor geometries, allowing the cross verification of the results. X-ray tomography and optical probe measurements were used to determine bubble property distributions for BFBs. These methods require the knowledge of the bubble rise velocity for the determination of the vertical bubble dimension. In this work, the rise velocities were determined and applied for each bubble individually, rather than measuring a mean rise velocity and applying it on all measured bubbles of a specific experimental setting, as it is commonly done in similar studies found in literature. This approach makes a significant difference, as it could be shown that the rise velocity is correlated to other bubble properties, mainly the shape and the size of the bubble. Not accounting for these correlations would distort the resulting bubble property distributions.

#### 6.1.1 X-Ray tomographic measurements

The reconstruction and evaluation of X-ray tomography measurements has been reexamined and features were added, some of which significantly influenced the results. These features included the consideration of the individual rise velocities of the bubbles for the calculation of the vertical dimension of each bubble, the determination of the surface area and shape of each bubble, as well as a new adaptive threshold method for the binarization of the reconstructed void fractions, which ensures that the measured void fraction is maintained through the reconstruction procedure.

Through a series of tomography simulations, the limitations of the reconstruction methods for the case without vertical internals were analyzed. By means of two-dimensional tomography simulations it could be shown that the quality of the reconstructions depends on the number of simultaneously measured bubbles, their size and their constellation in regards to the measurement angles. For example, distributions of small bubbles with mean diameters  $\bar{d}_{b,eq} \leq 4$  cm can only be reconstructed accurately, if the bubble hold-up is  $\leq 5\%$ , whereas the distributions of bubbles with a mean diameter of  $\bar{d}_{b,eq} = 6$  cm can be reconstructed well for hold-ups of up to 15%. If only the mean values are of interest, it could be shown that the mean  $\bar{d}_{b,eq}$  could be determined precisely for all simulated bubble size distributions and bubble hold-ups smaller 30%. The simulations also showed that bubbles with  $d_{b,eq} \leq 2.5$  cm are typically reduced in size through the reconstruction. Bubbles with  $d_{b,eq} \leq 1$  cm would experience a significant size reduction and would often not be recognized at all. On the other hand, the reconstructions of bubbles with  $d_{b,eq} \geq 5$  cm were slightly but insignificantly increased in size. As small bubbles



are not limiting the mass transfer between bubble and dense phase, these findings do not limit the value of the results for the reactor model. Additionally, a series of tomography simulations of semi three-dimensional bubbles that rise vertically with steady velocities was conducted. These simulations showed that the investigated bubble size distributions could be reconstructed precisely. According to the results of the simulations, the experimental determination of the bubble property distributions by means of X-ray tomography with the given setup is feasible for measurement heights larger 16 cm and fluidization numbers in the range of 1.5 – 6.

After filtering, 26,753 reconstructed bubbles were evaluated for the cases without internals and 13,858 for the case with internals. The evaluated data represents the measurement heights 16, 26, 36, 46 and 56 cm and fluidization numbers of 1.5, 2, 3, 4 and 6. For each setting, the bubble properties were broadly distributed and a clear correlation between the sizes, shapes and rise velocities of the bubbles was found. It was found that the individual bubble property distributions can be described with generalized extreme value distribution (GEV) functions and that their correlations can be accounted for with t-copula functions. The corresponding set of parameters needed to generate bubble property sample data that represent the experimental results was provided for each experimental setting. Data sampled by these distribution functions can serve as a benchmark for computational fluid dynamics (CFD) simulations or as a foundation for the development of semi-empirical correlations.

Correlations from literature that predict the bubble size as a function of the fluidization number, measurement height and in some case of the column diameter did not describe the data well, especially for higher fluidization numbers. However, a good agreement was found between the experimentally measured rise velocities and those predicted by the correlation from Davidson & Harrison [143], if the measured bubble diameters were used in the correlation.

It could be shown that the internals significantly influenced the bubble properties, as their presence lead to a reduced bubble hold-up and smaller bubbles with reduced rise velocities. This allows for better mass transfer between the dense phase and the bubble phase in comparison to reactors without internals. Some uncertainties persist considering the measurements with internals, as many small bubbles were measured. It was also found that the resolution of the applied reconstruction methods was not sufficient for the setup with internals and a correction factor was applied to account for the non-linear X-ray attenuation, which has not been verified.

### **6.1.2 X-Ray radiographic measurements**

X-ray radiography was mainly used as a cross-verification tool in this work. The availability of high resolution X-ray projections of bubbles from two or three angles that were either

individually injected with precise volumes or part of a BFB, allowed the determination of geometric bubble properties and rise velocities through image analysis.

For the case without internals, the bubble size distributions that were reconstructed in the X-ray tomography measurements of the BFB could be verified for the chosen settings. Additionally, the observed correlation between the shape of the bubble and its rise velocity could be verified through the measurement of injected isolated bubbles. When internals were inserted, the evaluation was more difficult as it was found that the installed tube spacer split the injected bubbles. It also was difficult to distinguish if clusters of multiple bubbles or single larger bubbles were observed, when internals were present. Nonetheless, qualitative assessments of the bubbling fluidization with internals were possible and it was observed that the same injected volumes would produce smaller bubbles with flattened shape with internals present in comparison to measurements without internals. Larger bubbles with  $d_{b,eq} \approx 10$  cm would appear significantly flattened, almost squared-nosed slug-like, even though they covered less than half of the reactor diameter. It was therefore hypothesized that local partial slugging may occur, due to the reduced degree of freedom for the displacement of the particles above the bubble, when vertical internals are inserted.

The radiographic measurements were also used for the verification of the optical probe measurements. For the case without vertical internals, it could be demonstrated, that the mathematically derived assumption that the mean pierced chord length equals  $2/3$  of the vertical bubble diameter, is correct. In some cases, the rise velocities would be severely over- or under-estimated, leading to a proportional over or under estimation of the measured chord length. However, the majority of the measured rise velocities were in the expected range. Similar measurements for the case with internals suffered from an experimental design error caused by the tube spacer as mentioned above. Besides that, it could be shown for the case with internals that the optical probe influences small bubbles, which accelerated significantly as they passed the probe, while larger bubbles are not influenced.

For both cases, with and without internals, the attenuation of the radiation could not be described accurately with a linear attenuation coefficient according to the Lambert Beer law. Doing so would result in bubbles that were measured to be significantly less deep than they were wide for all observed bubbles. Possible reasons for this are beam hardening or X-ray scattering.

### 6.1.3 Optical probe measurements

Comprehensive efforts were undertaken to ensure precise measurements of the hydrodynamics with the optical probes that were developed by PSI. The electronics of the optical probe sensor system were overhauled and the evaluation algorithm was revised. The functionality of

the system was verified through the measurement of a rotating disc with slits that simulate passing bubbles, as well as through measurements of precisely defined injected bubbles and the comparison of synchronized radiographic measurements. Preliminary studies showed that the measurement durations of previously published results were too short to ensure statistically robust results and that it was possible to measure with multiple probes simultaneously.

The experiments were conducted in the pilot plant GanyMeth at six measurement heights, six radial positions, seven pressures in the range of 1.14 - 11 bar and six fluidization numbers between 2 and 10 for two types of bed material, categorized as Geldart type A/B (NWa) and A (SCCa) with settled bed heights of 170 and 160 cm respectively. The measurements were conducted over 10, 15 or 20 minutes depending on the fluidization number, at a data acquisition rate of 5 kHz.

For the two available measurement heights that were comparable between the X-ray tomography and optical measurements, at ambient pressure and using the same bed material, an excellent agreement between the two measurement techniques was demonstrated. Thus, one of the main concerns of previous investigations, where the two methods produces significantly deviating results, could be resolved.

Additionally, the feasibility of a newly developed method to transform the measured chord length to the distributions of the corresponding volume-equivalent diameters was demonstrated. The method is based on the correlation between the bubble size, rise velocity and the aspect ratio, which was found in the evaluation of X-ray tomography measurements. It enables the estimation of the bubble shape from the measured chord length and rise velocity.

The results of the measurements showed a strong influence of the pressure on the hydrodynamics. Increasing the pressure leads to increased bubble hold-ups and reduced bubble sizes. Additionally, the measurements showed a growth of the measured chord lengths with the fluidization number which peak and then decrease with a further increase of  $u/u_{mf}$ . This could indicate the onset of slugging fluidization with flattened bubbles that could be partial slugs, similar to what was observed by means of X-ray radiography, or full slugs that occupy the entire cross-section. The onset of the presumed slugging was only observed for the NWa material and appears to occur at lower fluidization numbers with increasing pressure. For the SCCa material, similar trends for the growth and peaking of the chord lengths under the influence of the pressure were observed but the presumed slugging regime had seemingly not yet been fully reached for any of the experimental settings. There are also deviations of the local bubble hold-up at different heights, which appear to be influenced by the pressure. Especially for the SCCa type material, a significant increase of the hold-up with the pressure was measured at lower heights. However, these findings could not be explained conclusively.

Generally, the hydrodynamics differed significantly between the two chosen bed materials. For the SCCa powder, the onset of the bubbling fluidization occurred at gas velocities above  $u_{mf}$  and the overall bubble hold-up was significantly less with about 50% of that measured for the NWA bed material for the respective fluidization numbers. These findings are in agreements with the expected behaviors of the different powders according to their Geldart classifications [86].

### 6.2 Conclusions

The findings presented in this work benefit from the application of various independent measurement techniques that allowed the cross-verification of the main results. The feasibility and limitations of reconstructing individual bubbles in BFBs via X-ray tomography or measuring bubble chord lengths and rise velocity with optical probes have been demonstrated. Appropriate methodologies for the evaluation of such measurements were established, which are available for similar experiments in the future.

It could be shown that the bubble properties are broadly distributed for a given location within the investigated BFBs. This indicates that the description of the hydrodynamics in BFB merely by mean values of the bubble properties might not be sufficient. This is especially relevant for the prediction of critical reactor characteristics, such as mass transfer limitations that could be caused by bubbles that are faster and larger than the corresponding mean values suggest.

Other important findings of this work were the strong correlations between the size, the rise velocity and the shape of the bubbles. These correlations are particularly important in the context of measurements with optical probes or similar methods. The evaluation of such one-dimensional measurement techniques requires sophisticated statistical methods to retrieve the underlying bubble size distributions from the measured chord length distributions. These methods are often based on the assumptions of uniform bubble shapes and a homogeneous cross-sectional spatial distribution of the bubbles. These assumptions are too simplified, considering the described correlations concerning the bubble shape and the measured spatial distribution of the cross-sectional bubble hold-up. It could be shown that if these correlations are accounted for, the paired chord length and rise velocity distributions can be used to determine the underlying bubble shape and size distributions.

The influence of the internals on the hydrodynamics was found to be significant. In addition to the reduction of the bubble sizes and rise velocities, which have been already described in previous publications, it could be shown that the bubble hold-up is reduced and there were indications that the minimum bubbling velocity is increased through the presence of vertical internals. Therefore, it can be concluded that the insertion of vertical internals is beneficial for

catalytic BFB reactors as a larger fraction of the gas flows through the dense phase and the onset of mass transfer limitations caused by large and fast bubbles would therefore occur at increased fluidization numbers, which allows the operation with higher gas flows.

Some observations concerning the influence of vertical internals appeared to be conflicting. X-ray tomography reconstructions showed that bubbles are more elongated with vertical internals present, whereas X-ray radiograms of injected bubbles showed a flattened, almost slug-like appearance for the measurements with internals. It was speculated that the X-ray tomography reconstructions could be affected by the presence of internals, which may cause a erroneous reconstructions of single flat bubbles as multiple comparatively elongated bubbles. Another plausible explanation could be that smaller bubbles rise in between the internals and therefore adapt a more elongated shape, while larger bubbles rise in slug-like shapes. Thus, it is possible that the conflicting results between X-ray tomography and radiography show different stages of the bubble growth.

Experiments in a pilot-plant showed that the pressure has a significant influence on hydrodynamic characteristics of the BFB reactor. With increasing pressures the bubble hold-up increases, the pierced chord lengths reduce and what appears to be the onset of slugging fluidization occurs for lower fluidization numbers. The presumed transition between bubbling and slugging fluidization appears to ensue more smoothly with increasing pressures. It could also be shown that the mean Sauter diameter of the bed material significantly influences the fluidization, matching the expectations according to their Geldart powder type classification. For the catalytic methanation process, the observed influence of the pressure has several implications for the reactor performance. The most obvious consequence of the operation at elevated pressures is the increased throughput of the reactor, which would significantly increase the cost efficiency of the plant if mass transfer limitations are not reached. A reduced bubble growth rate suggests that the specific surface area of the bubble phase is increased and the higher values of the bubble hold-up indicate longer dwell times of the bubbles. Consequently, the mass transfer between the bubble phase and the dense phase would be increased for a given  $u/u_{mf}$  for elevated pressures. However, the consequences of an earlier onset of slugging fluidization and a possible misinterpretation of the reduced chord lengths, which also could be consequences of a flattening of the bubbles or increased bubble breakage rates, have to be considered. Slugging fluidization in reactors without internals is usually characterized by a decreased transport of particles in the wakes of slugs and locally restricted particle drift paths in comparison to what is observed for BFBs. Therefore, slugging is usually not desired for catalytic fluidized bed reactors due to the reduced vertical particle transport and the reduced gas and solids mixing. Another consequence of the increased bubble hold-up at elevated pressures is a higher height of the expanded bed.

This could improve the heat removal as more surface area would be available for the heat exchange but it could also lead to increased elutriation of bed material.

In total, several ten thousand bubbles have been reconstructed by means of X-ray tomography and several hundred thousand bubbles have been measured by optical probes. These measurements were conducted for a broad range of experimental settings, the same reactor geometry, both with and without vertical internals, and the same bed material. Additionally, a large set of radiographic X-ray images is available, which show BFBs, single injected bubbles and controlled bubble interactions between injected bubbles. The images were captured at various frame rates and resolutions, many of which still have not been processed yet. A coherent data set of this magnitude, which was captured with three independent measurement techniques, provides an excellent base for future validation of CFD simulations.

### 6.3 Recommendations for further research

Various research questions could be answered throughout the work on the present thesis, while some uncertainties persist. This section offers several suggestions for reducing remaining uncertainties and answering newly emerged research questions.

#### X-ray measurements

The application of X-ray measurements has proven to be a powerful tool for the measurements of bubble properties in BFBs. However, some limitations were discovered.

It was shown that the Lambert Beer law could not be applied to determine the bubble depth from X-ray radiographic images following a two-point calibration. By measuring defined phantom objects within a fixed bed, different methods to solve the issue could be investigated. These methods include mathematical correction factors to account for X-ray scattering or beam hardening or filtering the radiation to reduce beam hardening.

X-ray measurements of the fluidized bed with internals proved to be more challenging. The spatial resolution is insufficient for the accurate tomographic reconstruction of the bubbles in between the vertical internals due to the limited available angles. Furthermore, the application of a correction factor to account for the heterogeneous density distribution was never verified. The analysis of the X-ray radiograms indicated that the internals may distort the X-ray measurements of the bubbles. For the radiographic measurements, it is difficult to distinguish between clusters of small bubbles or single large bubbles, which indicates that the X-ray tomography measurements could be similarly affected.

One way to overcome these issues could be the utilization of the X-ray tomography systems

that are available in the Helmholtz-Zentrum Dresden Rossendorf (HZDR), which allow measurements from 240 angles with a spatial resolution of 1 mm at data acquisition rates of up to 8 kHz [197]. The HZDR is currently developing a new X-ray tomography setup, referred to as Hector (High Energy Computed Tomography Scanner Rossendorf), which will allow such measurements for columns with diameters of up to 400 mm and therefore is suited for experiments with the cold-flow model presented in this work.

It should also be assessed if X-ray tomography measurements at slightly increased pressures are feasible. If so, the influence of the pressure on the bubble properties, especially the shape, could be investigated which could be used to improve the evaluation of the optical probe measurements at elevated pressures.

#### **Optical probe measurements**

The feasibility of the transformation from chord lengths to bubble geometries was demonstrated, but some uncertainties persisted. The impact of the observed acceleration of small bubbles as they pass the probe when internals are present is unclear. It was also not understood, why accounting for the hit probabilities worsened the match of the volume-equivalent diameters between the X-ray tomography reconstructions and the processed optical probe results.

While the synchronized optical probe and X-ray radiographic measurements were successful for the case without vertical internals, the evaluation of the measurements with internals showed that the tube spacers as well as the limited bed height made the measurements unusable for the verification of the optical probe evaluation methods. It is therefore recommended to remove the middle tube spacer and repeat these measurements with an increased bed height. These measurements should also be conducted over longer time frames and could include varying radial positions of the optical probes to increase the statistical robustness of the resulting data.

It is also possible to investigate the issues by means of Monte Carlo simulations. Algorithms and fitted correlated bubble property distributions that were developed in this work could be used to generate three-dimensional bubble samples for simulated measurements with optical probes.

Another available option is the tomographic reconstruction of the BFB measurements that were conducted with the X-ray tomography area detector (XR-AD) setup with a decreased vertical resolution and increased frame rate of 200 Hz. These measurements were synchronized with optical probe measurements as well and have not been evaluated yet.

Further measurements in the pilot plant GanyMeth should be conducted to investigate the

influence of reactive conditions, once the reactive plant operation is available. The measurements at different temperatures and with different gas compositions is possible with the present setup, if alumina particles are used as bed material. However, the measurement at reactive conditions with nickel catalysts is not feasible with the current optical probe sensor system, as the particles themselves do not reflect enough light and it was proven that the reflector extensions significantly influence the measurements. It could be considered to revise the optical probe design to overcome the issue. Potentially the problem could be solved by using more powerful laser sources. It could also be considered to implement additional improvements. Recently, several researchers have demonstrated the possibility to utilize multi-fiber probes to measure not only pierced chord length and rise velocities of bubbles but also the particle motion within the dense phase [165], [259], [260]. The available Optimus test bench is well suited for the development and testing of such a sensor. Measurements of the particle flow could be important for the modelling of the particle circulation within the bed, as the influence of the vertical internals influence on the particle motion has not yet been investigated.

### Heat flux measurements

An experimental setup was built to measure the local heat flux between the fluidized bed and the vertical heat exchanger tube bundle, which was presented in Section 3.3.3. First experiments were successful and the direct impact of individual bubbles on the local heat flux could be measured.

However, due to time constrictions, a comprehensive measurement campaign that included multiple heights and radial positions was not carried out. The setup should allow the determination of the correlations between the local heat flux and the local bubble properties, which are simultaneously measured with optical probes. A thermodynamic model could be developed based on such correlations, which would allow the addition of the energy balance in the reactor model.

These correlations could eventually be verified through the evaluation of the global heat balance of the pilot plant GanyMeth at reactive or hot inert flow conditions.

### Slugging fluidization

The experiments in the GanyMeth pilot plant indicated, that a transition from the bubbling to the slugging fluidization regime occurred at different fluidization numbers, depending on the pressure. This assumption should be verified.

The vertical length of the cold-flow model could be extended to allow the measurement with



internals and increased bed heights and increased fluidization numbers. This should allow the observation of the presumed onset of slugging fluidization either visually or by means of X-ray measurements. The analysis of the measured reactor pressure might also indicate the onset of slugging fluidization.

#### **Reactor model**

After the presumed onset of a slugging fluidization regime has either been verified or disproved, the findings of the hydrodynamic investigations presented in this thesis and previous publications should be implemented in the existing reactor model.

Several correlations from the literature have been tested in this work to determine their accuracy in describing the X-ray tomography results for the case without internals. This practice should be extended to both, the results of the X-ray tomography measurements in the cold-flow model with internals and the results of the optical probe measurements in the pilot plant GanyMeth. The correlations that produce the best match can be a good basis for the fitting to the available experimental data.

In case the onset of a slugging fluidization regime is confirmed for some of the experimental settings, the transition between bubbling and slugging fluidization needs to be accounted for in the model as well.

For all fitted correlations, the influence of the pressure needs to be considered, as it has been shown to significantly influence the bubble properties and likely also the transition between fluidization regimes.

Once the heat flux measurements are evaluated and a correlation between the local heat flux and local bubble properties has been established, these should be added to the reactor model as well as proposed above.

Additionally, the relevance of accounting for the broad distributions of bubble properties as they were measured should be investigated, in comparison to solely using the respective mean values.

#### **CFD simulations**

The experimental investigations presented in this work demonstrate the difficulties and limitations of measuring the highly dynamic multiphase flows within BFBs, especially when one-dimensional sensor systems such as optical probes are used.

One possible way to reduce such uncertainties are CFD simulations. The availability of multiple coherent data sets, which include a broad spectrum of experimental settings and which were obtained by means of several independent and cross-verified experimental methods, provides a unique opportunity for the development and validation of a CFD model. Once heat flux and particle flow measurements are available, they could also be applied for the verification.

Such a model could be used for the simulation of experimental settings for which X-ray measurements are not available to support the evaluation of the optical probe measurements at increased heights and increased pressures. Additionally, the model could be applied for heat and mass transfer simulations, which can be helpful to improve the reactor model for the process simulation. This is especially useful considering that the experimental measurement of the mass transfer between bubble phase and dense phase is very challenging.

# A Fitted distributions for the X-Ray tomography data

The distribution function parameters that were fitted to the bubble property distributions, measured by means of X-Ray tomography for the case without internals as described in Section 4.3.4, are presented in the following.

Each of the fitted bubble properties ( $u_{br}$ ,  $d_{b,eq}$ ,  $l : w$  and  $r_b$ ) can be described with a GEV distribution according to Equation A.1, given the corresponding function parameters  $\mu$  (location),  $\sigma$  (scale) and  $\xi$  (shape), and the standardized variable  $s = (x - \mu)/\sigma$ .

$$F(s; \xi) = \begin{cases} \exp(-\exp(-s)) & \text{for } \xi = 0 \\ \exp(-(1 + \xi s)^{-1/\xi}) & \text{for } \xi \neq 0 \text{ and } \xi s > -1 \\ 0 & \text{for } \xi > 0 \text{ and } \xi s \leq -1 \\ 1 & \text{for } \xi < 0 \text{ and } \xi s \leq -1 \end{cases} \quad (\text{A.1})$$

Given the correlation matrix  $\hat{\rho}$  and the degrees of freedom  $\nu$ , random correlated samples from the t-copula can be generated with the Matlab function *copularnd*. The random sample data can then be transformed back to the original scale of the corresponding data with the Matlab function *ksdensity*, for which a random sample of the same size has to be generated through the provided GEV distribution function parameters.

In Tables A.1 to A.4 the required parameters that were fitted to all evaluated experimental data from the X-ray tomography measurements without internals are provided. Figures A.1 to A.4 show comparisons of the probability density functions that were generated with the provided parameters and measured experimentally for each setting (height and  $u/u_{mf}$ ).

Height [cm]	$u/u_{mf}$ [-]	GEV distribution function parameters			t-copula function parameters			
		$\mu$	$\sigma$	$\xi$	$\hat{\rho}(u_{br})$	$\hat{\rho}(d_{b,eq})$	$\hat{\rho}(l:w)$	$\hat{\rho}(r_b)$
16	1.5	1.98	0.50	-0.26	0.44	1	0.49	-0.10
16	2	2.23	0.65	-0.15	0.40	1	0.49	-0.05
16	3	3.01	1.00	-0.22	0.14	1	0.29	-0.44
16	4	3.71	1.43	-0.18	0.01	1	0.25	-0.56
16	6	4.92	2.27	-0.15	-0.01	1	0.29	-0.56
26	1.5	2.26	0.68	-0.19	0.51	1	0.54	-0.17
26	2	2.85	0.88	-0.21	0.39	1	0.47	-0.03
26	3	4.20	1.40	-0.25	0.09	1	0.22	-0.44
26	4	5.64	1.96	-0.28	0.07	1	0.20	-0.54
26	6	7.81	3.77	-0.42	-0.04	1	0.34	-0.63
36	2	3.55	1.20	-0.23	0.39	1	0.47	-0.19
36	3	5.34	1.95	-0.26	0.21	1	0.30	-0.49
36	4	6.94	2.84	-0.31	0.21	1	0.37	-0.65
36	6	10.72	4.39	-0.58	-0.24	1	0.14	-0.48
46	1.5	2.98	1.01	-0.25	0.56	1	0.60	-0.19
46	2	4.32	1.51	-0.30	0.44	1	0.52	-0.36
46	3	6.58	2.46	-0.37	0.33	1	0.43	-0.47
46	4	8.81	3.53	-0.46	0.04	1	0.32	-0.50
46	6	13.47	4.28	-0.61	-0.23	1	0.28	-0.42
56	1.5	3.47	1.17	-0.23	0.57	1	0.57	-0.29
56	2	5.18	1.92	-0.35	0.52	1	0.55	-0.49
56	3	8.44	2.87	-0.49	0.40	1	0.48	-0.56
56	4	11.01	3.79	-0.59	0.14	1	0.45	-0.39
56	6	15.63	4.53	-0.74	-0.16	1	0.40	-0.39
								2.65

Table A.1: GEV distribution function parameters and t-copula function parameters fitted to the distributions of  $d_{b,eq}$  that were measured by means of X-ray tomography for the case without internals.

Height [cm]	$u/u_{mf}$ [-]	GEV distribution function parameters			t-copula function parameters				
		$\mu$	$\sigma$	$\xi$	$\hat{\rho}(u_{br})$	$\hat{\rho}(d_{beq})$	$\hat{\rho}(l:w)$	$\hat{\rho}(r_b)$	$v$
16	1.5	0.308	0.062	0.053	1	0.44	0.66	0.06	14.12
16	2	0.315	0.080	0.115	1	0.40	0.70	0.13	16.54
16	3	0.410	0.146	0.045	1	0.14	0.72	0.23	11.29
16	4	0.482	0.195	0.029	1	0.01	0.73	0.15	7.92
16	6	0.583	0.269	0.069	1	-0.01	0.77	0.08	5.13
26	1.5	0.326	0.067	0.077	1	0.51	0.67	-0.09	15.35
26	2	0.351	0.089	0.133	1	0.39	0.72	0.00	9.84
26	3	0.453	0.154	0.139	1	0.09	0.79	0.24	8.42
26	4	0.504	0.187	0.188	1	0.07	0.78	0.10	5.18
26	6	0.667	0.268	0.057	1	-0.04	0.73	0.02	6.28
36	2	0.389	0.109	0.115	1	0.39	0.77	-0.17	9.28
36	3	0.479	0.158	0.133	1	0.21	0.79	0.01	5.53
36	4	0.539	0.202	0.168	1	0.21	0.82	-0.07	6.10
36	6	0.716	0.283	0.210	1	-0.24	0.79	0.19	5.11
46	1.5	0.364	0.086	0.093	1	0.56	0.76	-0.25	11.50
46	2	0.419	0.127	0.156	1	0.44	0.80	-0.35	8.28
46	3	0.511	0.180	0.180	1	0.33	0.81	-0.24	6.57
46	4	0.629	0.229	0.155	1	0.04	0.75	-0.15	4.14
46	6	0.777	0.242	0.199	1	-0.23	0.68	0.21	3.76
56	1.5	0.401	0.102	0.093	1	0.57	0.79	-0.28	10.25
56	2	0.472	0.147	0.115	1	0.52	0.83	-0.42	10.93
56	3	0.604	0.201	0.106	1	0.40	0.81	-0.31	6.12
56	4	0.721	0.221	0.110	1	0.14	0.78	-0.16	4.36
56	6	0.827	0.226	0.058	1	-0.16	0.67	0.31	2.65

Table A.2: GEV distribution function parameters and t-copula function parameters fitted to the distributions of  $u_{br}$  that were measured by means of X-ray tomography for the case without internals.

Height [cm]	$u/u_{mf}$ [-]	GEV distribution function parameters		t-copula function parameters				$v$
		$\mu$	$\sigma$	$\xi$	$\hat{\rho}(u_{pr})$	$\hat{\rho}(d_{b,eq})$	$\hat{\rho}(l:w)$	$\hat{\rho}(r_b)$
16	1.5	0.489	0.171	-0.055	0.66	0.49	1	0.41
16	2	0.550	0.187	0.069	0.70	0.49	1	0.39
16	3	0.702	0.272	0.027	0.72	0.29	1	0.36
16	4	0.826	0.332	0.002	0.73	0.25	1	0.24
16	6	0.952	0.424	0.069	0.77	0.29	1	0.13
26	1.5	0.502	0.162	-0.068	0.67	0.54	1	0.26
26	2	0.576	0.178	0.017	0.72	0.47	1	0.32
26	3	0.768	0.270	0.046	0.79	0.22	1	0.37
26	4	0.882	0.307	0.050	0.78	0.20	1	0.26
26	6	1.026	0.402	0.042	0.73	0.34	1	-0.03
36	2	0.611	0.182	0.008	0.77	0.47	1	0.10
36	3	0.782	0.256	0.012	0.79	0.30	1	0.21
36	4	0.856	0.299	0.082	0.82	0.37	1	0.02
36	6	1.121	0.444	0.008	0.79	0.14	1	0.15
46	1.5	0.530	0.155	-0.021	0.76	0.60	1	0.02
46	2	0.643	0.190	0.006	0.80	0.52	1	-0.11
46	3	0.783	0.254	0.044	0.81	0.43	1	-0.03
46	4	0.922	0.358	0.088	0.75	0.32	1	-0.01
46	6	1.210	0.443	-0.006	0.68	0.28	1	0.17
56	1.5	0.573	0.160	-0.009	0.79	0.57	1	-0.01
56	2	0.672	0.200	0.019	0.83	0.55	1	-0.20
56	3	0.858	0.271	0.064	0.81	0.48	1	-0.11
56	4	1.006	0.380	-0.017	0.78	0.45	1	-0.06
56	6	1.327	0.513	-0.037	0.67	0.40	1	0.20

Table A.3: GEV distribution function parameters and t-copula function parameters fitted to the distributions of  $l : w$  that were measured by means of X-ray tomography for the case without internals.

Height [cm]	$u/u_{mf}$ [-]	GEV distribution function parameters			t-copula function parameters				
		$\mu$	$\sigma$	$\xi$	$\hat{\rho}(u_{br})$	$\hat{\rho}(d_{beq})$	$\hat{\rho}(l:w)$	$\hat{\rho}(r_b)$	$v$
16	1.5	8.82	1.17	-0.631	0.06	-0.10	0.41	1	14.12
16	2	8.32	1.48	-0.634	0.13	-0.05	0.39	1	16.54
16	3	8.43	1.24	-0.573	0.23	-0.44	0.36	1	11.29
16	4	8.09	1.27	-0.508	0.15	-0.56	0.24	1	7.92
16	6	6.83	1.77	-0.467	0.08	-0.56	0.13	1	5.13
26	1.5	7.81	1.74	-0.629	-0.09	-0.17	0.26	1	15.35
26	2	7.04	2.16	-0.619	0.00	-0.03	0.32	1	9.84
26	3	7.65	1.45	-0.503	0.24	-0.44	0.37	1	8.42
26	4	6.99	1.47	-0.430	0.10	-0.54	0.26	1	5.18
26	6	4.61	2.33	-0.374	0.02	-0.63	-0.03	1	6.28
36	2	6.34	2.02	-0.492	-0.17	-0.19	0.10	1	9.28
36	3	6.44	1.75	-0.419	0.01	-0.49	0.21	1	5.53
36	4	5.47	1.99	-0.393	-0.07	-0.65	0.02	1	6.10
36	6	3.22	1.84	-0.136	0.19	-0.48	0.15	1	5.11
46	1.5	6.26	2.00	-0.508	-0.25	-0.19	0.02	1	11.50
46	2	5.79	1.84	-0.417	-0.35	-0.36	-0.11	1	8.28
46	3	5.04	2.02	-0.354	-0.24	-0.47	-0.03	1	6.57
46	4	3.91	2.03	-0.262	-0.15	-0.50	-0.01	1	4.14
46	6	2.57	1.57	-0.061	0.21	-0.42	0.17	1	3.76
56	1.5	5.65	1.83	-0.384	-0.28	-0.29	-0.01	1	10.25
56	2	4.98	1.76	-0.362	-0.42	-0.49	-0.20	1	10.93
56	3	4.16	1.85	-0.270	-0.31	-0.56	-0.11	1	6.12
56	4	3.27	1.64	-0.159	-0.16	-0.39	-0.06	1	4.36
56	6	2.71	1.45	0.009	0.31	-0.39	0.20	1	2.65

Table A.4: GEV distribution function parameters and t-copula function parameters fitted to the distributions of  $r_b$  that were measured by means of X-ray tomography for the case without internals.

## Appendix A. Fitted distributions for the X-Ray tomography data

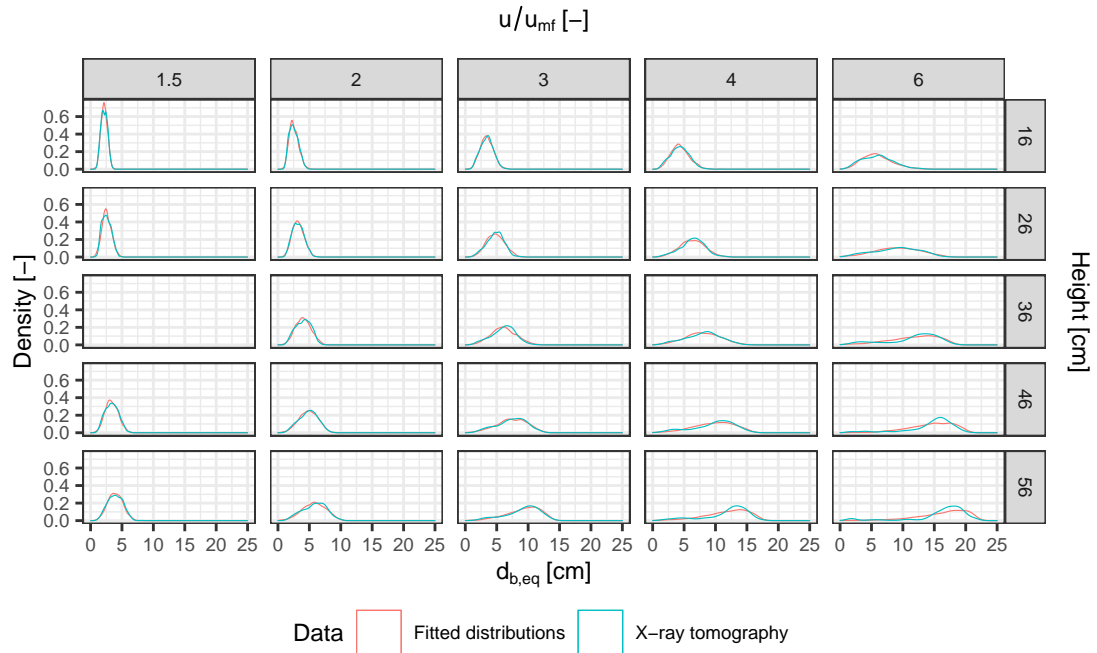


Figure A.1: Fitted and experimental PDF of  $d_{b,eq}$ .

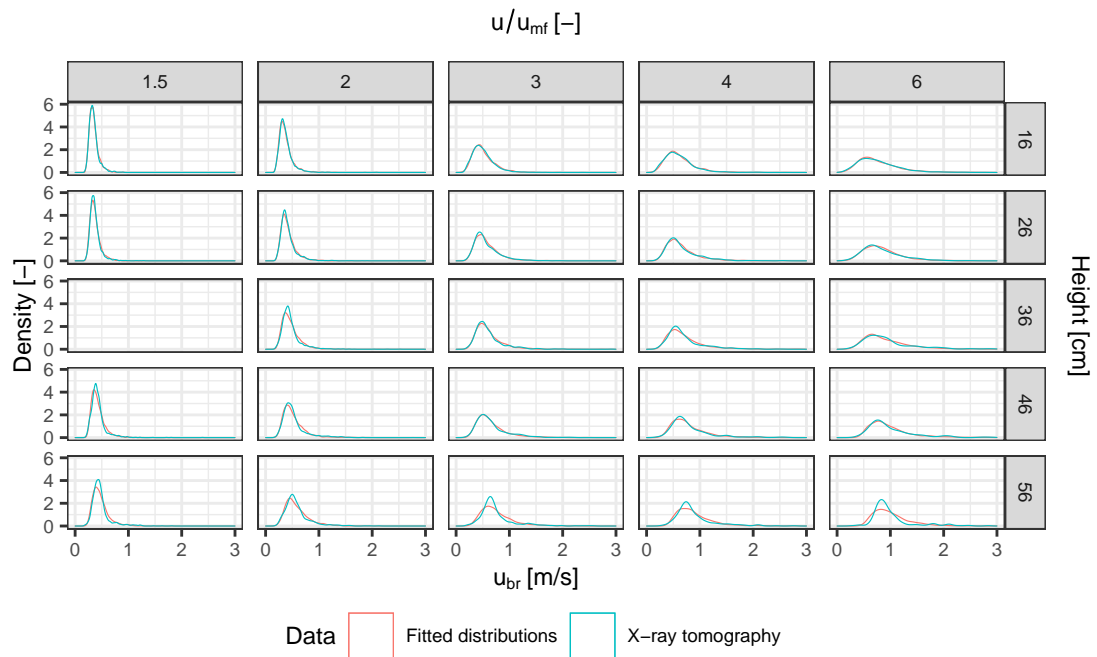


Figure A.2: Fitted and experimental PDF of  $u_{br}$ .



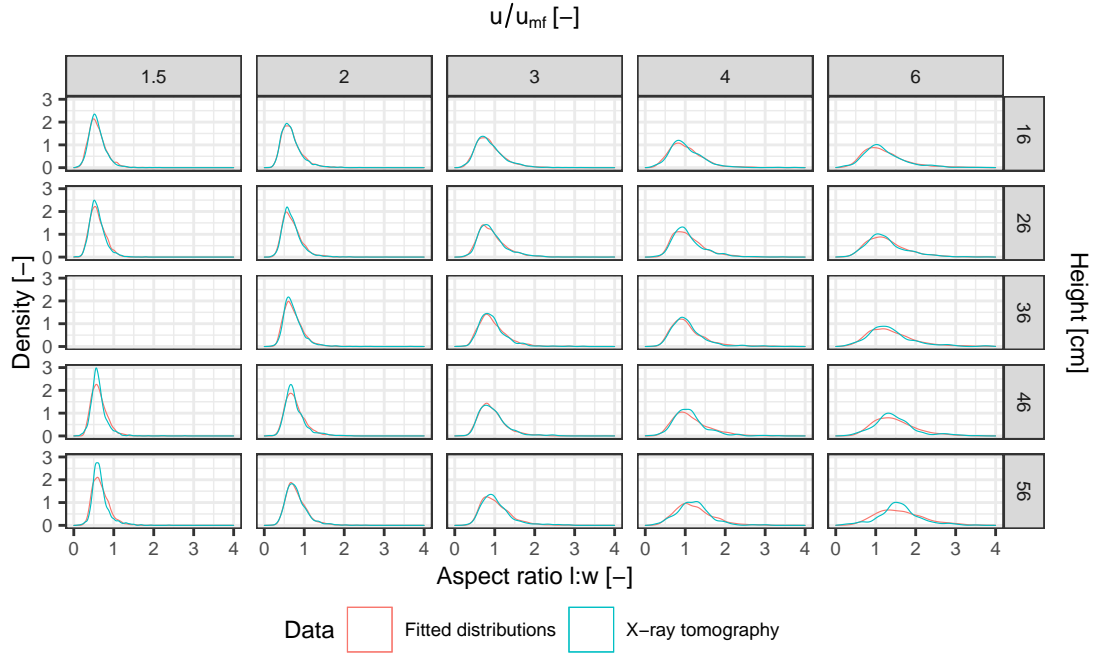


Figure A.3: Fitted and experimental PDF of  $l:w$ .

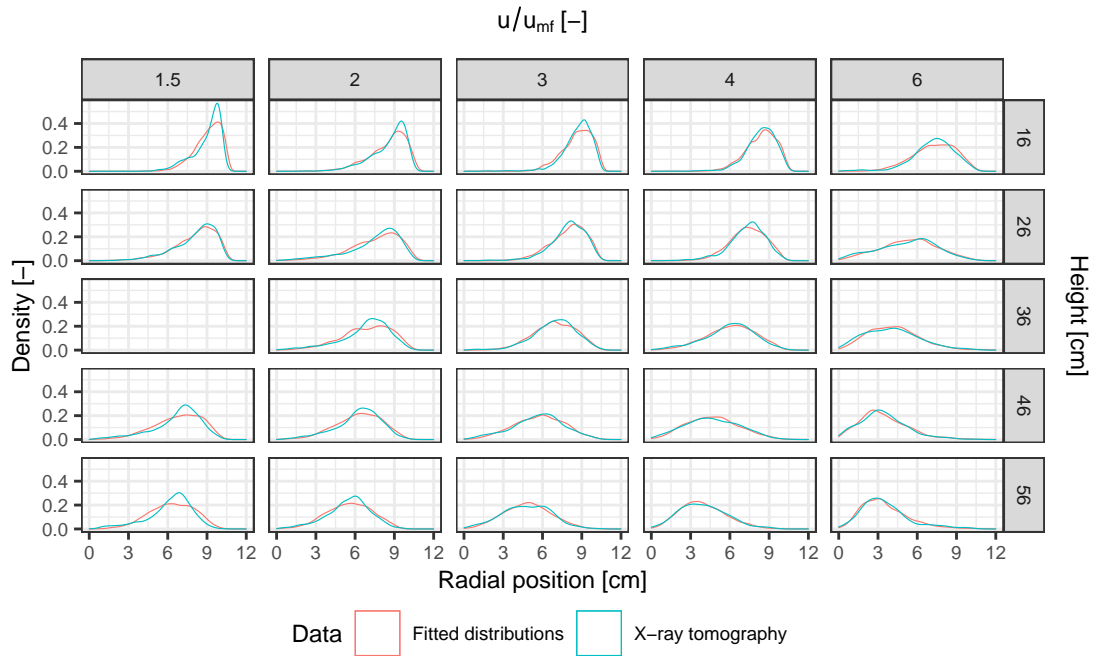


Figure A.4: Fitted and experimental PDF of  $r_b$ .



# Bibliography

- [1] M. Allen, P. Antwi-Agyei, F. Aragon-Durand *et al.*, ‘Technical summary: Global warming of 1.5 c. an ipcc special report on the impacts of global warming of 1.5 c above pre-industrial levels and related global greenhouse gas emission pathways, in the context of strengthening the global response to the threat of climate change, sustainable development, and efforts to eradicate poverty’, 2019.
- [2] *Climate Change: Evidence and Causes: Update 2020*. Washington, DC: The National Academies Press, 2020. DOI: 10.17226/25733.
- [3] D. Wuebbles, D. Fahey, K. Hibbard *et al.*, ‘Executive summary. Climate Science Special Report: Fourth National Climate Assessment, Volume I’, 2017. DOI: 10.7930/J0DJ5CTG.
- [4] United Nations, *Paris Agreement*, UN Treaty, 2015.
- [5] Swiss Federal Office of Energy (SFOE), *Energiestrategie 2050*, 2022.
- [6] M. Schmid and D. Decurtins, ‘Energieversorgung der Zukunft’, 2018.
- [7] Statistische Amt der Europäischen Union, ‘Pressemitteilung 27/2019 - Erneuerbare Energien in der EU’, 2019.
- [8] Bundesamt für Energie (BFE), *Schweizerische Statistik der erneuerbaren Energien. Ausgabe 2018*, 2019.
- [9] Statistische Amt der Europäischen Union, ‘Shedding light on energy in the EU - A guided tour of energy statistics — 2019 edition’, Statistische Amt der Europäischen Union, Tech. Rep., 2019. DOI: 10.2785/555325.
- [10] A. Poullikas, ‘A comparative overview of large-scale battery systems for electricity storage’, *Renewable and Sustainable Energy Reviews*, vol. 27, pp. 778–788, 2013. DOI: 10.1016/J.RSER.2013.07.017.
- [11] G. Dileep, ‘A survey on smart grid technologies and applications’, *Renewable Energy*, vol. 146, pp. 2589–2625, 2020. DOI: 10.1016/J.RENENE.2019.08.092.
- [12] C. House and N. Way, ‘The world’s water battery: Pumped hydropower storage and the clean energy transition International Hydropower Association’,
- [13] M. Budt, D. Wolf, R. Span and J. Yan, ‘A review on compressed air energy storage: Basic principles, past milestones and recent developments’, *Applied Energy*, vol. 170, pp. 250–268, 2016. DOI: 10.1016/J.APENERGY.2016.02.108.

- [14] A. Sauer, E. Abele and H. U. Buhl, *Energieflexibilität in der deutschen Industrie: Ergebnisse aus dem Kopernikus-Projekt-Synchronisierte und energieadaptive Produktionstechnik zur flexiblen Ausrichtung von Industrieprozessen auf eine fluktuierende Energieversorgung (SynErgie)*. Fraunhofer Verlag, 2019.
- [15] P. Gabrielli, A. Poluzzi, G. J. Kramer, C. Spiers, M. Mazzotti and M. Gazzani, 'Seasonal energy storage for zero-emissions multi-energy systems via underground hydrogen storage', *Renewable and Sustainable Energy Reviews*, vol. 121, p. 109 629, 2020. DOI: 10.1016/J.RSER.2019.109629.
- [16] A. M. Elberry, J. Thakur, A. Santasalo-Aarnio and M. Larimi, 'Large-scale compressed hydrogen storage as part of renewable electricity storage systems', *International Journal of Hydrogen Energy*, vol. 46, no. 29, pp. 15 671–15 690, 2021. DOI: 10.1016/J.IJHYDENE.2021.02.080.
- [17] P. Sabatier and J. B. Senderens, 'Comptes Rendus Des Séances De L'Académie Des Sciences, Section VI–Chimie', *Paris: Imprimerie Gauthier-Villars*, 1902.
- [18] A. S. Calbry-Muzyka and T. J. Schildhauer, 'Direct Methanation of Biogas—Technical Challenges and Recent Progress', *Frontiers in Energy Research*, vol. 8, 2020. DOI: 10.3389/FENRG.2020.570887.
- [19] S. Rönsch, J. Schneider, S. Matthischke *et al.*, 'Review on methanation - From fundamentals to current projects', *Fuel*, vol. 166, pp. 276–296, 2016. DOI: <http://dx.doi.org/10.1016/j.fuel.2015.10.111>.
- [20] J. Kopyscinski, T. J. Schildhauer and S. M. A. Biollaz, 'Production of synthetic natural gas (SNG) from coal and dry biomass - A technology review from 1950 to 2009', *Fuel*, vol. 89, no. 8, pp. 1763–1783, 2010. DOI: <http://dx.doi.org/10.1016/j.fuel.2010.01.027>.
- [21] A. S. Calbry-Muzyka, A. Gantenbein, J. Schneebeli *et al.*, 'Deep removal of sulfur and trace organic compounds from biogas to protect a catalytic methanation reactor', *Chemical Engineering Journal*, 2019. DOI: 10.1016/j.cej.2018.12.012.
- [22] A. Calbry-Muzyka, H. Madi, F. Rüscher-Pfund, M. Gandiglio and S. Biollaz, 'Biogas composition from agricultural sources and organic fraction of municipal solid waste', *Renewable Energy*, vol. 181, pp. 1000–1007, 2022. DOI: 10.1016/J.RENENE.2021.09.100.
- [23] A. Gantenbein, O. Kröcher, S. M. A. Biollaz and T. J. Schildhauer, 'Techno-Economic Evaluation of Biological and Fluidised-Bed Based Methanation Process Chains for Grid-Ready Biomethane Production', *Frontiers in Energy Research*, vol. 0, p. 1004, 2022. DOI: 10.3389/FENRG.2021.775259.
- [24] U. Kaufmann, 'Schweizerische Statistik der erneuerbaren Energien - Ausgabe 2020', Bundesamt für Energie BFE - Analysen und Perspektiven, Tech. Rep., 2021.
- [25] V. Burg, G. Bowman, S. Hellweg and O. Thees, 'Long-term wet bioenergy resources in Switzerland: Drivers and projections until 2050', *Energies*, vol. 12, no. 18, 2019. DOI: 10.3390/EN12183585.

- [26] A. Nogalska, A. Zukowska and R. Garcia-Valls, 'Atmospheric CO<sub>2</sub> capture for the artificial photosynthetic system', *Science of The Total Environment*, vol. 621, pp. 186–192, 2018. DOI: 10.1016/J.SCITOTENV.2017.11.248.
- [27] T. Wilberforce, A. Baroutaji, B. Soudan, A. H. Al-Alami and A. G. Olabi, 'Outlook of carbon capture technology and challenges', *Science of The Total Environment*, vol. 657, pp. 56–72, 2019. DOI: 10.1016/J.SCITOTENV.2018.11.424.
- [28] C. Beuttler, L. Charles and J. Wurzbacher, 'The Role of Direct Air Capture in Mitigation of Anthropogenic Greenhouse Gas Emissions', *Frontiers in Climate*, vol. 1, p. 10, 2019. DOI: 10.3389/FCLIM.2019.00010.
- [29] F. Holz, T. Scherwath, P. Crespo del Granado *et al.*, 'A 2050 perspective on the role for carbon capture and storage in the European power system and industry sector', *Energy Economics*, vol. 104, p. 105631, 2021. DOI: 10.1016/J.ENERCO.2021.105631.
- [30] M. Lehner, P. Biegger and A. R. Medved, 'Power-to-gas: Die rolle der chemischen speicherung in einem energiesystem mit hohen anteilen an erneuerbarer energie', *e & i Elektrotechnik und Informationstechnik*, vol. 134, no. 3, pp. 246–251, 2017. DOI: 10.1007/s00502-017-0502-6.
- [31] M. Thema, T. Weidlich, A. Bellack *et al.*, 'Biological CO<sub>2</sub>-Methanation: An Approach to Standardization Spatiotemporal Modelling RES View project Bubble Column Reactor View project Biological CO<sub>2</sub>-Methanation: An Approach to Standardization', vol. 12, p. 1670, 2019. DOI: 10.3390/en12091670.
- [32] M. Götz, J. Lefebvre, F. Moers *et al.*, 'Renewable Power-to-Gas: A technological and economic review', *Renewable Energy*, vol. 85, pp. 1371–1390, 2016. DOI: <http://dx.doi.org/10.1016/j.renene.2015.07.066>.
- [33] B. Lecker, L. Illi, A. Lemmer and H. Oechsner, 'Biological hydrogen methanation – A review', *Bioresource Technology*, vol. 245, pp. 1220–1228, 2017. DOI: 10.1016/J.BIORTECH.2017.08.176.
- [34] J. Witte, 'Experimental and Techno-Economic Assessment of Catalytic Methanation of Biogas for Power-to-Gas Processes', Ph.D. dissertation, ETH Zürich, Nr. 20209, 2018. DOI: 10.3929/ETHZ-B-000304900.
- [35] P. De Groot, M. Coulon and K. Dransfeld, 'Ni(CO)<sub>4</sub> formation on single Ni crystals: Reaction kinetics and observation of surface facetting induced by the reaction', *Surface Science*, vol. 94, no. 1, pp. 204–220, 1980. DOI: 10.1016/0039-6028(80)90164-8.
- [36] G. A. Mills and F. W. Steffgen, 'Catalytic Methanation', <http://dx.doi.org/10.1080/01614947408071860>, vol. 8, no. 1, pp. 159–210, 1974. DOI: 10.1080/01614947408071860.
- [37] K. Ghaib, K. Nitz and F.-Z. Ben-Fares, 'Chemical Methanation of CO<sub>2</sub>: A Review', *Chem-BioEng Reviews*, n/a–n/a, 2016. DOI: 10.1002/cben.201600022.
- [38] T. J. Schildhauer and S. M. A. Biollaz, 'Reactors for catalytic methanation in the conversion of biomass to synthetic natural gas (sng)', *CHIMIA*, vol. 69, no. 10, p. 603, 2015. DOI: 10.2533/chimia.2015.603.

## Bibliography

---

- [39] M. Lehner, R. Tichler, H. Steinmüller and M. Koppe, *Power-to-gas: technology and business models*. Springer, 2014.
- [40] T. J. Schildhauer, 'Methanation for Synthetic Natural Gas Production—Chemical Reaction Engineering Aspects', *Synthetic Natural Gas from Coal and Dry Biomass, and Power-to-Gas Applications*, 2016.
- [41] C. H. Bartholomew, 'Mechanisms of catalyst deactivation', *Applied Catalysis A General*, vol. 212, no. 1-2, pp. 17–60, 2001. DOI: 10.1016/S0926-860X(00)00843-7.
- [42] D. Schlereth, P. J. Donaubauer and O. Hinrichsen, 'Metallic Honeycombs as Catalyst Supports for Methanation of Carbon Dioxide', *Chemical Engineering and Technology*, vol. 38, no. 10, pp. 1845–1852, 2015. DOI: 10.1002/CEAT.201400717.
- [43] T. Boger and A. K. Heibel, 'Heat transfer in conductive monolith structures', *Chemical Engineering Science*, vol. 60, no. 7, pp. 1823–1835, 2005. DOI: 10.1016/J.CES.2004.11.031.
- [44] P. Biegger, F. Kirchbacher, A. R. Medved, M. Miltner, M. Lehner and M. Harasek, 'Development of honeycomb methanation catalyst and its application in power to gas systems', *Energies : open-access journal of related scientific research, technology development and studies in policy and management*, vol. 11.2018, p. 1679, 7 2018. DOI: 10.3390/EN11071679.
- [45] M. Goetz, F. Ortloff, R. Reimert, O. Basha, B. I. Morsi and T. Kolb, 'Evaluation of Organic and Ionic Liquids for Three-Phase Methanation and Biogas Purification Processes', *Energy Fuels*, vol. 27, no. 8, pp. 4705–4716, 2013. DOI: 10.1021/ef400334p.
- [46] J. Kopyscinski, T. J. Schildhauer and S. M. A. Biollaz, 'Employing Catalyst Fluidization to Enable Carbon Management in the Synthetic Natural Gas Production from Biomass', *Chemical Engineering Technology*, vol. 32, no. 3, pp. 343–347, 2009. DOI: 10.1002/ceat.200800413.
- [47] J. G. Yates and P. Lettieri, 'Catalytic Processes', pp. 23–65, 2016. DOI: 10.1007/978-3-319-39593-7\_2.
- [48] W.-C. Yang, *Handbook of Fluidization and Fluid-Particle Systems (Chemical Industries)*. CRC Press, 2003.
- [49] J. Werther, 'Fluidized-Bed Reactors', in *Ullmann's Encyclopedia of Industrial Chemistry*. Wiley-VCH Verlag GmbH Co. KGaA, 2000. DOI: 10.1002/14356007.b04\_239.
- [50] T. Aicher, M. Iglesias-Gonzales and M. Götz, 'Arbeitspaket 5: betrachtungen des Gesamtsystems im Hinblick auf Dynamik und Prozessintegration', *Energie wasser praxis*, pp. 51–55, 2014.
- [51] A. Gantenbein, J. Witte, S. M. Biollaz, O. Kröcher and T. J. Schildhauer, 'Flexible application of biogas upgrading membranes for hydrogen recycle in power-to-methane processes', *Chemical Engineering Science*, vol. 229, p. 116 012, 2021. DOI: 10.1016/J.CES.2020.116012.

- [52] H. Hofbauer, G. Veronik, T. Fleck, R. Rauch, H. Mackinger and E. Fercher, 'The FICFB — Gasification Process', *Developments in Thermochemical Biomass Conversion*, pp. 1016–1025, 1997. DOI: 10.1007/978-94-009-1559-6\_82.
- [53] T. J. Schildhauer and S. M. Biollaz, 'Fluidized bed methanation for SNG production - Process development at the Paul Scherrer Institut', in *Synthetic Natural Gas from Coal and Dry Biomass, and Power-to-Gas Applications*, Hoboken, NJ, USA: John Wiley Sons, Inc., 2016, pp. 221–230. DOI: 10.1002/9781119191339.ch8.
- [54] J. Kopyscinski, T. J. Schildhauer and S. M. A. Biollaz, 'Methanation in a fluidized bed reactor with high initial CO partial pressure: Part II— Modeling and sensitivity study', *Chemical Engineering Science*, vol. 66, no. 8, pp. 1612–1621, 2011. DOI: <https://doi.org/10.1016/j.ces.2010.12.029>.
- [55] J. Werther, 'Effect of gas distributor on hydrodynamics of gas fluidized beds', *German Chem. Eng.*, vol. 1, pp. 166–174, 1978.
- [56] K. Hilligardt and J. Werther, 'Local bubble gas hold-up and expansion of gas/solid fluidized beds', *German chemical engineering*, vol. 9, pp. 215–221, 4 1986.
- [57] J. Kopyscinski, T. J. Schildhauer, F. Vogel, S. M. Biollaz and A. Wokaun, 'Applying spatially resolved concentration and temperature measurements in a catalytic plate reactor for the kinetic study of CO methanation', *Journal of Catalysis*, vol. 271, no. 2, pp. 262–279, 2010. DOI: 10.1016/J.JCAT.2010.02.008.
- [58] J. Witte, J. Settino, S. M. A. Biollaz and T. J. Schildhauer, 'Direct Catalytic Methanation of Biogas - Part I: New Insights into Biomethane Production using Rate-Based Modelling and Detailed Process Analysis', *Energy Conversion and Management*,
- [59] J. Witte, A. Kunz, S. M. Biollaz and T. J. Schildhauer, 'Direct catalytic methanation of biogas – part ii: Techno-economic process assessment and feasibility reflections', *Energy Conversion and Management*, vol. 178, pp. 26–43, 2018. DOI: 10.1016/J.ENCONMAN.2018.09.079.
- [60] J. Witte, A. Calbry-Muzyka, T. Wieseler, P. Hottinger, S. M. Biollaz and T. J. Schildhauer, 'Demonstrating direct methanation of real biogas in a fluidised bed reactor', *Applied Energy*, vol. 240, pp. 359–371, 2019. DOI: 10.1016/j.apenergy.2019.01.230.
- [61] A. Gantenbein, 'Flexibilisation of Biogas-Based Power-to-Gas Processes: A Techno-Economic and Experimental Assessment', Ph.D. dissertation, EPF Lausanne, Nr. 10032, 2022.
- [62] M. Seemann, T. Schildhauer, S. Biollaz, S. Stucki and A. Wokaun, 'The regenerative effect of catalyst fluidization under methanation conditions', *Applied Catalysis A: General*, vol. 313, no. 1, pp. 14–21, 2006. DOI: 10.1016/j.apcata.2006.06.048.
- [63] A. S. Calbry-Muzyka, A. Gantenbein, J. Schneebeli *et al.*, 'Deep removal of sulfur and trace organic compounds from biogas to protect a catalytic methanation reactor', *Chemical Engineering Journal*, vol. 360, pp. 577–590, 2019. DOI: 10.1016/j.cej.2018.12.012.

- [64] A. J. Welch, E. Dunn, J. S. Duchene and H. A. Atwater, 'Bicarbonate or Carbonate Processes for Coupling Carbon Dioxide Capture and Electrochemical Conversion', *ACS Energy Letters*, vol. 5, no. 3, pp. 940–945, 2020. DOI: 10.1021/acsenenergylett.0c00234.
- [65] J. A. Valenzuela and L. R. Glicksman, 'Gas flow distribution in a bubbling fluidized bed', *Powder Technology*, vol. 44, no. 2, pp. 103–113, 1985. DOI: [http://dx.doi.org/10.1016/0032-5910\(85\)87016-9](http://dx.doi.org/10.1016/0032-5910(85)87016-9).
- [66] J. R. Grace, X. Bi and N. Ellis, 'Essentials of fluidization technology', *Essentials of Fluidization Technology*, pp. 1–604, 2020. DOI: 10.1002/9783527699483.
- [67] L. R. Glicksman, 'Scaling relationships for fluidized beds', *Chemical Engineering Science*, vol. 39, no. 9, pp. 1373–1379, 1984. DOI: [http://dx.doi.org/10.1016/0009-2509\(84\)80070-6](http://dx.doi.org/10.1016/0009-2509(84)80070-6).
- [68] S. Karimipour and T. Pugsley, 'A critical evaluation of literature correlations for predicting bubble size and velocity in gas-solid fluidized beds', *Powder Technology*, vol. 205, no. 1–3, pp. 1–14, 2011. DOI: <http://dx.doi.org/10.1016/j.powtec.2010.09.016>.
- [69] M. Rüdisüli, 'Characterization of rising gas bubbles in fluidized beds by means of statistical tools', Ph.D. dissertation, ETH Zürich, Nr. 20209, 2012. DOI: 10.3929/ethz-a-007089625.
- [70] S. Maurer, 'Hydrodynamic characterization and scale-up of bubbling fluidized beds for catalytic conversion', Ph.D. dissertation, ETH Zürich, Nr. 22722, 2015. DOI: 10.3929/ethz-a-010453120.
- [71] F. Schillinger, 'Systematic assessment and application of local optical and two-dimensional X-ray measurement techniques for hydrodynamic characterization of bubbling fluidized beds', Ph.D. dissertation, ETH Zürich, Nr. 25346, 2018. DOI: 10.3929/ethz-b-000306127.
- [72] F. Schillinger, S. Maurer, M. Küntle, T. J. Schildhauer and A. Wokaun, 'Hydrodynamic investigations by a local optical measurement technique designed for high-temperature applications – first measurements at a fluidized bed immersed by vertical internals at cold conditions', *Powder Technology*, 2019. DOI: 10.1016/j.powtec.2018.11.050.
- [73] D. Kunii and O. Levenspiel, *Fluidization engineering*. Butterworth-Heinemann, 1991.
- [74] F. Winkler, 'Verfahren zum herstellen von wassergas', 1926.
- [75] H. M. Larson, E. H. Knowlton and C. S. Popple, *History of Standard Oil Company (New Jersey): New Horizons, 1927-1950*. Harper & Row, 1971.
- [76] J. L. Enos, *Petroleum, progress and profits: a history of process innovation*. MIT Press, 1962.
- [77] C. E. Jahnig, D. L. Campbell and H. Z. Martin, 'History of fluidized solids development at Exxon', in *Fluidization*, J. R. Grace and J. M. Matsen, Eds. Boston, MA: Springer US, 1980, pp. 3–24. DOI: 10.1007/978-1-4684-1045-7\_1.
- [78] J. G. Yates and P. Lettieri, 'Fluidized-Bed Reactors: Processes and Operating Conditions', vol. 26, 2016. DOI: 10.1007/978-3-319-39593-7.



- [79] A. Squires, 'Proc. of the joint meeting of che. eng. soc. of china and aiche', Chemical Industry Press, 1982, pp. 322–353.
- [80] L. Reh, 'Fluidized bed processing', *Chemical Engineering Progress*, vol. 67, no. 2, p. 58, 1971.
- [81] T. M. Knowlton, S. B. R. Karri and A. Issangya, 'Scale-up of fluidized-bed hydrodynamics', *Powder Technology*, vol. 150, no. 2, pp. 72–77, 2005. DOI: <http://dx.doi.org/10.1016/j.powtec.2004.11.036>.
- [82] M. Rüdüsili, T. J. Schildhauer, S. M. A. Biollaz and J. R. van Ommen, 'Scale-up of bubbling fluidized bed reactors — A review', *Powder Technology*, vol. 217, pp. 21–38, 2012. DOI: [10.1016/j.powtec.2011.10.004](https://doi.org/10.1016/j.powtec.2011.10.004).
- [83] J. Lyu, H. Yang, W. Ling *et al.*, 'Development of a supercritical and an ultra-supercritical circulating fluidized bed boiler', *Frontiers in Energy*, vol. 13, pp. 114–119, 1 2019. DOI: [10.1007/s11708-017-0512-4](https://doi.org/10.1007/s11708-017-0512-4).
- [84] S. C. Saxena and G. J. Vogel, 'Segregation and fluidization characteristics of a dolomite bed with a range of particle sizes and shapes', *The Chemical Engineering Journal*, vol. 14, pp. 59–63, 1 1977. DOI: [10.1016/0300-9467\(77\)80023-3](https://doi.org/10.1016/0300-9467(77)80023-3).
- [85] A. C. Hoffmann and J. G. Yates, 'Experimental observations of fluidized beds at elevated pressures', *Chemical Engineering Communications*, vol. 41, no. 1-6, pp. 133–149, 1986. DOI: [10.1080/00986448608911716](https://doi.org/10.1080/00986448608911716).
- [86] D. Geldart, 'Types of gas fluidization', *Powder Technology*, vol. 7, no. 5, pp. 285–292, 1973. DOI: [10.1016/0032-5910\(73\)80037-3](https://doi.org/10.1016/0032-5910(73)80037-3).
- [87] R. G. Bait, S. B. Pawar, A. N. Banerjee, A. S. Mujumdar and B. N. Thorat, 'Mechanically agitated fluidized bed drying of cohesive particles at low air velocity', *Drying Technology*, vol. 29, no. 7, pp. 808–818, 7 2011. DOI: [10.1080/07373937.2010.541574](https://doi.org/10.1080/07373937.2010.541574).
- [88] S. Kaliyaperumal, S. Barghi, J. Zhu, L. Briens and S. Rohani, 'Effects of acoustic vibration on nano and sub-micron powders fluidization', *Powder technology*, vol. 210, no. 2, pp. 143–149, 2011. DOI: [10.1016/j.powtec.2011.03.007](https://doi.org/10.1016/j.powtec.2011.03.007).
- [89] S. S. Ali and M. Asif, 'Fluidization of nano-powders: Effect of flow pulsation', *Powder Technology*, vol. 225, pp. 86–92, 2012. DOI: [10.1016/J.POWTEC.2012.03.035](https://doi.org/10.1016/J.POWTEC.2012.03.035).
- [90] Y. Liu, H. Ohara and A. Tsutsumi, 'Pulsation-assisted fluidized bed for the fluidization of easily agglomerated particles with wide size distributions', *Powder Technology*, vol. 316, pp. 388–399, 2017. DOI: [10.1016/J.POWTEC.2016.12.049](https://doi.org/10.1016/J.POWTEC.2016.12.049).
- [91] J. M. Valverde Millán, 'The use of additives to control powder flow. mechanical properties of fine powder beds', in *Fluidization of Fine Powders: Cohesive versus Dynamical Aggregation*. Dordrecht: Springer Netherlands, 2013, pp. 99–120. DOI: [10.1007/978-94-007-5587-1\\_12](https://doi.org/10.1007/978-94-007-5587-1_12).
- [92] A. R. Abrahamsen and D. Geldart, 'Behaviour of gas-fluidized beds of fine powders part II. Voidage of the dense phase in bubbling beds', *Powder Technology*, vol. 26, no. 1, pp. 47–55, 1980. DOI: [10.1016/0032-5910\(80\)85006-6](https://doi.org/10.1016/0032-5910(80)85006-6).

## Bibliography

---

- [93] J. G. Yates, *Fundamentals of fluidized-bed chemical processes*. Butterworths, 1983, p. 222.
- [94] X. Yang, Y. Zhang, Y. Yang, E. Zhou, Z. Fu and Y. Zhao, 'Fluidization of Geldart D type particles in a shallow vibrated gas-fluidized bed', *Powder Technology*, vol. 305, pp. 333–339, 2017. DOI: 10.1016/J.POWTEC.2016.09.044.
- [95] J. R. Grace, 'Contacting modes and behaviour classification of gas—solid and other two-phase suspensions', *The Canadian Journal of Chemical Engineering*, vol. 64, no. 3, pp. 353–363, 1986. DOI: 10.1002/CJCE.5450640301.
- [96] W.-C. Yang, 'Modification and re-interpretation of Geldart's classification of powders', *Powder Technology*, vol. 171, no. 2, pp. 69–74, 2007. DOI: 10.1016/j.powtec.2006.08.024.
- [97] M. J. V. Goldschmidt, J. A. M. Kuipers and W. P. M. van Swaaij, 'Hydrodynamic modelling of dense gas-fluidised beds using the kinetic theory of granular flow: effect of coefficient of restitution on bed dynamics', *Chemical Engineering Science*, vol. 56, no. 2, pp. 571–578, 2001. DOI: 10.1016/S0009-2509(00)00262-1.
- [98] C. Loha, H. Chattopadhyay and P. K. Chatterjee, 'Effect of coefficient of restitution in euler–euler cfd simulation of fluidized-bed hydrodynamics', *Particuology*, vol. 15, pp. 170–177, 2014. DOI: <https://doi.org/10.1016/j.partic.2013.07.001>.
- [99] S. Ergun, 'Fluid flow through packed columns', *Chem. Eng. Prog.*, vol. 48, pp. 89–94, 1952.
- [100] C. Y. Wen and Y. H. Yu, 'A generalized method for predicting the minimum fluidization velocity', *AIChE Journal*, vol. 12, pp. 610–612, 3 1966. DOI: 10.1002/AIC.690120343.
- [101] A. Anantharaman, R. A. Cocco and J. W. Chew, 'Evaluation of correlations for minimum fluidization velocity (u) in gas-solid fluidization', *Powder Technology*, vol. 323, pp. 454–485, 2018. DOI: 10.1016/j.powtec.2017.10.016.
- [102] C. Y. Wen and L. H. Chen, 'Fluidized bed freeboard phenomena: Entrainment and elutriation', *AIChE Journal*, vol. 28, no. 1, pp. 117–128, 1982. DOI: 10.1002/AIC.690280117.
- [103] S. T. Pemberton and J. F. Davidson, 'Elutriation from fluidized beds—I. Particle ejection from the dense phase into the freeboard', *Chemical Engineering Science*, vol. 41, no. 2, pp. 243–251, 1986. DOI: 10.1016/0009-2509(86)87005-1.
- [104] C. R. Müller, D. J. Holland, J. F. Davidson *et al.*, 'Rapid two-dimensional imaging of bubbles and slugs in a three-dimensional, gas-solid, two-phase flow system using ultrafast magnetic resonance', *Phys. Rev. E*, vol. 75, no. 2, p. 20 302, 2007. DOI: 10.1103/PhysRevE.75.020302.
- [105] X. Bi, 'Gas Fluidization Flow Regimes', *Essentials of Fluidization Technology*, pp. 55–74, 2020. DOI: 10.1002/9783527699483.CH4.
- [106] J. Baeyens and D. Geldart, 'An investigation into slugging fluidized beds', *Chemical Engineering Science*, vol. 29, no. 1, pp. 255–265, 1974. DOI: [https://doi.org/10.1016/0009-2509\(74\)85051-7](https://doi.org/10.1016/0009-2509(74)85051-7).

- [107] J. R. Grace, 'Slug flow', *Essentials of Fluidization Technology*, pp. 153–162, 2020. DOI: 10.1002/9783527699483.CH8.
- [108] X. Bi, 'Turbulent fluidization', *Essentials of Fluidization Technology*, pp. 163–180, 2020. DOI: 10.1002/9783527699483.CH9.
- [109] H. T. Bi, N. Ellis, I. A. Abba and J. R. Grace, 'A state-of-the-art review of gas–solid turbulent fluidization', *Chemical Engineering Science*, vol. 55, no. 21, pp. 4789–4825, 2000. DOI: 10.1016/S0009-2509(00)00107-x.
- [110] O. Molerus, 'Overview: Pneumatic transport of solids', *Powder Technology*, vol. 88, pp. 309–321, 3 1996. DOI: 10.1016/S0032-5910(96)03136-1.
- [111] R. Toomey and H. Johnstone, 'Chemical engineering progress', *Volume*, vol. 48, p. 220, 1952.
- [112] J. F. Davidson, R. Clift and D. Harrison, *Fluidization*. Academic Press, 1985.
- [113] D. Geldart, *Gas fluidization technology*. John Wiley and Sons Inc., New York, NY, 1986.
- [114] K. Anderson, S. Sundaresan and R. Jackson, 'Instabilities and the formation of bubbles in fluidized beds', *Journal of Fluid Mechanics*, vol. 303, pp. 327–366, 1995. DOI: 10.1017/S0022112095004290.
- [115] J. F. Davidson, D. Harrison and J. R. F. G. D. Carvalho, 'On the Liquidlike Behavior of Fluidized Beds', *Annual Review of Fluid Mechanics*, vol. 9, no. 1, pp. 55–86, 1977. DOI: 10.1146/annurev.fl.09.010177.000415.
- [116] P. Rowe, P. BA, A. Cheney, G. Henwood and E. Lyall, 'Mechanisms of solids mixing in fluidised beds', *Transactions of the Institution of Chemical Engineers and the Chemical Engineer*, vol. 43, no. 9, T271, 1965.
- [117] M. Stein, Y. L. Ding, J. P. K. Seville and D. J. Parker, 'Solids motion in bubbling gas fluidised beds', *Chemical Engineering Science*, vol. 55, no. 22, pp. 5291–5300, 2000. DOI: 10.1016/S0009-2509(00)00177-9.
- [118] P. N. Rowe and B. A. Partridge, 'An x-ray study of bubbles in fluidised beds', *Chemical Engineering Research and Design*, vol. 75, no. 1 SUPPL. S116–S134, 1965. DOI: 10.1016/S0263-8762(97)80009-3.
- [119] J. R. Grace, 'The viscosity of fluidized beds', *The Canadian Journal of Chemical Engineering*, vol. 48, no. 1, pp. 30–33, 1970. DOI: 10.1002/CJCE.5450480106.
- [120] B. Singh, C. Fryer and O. E. Potter, 'Solids motion caused by a bubble in a fluidized bed', *Powder Technology*, vol. 6, no. 4, pp. 239–244, 1972. DOI: 10.1016/0032-5910(72)83018-3.
- [121] I. Eames and M. Gilbertson, 'Mixing and drift in gas-fluidised beds', *Powder Technology*, vol. 154, no. 2, pp. 185–193, 2005. DOI: <https://doi.org/10.1016/j.powtec.2005.04.036>.
- [122] J. F. Davidson, 'D., Harrison', *Fluidized Particles*, Cambridge Univ. Press, Cambridge, England, 1963.
- [123] M. Kraume, *Transportvorgänge in der Verfahrenstechnik : Grundlagen und apparative Umsetzungen ; mit 31 Tabellen*. Springer, 2004.

## Bibliography

---

- [124] R. Clift, 'Bubble interaction in fluidised beds.', 1970.
- [125] C. M. Boyce, A. Penn, M. Lehnert, K. P. Pruessmann and C. R. Müller, 'Magnetic resonance imaging of interaction and coalescence of two bubbles injected consecutively into an incipiently fluidized bed', *Chemical Engineering Science*, 2019. DOI: 10.1016/j.ces.2019.08.010.
- [126] S. P. Sit and J. R. Grace, 'Effect of bubble interaction on interphase mass transfer in gas fluidized beds', *Chemical Engineering Science*, vol. 36, no. 2, pp. 327–335, 1981. DOI: 10.1016/0009-2509(81)85012-9.
- [127] J. A. Medrano, F. Gallucci, F. Boccia, N. Alfano and M. van Sint Annaland, 'Determination of the bubble-to-emulsion phase mass transfer coefficient in gas-solid fluidized beds using a non-invasive infra-red technique', *Chemical Engineering Journal*, vol. 325, pp. 404–414, 2017. DOI: 10.1016/J.CEJ.2017.05.089.
- [128] J. R. Grace, 'Hydrodynamics of bubbling fluidization', in Wiley Online Library, 2020, pp. 131–152.
- [129] J. F. Davidson, D. Harrison and R. Jackson, *Fluidized particles: Cambridge University Press*, 1963. 155 pp. 35s, 1964.
- [130] R. Clift and J. R. Grace, 'The mechanism of bubble break-up in fluidised beds', *Chemical Engineering Science*, vol. 27, no. 12, pp. 2309–2310, 1972. DOI: 10.1016/0009-2509(72)85111-x.
- [131] G. Taylor, 'The Instability of Liquid Surfaces when Accelerated in a Direction Perpendicular to their Planes. I', *Proceedings of the Royal Society A: Mathematical, Physical and Engineering Sciences*, vol. 201, no. 1065, pp. 192–196, 1950. DOI: 10.1098/rspa.1950.0052.
- [132] J. Werther and O. Molerus, 'The local structure of gas fluidized beds —II. The spatial distribution of bubbles', *International Journal of Multiphase Flow*, vol. 1, no. 1, pp. 123–138, 1973. DOI: 10.1016/0301-9322(73)90008-6.
- [133] S. Maurer, E. C. Wagner, T. J. Schildhauer, J. R. van Ommen, S. M. A. Biollaz and R. F. Mudde, 'X-ray measurements of bubble hold-up in fluidized beds with and without vertical internals', *International Journal of Multiphase Flow*, vol. 74, pp. 118–124, 2015. DOI: <http://dx.doi.org/10.1016/j.ijmultiphaseflow.2015.03.009>.
- [134] S. Mori and C. Y. Wen, 'Estimation of bubble diameter in gaseous fluidized beds', *AIChE Journal*, vol. 21, no. 1, pp. 109–115, 1975. DOI: 10.1002/aic.690210114.
- [135] R. Darton, L. RD, D. JF and H. D, 'Bubble Growth Due To Coalescence in Fluidized Beds', *Transactions of the Institution of Chemical Engineers*, vol. 55, pp. 274–280, 1977.
- [136] R. Turton and N. N. Clark, 'Interpreting probe signals from fluidized beds', *Powder Technology*, 1989. DOI: 10.1016/0032-5910(89)80035-X.
- [137] D. Geldart, 'The effect of particle size and size distribution on the behaviour of gas-fluidised beds', *Powder Technology*, vol. 6, pp. 201–215, 4 1972. DOI: 10.1016/0032-5910(72)83014-6.

- [138] K. Lim and P. K. Agarwal, 'Conversion of pierced lengths measured at a probe to bubble size measures: An assessment of the geometrical probability approach and bubble shape models', *Powder Technology*, vol. 63, no. 3, pp. 205–219, 1990. DOI: 10.1016/0032-5910(90)80046-2.
- [139] W. Liu, N. N. Clark and A. I. Karamavruç, 'Relationship between bubble size distributions and chord-length distribution in heterogeneously bubbling systems', *Chemical Engineering Science*, vol. 53, no. 6, pp. 1267–1276, 1998. DOI: 10.1016/S0009-2509(97)00426-0.
- [140] R. Turton and N. N. Clark, 'Interpreting probe signals from fluidized beds', *Powder Technology*, 1989. DOI: 10.1016/0032-5910(89)80035-X.
- [141] W. J., 'Bubbles in gas fluidised beds (parts i and ii).', *Trans. Instn Chem. Engrs.*, vol. 52, pp. 149–169, 1974.
- [142] J. Werther, 'Messung iokaler blasengrößenverteilungen in gas/feststoff-wirbelschichten', *Chemie Ingenieur Technik*, vol. 45, pp. 375–377, 6 1973. DOI: 10.1002/CITE.330450607.
- [143] J. Davidson and D. Harrison, 'Fluidized particles', *Cambridge University Press*, 1963.
- [144] J. R. Grace and D. Harrison, 'The behaviour of freely bubbling fluidised beds', *Chemical Engineering Science*, vol. 24, no. 3, pp. 497–508, 1969. DOI: 10.1016/0009-2509(69)85021-9.
- [145] J. M. Matsen, 'Scale-up of fluidized bed processes: Principle and practice', *Powder Technology*, vol. 88, no. 3, pp. 237–244, 1996. DOI: 10.1016/s0032-5910(96)03126-9.
- [146] M. Rüdisüli, T. J. Schildhauer, S. M. Biollaz and J. R. Van Ommen, 'Scale-up of bubbling fluidized bed reactors — A review', *Powder Technology*, vol. 217, pp. 21–38, 2012. DOI: 10.1016/J.POWTEC.2011.10.004.
- [147] N. Ellis and A. Mahecha-Botero, 'Scale-up of fluidized beds', *Essentials of Fluidization Technology*, pp. 405–429, 2020. DOI: 10.1002/9783527699483.CH17.
- [148] V. V. Kelkar and K. M. Ng, 'Development of fluidized catalytic reactors: Screening and scale-up', *AIChE Journal*, vol. 48, no. 7, pp. 1498–1518, 2002. DOI: 10.1002/aic.690480714.
- [149] G. Chen, Z. Wang, G. Sun and J. Chen, 'On the methodology of process development of fluidized bed reactors', in *Fluidization: Proceedings of Fourth International Conference on Fluidization*, Engineering Foundation New York, 1984, pp. 583–590.
- [150] E. Buckingham, 'Illustrations of the use of dimensional analysis on physically similar systems', *Physics Review*, vol. 4, no. 4, pp. 354–377, 1914.
- [151] L. R. Glicksman and G. McAndrews, 'The effect of bed width on the hydrodynamics of large particle fluidized beds', *Powder Technology*, vol. 42, pp. 159–167, 2 1985. DOI: 10.1016/0032-5910(85)80049-8.
- [152] L. R. Glicksman, M. Hyre and K. Woloshun, 'Simplified scaling relationships for fluidized beds', *Powder Technology*, vol. 77, pp. 177–199, 2 1993. DOI: 10.1016/0032-5910(93)80055-F.

## Bibliography

---

- [153] J. Sanderson and M. Rhodes, 'Bubbling fluidized bed scaling laws: Evaluation at large scales', *AIChE Journal*, vol. 51, no. 10, pp. 2686–2694, 2005. DOI: 10.1002/aic.10511.
- [154] J. R. van Ommen, M. Teuling, J. Nijenhuis and B. G. M. van Wachem, 'Computational validation of the scaling rules for fluidized beds', *Powder Technology*, vol. 163, no. 1-2, pp. 32–40, 2006. DOI: 10.1016/j.powtec.2006.01.010.
- [155] B. Leckner, P. Szentannai and F. Winter, 'Scale-up of fluidized-bed combustion – A review', *Fuel*, vol. 90, no. 10, pp. 2951–2964, 2011. DOI: 10.1016/j.fuel.2011.04.038.
- [156] P. U. Foscolo, L. G. Gibilaro and R. Felice, 'Hydrodynamic scaling relationships for fluidisation', *Applied Scientific Research*, vol. 48, no. 3-4, pp. 315–328, 1991. DOI: 10.1007/bf02008203.
- [157] J. R. Grace and F. Taghipour, 'Verification and validation of cfd models and dynamic similarity for fluidized beds', *Powder Technology*, vol. 139, pp. 99–110, 2 2004. DOI: 10.1016/J.POWTEC.2003.10.006.
- [158] M. S. Detamore, M. A. Swanson, K. R. Frender and C. M. Hrenya, 'A kinetic-theory analysis of the scale-up of circulating fluidized beds', *Powder Technology*, vol. 116, pp. 190–203, 2-3 2001. DOI: 10.1016/S0032-5910(00)00397-1.
- [159] N. G. Deen, M. V. S. Annaland, M. A. V. der Hoef and J. A. Kuipers, 'Review of discrete particle modeling of fluidized beds', *Chemical Engineering Science*, vol. 62, pp. 28–44, 1-2 2007. DOI: 10.1016/J.CES.2006.08.014.
- [160] M. Horio, A. Nonaka, Y. Sawa and I. Muchi, 'A new similarity rule for fluidized bed scale-up', *AIChE Journal*, vol. 32, no. 9, pp. 1466–1482, 1986. DOI: 10.1002/aic.690320908.
- [161] M. Rüdisüli, T. J. Schildhauer, S. M. A. Biollaz and J. R. van Ommen, 'Evaluation of a sectoral scaling approach for bubbling fluidized beds with vertical internals', *Chemical Engineering Journal*, vol. 197, pp. 435–439, 2012. DOI: 10.1016/j.cej.2012.04.097.
- [162] S. Maurer, T. J. Schildhauer, J. R. van Ommen, S. M. A. Biollaz and A. Wokaun, 'Scale-up of fluidized beds with vertical internals: Studying the sectoral approach by means of optical probes', *Chemical Engineering Journal*, vol. 252, pp. 131–140, 2014. DOI: <http://dx.doi.org/10.1016/j.cej.2014.04.083>.
- [163] S. Sasic, B. Leckner and F. Johnsson, 'Characterization of fluid dynamics of fluidized beds by analysis of pressure fluctuations', *Progress in Energy and Combustion Science*, vol. 33, no. 5, pp. 453–496, 2007. DOI: 10.1016/J.PECS.2007.03.001.
- [164] F. Schillinger, S. Maurer, E. C. Wagner, J. R. van Ommen, R. F. Mudde and T. J. Schildhauer, 'Influence of vertical heat exchanger tubes, their arrangement and the column diameter on the hydrodynamics in a gas-solid bubbling fluidized bed', *International Journal of Multiphase Flow*, vol. 97, pp. 46–59, 2017. DOI: <http://dx.doi.org/10.1016/j.ijmultiphaseflow.2017.07.013>.
- [165] J. Liu, J. R. Grace and X. Bi, 'Novel multifunctional optical-fiber probe: I. Development and validation', *AIChE Journal*, vol. 49, no. 6, pp. 1405–1420, 2003. DOI: 10.1002/aic.690490607.

- [166] S. Maurer, M. Rüdisüli, T. J. Schildhauer, S. M. A. Biollaz, J. Ruud Van Ommen and J. A. M. Kuipers, 'Scale-up of bubbling fluidized bed reactors with vertical internals: a new approach accounting for chemistry and hydrodynamics', *ECI Symposium Series*, 2013.
- [167] S. Maurer, E. C. Wagner, T. J. Schildhauer, J. R. van Ommen, S. M. A. Biollaz and R. F. Mudde, 'X-ray measurements on the influence of optical probes on gas–solid fluidized beds', *International Journal of Multiphase Flow*, vol. 74, pp. 143–147, 2015.
- [168] S. Maurer, D. Gschwend, E. C. Wagner *et al.*, 'Correlating bubble size and velocity distribution in bubbling fluidized bed based on X-ray tomography', *Chemical Engineering Journal*, vol. 298, pp. 17–25, 2016. DOI: <http://dx.doi.org/10.1016/j.cej.2016.02.012>.
- [169] F. Schillinger, T. Schildhauer, S. Maurer, E. Wagner, R. Mudde and J. van Ommen, 'Generation and evaluation of an artificial optical signal based on X-ray measurements for bubble characterization in fluidized beds with vertical internals', *International Journal of Multiphase Flow*, 2018. DOI: [10.1016/j.ijmultiphaseflow.2018.03.002](https://doi.org/10.1016/j.ijmultiphaseflow.2018.03.002).
- [170] R. F. Mudde, 'Bubbles in a fluidized bed: A fast X-ray scanner', *AIChE J.*, vol. 57, no. 10, pp. 2684–2690, 2011. DOI: [10.1002/aic.12469](https://doi.org/10.1002/aic.12469).
- [171] T. J. Seebeck, *Ueber den Magnetismus der galvanischen Kette*. 1822.
- [172] S. Brunauer, P. H. Emmett and E. Teller, 'Adsorption of gases in multimolecular layers', *Journal of the American Chemical Society*, vol. 60, pp. 309–319, 2 1938. DOI: [10.1021/JA01269A023](https://doi.org/10.1021/JA01269A023).
- [173] M. Rüdisüli, T. J. Schildhauer, S. M. A. Biollaz, A. Wokaun and J. R. van Ommen, 'Comparison of bubble growth obtained from pressure fluctuation measurements to optical probing and literature correlations', *Chemical Engineering Science*, vol. 74, pp. 266–275, 2012. DOI: <http://dx.doi.org/10.1016/j.ces.2012.01.045>.
- [174] F. A. Zenz and D. F. Othmer, *Fluidization and fluid particle systems*. Reinhold, 1960.
- [175] M. P. Dudukovic, 'Opaque multiphase reactors: Experimentation, modeling and troubleshooting', *Oil Gas Science and Technology-Rev. IFP*, vol. 55, pp. 135–158, 2 2000.
- [176] T. J. Heindel, 'A review of x-ray flow visualization with applications to multiphase flows', *Journal of Fluids Engineering*, vol. 133, no. 7, 2011.
- [177] M. P. Dudukovic, F. Larachi and P. L. Mills, 'Multiphase reactors – revisited', *Chemical Engineering Science*, vol. 54, pp. 1975–1995, 13-14 1999. DOI: [10.1016/S0009-2509\(98\)00367-4](https://doi.org/10.1016/S0009-2509(98)00367-4).
- [178] S. Sundaresan, 'Modeling the hydrodynamics of multiphase flow reactors: Current status and challenges', *AIChE Journal*, vol. 46, pp. 1102–1105, 6 2000. DOI: [10.1002/AIC.690460602](https://doi.org/10.1002/AIC.690460602).
- [179] C. Poelma, 'Measurement in opaque flows: A review of measurement techniques for dispersed multiphase flows', *Acta Mechanica*, vol. 231, pp. 2089–2111, 6 2020. DOI: [10.1007/S00707-020-02683-X](https://doi.org/10.1007/S00707-020-02683-X).

## Bibliography

---

- [180] C. R. Müller, D. J. Holland, A. J. Sederman, M. D. Mantle, L. F. Gladden and J. F. Davidson, 'Magnetic resonance imaging of fluidized beds', *Powder Technology*, vol. 183, pp. 53–62, 1 2008. DOI: 10.1016/J.POWTEC.2007.11.029.
- [181] C. M. Boyce, A. Penn, M. Lehnert, K. P. Pruessmann and C. R. Müller, 'Magnetic resonance imaging of single bubbles injected into incipiently fluidized beds', *Chemical Engineering Science*, 2019. DOI: 10.1016/j.ces.2019.01.047.
- [182] C. Boyce, A. Penn, M. Lehnert, K. Pruessmann and C. Müller, 'Wake volume of injected bubbles in fluidized beds: A magnetic resonance imaging velocimetry study', *Powder Technology*, vol. 357, pp. 428–435, 2019. DOI: 10.1016/j.powtec.2019.02.021.
- [183] D. Feng, X. Cong, Z. ZHANG and R. Shangjie, 'Design of parallel electrical resistance tomography system for measuring multiphase flow', *Chinese Journal of Chemical Engineering*, vol. 20, no. 2, pp. 368–379, 2012.
- [184] F. Ricard, C. Brechtelsbauer, X. Xu and C. Lawrence, 'Monitoring of multiphase pharmaceutical processes using electrical resistance tomography', *Chemical Engineering Research and Design*, vol. 83, no. 7, pp. 794–805, 2005.
- [185] Q. Marashdeh, L.-S. Fan, B. Du and W. Warsito, 'Electrical capacitance tomography- a perspective', *Industrial & Engineering Chemistry Research*, vol. 47, no. 10, pp. 3708–3719, 2008.
- [186] E. Mohamad, R. Rahim, M. Rahiman, H. Ameran, S. Muji and O. Marwah, 'Measurement and analysis of water/oil multiphase flow using electrical capacitance tomography sensor', *Flow Measurement and Instrumentation*, vol. 47, pp. 62–70, 2016.
- [187] M. Vatanakul, Y. Zheng and M. Couturier, 'Application of ultrasonic technique in multiphase flows', *Industrial and Engineering Chemistry Research*, vol. 43, pp. 5681–5691, 18 2004. DOI: 10.1021/IE034184C.
- [188] M. T. M. Khairi, S. Ibrahim, M. A. M. Yunus *et al.*, 'Ultrasound computed tomography for material inspection: Principles, design and applications', *Measurement*, vol. 146, pp. 490–523, 2019. DOI: 10.1016/J.MEASUREMENT.2019.06.053.
- [189] R. Mudde, P. Bruneau and T. Van der Hagen, 'Time-resolved  $\gamma$ -densitometry imaging within fluidized beds', *Industrial & engineering chemistry research*, vol. 44, no. 16, pp. 6181–6187, 2005.
- [190] T. J. Heindel, J. N. Gray and T. C. Jensen, 'An X-ray system for visualizing fluid flows', *Flow Measurement and Instrumentation*, vol. 19, no. 2, pp. 67–78, 2008. DOI: 10.1016/j.flowmeasinst.2007.09.003.
- [191] M. Bieberle, F. Barthel and U. Hampel, 'Ultrafast X-ray computed tomography for the analysis of gas–solid fluidized beds', *Chemical Engineering Journal*, vol. 189–190, pp. 356–363, 2012. DOI: 10.1016/j.cej.2012.02.028.
- [192] U. Hampel, L. Babout, R. Banasiak *et al.*, 'A Review on Fast Tomographic Imaging Techniques and Their Potential Application in Industrial Process Control', *Sensors*, vol. 22, no. 6, p. 2309, 2022. DOI: 10.3390/S22062309.



- [193] J. H. Scatliff and P. J. Morris, 'From roentgen to magnetic resonance imaging: The history of medical imaging', *North Carolina medical journal*, vol. 75, no. 2, pp. 111–113, 2014.
- [194] R. A. Brooks and G. Di Chiro, 'Beam hardening in x-ray reconstructive tomography', *Physics in medicine & biology*, vol. 21, no. 3, p. 390, 1976.
- [195] R. F. Mudde, J. Alles and T. H. J. J. van der Hagen, 'Feasibility study of a time-resolving x-ray tomographic system', *Measurement Science and Technology*, vol. 19, no. 8, p. 85 501, 2008.
- [196] F. Fischer, D. Hoppe, E. Schleicher *et al.*, 'An ultra fast electron beam x-ray tomography scanner', *Measurement science and technology*, vol. 19, no. 9, p. 094 002, 2008.
- [197] F. Fischer and U. Hampel, 'Ultra fast electron beam X-ray computed tomography for two-phase flow measurement', *Nuclear Engineering and Design*, vol. 240, no. 9, pp. 2254–2259, 2010. DOI: 10.1016/j.nucengdes.2009.11.016.
- [198] M. Bieberle and F. Barthel, 'Combined phase distribution and particle velocity measurement in spout fluidized beds by ultrafast X-ray computed tomography', *Chemical Engineering Journal*, vol. 285, pp. 218–227, 2016. DOI: <https://doi.org/10.1016/j.cej.2015.10.003>.
- [199] Y. M. Lau, F. Möller, U. Hampel and M. Schubert, 'Ultrafast X-ray tomographic imaging of multiphase flow in bubble columns - Part 2: Characterisation of bubbles in the dense regime', *International Journal of Multiphase Flow*, 2018. DOI: 10.1016/j.ijmultiphaseflow.2018.02.009.
- [200] S. Maurer, E. C. Wagner, J. R. van Ommen *et al.*, 'Influence of vertical internals on a bubbling fluidized bed characterized by X-ray tomography', *International Journal of Multiphase Flow*, vol. 75, pp. 237–249, 2015. DOI: 10.1016/j.ijmultiphaseflow.2015.06.001.
- [201] R. F. Mudde, 'Time-resolved X-ray tomography of a fluidized bed', *Powder Technology*, vol. 199, no. 1, pp. 55–59, 2010. DOI: <http://dx.doi.org/10.1016/j.powtec.2009.04.021>.
- [202] P. J. Green, 'Bayesian reconstructions from emission tomography data using a modified em algorithm', *IEEE transactions on medical imaging*, vol. 9, no. 1, pp. 84–93, 1990.
- [203] J. Saayman, W. Nicol, J. R. Van Ommen and R. F. Mudde, 'Fast x-ray tomography for the quantification of the bubbling-, turbulent-and fast fluidization-flow regimes and void structures', *Chemical engineering journal*, vol. 234, pp. 437–447, 2013.
- [204] X. Yang, J. R. van Ommen and R. F. Mudde, 'Comparison of genetic algorithm and algebraic reconstruction for x-ray tomography in bubbling fluidized beds', *Powder technology*, vol. 253, pp. 626–637, 2014.
- [205] Y. Lau, U. Hampel and M. Schubert, 'Ultrafast x-ray tomographic imaging of multiphase flow in bubble columns-part 1: Image processing and reconstruction comparison', *International Journal of Multiphase Flow*, vol. 104, pp. 258–271, 2018.

## Bibliography

---

- [206] C. Rautenbach, R. F. Mudde, M. C. Melaaen and B. M. Halvorsen, 'The influence of the experimental span of Time- resolved X-ray tomography on dynamic parameters in a fluidized bed', *Group*, no. November, pp. 1–10, 2011.
- [207] Yury, *Ellipsoid fit*, MATLAB Central File Exchange. Retrieved May 27, 2022.
- [208] S. Demarta and A. J. Mcneil, 'The t copula and related copulas', vol. 73, pp. 111–129, 1 2005.
- [209] A. Kantzas, 'X-ray tomography of fluidized beds', *Industrial Tomography: Systems and Applications*, pp. 451–475, 2015. DOI: 10.1016/B978-1-78242-118-4.00017-4.
- [210] J. Werther, 'Scale-up modeling for fluidized bed reactors', *Chemical Engineering Science*, vol. 47, no. 9, pp. 2457–2462, 1992. DOI: [http://dx.doi.org/10.1016/0009-2509\(92\)87076-3](http://dx.doi.org/10.1016/0009-2509(92)87076-3).
- [211] A. Kiashemshaki, N. Mostoufi and R. Sotudeh-Gharebagh, 'Two-phase modeling of a gas phase polyethylene fluidized bed reactor', *Chemical Engineering Science*, vol. 61, no. 12, pp. 3997–4006, 2006.
- [212] P. Kaushal, T. Proell and H. Hofbauer, 'Application of a detailed mathematical model to the gasifier unit of the dual fluidized bed gasification plant', *Biomass and Bioenergy*, vol. 35, no. 7, pp. 2491–2498, 2011.
- [213] P. N. Rowe and C. X. R. Yacono, 'The bubbling behaviour of fine powders when fluidised', *Chemical Engineering Science*, vol. 31, no. 12, pp. 1179–1192, 1976. DOI: 10.1016/0009-2509(76)85027-0.
- [214] N. N. Clark, W. Liu and R. Turton, 'Data interpretation techniques for inferring bubble size distribution from probe signals in fluidized systems', *Powder Technology*, 1996. DOI: 10.1016/0032-5910(96)03113-0.
- [215] H. Ohya, M. Okada, K. Okuno *et al.*, 'Bubble size and frequency in gas fluidized beds', *Journal of Chemical Engineering of Japan*, vol. 21, no. 2, pp. 171–178, 1988. DOI: 10.1252/JCEJ.21.171.
- [216] J. S. Halow, G. E. Fasching, P. Nicoletti and J. L. Spenik, 'Observations of a fluidized bed using capacitance imaging', *Chemical Engineering Science*, vol. 48, no. 4, pp. 643–659, 1993. DOI: 10.1016/0009-2509(93)80133-B.
- [217] W. Liu and N. N. Clark, 'Relationships between distributions of chord lengths and distributions of bubble sizes including their statistical parameters', *International Journal of Multiphase Flow*, 1995. DOI: 10.1016/0301-9322(95)00039-Z.
- [218] J. Werther and O. Molerus, 'The local structure of gas fluidized beds - I. A statistically based measuring system', *International Journal of Multiphase Flow*, vol. 1, no. 1, pp. 103–122, 1973. DOI: [http://dx.doi.org/10.1016/0301-9322\(73\)90007-4](http://dx.doi.org/10.1016/0301-9322(73)90007-4).
- [219] T. Kai, M. Misawa, T. Takahashi, I. Tiseanu and N. Ichikawa, 'Observation of 3-D Structure of Bubbles in a Fluidized Catalyst Bed', *The Canadian Journal of Chemical Engineering*, vol. 83, no. 1, pp. 113–118, 2008. DOI: 10.1002/cjce.5450830119.

- [220] V. Verma, J. T. Padding, N. G. Deen *et al.*, 'Bubble dynamics in a 3-D gas-solid fluidized bed using ultrafast electron beam X-ray tomography and two-fluid model', *AIChE Journal*, vol. 60, no. 5, pp. 1632–1644, 2014. DOI: 10.1002/aic.14393.
- [221] T. Chiba, K. Terashima and H. Kobayashi, 'Behaviour of bubbles in gas-solids fluidized beds: Initial formation of bubbles', *Chemical Engineering Science*, vol. 27, pp. 965–972, 5 1972. DOI: 10.1016/0009-2509(72)80011-3.
- [222] X. Yang, J. R. van Ommen and R. F. Mudde, 'Comparison of genetic algorithm and algebraic reconstruction for X-ray tomography in bubbling fluidized beds', *Powder Technology*, vol. 253, pp. 626–637, 2014. DOI: <http://dx.doi.org/10.1016/j.powtec.2013.12.007>.
- [223] G. C. Brouwer, E. C. Wagner, J. R. van Ommen and R. F. Mudde, 'Effects of pressure and fines content on bubble diameter in a fluidized bed studied using fast X-ray tomography', *Chemical Engineering Journal*, vol. 207-208, pp. 711–717, 2012. DOI: 10.1016/J.CEJ.2012.07.040.
- [224] J. Gómez-Hernández, J. Ruud van Ommen, E. Wagner and R. F. Mudde, 'A fast reconstruction algorithm for time-resolved X-ray tomography in bubbling fluidized beds', *Powder Technology*, vol. 290, pp. 33–44, 2016. DOI: 10.1016/J.POWTEC.2015.08.038.
- [225] J. Ma, J. R. van Ommen, D. Liu *et al.*, 'Fluidization dynamics of cohesive Geldart B particles. Part I: X-ray tomography analysis', *Chemical Engineering Journal*, vol. 359, pp. 1024–1034, 2019. DOI: 10.1016/J.CEJ.2018.11.082.
- [226] D. Verhoeven, 'Limited-data computed tomography algorithms for the physical sciences', *Applied Optics*, Vol. 32, Issue 20, pp. 3736-3754, vol. 32, no. 20, pp. 3736–3754, 1993. DOI: 10.1364/AO.32.003736.
- [227] P. Dirac, 'Approximate rate of neutron multiplication for a solid of arbitrary shape and uniform density', *Declassified British Report MS-D-5, Part I*, 1943.
- [228] P. Rowe, P. Foscolo, A. Hoffmann and J. Yates, 'X-ray observation of gas fluidized beds under pressure', *Fluidization IV*, p. 53, 1984.
- [229] H. W. Piepers, E. J. Cottaar, A. H. Verkooyen and K. Rietema, 'Effects of pressure and type of gas on particle-particle interaction and the consequences for gas—solid fluidization behaviour', *Powder Technology*, vol. 37, pp. 55–70, 1 1984. DOI: 10.1016/0032-5910(84)80006-6.
- [230] K. V. Jacob and A. W. Weimer, 'High-pressure particulate expansion and minimum bubbling of fine carbon powders', *AIChE Journal*, vol. 33, pp. 1698–1706, 10 1987. DOI: 10.1002/AIC.690331013.
- [231] A. Marzocchella and P. Salatino, 'Fluidization of solids with co<sub>2</sub> at pressures from ambient to supercritical', *AIChE Journal*, vol. 46, pp. 901–910, 5 2000. DOI: 10.1002/AIC.690460505.
- [232] T. Varadi and J. R. Grace, *High pressure fluidization in a two-dimensional bed*. J. E. Davidson and D. L. Keairns, Eds., 1978.

## Bibliography

---

- [233] L. E. Sobreiro and J. L. Monteiro, 'The effect of pressure on fluidized bed behaviour', *Powder Technology*, vol. 33, pp. 95–100, 1 1982. DOI: 10.1016/0032-5910(82)85043-2.
- [234] A. W. Weimer and G. J. Quaderer, 'On dense phase voidage and bubble size in high pressure fluidized beds of fine powders', *AIChE Journal*, vol. 31, no. 6, pp. 1019–1028, 1985. DOI: 10.1002/aic.690310619.
- [235] I. H. Chan, C. Sishla and T. M. Knowlton, 'The effect of pressure on bubble parameters in gas-fluidized beds', *Powder Technology*, vol. 53, pp. 217–235, 3 1987. DOI: 10.1016/0032-5910(87)80096-7.
- [236] J. Wiman and A. E. Almstedt, 'Influence of pressure, fluidization velocity and particle size on the hydrodynamics of a freely bubbling fluidized bed', *Chemical Engineering Science*, vol. 53, pp. 2167–2176, 12 1998. DOI: 10.1016/S0009-2509(98)00056-6.
- [237] D. F. King and D. Harrison, 'The bubble phase in high-pressure fluidised beds', in *Fluidization*, J. R. Grace and J. M. Matsen, Eds. Boston, MA: Springer US, 1980, pp. 101–108. DOI: 10.1007/978-1-4684-1045-7\_5.
- [238] J.-I. Kawabata, M. Yumiyama, Y. Tazaki, S. Honma, T. Sumiya and K. Endo, 'Characteristics of gas-fluidised beds under pressure',
- [239] A. C. Hoffmann and J. G. Yates, 'Experimental observations of fluidized beds at elevated pressures', <https://doi.org/10.1080/00986448608911716>, 1- 1986. DOI: 10.1080/00986448608911716.
- [240] P. A. Olowson and A. E. Almstedt, 'Hydrodynamics of a bubbling fluidized bed: influence of pressure and fluidization velocity in terms of drag force', *Chemical Engineering Science*, vol. 47, no. 2, pp. 357–366, 1992. DOI: 10.1016/0009-2509(92)80026-9.
- [241] M. Gilbertson, D. Cheesman and J. Yates, 'Observations and measurements of isolated bubbles in a pressurized gas-fluidized bed', in *Fluidization IX*, Engineering Foundation Durango, 1998, p. 61.
- [242] P. Olowson and A.-E. Almstedt, 'Influence of pressure and fluidization velocity on the bubble behaviour and gas flow distribution in a fluidized bed', *Chemical Engineering Science*, vol. 45, no. 7, pp. 1733–1741, 1990.
- [243] J. Shabanian and J. Chaouki, *Effects of temperature, pressure, and interparticle forces on the hydrodynamics of a gas-solid fluidized bed*, 2017. DOI: 10.1016/j.cej.2016.12.061.
- [244] V. Verma, J. T. Padding, N. G. Deen *et al.*, 'Bubble dynamics in a 3-D gas-solid fluidized bed using ultrafast electron beam X-ray tomography and two-fluid model', *AIChE Journal*, vol. 60, no. 5, pp. 1632–1644, 2014. DOI: 10.1002/aic.14393.
- [245] D. Santana, J. Rodríguez-Rodríguez, J. Almendros-Ibáñez and C. Martínez-Bazán, 'Characteristic lengths and maximum entropy estimation from probe signals in the ellipsoidal bubble regime', *International Journal of Multiphase Flow*, vol. 32, no. 9, pp. 1123–1139, 2006. DOI: 10.1016/j.ijmultiphaseflow.2006.05.006.
- [246] M. Rüdisüli, T. J. Schildhauer, S. M. Biollaz and J. R. van Ommen, 'Monte Carlo simulation of the bubble size distribution in a fluidized bed with intrusive probes', *Interna-*

- tional Journal of Multiphase Flow*, vol. 44, pp. 1–14, 2012. DOI: 10.1016/j.ijmultiphaseflow.2012.03.009.
- [247] S. Dias, F. França and E. Rosa, ‘Statistical method to calculate local interfacial variables in two-phase bubbly flows using intrusive crossing probes’, *International journal of multiphase flow*, vol. 26, no. 11, pp. 1797–1830, 2000.
- [248] N. N. Clark and R. Turton, ‘Chord length distributions related to bubble size distributions in multiphase flows’, *Int. J. Multiphase Flow*, vol. 14, no. 4, pp. 413–424, 1988. DOI: [http://dx.doi.org/10.1016/0301-9322\(88\)90019-5](http://dx.doi.org/10.1016/0301-9322(88)90019-5).
- [249] W. Liu, N. N. Clark and A. I. Karamavruc, ‘General method for the transformation of chord-length data to a local bubble-size distribution’, *AIChE Journal*, vol. 42, no. 10, pp. 2713–2720, 1996. DOI: 10.1002/aic.690421003.
- [250] E. T. Jaynes, ‘Information theory and statistical mechanics’, *Physical review*, vol. 106, no. 4, p. 620, 1957.
- [251] C. Sobrino, J. A. Almendros-Ibáñez, D. Santana, C. Vázquez and M. de Vega, ‘Maximum entropy estimation of the bubble size distribution in fluidized beds’, *Chemical Engineering Science*, 2009. DOI: 10.1016/j.ces.2009.01.046.
- [252] P. A. Olowson and A. E. Almstedt, ‘Influence of pressure on the minimum fluidization velocity’, *Chemical Engineering Science*, vol. 46, pp. 637–640, 2 1991. DOI: 10.1016/0009-2509(91)80023-R.
- [253] Z. Zhiping, N. Yongjie and L. Qinggang, ‘Effect of pressure on minimum fluidization velocity’, *Journal of Thermal Science*, vol. 16, pp. 264–269, 3 2007. DOI: 10.1007/S11630-007-0264-2.
- [254] L. Li, Y. Duan, L. Duan, C. Xu and E. J. Anthony, ‘Flow characteristics in pressurized oxy-fuel fluidized bed under hot condition’, *International Journal of Multiphase Flow*, vol. 108, pp. 1–10, 2018. DOI: 10.1016/J.IJMULTIPHASEFLOW.2018.06.020.
- [255] Y. Shao, Z. Li, W. Zhong, Z. Bian and A. Yu, ‘Minimum fluidization velocity of particles with different size distributions at elevated pressures and temperatures’, *Chemical Engineering Science*, vol. 216, p. 115 555, 2020. DOI: 10.1016/J.CES.2020.115555.
- [256] J. G. Yates, ‘Effects of temperature and pressure on gas-solid fluidization’, *Chemical Engineering Science*, vol. 51, pp. 167–205, 2 1996. DOI: 10.1016/0009-2509(95)00212-X.
- [257] M. Tsukada, D. Nakanishi and M. Horio, ‘The effect of pressure on the phase transition from bubbling to turbulent fluidization’, *International journal of multiphase flow*, vol. 19, no. 1, pp. 27–34, 1993.
- [258] X. Zhu, P. Dong, Z. Zhu, R. Ocone, W. Yang and H. Wang, ‘Effects of pressure on flow regimes transition velocities and bubble properties in a pilot-scale pressurised circulating fluidised bed’, *Chemical Engineering Journal*, vol. 410, p. 128 438, 2021. DOI: 10.1016/J.CEJ.2021.128438.

## Bibliography

---

- [259] X. Ma, Z. Sun, H. Luo and X. Li, 'A novel fiber optic sensor for microparticle velocity measurement using multicore fiber', *Applied Sciences* 2020, Vol. 10, Page 4829, vol. 10, p. 4829, 14 2020. DOI: 10.3390/APP10144829.
- [260] S. Golshan, G. S. Patience, R. Zarghami, J. Chaouki and B. Blais, 'Experimental methods in chemical engineering: Optical fibre probes in multiphase systems', *The Canadian Journal of Chemical Engineering*, 2022.

# Curriculum Vitae

## PERSONAL INFORMATION

---

Philipp Fedor Riechmann

Birth date: 18 February 1987

Place of birth: Berlin, Germany

Nationality: German

## EDUCATION

---

- Since 05/2018     **PhD student**  
EPF Lausanne, Paul Scherrer Institut, Switzerland  
**Advisor:** Professor Oliver Kröcher  
**Co-Advisor:** Dr. Tilman Schildhauer  
**Thesis:** Cross verified independent measurements of correlated bubble property distributions as part of the scale-up of a catalytic bubbling fluidized bed reactor
- 10/2006–04/2017     **Dipl.Eng., Energy and process technology**  
Technical University Berlin, Germany  
**Thesis:** Investigation of the influence of the metal masses of a packed column on the dynamics of the rectification system of an air separation plant  
*Linde Engineering Division, Pullach*  
**Advisor:** Professor Jens-Uwe Repke  
**Co-Advisors:** Dr. Bernd Wunderlich, Dr. Erik Esche
- 08/2015–03/2016     **Semester project**  
Technical University Berlin, Germany  
**Thesis:** Experimental investigation of the influence of ions on coalescence in liquid/liquid dispersions  
**Advisor:** Dr. Jörn Villwock

## PROFESSIONAL EXPERIENCE

---

- 02/2016–05.2016     **Linde Engineering Division, Pullach, Germany**  
Position: Internship  
Project: FlexASU, dynamic process simulation  
Supervisor: Dr. Christoph Windmeier

Wettingen - Switzerland, November 2, 2022